VHF BOUNDARY LAYER RADAR AND RASS

By

Andrew D. MacKinnon, B.Sc (Hons)

Thesis
submitted for the degree of
DOCTOR OF PHILOSOPHY
at the
UNIVERSITY OF ADELAIDE
(Department of Physics and Mathematical Physics)

February 2001

This work contains no material which has been accepted for the award of any other degree or diploma in any university or other tertiary institution and, to the best of my knowledge and belief, contains no material previously published or written by another person, except where due reference has been made in the text.

I give consent to this copy of my thesis, when deposited in the University Library, being available for loan and photocopying.

Signed: .... dated: ....

Andrew D. MacKinnon, B.Sc (Hons)

Abstract

This thesis describes the refinements, modifications and additions to a prototype Very High Frequency (VHF) Boundary Layer (BL) Spaced Antenna (SA) radar initially installed at the University of Adelaide's Buckland Park field site in 1997.

Previous radar observations of the lowest few kilometres of the atmosphere, in particular the Atmospheric Boundary Layer, have used Ultra-High Frequency (UHF) radars. Unlike VHF radars, UHF radars are extremely sensitive to hydro-meteors and have difficulty in distinguishing clear-air echoes from precipitation returns. The advantages and requirements of using a VHF radar to observe the lowest heights is discussed in conjunction with some of the limitations.

The successful operation of the system over long periods has enabled in-depth investigation of the performance of the system in a variety of conditions and locations. Observations were made from as low as 300m and as high as 8 km, dependent upon conditions. Comparisons between the radar and alternative wind measuring devices were carried out and examined.

The antenna system of the radar is a critical component which was analysed in depth and subsequently re-designed. Through the use of numerical models and measurements, evaluation of different designs was accomplished. Further calibration of the remaining components of the full system has enabled estimations of the absolute received power. Additional parameters which can be derived with a calibrated radar were compared with values obtained by other authors, giving favourable results.

Full Correlation Analysis (FCA) is the predominant technique used in this work. A brief discussion of the background theory and parameters which can be measured is described. A simple one-dimensional model was developed and combined with a "radar backscatter model" to investigate potential sources of errors in the parameters determined using FCA with the VHF Boundary Layer Radar. In particular, underestimations in the wind velocity were examined.

The integration of a Radio Acoustic Sounding System (RASS) to obtain temperature profiles is discussed. The theory of RASS measurements including the limitations and considerations which are required for the VHF BL radar are given. The difficulties encountered trying to implement such a system and the subsequent success using a Stratospheric Tropospheric (ST) Profiler in place of the BL radar is presented.

Taken as a whole this thesis shows the success of the VHF BL to obtain measurements from as low as 300m. The validation of this prototype radar provides an alternative and, in certain situations, a superior device with which to study the lower troposphere.

Acknowledgements

Inevitably the acknowledgements is the last thing written and often the first thing (and in many case the only thing) people will read. The light at the end of the tunnel is suddenly a lot brighter and everything looks...well the same, albeit through tired eyes. Its a strange feeling to think that something that has completely dominated my life for the last few months is suddenly gone, (and I think it has taken a fair old chunk of my hair with it). There are so many people that are deserving of thanks, that an appendix could be added. However, I will try to thank as many of those people as I can.

Firstly I would like to thank my supervisors Dr. Bob Vincent and Dr. Iain Reid. I would particularly like to thank Bob for all the help he has given, especially in the last few months. His advice, knowledge, proof-reading and willingness to be, but a phone call away have been very much appreciated. Thanks is extended to Dr. David Holdsworth for providing the code for the backscatter model and in all respects, other than name, being an additional supervisor.

The members of the Atmospheric Physics group have, to the most part, been a great bunch of people to work with and their assistance and help is acknowledged. Of the (many) years the group has consisted of Alireza Kazempour, Andrew Dowdy, Andrew Taylor, Brenton Vandepeer, Bridget Hobbs, Chris Lucas, Daniel Badger, David Low, David Holdsworth, Deepak Rajopadhyaya, Dorothy Gibson-Wilde, Florian Zink, Graham Elford, Jonathan Woithe, Karen Berkefeld, Laurie Campbell, Manuel Cervera, Minh Nguyen, Pham Nga, Rupa Vuthaluru, Scott Dullaway, Simon Allen, Stephen Grant and Sujata Kovalam.

For helping keep the radar working, I would like to thank Scott, Brian Fuller and the rest of the Genesis team, Florian, Alex Didenko and Malcolm Kirby. I would like to thank the guys at ATRAD, for help with the RASS sound card and for providing a great working environment.

Thanks is extended to Dr. Chris Coleman for his help with NEC and the measuring of the antenna coupling. I would like to thank Jon Barnes for his help with the antenna ("black magic") side of things.

Field campaigns are always fun exciting things, until everything goes wrong, it starts to rain, a hundred flies decided to take a personal interest or you find yourself in fog at 3 o'clock in the morning struggling to stay awake as you launch yet another balloon. Luckily the people who I shared these experiences with were all a great bunch of people. Thanks must be given to the the following: the CAFE 98 crew, Michael Reader (for giving me the opportunity in the first place), Roger Smith, Todd Lane, Zsuzsanna Racz and Maria Peristeri; Florian, Bob and Chris for helping drag the RASS speakers around. Bob and Richard McMahon for the Sydney trials; Steve, Bridget, Florian, Laurie, and Harold Richter for the sonde launching and the staff at the Bureau of Meteorology's stations at Adelaide airport, Kent Town, Alice Springs, Mt. Gambier and Sydney's Mascot airport.

Peter May's helpful comments, suggestions and knowledge was highly appreciated. I would like to thank Dallas Kirby for being a wonderful source of information and Donna Riordan for her access to Adelaide airport sonde data.

My sanity has been maintained through my Ph.D by a great group of friends and family. I would like to thank Florian, (the most tolerate person I've ever met), and Vic 'Luigi' Pisani for being two wonderful people to live with. Thanks must be extended to Pete Murenu, who was always happy to go for a spin not matter what time and is a great friend as he made the mistake of offering to proof-read my thesis. A great deal of gratitude must be given to Ma, Ba and Eilin who helped keep me feed and made me feel part of their family. The support of my Mum and Dad was without bounds, I only hope when I beome a father I can be as great a parent as they have been to me.

The last person and the most important person that I want to thank is my partner ('buddy') Linda. She maintained my grip and link to the outside world in so many ways during these last final months. For this, and so many other reasons I love her dearly. To both my parents and Linda I thank you for reading through my thesis even though it was not the most interesting things to read.

A brief anti-acknowledgement is extend to the bastard who stole my motorbike while I was writing up and Western QBE who verified all the preconceived ideas I had about insurance companies.

Contents

List of Tables

List of Figures

Chapter 1

Introduction

The need to obtain profiles of atmospheric parameters in the lower troposphere, especially the boundary layer, has increased in the last decade. This has been driven by the need to better understand local meteorology (i.e. sea breezes, nocturnal inversions and jets, lee waves, etc.), for improved forecasting. The significant operational cost of radiosondes, plus their inability to obtain more than a "snapshot" of the atmosphere, has encouraged the development and acceptance of ground-based radars[1] as an alternative measuring device. The detection of wind shears at airports and the tracking of pollution plumes are two applications that take advantage of the abilities offered by radars. The increasing complexity of atmospheric models has spawned the need for high-temporal resolution information that radars can provide.

Very-High Frequency (VHF) radars (f $\sim$ 50 MHz) have been used in the past to observe the atmosphere above 1.5 - 2.0 km altitude, while below these heights Ultra-High Frequency (UHF) (f $\sim$ 1 GHz) radars have provided observations. UHF radars are however, extremely sensitive to Rayleigh scattering from birds, insects and precipitation, while VHF radars are not. This has led to the interest in using VHF radars to probe the lowest heights in the atmosphere, including the planetary boundary layer.

This thesis describes the development and refinement of a VHF Boundary Layer

---

[1] Radar: *Ra*dio *d*etecting *a*nd *r*anging of objects

Radar (BLR).

In this first chapter, the motivation and associated considerations are introduced to provide a perspective. The structure of the atmosphere is discussed with emphasis on the lowest heights. Different measurements and methods used in observations of atmospheric parameters are summarised. Various classifications of scattering which may be observed are mentioned. Observations of the atmosphere via radar and the different analysis techniques used are discussed. The chapter is concluded with a brief description of the field sites and types of equipment used, which are discussed further within the thesis.

1.1 Structure of the atmosphere

The vertical structure of the atmosphere can be classified in a variety of ways depending on which physical property is used.

The ratios of atmospheric constituents in the absence of sources or sinks is determined by either molecular diffusion or mixing due to fluid motions. Molecular diffusion will attempt to order the atmosphere in such a way the lightest gases are present at the top of the atmosphere while the heaviest molecules occupy the bottom. Mixing due to motion of the molecules is independent of molecular mass. If this is the dominant process, the atmosphere's composition will be independent of height. At lower heights the mean free path between molecular collision is so small that the time necessary for molecular diffusion is many orders of magnitude greater than that required for turbulent motions to homogenise them. However, at higher heights the mean free path increases to such an extent that molecular diffusion is the dominant mechanism. At an altitude near 100 km the two processes are approximately comparable. The region below this height is known as the *homosphere* while the region above is called the *heterosphere*. The level of transfer of dominance from turbulent mixing to molecular diffusion is called the *turbopause*. The increase in mean free path of particles with height, combined with the transition to more stable species of ions, results in an increase in the number of free electrons. These electrons and positive ions are produced by the ionization of molecular oxygen, nitrogen and nitrogen monoxide by the sun's radiation and have longer lifetimes than electrons produced at lower levels. This region where the number of free electrons is significant begins around 60 km and is known as the *ionosphere*. This thesis does not consider the ionosphere. For further information on the behaviour and structure of the ionosphere, refer to *Rishbeth & Garriot* [1969].

The most common classification of the Earth's atmosphere is based upon the temperature profile. As indicated in Figure 1.1 the vertical profiles can be divided into four regions, the *troposphere*, *stratosphere*, *mesosphere* and *thermosphere*. The transition areas between these layers contain local extrema and are labelled *tropopause*, *stratopause* and *mesopause*, respectively. The behaviour of the temperature profile shown in in Figure 1.1 can be understood by considering the dominant processes occurring at specific heights.

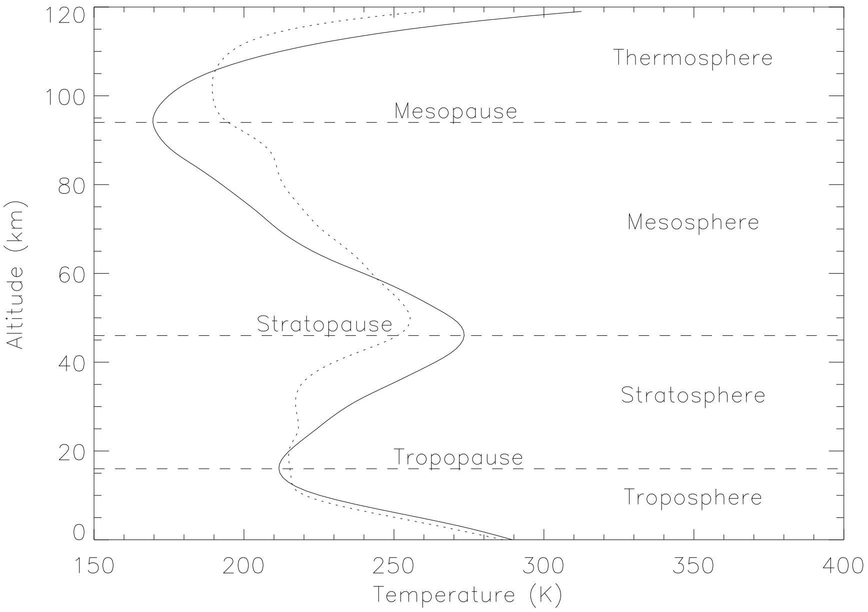

Figure 1.1: Classification of regions and local extrema for the Mean Temperature profile for 40°S. Summer (solid) and Winter (dotted) values from the COSPAR International Reference Atmosphere 1986 (CIRA).

The Earth's surface is heated by incoming solar radiation, and re-radiates the absorbed energy as a black-body spectrum. The heating of the atmosphere by the ground causes active convection and a decrease in temperature due to volume expansion. Molecules and gases, like water vapour, absorb some of the re-radiated energy, thus heating the atmosphere.

In the stratosphere the temperature gradient is reversed due to the absorption of ultraviolet solar radiation by ozone. The local temperature minimum between the troposphere and stratosphere is labelled the tropopause. The dissociation of ozone molecules heats the atmosphere creating an increase in temperature. The local region where the temperature is a maximum is labelled the stratopause. Above the stratopause, the ozone concentration decreases, along with a subsequent decrease in temperature. This decrease continues up to the mesopause at ∼100 km, where a reversal in the temperature gradient is observed due to the absorption of solar ultra-violet radiation by atomic and molecular oxygen. The region above the mesopause is known as the thermosphere.

1.1.1 Equations for atmospheric stability

Thermodynamics play an important role in the stability of the local atmosphere. The atmosphere can be considered to be vertically stable with small vertical motion. The hydrostatic equation, which defines the balance between gravity and vertical pressure gradient force, is given by,

$$dp = -g\rho dz, \tag{1.1}$$

where p, ρ, g and z are the pressure, density, acceleration of gravity and altitude, respectively. The ideal gas equation is given by,

$$p = \rho RT, \tag{1.2}$$

where R is the gas constant which depends upon the composition of the mixed gas, for dry air $R_d = 287.04$ J kg^{-1} K^{-1}.

The first law of thermodynamics can be written as [*Houze*, 1993],

$$Q = C_p \frac{dT}{dt} - \frac{1}{\rho} \frac{dp}{dt}, \tag{1.3}$$

where Q is the heat input, T is the temperature and C_p is the specific heat at a constant pressure, for dry air $C_{pd} = 1005.7 \pm 2.5$ J kg^{-1} K^{-1}. By inserting Equation 1.2 into Equation 1.3 and assuming Q is zero, (i.e. *adiabatic* processes), then Equation 1.3 can be written,

$$c_p d(\ln T) = R_d d(\ln p). \tag{1.4}$$

Integrating Equation 1.4 from a state at pressure p and temperature T, to a state at pressure p_o and temperature θ,

$$\int_{\theta}^{T} c_p \frac{d(\ln T)}{dt} = \int_{po}^{p} R \frac{d(\ln p)}{dt}, \tag{1.5}$$

derives the potential temperature θ,

$$\theta = T \left(\frac{p_o}{p} \right)^{R/c_p}. \tag{1.6}$$

Up to this point it has been assumed that the atmosphere is dry. However, in the troposphere R depends upon water vapour content. R_m is therefore given as the gas constant for moist air where [*Gill*, 1982],

$$R_m = R_d(1 + 0.608q), \tag{1.7}$$

where q is the specific humidity or mixing ratio of water vapour in air (mass of water vapour per unit mass of air). From the ideal gas law for moist air,

$$p = \rho R_d T_v, \tag{1.8}$$

the definition for virtual temperature T_v is obtained and is simply given by,

$$T_v = T(1 + 0.608q). \tag{1.9}$$

Inserting T_v into Equation 1.6 gives θ_v, the virtual potential temperature

$$\theta_v = T_v \left(\frac{p_o}{p} \right)^{R_d/c_{pd}}. \tag{1.10}$$

Both θ and θ_v are constant for an air parcel in an adiabatic process. θ_v has greater flexibility, as it can be used for both dry and unsaturated moist air. Differentiating 1.10 with respect to z, gives

$$\frac{d\theta_v}{dz} = \frac{dT_v}{dz} - T_v \frac{R_d}{c_{pd}} \frac{1}{p} \frac{dp}{dz}. \tag{1.11}$$

Combining the hydrostatic equation (1.1) with Equation 1.11 and assuming adiabatic expansion, gives the dry adiabatic lapse rate Γ_d,

$$\Gamma_d = -\frac{dT_v}{dz} = \frac{g}{c_{pd}}, \tag{1.12}$$

($\Gamma_d = 9.76$ K km^{-1}).

The environmental lapse rate is defined as,

$$\Gamma = -\frac{dT}{dz}. \tag{1.13}$$

If $\Gamma < \Gamma_d$, then a parcel of air that is adiabatically displaced upwards will be negatively buoyant and positively buoyant if displaced downwards. In this situation the atmosphere is statically stable as the parcel will return to its equilibrium position. Under stable conditions a parcel of air given a small displacement will oscillate at the Brunt-Väisälä frequency due to buoyancy. The Brunt-Väisälä is defined [*Holton*, 1992],

$$N^2 = g\frac{\partial(\ln\theta)}{\partial z} \tag{1.14}$$

or

$$N^2 = \frac{g}{T}\left(\frac{dT}{dz} + \Gamma_d\right) \tag{1.15}$$

If $\Gamma > \Gamma_d$ then the atmosphere is unstable. Observations of instability are often precursors to the development of precipitation. If a moderately saturated region of air undergoes instability and subsequent convection, cloud formation followed by precipitation may occur.

1.1.2 Boundary layer

The atmospheric boundary layer (ABL) is the layer of the atmosphere in which the air motion is strongly influenced by effect of the surface of the earth, primarily via turbulence. The two major source of turbulence in the ABL are surface friction and convection. In the ABL the turbulent forces are comparable in magnitude to pressure-gradient and Coriolis forces[2] [*Houze*, 1993].

Under neutrally-stratified conditions ($\Gamma = \Gamma_d$) the ABL is characterized predominantly by frictional interaction with the earth's surface. Under these conditions, the turbulent mixing is generated by dynamical instability due to the strong vertical shear of the wind near the ground. The structure is characterized by the *surface layer*, which is closest to the surface, and the *Ekman layer* (Figure 1.2).

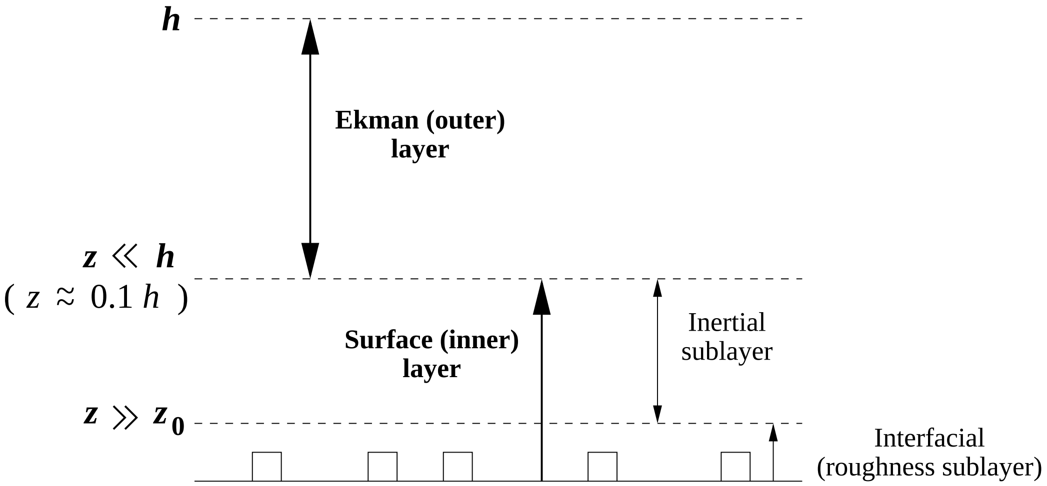

Figure 1.2: Schematic atmospheric boundary layer structure for aerodynamically rough flow in neutrally-stratified conditions, h is the boundary layer depth, z is height and z_0 is the aerodynamic roughness length. Adapted from *Garratt* [1994]

The *surface layer* thickness is typically 0.1 of the thickness of the *Ekman layer*. Inside the *surface layer* the horizontal friction stress is independent of height, and the wind u, has a logarithmic profile given by [*Holton*, 1992],

$$u = \frac{u_*}{k} \ln\left(\frac{z}{z_o}\right), \tag{1.16}$$

where $u_* = \tau_o/\rho$ is the frictional velocity, τ_o is the surface stress, $k \approx 0.4$ is von Karman's constant and z_o is the aerodynamic roughness length, which is representative of the surface geometry.

---

[2] The Coriolis force is a pseudo-force due to the rotation of a reference frame at a constant angular velocity, relative to an inertial system

The *Ekman layer* is the region above the *surface layer* where the Coriolis force, pressure gradient force and viscous stress are balanced. The wind profile is given by the solutions to [*Holton*, 1992],

$$\begin{aligned} -fv &= -\frac{1}{\rho}\frac{\partial p}{\partial x} + \frac{\partial}{\partial z}\left(\frac{\tau_x}{\rho}\right) \\ +fu &= -\frac{1}{\rho}\frac{\partial p}{\partial y} + \frac{\partial}{\partial z}\left(\frac{\tau_y}{\rho}\right), \end{aligned} \tag{1.17}$$

where $f = 2\Omega\sin(\phi)$ is the Coriolis parameter, ϕ is the latitude, ρ is the density, p is the pressure and $\tau_x = -\rho < u'w' >$ and $\tau_y = -\rho < v'w' >$ are the vertical stresses due to motion in the x and y direction, respectively. The solution to (1.17) is only applicable above the surface layer, therefore, it must be matched to (1.16) at the top of the surface layer. In the southern hemisphere, the horizontal wind components for the modified Ekman solution are [*Holton*, 1992],

$$\begin{aligned} u &= u_g[1 - \sqrt{2}\, sin(\alpha)\ \exp(-\gamma z)\ \cos(\gamma z - \alpha + \pi/4)] \\ v &= -u_g\sqrt{2}\ \sin(\alpha)\ \exp(-\gamma z)\ \sin(\gamma z - \alpha + \pi/4), \end{aligned} \tag{1.18}$$

where u_g is the geostropic wind component in the x direction (the coordinate axes are oriented such that $v_g = 0$), α is the surface wind angle, $\gamma = \sqrt{f\rho/2A_z}$ and A_z is the eddy exchange coefficient.

Ideal *Ekman* layers are not usually observed in the ABL. However, they do provide a qualitative description of the dynamical properties of boundary layer flow under steady state and horizontally homogeneous conditions. In the derivations above, the influence of heating and cooling of the earth's surface was neglected. This effect can be included by considering the influence buoyancy can have on the turbulent kinetic energy.

Three diverse conditions can be considered; *neutral*, *stable* and *unstable* limits. The *neutral* limit occurs when the buoyancy contribution is very small and the *Ekman layer* as previously described can be used to approximate the conditions. In the *stable* case, the turbulence produced by the velocity shear, as described for the *Ekman layer*, is suppressed by buoyancy forces. This may occur in situations of strong radiative cooling of the ground, with the top of the ABL possibly falling to as low as 10 m. The *unstable* limit often occurs when the winds are light and a state of local free convection, due to surface heating, is approached. In this situation the buoyancy reinforces or completely dominates over the shear production, with the turbulent layer becoming very deep, (2-3 km).

The actual behaviour of the ABL is a combination of the three conditions described above. Over land, the diurnal cycle of heating and cooling of the earth's surface strongly affects the structure of the ABL. The convective boundary layer (CBL) is an example of the *unstable* limit. The development of the CBL is shown in Figure 1.3, and can be summarized by the following characteristics. Following sunrise, the nocturnal boundary layer (NBL) breaks down through heating and the development of a shallow, well-mixed layer. The development of a deep, well-mixed boundary layer which comprises most of the CBL follows ($0.1 < z/h < 1.0$, where h is the CBL depth). An inversion layer at the top of the CBL often develops. This region is known as the *entrainment zone* or the *interfacial layer*. The *entrainment zone* is where the free atmosphere is entrained and mixed into the aerosol-laden, moister boundary layer and may be as thick as $0.5h$. During the late afternoon, before the sunset, the turbulence aloft can not be maintained against viscous dissipation, hence the CBL starts to decay. After sunset, while the day-time boundary layer continues to decay, a surface inversion (often called the *nocturnal inversion*) and a shallow, nocturnal boundary layer develop. The remnants of the daytime CBL form a residual layer above the NBL.

The nocturnal boundary layer is an example of a *stable* limit case. The cooling of the surface acts to suppress the turbulence, so that the turbulence levels are lower and the boundary layer is shallower (i.e. 30-100 m). The nocturnal inversion deepens through the night and can become several hundred metres deep, with the temperature increase being as large as 10-15 K under the right conditions (i.e. clear skies, 12 hour night), [*Garratt*, 1994]. It should be noted that the height of the inversion, which is marked by the temperature change, is often much greater than the top of the NBL which is determined by the turbulence.

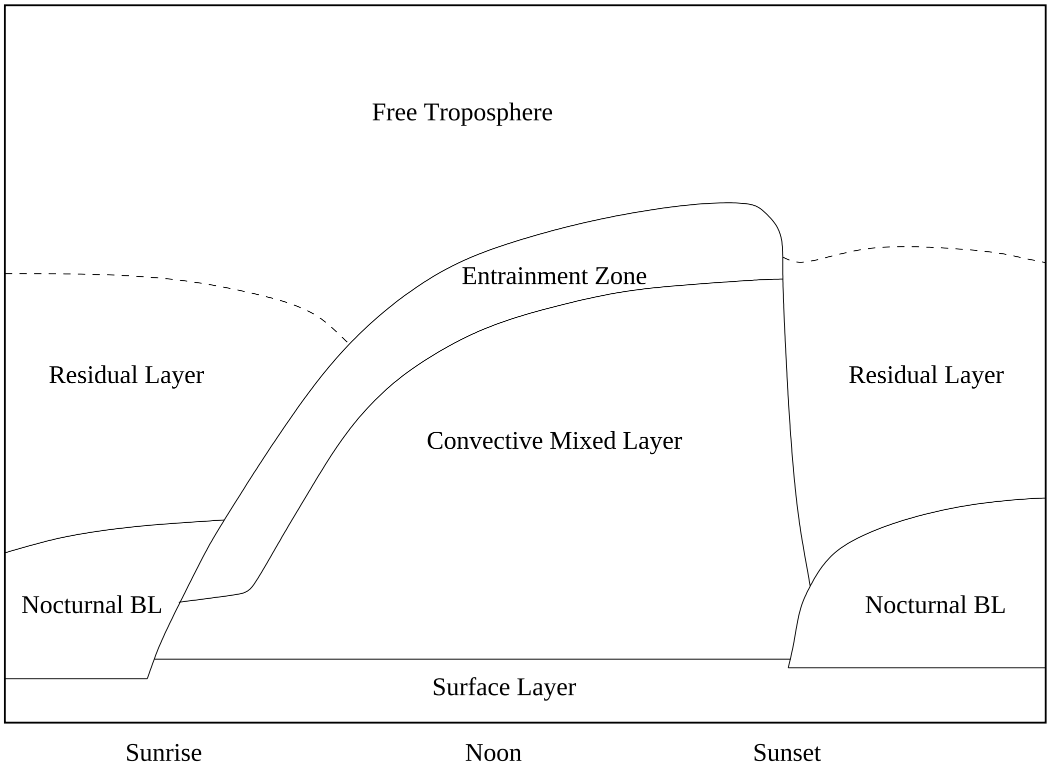

Figure 1.3: Sketch of idealized boundary layer evolution (after *Cohn et al.* [2000])

A low-level super-geostrophic wind maximum called the *nocturnal jet* sometimes forms above the NBL. The *nocturnal jet* occurs when the frictional effects are confined to the NBL, therefore the region above which was previously in the day-time ABL is effectively released from frictional influence. In response, the wind begins an inertial oscillation that continues till mixing resumes at sunrise. The development and lifetime of the *nocturnal jet* is dependent upon: the inertial period and hence the latitude; the length of night relative to the inertial period and the roughness of the surface (the greater z_o, the greater the velocity of the jet).

The marine atmospheric boundary layer (MABL) can be approximated by the *neutral* case. The main difference between the MABL and the continental BL is related to the water surface in the MABL. Buoyancy influences are much weaker, due to the large heat capacity of water, so, diurnal influences are small. The sea surface is relatively uniform, resulting in small values for z_o.

Cloud topped boundary layers (CTBL) describes the situation where clouds are present under the capping inversion of the boundary layer. Very often MABL's fall into this category. There are three main cloud types associated with the CTBL: shallow cumulus, stratocumulus and stratus. The CTBL can be greatly influenced by sources of heating and cooling within its interior, created by radiative fluxes. The presence of clouds reduces the amount of radiation reaching the ground, which reduces the surface fluxes, hence weakening the buoyancy component. As the amount of cloud cover increases, the CTBL becomes more like the *neutral* case. The incidence of CTBL is greater over the sea because of the increased moisture due to evaporation.

The continuous profiles of atmospheric parameters obtained with radiosondes, are used to determine the height of the ABL. However, the variation in height of the top of the BL can mean such "snapshots" of the atmosphere are only accurate for a very short time and in a very localized region, with altitude changes of over 1 km within an hour commonly observed [*White et al.*, 1999]. A schematic representation of the potential temperature vertical structure of the CBL is shown in Figure 1.4.

A mixed layer maintains constant mean equivalent potential temperature within its entire depth, as shown in Figure 1.4, [*Cohn & Angevine*, 2000]. Therefore when using radiosonde measurements the height of the mixed layer can be determined by where θ_v is no longer constant.

1.2 Measurements of the atmosphere

A wide variety of apparatus are used to observe and measure the atmosphere. Measurements can either be obtained *in-situ* or by *remote sensing*. *In-situ* techniques involve the apparatus and region of interest being co-located. *Remote sensing* is the conveying of information about an object by observing the interaction between radiation and the object of interest.

In-situ measuring devices are the most common method for observing the atmosphere. Automatic and manned weather stations, which obtain surface measurements

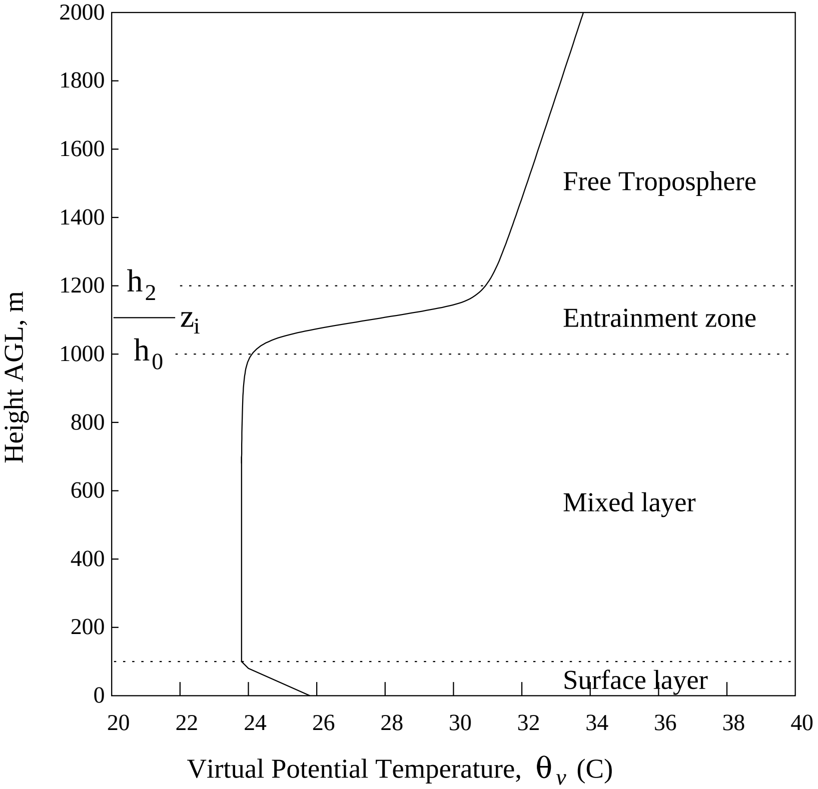

Figure 1.4: Schematic representation of the temperature profile of the CBL. The top of the CBL is defined as z_i, the inversion height. The height of the surface layer is at 0.1 z_i, a mixed layer can be seen between 0.1 z_i and 0.8 z_i and the entrainment zone is from 0.8 to 1.2 z_i. The height measurements are typical values observed in the CBL (adapted from [*Angevine et al.*, 1994])

of the atmosphere, are situated throughout the world. The first radiosonde, (commonly referred to as weather balloons), was flown in 1927. At the present, they are the most commonly used method for obtaining profiles of atmospheric parameters. Radiosondes can provide information on temperature, humidity and pressure as they ascend through the atmosphere, with the information transmitted back to a ground station via a telemetry system. Wind profiles can be measured by utilizing a secondary system for tracking the motion of the balloon. Initial tracking methods involved manual theodolites, while more modern tracking systems utilize ground based Doppler radars or navigation systems such as GPS[3]. An alternative to the ascending radiosonde is the

---

[3] Global Positioning System (GPS) is a space-based three dimensional positioning velocity and time system which is operated by the United States Air Force

drop-sonde, which is usually released from an aircraft and descends slowly through the atmosphere on a parachute. Both the radiosonde and drop-sonde provide accurate, high vertical resolution data, however, they only provide a “snapshot” of the atmosphere.

The need for *in-situ* data to corroborate measurements obtained by remote sensing methods has driven a resurgence in the use of tethered balloons and kites. The first temperature soundings of the atmosphere were accomplished in 1748, by taking a thermometer on a kite. With the advent of radiosondes, aeroplanes and telemetry systems, the use of such tethered devices was reduced. However, recent campaigns involving tethered kites and balloons have highlighted the excellent vertical resolution that can be obtained with such systems [*Balsley et al.*, 1998; *Muschinski et al.*, 2000].

By the end of World War I, planes were being used to obtain measurements of the lowest 4 km in the atmosphere. Aeroplanes and helicopters provide an observation platform which has controllable altitude, unlike radiosondes. Planes have the advantage of being able to carry considerable payloads and a multitude of experiments simultaneously [*Hacker*, 1997]. However, complications are created by the flow of air past the platform, which must be taken into account when attempting to measure the background winds or turbulence. The substantial cost involved in operating planes and helicopters mean they are usually used for short-duration campaigns only. The issue of cost has been addressed with the development of robotic aircraft [*Holland et al.*, 2000]. These unmanned aircraft have the advantage of cheaper running costs, automation once in the air, long range and high endurance abilities. However, the size of the payload is restricted compared with conventional aircraft.

All of the techniques discussed so far are *in-situ*, which have high accuracy in individual measurements but are restricted to being able to measure parameters at only one position at any given moment. Remote sensing systems have the advantage of being able to make multiple measurements from a range of heights simultaneously. However, the vertical resolution of the measurements is usually quite coarse when compared with *in-situ* techniques.

The number and type of systems used for remote sensing of the atmosphere are large and varied, therefore only a brief overview will be given. The method of remote sensing can be broken into two categories *passive* and *active*.

Passive sensing involves the observation and measuring of the interaction of the atmosphere with natural radiation, (i.e. sun, the Earth's surface, radio-waves from space). Examples of passive experiments include interferometers, radiometers, spectrometers and photometers. Interferometers can be used to measure the vertical structure of the temperature and water vapour [*Feltz et al.*, 1998]. Radiometers provide profiles of temperature, water vapour and cloud liquid water, by measuring the brightness temperatures [*Solheim et al.*, 1998]. Spectrometers have been used to derive temperatures at the top of the mesosphere [*Hobbs et al.*, 1996]. Photometers measure the ionospheric optical emission to obtain temperature estimations [*Woithe*, 2000].

Active sensing techniques involve transmitting energy and observing the subsequent interaction with the atmosphere. Active experiments can be located at a fixed location or upon vehicles, depending upon the size and weight of the specific equipment. Examples of active experiments include optical lidars, acoustic radars or sodars, radars and RASS.

There are three basic types of lidar in operation at the moment. Doppler lidars measure the vertical (w) wind profile, obtaining a profile [*Grund et al.*, 2000], and have been installed on ships [*Wulfmeyer et al.*, 2000]. Raman lidars obtain temperature profiles [*Arshinov et al.*, 1983], while Differential Absorption Lidars (DIAL) can obtain profiles of water vapour, temperature and gaseous atmospheric constituents. DIAL systems have been successfully operated as both ground-based [*Wulfmeyer & Bösenberg*, 1998] and airborne [*Ehret et al.*, 1999] experiments.

Acoustic radars, or sodars, use sound to "probe" the atmosphere and can be used to observe the boundary layer structure, including wind and inversion tracking. They achieve good height resolution, but with limited height coverage, which is often strongly restricted in adverse weather conditions.

Radars are the most common form of active remote sensing systems. Radars range from large Medium Frequency (MF) systems observing the ionosphere [*Vincent & Lesicar*, 1991], through to small Ultra High Frequency (UHF) cloud radars operating between $\sim$ 30 GHz and $\sim$ 100 GHz [*Peters*, 2000]. UHF wind profiling radars are used throughout the world for meteorological observations, typically operating as Doppler radars [*Ecklund et al.*, 1990]. UHF radars have been successfully installed on ships [*Carter et al.*, 1992] and buoys [*Jordan et al.*, 2000]. Fully transportable UHF systems have been developed [*Hashiguchi et al.*, 1995], enabling observations to be carried out in a wide range of situations and conditions. UHF and VHF radars are able to obtain rainfall distributions, as they are both sensitive to precipitation [*Rajopadhyaya et al.*, 1999].

VHF radars have been used to observe the troposphere for two to three decades. Initially, VHF radars used for wind profiling, measured the winds using Doppler techniques [*Gage & Balsley*, 1980]. Application of spaced antenna methods provided an alternative method of operation [*Röttger & Vincent*, 1978]. Until recent developments, observations using VHF radars were restricted to altitudes above $\sim$1.5 - 2 km. Through advances in technology and the use of smaller antenna arrays, observations as low as 300 m have been obtained at VHF [*Vincent et al.*, 1998; *Fillol et al.*, 1997].

Radio Acoustic Sounding Systems (RASS) use a sound source to create fluctuations in the index of refraction, from which radars obtain backscatter. The Doppler shift of the reflected signal is dependent upon the background virtual temperature. Hence, given the Doppler shift at each height a temperature profile can be obtained. RASS has been integrated into UHF systems [*May et al.*, 1988] and VHF systems, with the latter being able to obtain measurements of temperature as high as 20 km [*Matuura et al.*, 1986*a*].

Spaced-based platforms are becoming increasingly important for obtaining measurement on a synoptic or even global scale. A variety of instruments are employed, using both active and passive sensing, and cover a wide range of wavelengths. The range of instruments used includes atmospheric sounders (Infra-red (IR) and microwave), cloud profile and rain radars, earth radiation budget radiometers, high resolution imagers, imaging multi-spectral radiometers (visual and IR), imaging multi-spectral radiometers (microwave), imaging radars, lidars, multi-directional radiometers, ocean colour radiometers and polarimeter radiometers [*CEOS*, 2000].

1.3 Scattering mechanisms

In order to understand the source of reflections and scatter measured by the radar, background knowledge about the refractive index and its variations are required. The type of echoes received by the radar can be divided into several groups, depending on the source of the variations in refractive index.

All atmospheric radar echoes are caused by reflections or scattering from inhomogeneities in the refractive dielectric constant ϵ or the refractive index of air n, given approximately by

$$n - 1 = \frac{0.373e}{T^2} + \frac{77.6 \times 10^{-6} p}{T} - \frac{N_e}{2N_c}, \tag{1.19}$$

where p (hPa) is the atmospheric pressure, e (hPa) is the partial pressure of water vapour, T (K) is the absolute temperature, N_e is the number density of electrons, and N_c is the critical plasma density. The first term in Equation 1.19 is known as the *wet term*. It is more important in the lower troposphere because of the high humidity. The second term, known as the *dry term*, is dominant in the mid-troposphere up to the stratosphere. The third term is the major contributing factor due to free electrons and can be considered negligible below 50 km. As all measurements and theory discussed in this thesis are associated with the troposphere, and in particular the lower troposphere, hence the effect of the third term will not be considered.

The variations in the radio refractive index are defined by the vertical gradient of the potential refractive index [*VanZandt et al.*, 1978],

$$M = -77.6 \times 10^{-6} \frac{P}{T} \left(\frac{\partial \ln \theta}{\partial z} \right) \left[1 + \frac{15,500q}{T} \left(1 - \frac{1}{2} \frac{\partial \ln q / \partial z}{\partial \ln \theta / \partial z} \right) \right], \tag{1.20}$$

$$M = -77.6 \times 10^{-6} \frac{P}{N} \left(\frac{N}{g} + 15,500 \frac{Nq}{gT} - \frac{7800}{T} \frac{dq}{dz} \right), \tag{1.21}$$

In (1.21) the second and third terms within the brackets are the *wet term* contributions. The strength of the scattered signal is proportional to M^2. In the lower troposphere, M is often dominated by the wet term [*Tsuda et al.*, 1988].

Radio waves are scattered in clear air by refractive index fluctuations having dimensions comparable to one-half the radar wavelength (Bragg Scale). In the troposphere three main groups of scattering mechanisms are present, *turbulent scatter*, *Fresnel or partial reflections* and *Fresnel scatter*.

Turbulent scatter [*Gossard et al.*, 1982] can be further divided into two groups, *isotropic* and *anisotropic*. Isotropic scatter occurs when the turbulent irregularities of the refractive index are homogeneously random and statistically similar in all directions. Anisotropic scatter occurs when the statistical properties of the irregularities are dependent on direction (i.e. aspect sensitivity[4]) [*Gage & Balsley*, 1980]. Due to the similar randomly fluctuating irregularities present in isotropic and anisotropic turbulent scatter, the temporal variations of the radar echoes should be similar.

Fresnel or partial reflections occur from thin stable laminae of radio index of refraction [*Gage & Green*, 1978], which show strong aspect sensitivity [*Röttger & Vincent*, 1978]. These horizontally coherent layers occur in horizontally stable regions, with horizontal correlation distances being of the order of a Fresnel zone, $(r\lambda)^{1/2}$. In-situ observations of these thin-stable layers have shown regions commonly made up of regions with very high gradients in wind, humidity and temperature [*Gossard et al.*, 1985; *Dalaudier et al.*, 1994; *Muschinsk & Wode*, 1998]

Fresnel scatter occurs if the radar observing volume is filled by a collection of transversely coherent, horizontally stratified, stable laminae of radio refractive index [*Gage et al.*, 1981; *Gage et al.*, 1985]. The radar echoes will show aspect sensitivity similar to Fresnel reflection, but exhibit temporal characteristics similar to Bragg scatter due to the statistically independent nature of the discontinuities.

---

[4] The returned power is dependent upon zenith (and azimuth) angle

1.4 Observations of the atmosphere using radars

The radar equation gives the relationship between the power received at the antennas in terms of the radar parameters and the scattering/reflecting mechanism. The radar equation can take many forms depending upon which type of mechanism is being observed, [*Tatarskii*, 1961; *Gage & Balsley*, 1980; *Doviak & Zrnić*, 1993]. Three main cases of interest will be outlined here.

Firstly consider a single isolated hard target at range r with scattering cross section area σ. The returned power is given by

$$P_r = \frac{P_t A_e^2 \alpha}{4\pi\lambda^2 r^4}\sigma, \tag{1.22}$$

where A_e is the effective antenna area for both the transmitting and receiving antennas, α is the efficiency (loss) factor of the system as a whole and λ is the operating wavelength of the radar.

Secondly, consider isotropic volume scatter. The returned power is given by,

$$P_r = \frac{\pi}{64}\frac{P_t A_e \alpha \Delta R}{r^2}\eta, \tag{1.23}$$

ΔR is the radar pulse length and η is the volume reflectivity; note the r^{-2} dependence compared with r^{-4} for a hard target.

The final equation is for partial (Fresnel) reflections from a single discontinuity, given by

$$P_r = \frac{P_t A_e^2 \alpha^2}{4\lambda^2 r^2} \mid \rho \mid^2 \tag{1.24}$$

where, ρ is the amplitude reflection coefficient of the discontinuity.

If the power of the radar echoes can be measured and the appropriate radar parameters are known, then calculation of η and ρ is possible.

Equations 1.22, 1.23 and 1.24 all assume the target is situated in the *far field* of the radar. The *far field* is where the transmitted wave can be regarded as planar. thus implying the radar can be effectively considered as a point source. The *near field* is the region where the transmitted wave from the radar is spherical. The boundary between the two regions r_o is given by the Rayleigh criterion,

$$r_o = \frac{D^2}{\lambda}, \tag{1.25}$$

where D is the diameter of the antenna and λ is the radar wavelength. The values of r_o can vary dramatically from one system to another. For the 54.1 MHz VHF Boundary Layer Radar as discussed here, $D \simeq 15$ m and $r_o \simeq 40$ m, for the 54.1 MHz Buckland Park VHF Stratosphere-Troposphere radar $D \simeq 100$ m and $r_o \simeq 1.8$ km, while for the Arecibo UHF radar operating at 430 MHz, $D \simeq 300$ m and $r_o \simeq 129$ km. Atmospheric measurements are still possible provided suitable modifications with regard to antenna polar diagrams and radar equations are included into any calculations. To avoid the inherent complications that *near field* measurements would introduce, only operations of a radar within the *far field* are considered in this thesis.

Observations suggest that in the lower troposphere a mixture of both isotropic and anisotropic scatter is present.

1.4.1 Atmospheric radars: Analysis techniques

Numerous techniques have been devised for measuring various atmospheric parameters with UHF/VHF/MF atmospheric radars. Outlined below are some examples of techniques which are used. For further information the reader is directed to the appropriate references.

The main technique used at VHF is Doppler beam swinging (DBS). DBS involves measuring the mean Doppler shift of the returned signal using a narrow beam pointed in different directions. Typically, three to five different directions are used, one vertically pointing, and the remaining ones in orthogonal directions at a given zenith angle. Steering of the radar beam is accomplished by either inserting different phase-delay cables between antennas, electronically inserting a phase delay or by physically pointing the antenna array in the appropriate direction. While the last technique is valid at UHF, it is not feasible at VHF, due to the large antennas used.

Scanning in the azimuth and zenith directions can be considered as an advanced variation of DBS. However, it does increase the sampling time. Doppler weather radars use this technique to measure wind divergence and can obtain a three-dimensional image of the reflectivity of the surrounding atmosphere.

Spaced antenna techniques were initially applied to MF radars [*Mitra*, 1949; *Vincent*, 1984], later they were utilized at VHF [*Vincent & Röttger*, 1980; *Röttger*, 1981] and more recently at UHF [*Cohn et al.*, 1997]. The number of variations of spaced antenna analysis techniques is extensive, therefore only a rudimentary description of several of the major techniques will be given.

Basically, the SA technique uses a minimum of three non-collinear antennas to measure the background wind, via sampling of the diffraction pattern on the ground, produced by scatterers moving with the background wind [*Briggs*, 1984]. Several variations have been developed, using both the time and frequency domain [*Briggs & Vincent*, 1992; *Doviak et al.*, 1996; *Holloway et al.*, 1997].

Post-set beam steering (PBS) and post-statistics beam steering (PSS), effectively steer the direction of the radar beam in software. PBS involves multiplying the time-series at each antenna by an appropriate phase such that the combination of all time-series effectively steers the effective beam in a specific direction [*Röttger & Ierkic*, 1985]. PBS is equivalent to the hardware steering employed by DBS. PSS involves multiplying the auto- and cross-correlation functions, (or auto- and cross-spectra functions), by an appropriate phase [*Kudeki & Woodman*, 1990; *Palmer et al.*, 1990].

Radar interferometry involves the analysis of several correlated radar signals obtained from the same scattering medium. In the spatial domain this involves signals obtained from two spatially separated antennas, while in the frequency domain the signals correspond to the use of slightly different operating frequencies. The simplest interferometric technique is angle of arrival (A0A) estimations, which are obtained by using phase path differences between signal returns at three or more spatially separated antennas [*Chau & Balsley*, 1998*a*]. Full spectral analysis (FSA) is the spectral equivalent of FCA, therefore it has the same underlying principles with similar restrictions and limitations [*Briggs*, 1968]. Spatial interferometric techniques can be divided into "imaging" and "non-imaging" techniques. Imaging techniques can be further divided into "Doppler sorted" and "non-Doppler sorted". Frequency domain interferometry (FDI), uses multiple frequencies to improve the range resolution, by using the cross frequency coherence and phase [*Stitt & Bowhill*, 1986; *Kudeki & Stitt*, 1987; *Franke*, 1990]. For a detailed overview of radar interferometry, the reader is directed to *Kudeki* [1993].

The radar system developed and described in this thesis used spaced antenna techniques. Observations were carried out at a number of locations in Australia.

1.5 Observation sites

Observations and campaigns were conducted at a number of field sites and with a variety of equipment to obtain measurements and comparisons. Sites used include Buckland Park, Alice Springs, Sydney Airport and Mt. Gambier, see Figure 1.5.

Figure 1.5: Field Sites

1.5.1 Buckland Park field site

The Buckland Park Field Site (BP) is located approximately 35 km north of Adelaide (34° 37' S, 138° 29' E). A number of instruments for observation of atmosphere parameters are housed there. These include a Medium/High Frequency (MF/HF) Doppler and Spaced Antenna Radar, three-field photometer, automatic weather station, Very High Frequency Stratospheric Tropospheric Radar (VHF ST) and for most of the time, a Boundary Layer Radar (BL or BLR). The evolution and present configuration of the BL antenna array is described in detail in Chapter 3.

The VHF ST radar [*Vincent et al.*, 1987], was recently upgraded in 1998. For a full description see *Hobbs* [1998], *Hobbs et al.* [2000].

The facilities for attempting radio acoustic sounding system (RASS) measurements were established using a single Electro Voice MH4020 acoustic source. Additional speakers constructed by VAF Research Pty Ltd were added later in May 1998. The acoustic sources are controlled by a separate computer independent of the radar. Further information regarding the implementation of RASS is given in Chapter 7.

A Davis Instruments (Weather Monitor II) automatic weather station was installed at BP on 1st April 1999. Measurements which are obtained every minute are archived and displayed on the Atmospheric Physics Group's Web Page [5].

Radiosondes launched from Buckland Park plus radiosondes launched from Adelaide Airport[6] provide additional information about the structure of the atmosphere at specific times. Vaisala RS80 radiosonde is the base package used in all launches to obtain pressure, temperature and humidity measurements. Radiosondes launched from Adelaide Airport are tracked via a wind-finding radar to obtain horizontal wind measurements. Wind measurements were obtained for some of the launches from Buckland Park when the radiosondes were equipped with either Omega[7] or GPS receivers. Dates and times of soundings are in Appendix H.

---

[5] www.physics.adelaide.edu.au/atmospheric/

[6] Adelaide Airport (AAP) is situated approximately 36 km south of Buckland Park

[7] A very low frequency (VLF) hyperbolic radio-navigation system based on phase comparison techniques, which ceased operation in September 1997

Airborne Research Australia's (ARA) [*Hacker*, 1997] Grob G109B single engine two-seater motorised glider, flying near the radar site, was used for *in-situ* comparison with radar observations during 2000, with interest in the vertical structure of horizontal layers of strong reflectivity being one of the major sources of motivation for this campaign. The aircraft is equipped with a set of standard instrumentation for atmospheric measurements. Included are fast sensors for air temperature and humidity, pressures, wind, turbulence and some trace gases. Multiple GPS sensors combined with Laser gyro based Inertial Navigation systems enable accurate measurement of aircraft parameters. Dates and times of flights are in Appendix H.

1.5.2 Alice Springs (CAFE)

The boundary layer radar was relocated to the Australian Bureau of Meteorology's observation station near Alice Springs Airport (23° 42' S, 133° 53'E) for CAFE 98 (Central Australian Fronts Experiment). The campaign was run in collaboration with Monash University for approximately one month, from 15th September 1998 to 12th October 1998. In conjunction with daily radiosonde launches from the nearby observation station, pi-ball observations of frontal passages were attempted. Two RASS speakers were transported to Alice Springs along with the radar to attempt to gain concurrent temperature profiles.

1.5.3 Sydney airport

Following the CAFE campaign, the BLR was moved to Sydney's Mascot Airport (33° 58' S, 151° 11'E) as part of a trial for a permanent installation of a Boundary Layer Radar. The radar was assembled at the beginning of December 1998 and dismantled at the beginning of January 1999. However, an oversight by a third party resulted in a lack of constant power being supplied to the field site for all but the last three days of observation.

1.5.4 Mt. Gambier

At the Bureau of Meteorology's (BoM) Mt. Gambier observation station (37° 45' S, 140° 47'E) a 44.75 MHz tropospheric profiler is situated. This profiler is a collaboration between BoM, the University of Adelaide and Atmospheric Radar Systems Pty Ltd (ATRAD) [*Reid et al.*, 1998]. A single acoustic source was temporarily relocated to this field site for two RASS campaigns, the first during August 1998 and the second during December 1999. The co-location of the weather observation station enabled accurate comparison of RASS derived temperatures with radiosonde measured temperatures.

1.6 Scope of thesis

During the course of the research described in this thesis, a VHF Boundary Layer radar was developed and operated for over three years. Over this period, the system has been steadily modified and has achieved nearly all the initial design goals.

Chapter 2 describes the reason behind the selection of the configuration and type of radar used. In particular, advantages and disadvantages of UHF vs VHF and spaced antenna vs DBS are discussed. Chapter 3 focuses on the antenna arrays used and examines the parameters which need to be optimized in order to obtain the desired height coverage. The motivation behind the improvement of the array is discussed, along with the actual changes applied.

Chapter 4 details the calibration of the entire system. This entails noise calibration of the receivers, measuring the gain or loss in various components of the system and numerical modelling of the antenna array to obtain beam-pattern and gain information. Calculation of coupling within the array, using the numerical models and subsequent actual measurements, is presented and compared.

In Chapter 5 the performance of the system is discussed. The coverage obtained at different sites and with different modes of operation is examined. Comparisons of the winds obtained by the BLR with radiosonde and aerosonde measurements is presented. The behaviour of the receivers, in particular at the lowest heights, is examined. Using the calibration values obtained in Chapter 4, measurements of received power and turbulence are obtained, with the validity of such measurements discussed. Observations of precipitation and rainfall rates are briefly presented.

Chapter 6 deals with the application of spaced antenna analysis techniques upon the BLR. Potential sources of error and underestimation in wind velocity measurements are investigated using simulated data from two different computer models. The integration of a Radio Acoustic Sounding System (RASS) to the BLR and two larger ST VHF radars is presented in Chapter 7. The inherent problems and considerations of applying RASS to the BLR are discussed. A thesis summary with suggestions for future research is provided in Chapter 8.

Chapter 2

VHF BLR

This chapter describes the motivation and reasons why a VHF spaced antenna radar was selected to probe the lower troposphere. The background fundamentals of a profiling radar system are discussed and an overview of the application of signal processing in the frequency and time domains is presented.

A brief history of boundary layer radars is provided together with a discussion of the limitations encountered with such systems. This leads to a comparison of UHF and VHF radars operating in the lower troposphere. Spaced antenna and Doppler techniques applied to VHF studies in the lower troposphere are presented, with the advantages and disadvantages of each technique discussed. In closing, the VHF BLR as used in this thesis is introduced.

2.1 Radar fundamentals

For simplicity, only the theory for a fixed-frequency radar will be discussed. For discussions and examples regarding frequency-agile radars the reader is directed to *Kudeki & Stitt* [1987], *Franke* [1990] and *Palmer et al.* [1999].

The operation of a radar is illustrated in Figure 2.1, which schematically shows the transmission and reception of a purely rectangular pulse, width τ_{tx}. The distance, or *range* R to the scatterer from the radar is given by,

$$R = \frac{cT_R}{2}, \tag{2.1}$$

where c is the speed of light $3.00 \times 10^8 \mathrm{ms}^{-1}$), T_R is the time between transmission and reception of the pulse. The period between the successive pulses is called the *inter-pulse-period* (IPP); the *pulse repetition frequency* (PRF) is the inverse of the IPP.

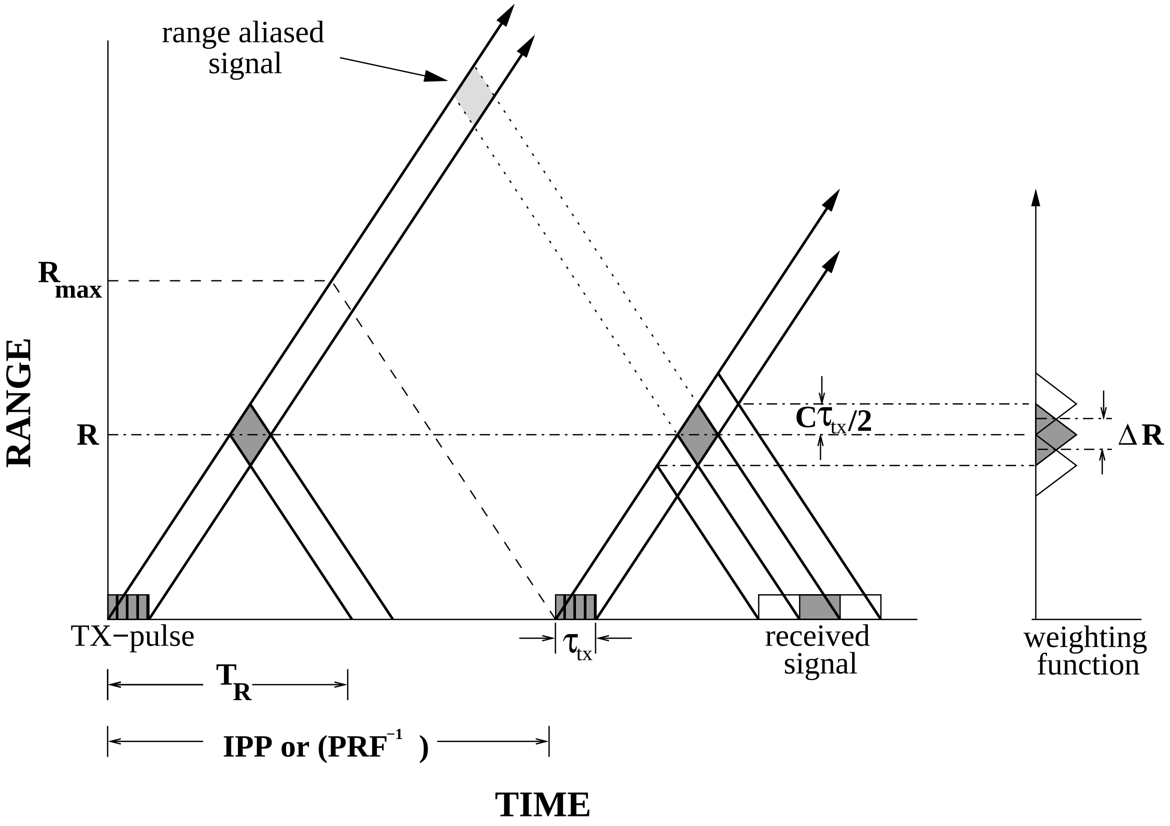

Figure 2.1: Time-height chart for a single-frequency radar. Solid lines correspond to transmitted or scattered radio-waves. Dashed lines mark maximum height coverage before range aliasing, R_{max}. Dotted lines show a range-aliased signal from a range greater than R_{max}. Sampling weight when a rectangular pulse is transmitted is shown on the right.

As can be seen from Figure 2.1, echoes from earlier pulses can be observed simultaneously with echoes from later pulses. This effect is known as range aliasing. If the PRF is too high, range aliasing can cause an ambiguity in the determination of the range of the scatterer. For normal operation, the PRF is set low enough that the signal strength of returns from greater than R_{max} is negligible when compared with returns from lower heights. The sampling volume extends from $R - c\tau_{tx}/2$ to $R + c\tau_{tx}/2$, with a triangular weighting function overlapping previous and successive sampling volumes. The *range resolution* ΔR, corresponds to the half-power width of the weighting function, expressed as $c\tau_{tx}/2$. The weighting function illustrated in Figure 2.1 is for an ideal situation, where the bandwidth (or filter) of the receiver is *matched* to the transmitted pulse. If the bandwidth of the receiver is too narrow, the signal energy is not effectively detected. If the bandwidth of the receiver is too large unnecessary extra noise is added to the signal, reducing the signal to noise (SNR) ratio. The optimal filter bandwidth is $\sim 1/\tau_{tx}$, depending on the type of filter and transmitted pulse. If a rectangular transmitted pulse is used, the optimum bandwidth for a rectangular filter is $1.4/\tau_{tx}$ [*Tsuda*, 1989].

The effective power of the transmitted pulse is customarily given in terms of duty cycle d and peak pulse power P_p. The duty cycle is the ratio of the transmitted pulse length τ_{tx} to the IPP. The average transmitted power P_a is the product of the duty cycle and the transmitter pulse peak power.

The basic configuration of a mono-static mesospheric stratospheric tropospheric (MST) radar system is illustrated in Figure 2.2. A local oscillator generates a sinusoidal signal at angular frequency $\omega = 2\pi f_o$, where f_o is the operating frequency of the radar. The radar controller modulates this signal to produce a pulse of finite duration τ_{tx}. The modulation involves shaping the pulse or as in the case of the prototype BLR, simply creating a rectangular pulse. The transmitter amplifies the pulse, which is then passed through the transmit/receiver (T/R) switch and radiated via the antennas.

The radar signal is scattered/reflected by refractive index variations, with a small fraction of the incident power being received by the antennas. The received radio frequency (RF) signal, which is a combination of the backscattered signal and noise (sky noise and interference), is fed to a receiving system through the T/R switch. The T/R switch protects the sensitive receivers from damage during transmission. In

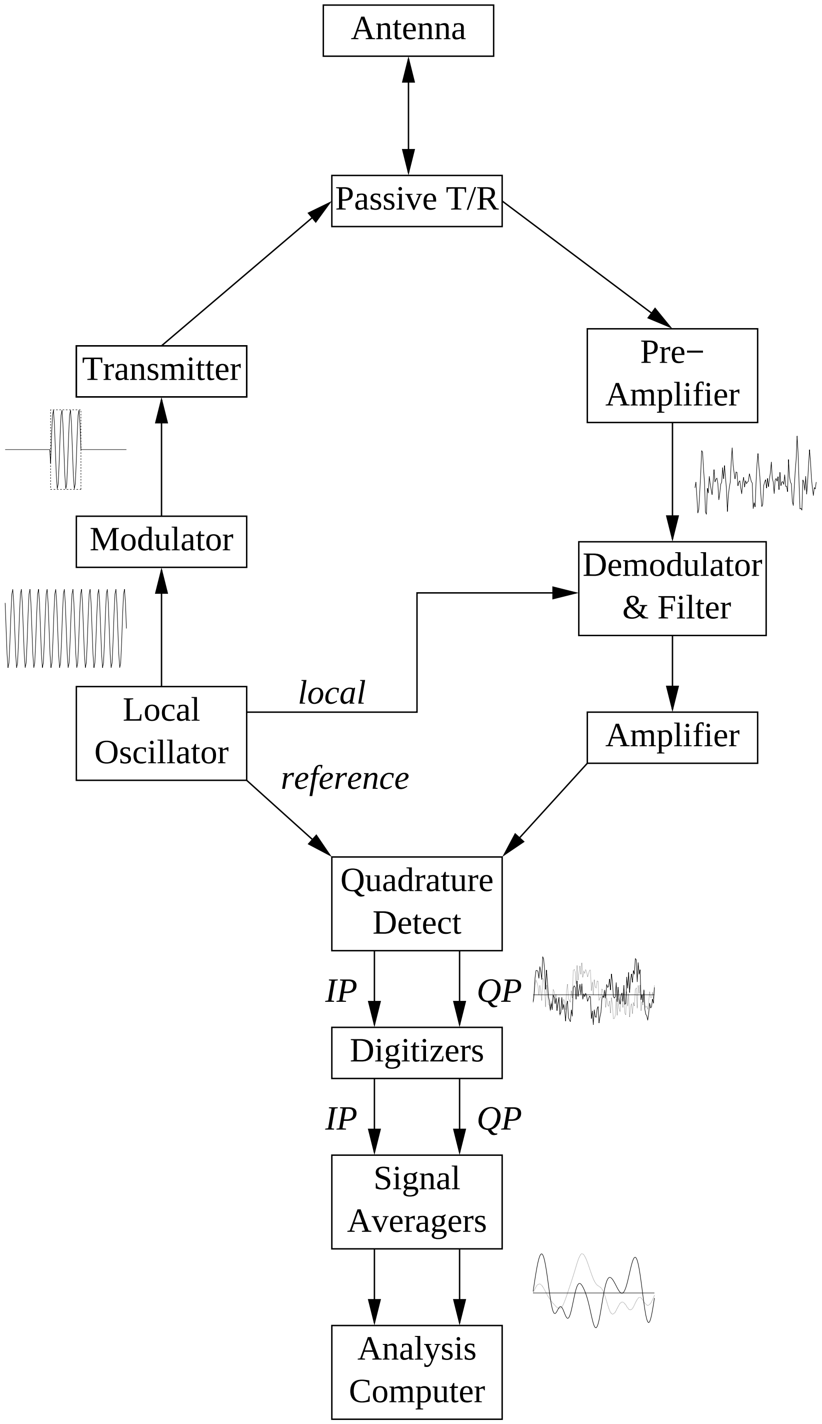

Figure 2.2: Block diagram of a typical MST radar system, together with signal waveforms (after *Tsuda* [1989])

the BLR a *passive T/R switch* is used, while in other systems the switches may be externally controlled (i.e. via the radar controller [*Vincent et al.*, 1987]). Passive T/R switches are discussed in detail in Appendix B.

The received signal is pre-amplified before being demodulated by mixing with a coherent local signal. A filter is applied to the demodulated signal to reduce additional noise, followed by linear amplification to maximise the peak-signal-to-noise. A quadrature detector separates the in-phase (IP) and quadrature (QP) components of the demodulated signal by mixing with a reference frequency generated by the local oscillator. Using the IP and QP components of the signal it is possible to measure the amplitude, which is a measure of the reflectivity of the scattering process and the phase, caused by fluctuations of the scatterers in the radar volume.

The individual components of the demodulated signal are digitized via analogue-to-digital converters, then transferred to signal averagers. To increase the SNR the digital signals are usually integrated over many pulses. This requires that the signals are phase locked to the local oscillator so that consecutive signals have phase coherence. The SNR of the signal is improved by a factor of N_c, the number of coherent integrations. Coherent integration does not increase the signal-to-noise ratio per unit bandwidth in the signal band as it simply filters out much of the wideband noise, which would otherwise be aliased into the signal band [*Farley*, 1983]. The number of coherent integrations is limited by the atmospheric processes being observed. In order to gain successful measurements, the sampling time T, must be less than the characteristic time of the atmospheric processes [*Rüster*, 1994]. For the BLR system, the sampling time is $\sim 0.05s$, compared with the observed echo fading times which are usually $> 0.2s$. Finally, the coherently-averaged signals are combined into a time-series for analysis.

2.2 Signal processing

Analysis of the raw time-series is carried out in either the frequency or the time domain. Each domain has advantages over the other, with the choice often being a consideration of which atmospheric parameters are being observed.

2.2.1 Frequency domain

A typical power spectrum $P(f)$ of a radar time series is shown in Figure 2.3a. The noise can be described by the noise level $\overline{N}$ and its standard deviation σ_N, or by the noise power $< N >$. The noise power is given by the total area beneath $\overline{N}$. The Doppler shifted scattered signal can be characterized by its position f_D, width W_f and height P_S. Alternatively the signal power $< S >$ can be used, defined as the total area under the signal peak and above the noise level. The signal to noise ratio (SNR) can thus be given by,

$$SNR = \frac{< S >}{< N >}. \tag{2.2}$$

The Doppler shift of the returned signal is proportional to the component of the scatterer's velocity V along the line-of-sight,

$$V = \frac{\lambda}{2} f_D. \tag{2.3}$$

The width of the signal is a measure of the effect of the turbulence, finite beam-width and vertical shears in the horizontal velocity within the radar volume [*Hocking*, 1983].

A limit is placed upon the maximum measurable Doppler shift by the data sampling rate. The maximum frequency which can be observed is named the Nyquist frequency N_f, where $N_f = 1/2T$ and T is the sampling interval. Frequencies greater than N_f are folded into the opposite side of the spectrum. This can become an appreciable concern if the background winds are large. If relatively strong signals or interference lie outside the Nyquist frequencies, they will be folded in and may coincide with the actual signal of interest, resulting in an inability to distinguish the signal from the interference.

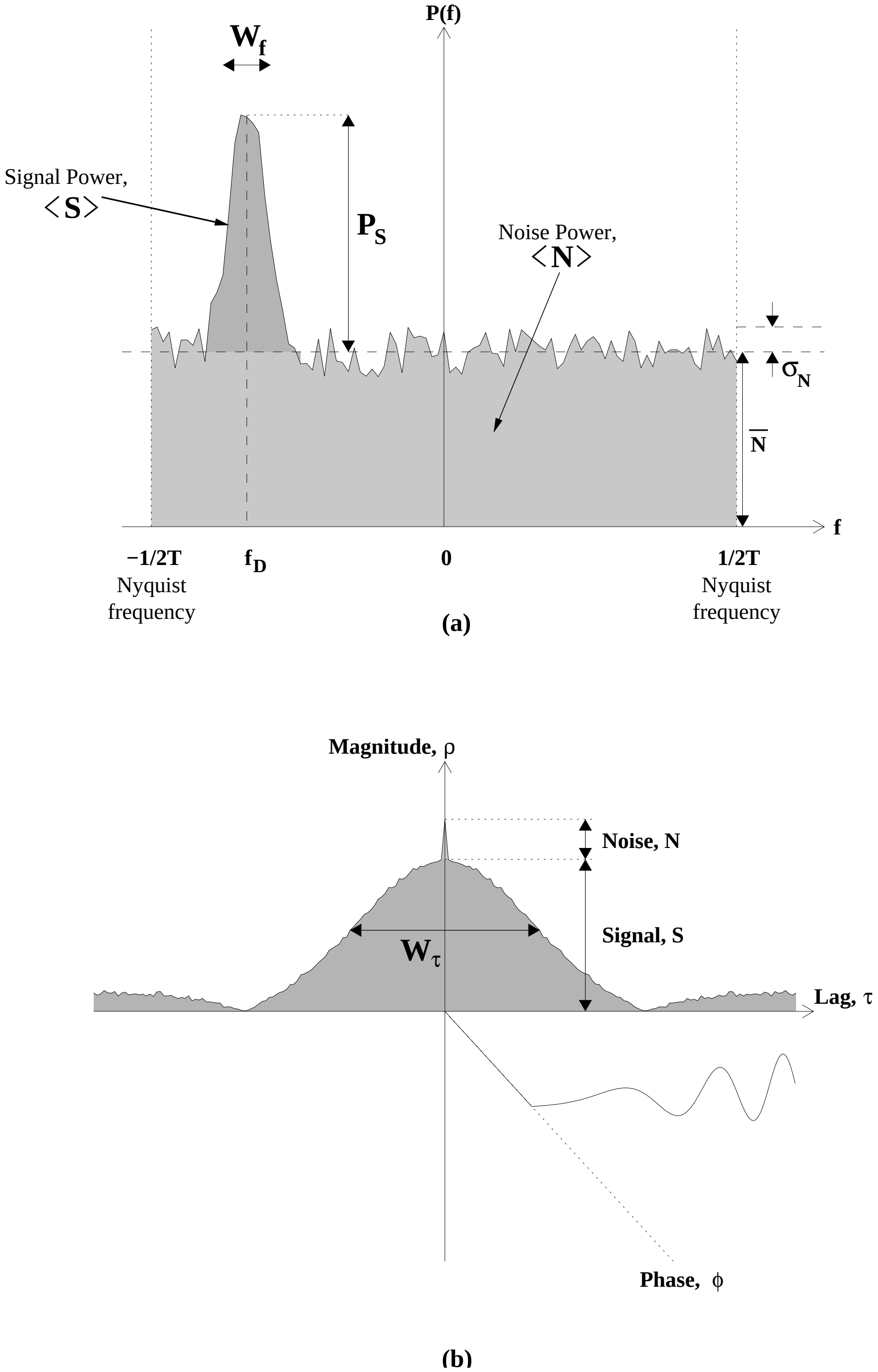

Figure 2.3: Illustrations of typical (a) power spectrum and (b) auto-correlation function, showing measurement parameters, see text for further description.

The frequency resolution is,

$$\Delta f = \frac{1}{MT}, \tag{2.4}$$

where M is the number of points (or samples) in the time-series. Increasing the length of the time-series will improve the frequency resolution, but will increase the total acquisition time of each time-series, hence decreasing the time resolution of wind measurements.

The frequency domain allows the determination of echoes originating from different types of scatterers, providing the frequencies involved are sufficiently separated. For example, clear-air and precipitation echoes, which are sufficiently separated in the spectra at VHF, or the frequency domain can be used to identify and remove undesirable signals.

The detectability of a Doppler spectrum can be defined as,

$$D = \frac{P_S}{\sigma_N}. \tag{2.5}$$

If N_i Doppler spectra are incoherently integrated then D will increase by $\sqrt{N_i}$ [*Tsuda*, 1989]. However, the SNR remains constant, as $< S >$ and $< N >$ are unaffected by incoherent integration, only σ_N is modified. Incoherent averaging can be used to help discriminate signals with low signal strength from background noise which has large deviations in the noise.

The majority of the analysis for the BLR is done in the time domain, however, the frequency domain is used for at least two alternative analyses performed with the BLR. RASS, (discussed in Chapter 7) and rain detection, (discussed in Section 5.4) require the separation of clear air echo returns and scatter from acoustic wavefronts and precipitation, respectively. Both of these measurements often require the application of incoherent averaging due to low detectability.

2.2.2 Time domain

A typical auto-correlation function is illustrated in Figure 2.3b, with the magnitude of the correlation ρ and phase ϕ shown as a function of the lag, τ. The random background noise decorrelates rapidly, producing a spike at zero-lag, with amplitude N. The noise spike can be removed by interpolating over the zero-lag, giving a (pseudo) Gaussian peak. The amplitude of the Gaussian is a measure of the echo strength and the width W_τ is a measure of the lifetime of the echo.

The auto-correlation function is simply the Fourier transform of the normalized power spectrum [*Bracewell*, 1978]. Hence the n-th classical spectral moment M_n and the n-th derivative of the auto-correlation function $R^{[n]}$ at zero lag are related by,

$$M_n = \frac{R^{[n]}(0)}{(2\pi i)^n} \tag{2.6}$$

where M_n is given as,

$$M_n = \int_{-N_f}^{N_f} f^n P(f) df \tag{2.7}$$

and the auto-covariance function of a M-point complex time series z_i is defined as:

$$\begin{aligned} R(m) &= \frac{1}{M-m} \sum_{k=0}^{M-m-1} z_k^* z_{k+m} \\ &= \rho(\tau) \exp(-i\phi(\tau)). \end{aligned} \tag{2.8}$$

As the power spectrum and auto-correlation function form a discrete Fourier transform pair, they contain identical information about lower spectral moments [*Woodman & Guillén*, 1974]. Using Equation 2.6, and if τ is sufficiently small, we obtain,

$$< S > = S \tag{2.9}$$

$$< N > = N \tag{2.10}$$

$$f_D \approx \frac{\phi(\tau)}{2\pi\tau} \tag{2.11}$$

$$(W_f)^2 \approx 2\frac{1-\rho(\tau)}{S\tau^2}, \tag{2.12}$$

Equation 2.11 is only true if the power spectrum is symmetric about its peak and no extra spikes are present in the spectrum, as this implies the phase of the auto-correlation may be oscillatory [*May*, 1986].

From Equation 2.11 it can be seen that the radial velocity of the scatterers can be obtained from the slope of the auto-correlation phase, provided that only the linear phase slope region is considered.

The majority of analyses performed on BLR data uses the Full Correlation Analysis (FCA). FCA uses the correlation functions of the time-series, computed for each individual receiver and between pairs of receivers, to obtain an estimate of the horizontal and vertical winds and the spatial and temporal characteristics of the scatterers. Chapter 6 discusses the theory and application of FCA in greater detail.

2.3 UHF boundary layer radars

The growth in the use of profilers to observe the boundary layer and lower troposphere has accelerated in the past decade. The earliest profilers typically operated at frequencies around 915 MHz [*Strauch et al.*, 1984] with height coverage from 350 m up to 10 km, albeit only under certain situations and using a very long transmit pulse (> 1 km). Concurrent development of a 405 MHz profiler for use in a demonstration network occurred during the same period. The coverage of the 405 MHz profiler was from 500 m up to 16.2 km [*Frisch et al.*, 1986].

In the late 1980's and early 1990's a smaller, portable 915 MHz wind-profiling Doppler radar was developed, to operate in a hybrid mode with 50 MHz wind profilers [*Ecklund et al.*, 1988]. The initial aim for the 915 MHz system was to fill in the lower heights below the coverage of the 50 MHz profiler. However, the smaller UHF system proved to be a versatile system in its own right, with coverage from around 100 m to 5.5 km [*Ecklund et al.*, 1990]. By 1994, there were over fifty 915 MHz profilers in the use of research and commercial groups [*Carter et al.*, 1995]. In the second half of the 1990's successful trials of a 915 MHz spaced antenna wind profiler began [*Cohn et al.*, 1997]. Previous 915 MHz profilers had used Doppler techniques, with either mechanical or electronic steering to measure the wind velocity, but by using spaced antenna techniques, improved time resolution could be obtained.

Profilers operating at UHF are very sensitive to small cloud droplets. This led to the development of cloud radars which are used to observe clouds and precipitation, they operate in the range of frequencies 30-100 GHz [*Lhermitte*, 1987; *Peters*, 2000].

More recently a 3-GHz profiler, which exploits the sensitivity of UHF, has been developed with a substantial improvement in the ability to observe deep cloud systems in comparison with the 915 MHz profiler [*Ecklund et al.*, 1999].

The sensitivity of UHF to precipitation means echoes from hydro-meteors overwhelm clear air returns such that determination of the vertical velocity of the air is not possible. This has lead to the development of VHF boundary layer radars [*Crochet et al.*, 1994; *Fillol et al.*, 1997; *Vincent et al.*, 1998], which are able to determine the vertical motion of the air in the presence of precipitation.

2.4 VHF BLR: Design criteria and considerations

A VHF boundary layer radar not only provides an alternative to a UHF profiler, but in conjunction with a UHF BL radar offers the ability to make measurements at different frequencies. There is much that is still not understood in regard to scattering processes from the atmosphere. Increased understanding will come from observations at a range of frequencies, using a variety of measuring techniques.

Operation at either UHF or VHF has advantages and disadvantages relative to each other. Similarly the techniques used by the radars to probe the atmosphere have relative advantage and disadvantages. The two predominant techniques which could be used for a boundary layer profile are spaced antenna (SA) or Doppler beam steering (DBS). A brief comparison of UHF and VHF followed by a comparison between SA and DBS will be presented. The comparisons will focus on the characteristics which are important for use in a boundary layer radar.

2.4.1 UHF vs VHF

Historically speaking, VHF radars were typically associated with height coverage, with the main focus being upon attaining measurements from as high as possible. Such systems are generally unsuitable for probing the lowest 1-2 km of the atmosphere for a variety of reasons. The size of the arrays often means the lowest kilometre is not in the far field of the antenna. The large lengths of cable and antenna connections required, increase reflections and ringing within the antenna system. This necessitates long delays before reception can commence. The transmit-receiver (TR) switches of these systems, have recovery times which are appreciable if attempting to measure returns from low heights. Measurments have been obtained using a large VHF radar from heights as low as 600 m, however, this required a decrease in transmitted power, carefully tuned antennas and modifications to TR switches [*Crochet & Bourdier*, 1989].

Alternatively, UHF radars were specifically developed in the late 1980's for profiling the lowest few kilometres [*Ecklund et al.*, 1988]. The shorter wavelength at UHF resulted in physically smaller antennas, although they were still large compared with the wavelength. Therefore UHF systems are able to have narrow beam-widths, while still maintaining a degree of portability. The wide bandwidths available in the UHF spectrum means good height resolution is possible. Additionally, the external noise is lower compared with VHF.

However, VHF systems have several advantages over UHF systems. In the presence of precipitation, the clear air echo and the precipitation echo are separately distinguishable. Therefore simultaneous measurements of rainfall distributions and the vertical velocity of the air can be made. This is of particular aid when attempting to measure the vertical gradient of the vertical velocity which gives the divergence of the wind field in storm conditions. Bragg scatter causes enhanced returns from objects whose dimensions are comparable with the operating wavelength of the radar. This has the unfortunate effect of making UHF radars extremely sensitive to birds, insects, bats, etc., while VHF radars are sensitive to airplanes. However, airplane echoes are normally singular localized events, relatively easy to distinguish and can be either removed or the time-series rejected. Birds, insects and bats on the other hand can be a concern when in large numbers, especially during migration seasons [*Wilczak et al.*, 1995]. Scatter from birds can result in large sequences of measurements being useless, (unless the radar operator is interested in radar ornithology).

VHF radars have additional advantages over UHF if radio acoustic sounding system

(RASS) techniques are being applied. At UHF, acoustic attenuation is significant, resulting in a severe restriction on the range of heights over which temperature profiles can be obtained. In periods of precipitation, UHF RASS observations are unable to account for the vertical wind due to precipitation echoes dominating the clear air echoes.

An additional advantage of VHF, which is relevant to the Atmospheric Physics Group at the University of Adelaide, is the use of the same frequency which is being used on a large VHF stratosphere-troposphere ST radar at the same field site. This has advantages in frequency allocation, technical realization and costs.

2.4.2 DBS vs SA

Many comparisons between spaced antenna and Doppler beam steering techniques have been conducted over the years, both theoretical/modelled and experimental [*Briggs*, 1980; *Röttger*, 1981; *Reid*, 1988; *Larsen & Röttger*, 1989; *May*, 1990; *Van Baelen et al.*, 1990; *Chau & Balsley*, 1998*b*]. Therefore only a brief overview will be presented here.

Both SA and DBS techniques use the same information although in slightly different ways [*Briggs*, 1980]. In both cases, scattering is produced by irregularities in the index of refraction.

For accurate measurements, DBS radars require narrow beam-widths, as wide beam-widths cause height-smearing when using obliquely-pointed beams. Narrow beam-widths imply large array sizes (relative to wavelength), which are easier to construct at higher radio frequencies (i.e. $\geq$50 MHz). However, the large array size will increase the range of the far field for the array, see Equation (1.25). This increases the minimum height from which measurements can be obtained, and is not desirable for boundary layer measurements. SA radar arrays need not have such narrow beam-widths, in fact the receiving array beam-width should not be too narrow ($\geq 5^\circ$) [*Larsen & Röttger*, 1989].

A DBS array needs to be steerable (either mechanically or electronically) in order to point the radar beam off zenith. SA arrays do not need to be steerable thus removing one source of complication. Additionally SA systems can be bi-static thus removing the need for T/R switches, that are required for DBS systems. However, in SA systems the need for three separate receiving arrays will effectively split the maximum possible gain of the system by at least three.

At VHF, echoes from the vertical are usually greater than echoes from oblique directions, an effect known as *aspect sensitivity.* UHF are not aspect sensitive. Aspect sensitivity results in an increase in the received power of the vertical beam used in SA, which helps counter-act the reduction in gain, due to having three separate smaller receiving arrays compared with the single large array used in DBS. Side-lobes are slightly suppressed when using a vertical beam, due to the relative enhancement of the zenith echoes. However, aspect sensitivity can bias radial measurements made close to zenith using DBS techniques at VHF. The enhancement of returns from the zenith results in the effective beam direction being closer to the zenith. In order to avoid the effects of aspect sensitivity on oblique beams, the zenith angle must be greater than $\sim 10°$ [*Tsuda et al.*, 1986]. Aspect sensitivity can also contaminate measurements using large oblique angles if the side-lobes are pointed towards the zenith, therefore, it is usually desirable for the first minimum in the antenna beam pattern to be pointing at the zenith when the array is pointed obliquely.

The DBS signal processing is able to obtain measurements with a SNR of -13 dB while SA requires 3 dB [*May*, 1990]. However, the apparent large difference in performance of the two techniques is greatly reduced due to a number of reasons. The dwell time[1] for DBS measurements is at least three times that for SA measurements due to the necessity to measure the radial velocity in three directions, thus decreasing the detectability of DBS with respect to SA. The good frequency resolution required for DBS is not as important for SA systems, hence the number of coherent integrations for SA can be increased, and hence improving the detectability for SA. The decrease in sensitivity for SA due to the smaller antenna area is more than compensated for

---

[1] Time between each measurements

in the gain due to aspect sensitivity when using VHF. Differences between DBS and SA obtained for larger ST radars operating at VHF are of the order of less than 3 dB [*May*, 1990]. Using similar values given by *May* [1990], UHF DBS radars would have a total system sensitivity ∼13 dB greater than UHF SA radars.

The analysis technique of DBS involves determination of only three parameters compared with six parameters for FCA, suggesting sources of error would be greater with FCA. However, DBS analysis is susceptible to spatial variations in the wind field, due to the oblique orthogonal measurements being of different areas at different times. In contrast, SA radars observe a single region. Measurements of vertical velocity using a DBS radar at VHF will be sensitive to tilting of aspect sensitive layers of scatterers. Spaced antenna measurements can account for discrepancies in the angle-of-arrival (AoA) by measuring the phase differences between receivers. DBS measurements can measure the AoA, but they require variation of the zenith angle, by small increments, to determine the direction of maximum received power, which increases the dwell time. Spaced antenna measurements of wind velocity may be underestimated if the antenna spacing is too small. This is known as the *triangle size effect* and is discussed further in Section 6.5.

RASS measurements can be obtained with either radar, however, the beam steering capabilities of the DBS system means measurements can be obtained to greater heights by tracking the acoustic wavefront [*Matuura et al.*, 1986*a*].

The French group in Toulon, has developed a DBS VHF boundary layer radar, operating at 45 MHz. A four by four array of dipoles was used for the antenna array, giving an antenna beam-width of 30°, with an oblique angle of 38° being used [*Candusso et al.*, 1998]. The larger than typical oblique angle was used to decrease the lowest observable altitude for a given range. However, the broad bandwidth and large oblique angle lead to low directivity of the antenna beam pattern and a mixing of contributions of different altitude at a given range [*Crochet et al.*, 1994]. A number of retrieval techniques were developed to attempt to obtain the reflectivity and wind velocity profiles, namely a least-squares-method and a maximum-entropy-method [*Fillol* *et al.*, 1997]. Results from a campaign in Antarctica show good agreement between radar and co-located radiosonde wind measurements [*Candusso et al.*, 1998]. Excellent agreement between the location of the tropopause height was obtained using the radiosonde measurements and the radar's vertical echo power. The minimum altitude obtained by the radar was 600 m, due to ground clutter. However, previous experiments involving the radar showed the capability of the system to obtain wind measurements from as low as 300 m [*Crochet et al.*, 1994].

The problems using DBS for boundary layer work at VHF led us to develop a SA radar, as outlined in the next section.

2.4.3 Preliminary design

The Buckland Park (BP) Boundary Layer Radar (BLR)[2] was chosen to use a spaced antenna system, which involves only vertically pointing beams. This eliminates the height-smearing problem introduced by large beam-width obliquely pointing beams, that are necessary for Doppler operation. The spaced-antenna layout also enables interferometric techniques to be applied, which can in principle correct for contamination of vertical velocity measurements caused by tilted layers [*Vincent & Röttger*, 1980].

The principle design goals for the BLR were that (1) the system was flexible in operation, (2) easily transportable and (3) power efficient, such that it could be used at remote locations. The desired height coverage was from 300 m up to 2-3 km.

Modular solid-state transmitters capable of providing high mean power with duty cycles being 10% are used. These modules are compact, power efficient and reliable. The modular nature of the transmitter means reconfiguration of the system to allow different wind measuring techniques to be applied, can be done with relative ease. The antenna array's lower height performance is crucial for successful lower height coverage. The design criteria for the antenna array is discussed in detail in Chapter 3

---

[2] From this point, references to a 'Boundary Layer Radar' or BLR, specify the system initially installed at Buckland Park, unless otherwise stated.

and fast passive T/R switches are used, (see Appendix B for further details).

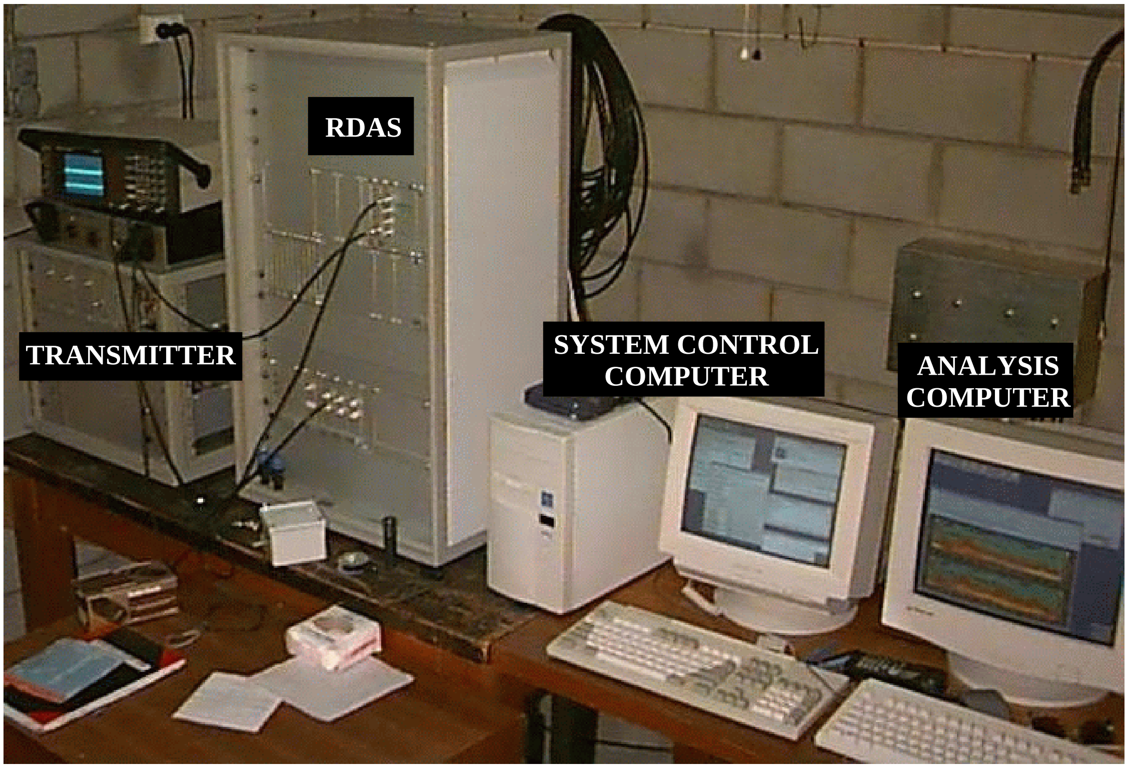

Figure 2.4: Components from the BLR (from the left), transmitter, RDAS, system control computer and analysis computer.

The receiver and data acquisition system (RDAS) used has a wide dynamic range and large amount of memory (RAM) for temporary storage of raw data. Three individual receivers corresponding to the three receiving arrays are used, thus removing any requirement for a multiplexer. The raw data is downloaded to a computer for online analysis or storage. As soon as the data is downloaded, the next acquisition begins, which is crucial for analysis techniques where the analysis time can be appreciable. Initially, the same computer was used for analysis and system control. However, analysis was later moved to a faster computer to enable more complicated and lengthy analysis to be performed on the data. Although the original computer was used for system control, once an experiment or campaign was initiated, the system would run with no further control necessary.

For operational flexibility, as many operating parameters as possible can be changed via the system control computer. These parameters included: transmitted pulse length, receiver bandwidth and gain, PRF, sampling range and resolution, number of coherent integrations and duration of time-series. It is possible to schedule multiple experiments, which is necessary when alternating different modes of operation.

A picture of the transmitter, RDAS, system control computer and analysis computer is given in Figure 2.4.

2.5 Summary

In this chapter an overview of the fundamentals of a profiling radar system was given. The choice of analysis in frequency or time domain depends on what measurements are being attempted, with advantages being offered by each domain. The majority of analysis in this thesis uses the time-domain for analysis of winds via correlation analysis, although the frequency domain is used for spectral analysis of rain echoes and RASS echoes.

The growth of UHF boundary layer profiling radars has increased over the past decade. Initially, these radar were designed to complement large VHF profilers, which were unable to obtain measurements in the lowest 1-2 km of the atmosphere. However, UHF profilers have proven to be a versatile ‘stand-alone’ system.

The additional knowledge obtained by using different frequencies to probe the atmosphere and the advantages of VHF over UHF motivated the design and construction of a VHF boundary layer profiler. At UHF, echoes from precipitation dominate over clear air echoes, hence measurements of vertical wind velocities at UHF are not possible in the presence of precipitation. UHF profilers are extremely sensitive to echoes from birds, insects and bats which interfere with atmospheric echoes, which can have serious consequences to the validity of data obtained during migration seasons. In the application of a RASS system to the two radars, the required acoustic frequencies for UHF radars are significantly attenuated compared with the acoustic frequencies for VHF systems, therefore restricting maximum coverage possible with a UHF RASS.

A spaced antenna radar was chosen over a doppler beam steering radar for the configuration of the VHF BLR. In order for the lowest heights to be in the far-field of the radar, small array sizes were necessary. Because of the small array size, the beam-width would be wide and the effect of side-lobes could be appreciable. To operate a wide beam-width array as a DBS system would require large oblique angles, to avoid aspect sensitivity biasing echoes. However, large oblique angles increase ground clutter echoes. A spaced antenna system avoids this complication. Aspect sensitivity helps to minimize the effects of the side-lobes, for a spaced antenna radar, as the echoes received from vertical are enhanced with respect to echoes received through the side-lobes.

The initial design of the VHF BLR spaced antenna array consisted of three groups of four Yagis. A substantial proportion of the development of the VHF BLR centred around the antenna array, which is discussed in the next chapter.

Chapter 3

Antennas

A major part of the development of the VHF Boundary Layer Radar (BLR) involved the antenna arrays. As the antennas are the final section of the system to be used upon transmission and the first section upon reception, it is important to optimize them. Ideally, the effect of the transition between transmit and receive states should be negligible. The antennas should be maintenance-free, easily tunable, low cost and quick to construct. However, this is not an ideal world so compromise is required. In this chapter, the design considerations for an effective antenna system are stated and the subsequent evolution of the antenna array is discussed. Three stages of development are considered, with the respective antenna arrays labelled *first generation*, *second generation* and *third generation*.

3.1 Design considerations

The primary goals of the VHF BLR imposed several design criteria on the antenna system that would be used [*Vincent et al.*, 1998].

- The arrays used for transmitting and receiving should be small enough that sampling of the diffraction pattern is in the far field and hence Fraunhofer diffraction applies.

- To achieve a physically small array size, a minimal number of antennas must be used. For adequate received signal strength these antennas must have high gain and directivity.

- Contamination of data due to transmission and reception via antenna side-lobes should be minimal.

- The beam-widths should be as narrow as possible, which will reduce the size of the scattering volume and the subsequent spread in the spectrum. However, decreasing the size of the array has the effect of increasing the beam-width, therefore a compromise between the two must be obtained.

- To obtain successful measurements from the lower heights, ringing in the system due to mismatching should be minimized. Hence good matching is required across a wide bandwidth. The short duration transmit pulses, necessary for acceptable height resolution, require a wide bandwidth on all parts of the receiving system.

- The array should require the minimal amount of maintenance. Hence the antennas need to be robust, both physically and electrically. Once tuned the antennas should not deviate too far from the ideal impedances both on a daily and a long-term basis.

- For maximum efficiency the system needs to have minimal losses.

3.1.1 Antenna fundamentals

The bandwidth of an antenna can be expressed in terms of impedance of the Voltage Standing Wave Ratio (VSWR or SWR). SWR is a measure of the ratio of the maximum voltage to the minimum voltage, resulting from the interaction of the incident and reflected voltages along the line. It is defined as

$$SWR = \frac{1+ \mid \rho \mid}{1- \mid \rho \mid}, \tag{3.1}$$

where ρ is the voltage reflection coefficient, which is the ratio of the reflected to the incident voltage. Therefore

$$\frac{P_r}{P_t} = \rho^2 \tag{3.2}$$

where P_r is the reflected power and P_t is the transmitted power. The magnitude of ρ is given by

$$\mid \rho \mid = \sqrt{\frac{(R_a - R_o)^2 + X_a^2}{(R_a + R_o)^2 + X_a^2}} \tag{3.3}$$

where R_a is the impedance of load, X_a is the reactance of load and R_o is the characteristic impedance of the line used to feed the antenna. The bandwidth is therefore given in terms of the frequency range over which the SWR is less than a certain level. A SWR of 1:1 implies all power is transmitted and none is reflected. For amateur work, a SWR of 2:1 is used for antenna bandwidth comparisons, [*ARRL*, 1994]. For the Boundary Layer Radar system developed here, a smaller value of 1.5:1 was used to define the effective bandwidth of the system. Equation 3.3 can be generalized and used to calculate the bandwidth at a given point, if the impedance frequency response is known over a given frequency range. By setting R_o to be equal to the ideal impedance value, such that no reflection would occur at the operating frequency, values of $|\rho|$ over the frequency range were obtained.

To measure the impedance, a Vector Impedance Meter was used, with a program written in Pascal to automate the procedure (Appendix C).

The power pattern of an antenna helps characterize its behaviour. The *gain* is a measure of the response of the antenna as a function of direction, defined as [*Kraus*, 1988],

$$G(dBi) = \frac{U_m}{U_i}, \tag{3.4}$$

where U_m is the maximum radiation intensity and U_i is the radiation intensity from a (lossless) isotropic source with the same power input. The half-power beam-width describes the spread or concentration of the beam, where the power has fallen to half of the maximum power (3 dB below maximum), sometimes given as the *3-dB points*.

Given the power pattern of an antenna, we can determine its *effective aperture* or *effective area* A_e, defined as,

$$A_e = \frac{G\lambda^2}{4\pi} = \frac{\lambda^2}{\theta_{HP}\phi_{HP}}, \tag{3.5}$$

where θ_{HP} and ϕ_{HP} are the half-power beam-widths in the θ and ϕ planes, respectively (radians).

3.2 First generation array

The first generation boundary layer radar array [*Vincent et al.*, 1998], consisted of twelve antennas, which were divided into three groups, each comprising of four antennas, as shown in Figure 3.2. In reception, each group was connected to a separate receiver, while in transmission, all three groups were used simultaneously.

Figure 3.1: First generation array during sunset at Alice Springs, 1998.

3.2.1 Three element folded Yagis

The antennas chosen to be used for the initial system were three-element Yagis with a folded dipole driven element, see Figure 3.3.

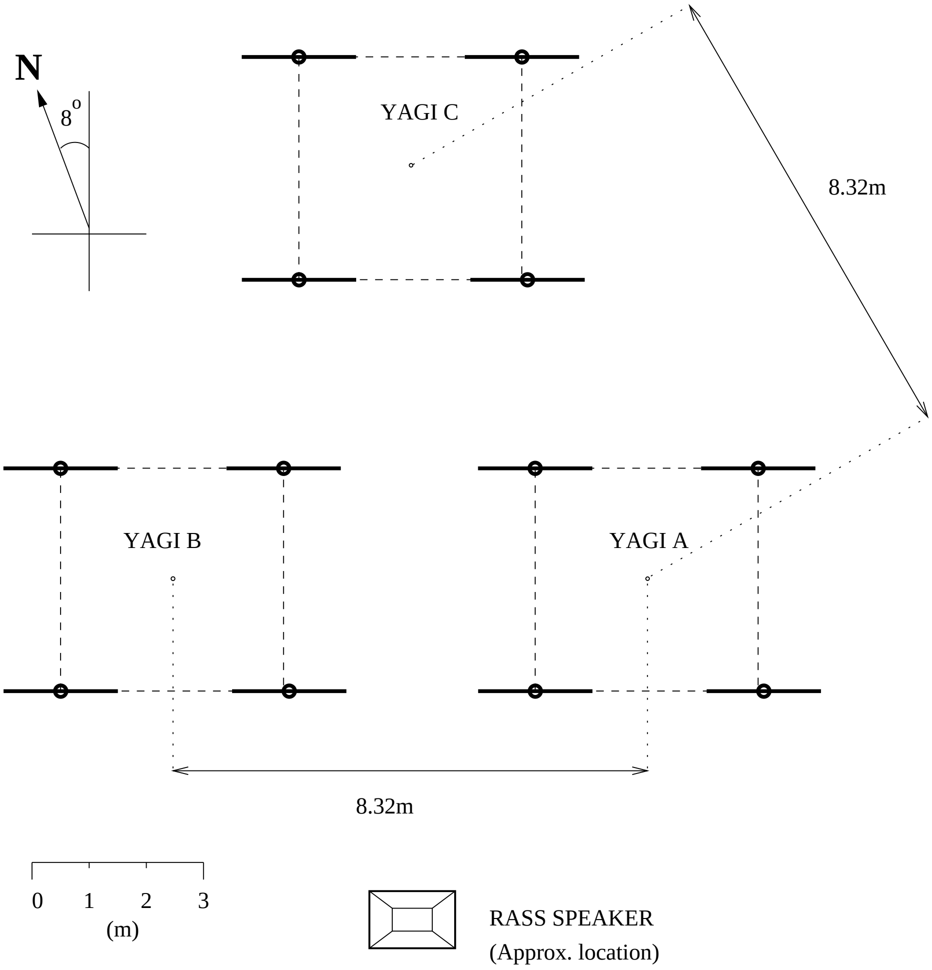

Figure 3.2: First Generation array setup - Plan arrangement.

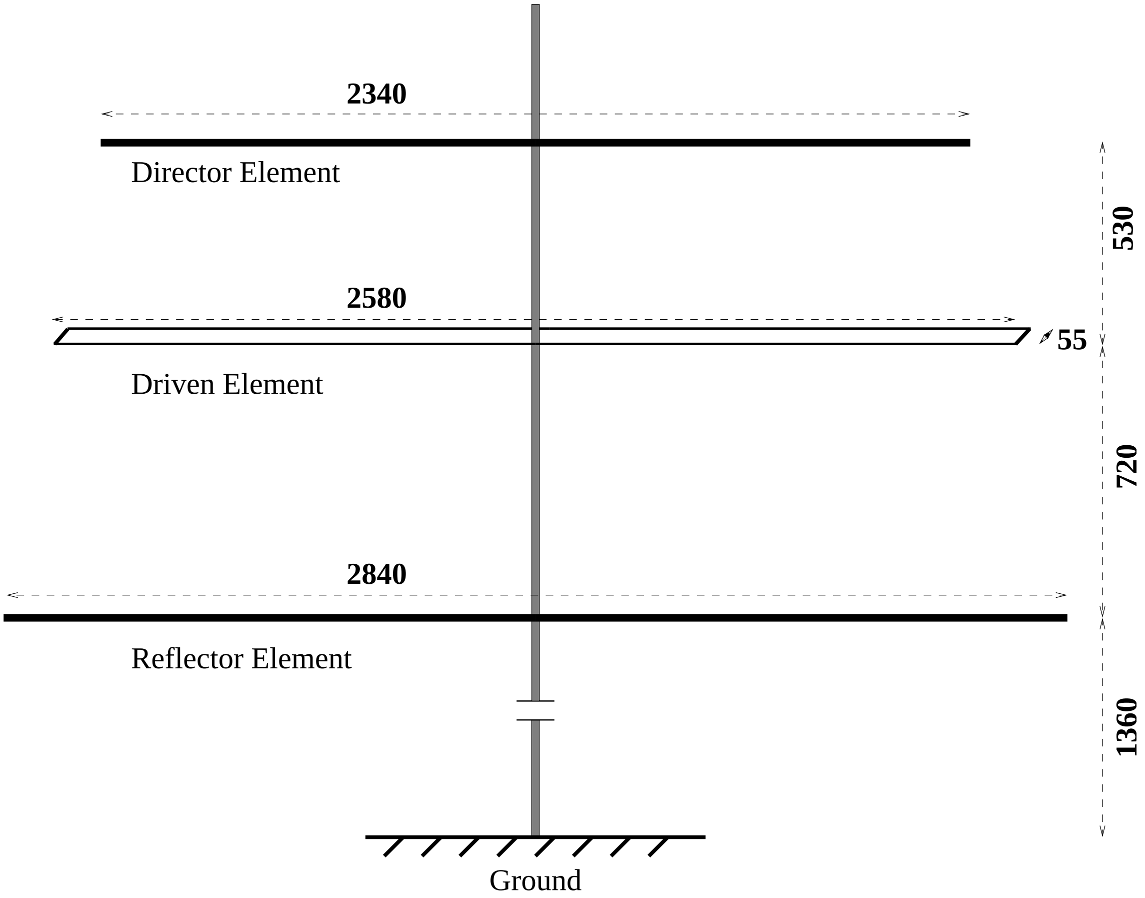

Figure 3.3: Three element folded Yagi - Elevation, (measurements in mm.)

These Yagis managed to fulfill many of the requirements mentioned above. They are identical to antennas used on the larger BP VHF ST radar for spaced antenna measurements, therefore spare parts were readily available. They are easy to construct and install and have a gain of greater than 6 dBi with a beam-width of 72° in the E-Plane and 146° in the H-Plane, with an efficiency of greater than 95%. Yagis were chosen over dipoles, despite dipoles being cheaper and simpler to construct, for a variety of reasons. Yagis have superior gain (or directivity) due to the reflector and director making the beam-width narrower. Superior portability is attained by the Yagis, due to the absence of a ground plane, which is required when using dipoles.

3.2.2 Baluns

In order to efficiently transmit and receive power, the antenna must be balanced and well matched to the output/input impedance of the transmitter/receiver, respectively. Several methods of transforming the feed impedance of the Yagis were investigated, including coaxial-cable tuning circuits and inductor-capacitor (LC) tuning circuits using coiled wire inductors, [*Dullaway*, 1999]. A 4:1 wound toroid Balanced to Unbalanced (balun) device was selected (see Figure 3.4) as the most appropriate due to its intrinsically wide bandwidth. By altering the spacing between the coils around the toroid and adjusting the tunable capacitor, it was possible to tune the antenna impedance to $50.0 + j0.0\Omega$ with an accuracy of $\pm 0.1 \pm 0.1j\Omega$. This arrangement, although sensitive in the initial tuning stage, was found to be quite robust. During trials in Alice Springs and Sydney the entire antenna was dismantled with the balun remaining undisturbed in its container. Upon reassembly, the impedance of each antenna was found in the majority of cases to still be within the range $48 - 52\Omega$, which allowed immediate use, although not at full efficiency. The bandwidth of a single Yagi fed via the balun is greater than 4 MHz as shown in Figure 3.5. The balun was placed inside a weatherproof, UV-resistant box with a BNC external input.

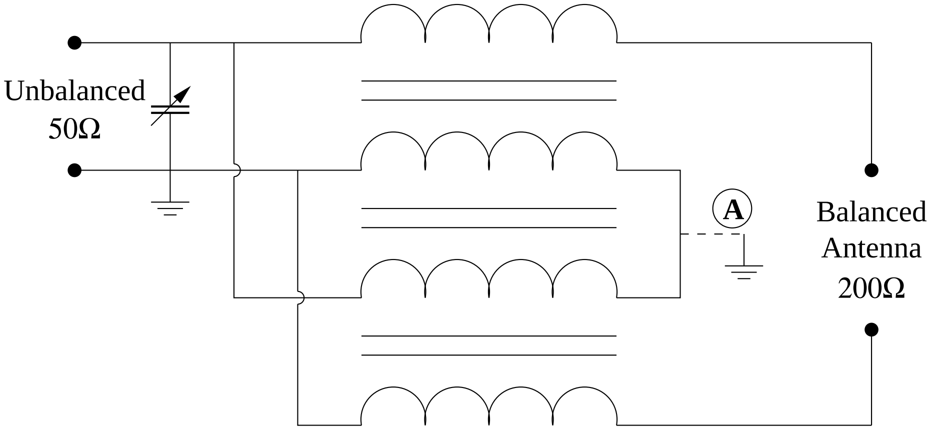

Figure 3.4: Simplified circuit diagram for a 4:1 Ferrite core balun used for matching the antenna to the transmission line. Point A in theory is effectively at ground, in practice it was electrically grounded to improve the balancing. This type of balun was used in the first generation array.

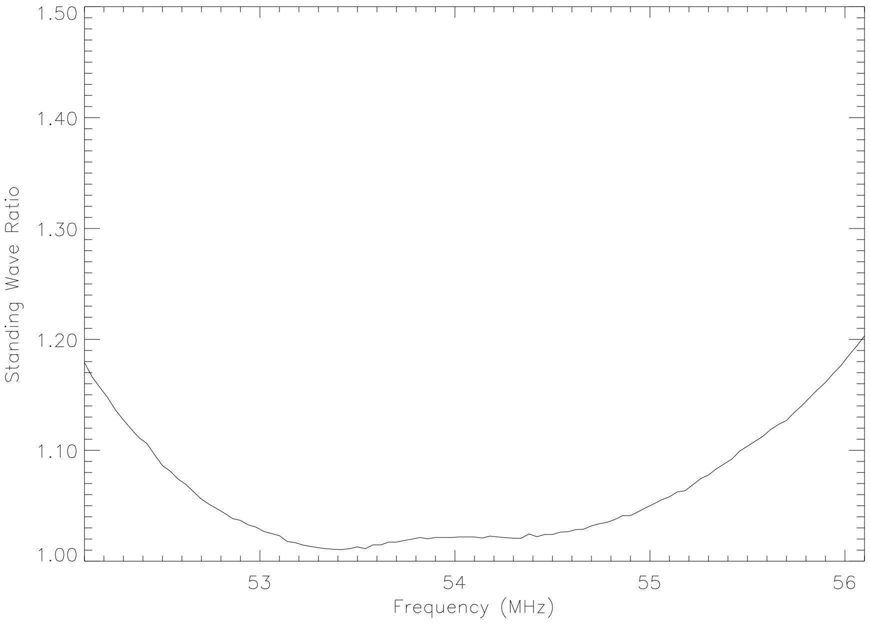

Figure 3.5: SWR vs frequency, three-element folded Yagi with toroid balun, measurements taken 9th September 1996.

3.2.3 Receiving array

It was decided that each receiving array would consist of four Yagis arranged in a square, with sides 0.7λ long. This arrangement gave the receiving array sufficient gain while maintaining a relatively small aperture. The Yagis were held in place by tubes running along the ground on the sides of the square and attached to the bottom of the Yagi's boom via knuckle joints. To provide extra stability, the antennas were fastened to pegs in the ground via guy ropes. Having the entire antenna system situated on top of the ground made installation simple, as no digging was required. With hard or rocky ground the guy ropes were attached to rocks or bricks, used in place of the pegs.

A means of combining the received signal and splitting the transmit signal was required. To maintain the wide bandwidth achieved with the individual Yagis a tunable wide-bandwidth splitter was built, (see Figure 3.6). The T-Section in the splitter box, was added to bring the output of the box, when loaded with the final antennas, closer to the optimal impedance of $50 + j0\Omega$. The design of the T-Section uses two L-Networks [*Bowick*, 1982] designed to match 50Ω to 200Ω, with the second L-Network reversed and attached to the first, giving an effective transformation of 50Ω : 200Ω :

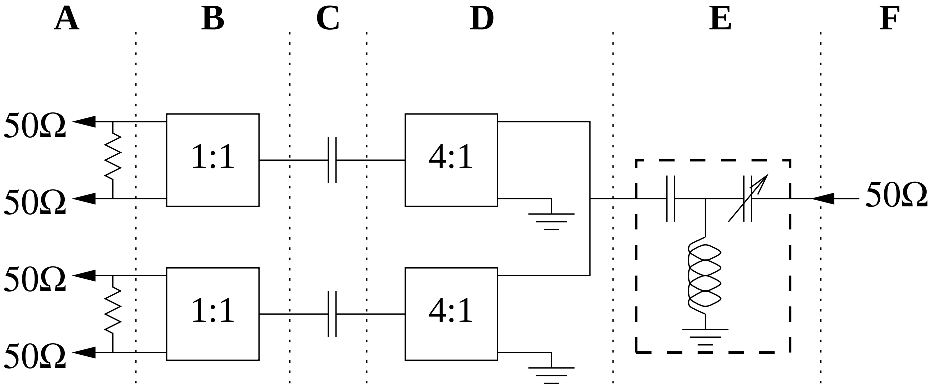

Figure 3.6: Splitter box circuit. Section A is the antenna input/output. The resistors shown at this stage helped isolate the antennas, especially when one of the antennas is no longer optimally tuned. B consists of a ferrite core inductor which helps isolate the antennas. C is a capacitor which removes any stray inductance at this point. D is a 4:1 toroid wound transformer, E consists of a T-Section which gives the ability to optimize the splitter box in-situ.

200Ω : 50Ω or 50Ω : 50Ω (see Appendix D). By using the tunable capacitor and varying the inductor's value via manipulation of the distance between the coils, the T-Section's impedance transformation can be changed slightly. The resulting bandwidth, as measured at the output of the splitter when attached to the tuned antennas, can be seen for all three receiving arrays in Figure 3.7. The wider bandwidth of group C, is due to the die-cast box which contained the splitter circuitry being substantially larger than those used for group A and B. It was found that the actual die-cast container can have a substantial affect on the tuning due to its interaction with the components. Placing the lids on the smaller boxes caused the magnitude of the output impedance to drop by up to 5Ω and the phase to change by several degrees.

The bandwidth of the receiving array when measured directly at the output of the combiner box was greater than 2 MHz, (Figure 3.7). Although this is much narrower than the bandwidth for a single Yagi, see Figure 3.5, it is considered wide enough for the desired purpose.

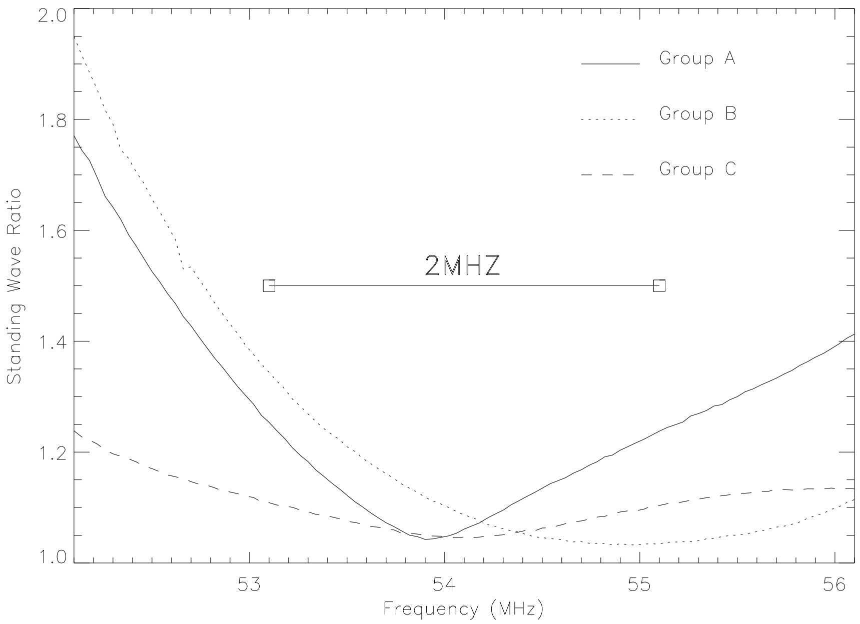

Figure 3.7: SWR vs Frequency, First Generation Receiving array, measurements taken 9/10/1996.

The Yagi antennas in the receiving array were connected to the tuning boxes by feeder cables made of RG213-MIL. This cable has an impedance of 50Ω, which is identical to the antennas impedance and the output of the splitter box, and minimizes any mismatching in the antenna system. Military Spec RG213 was chosen because of the lower loss characteristics of the cable over normal RG213. By placing the splitter box in the middle of the receiving array, the length of the feeders from the antennas to the splitter box was 1.5λ.

3.2.4 Transmitting array

During transmission all three receiving arrays were used simultaneously. For symmetry, the position of the centres of each receiving array would be at the vertices off an equilateral triangle. To achieve optimal wind measurements, with spaced antenna techniques, the average spatial cross correlation between pairs of receivers should be ~0.5, [*Briggs*, 1984]. Previous experiments to determine the optimal spacing used three similar receiving arrays placed in a line at 3λ and 1.5λ spacing [*Dullaway*, 1999]. By transmitting on just the centre array and receiving on all three, it was possible to obtain correlation functions at 1.5λ, 3.0λ and 4.5λ spacings simultaneously, see Figure 3.8. Trials conducted with the above setup and using the results obtained from an altitude of 600 m to 1000 m showed that a spacing of 1.5λ was optimal [*Dullaway*, 1999].

Ideally the radar site should be localised and flat. To minimize any losses, the cables from the transmitter/receiver to the array need to be as short as possible. Some concessions were made due to the constraint of needing a reliable power source and weatherproof enclosure. The final position of the system at Buckland Park was in close proximity to a building which was previously used to house the transmitter of a MF radar and still had the transmitting dipoles situated around it. It was hoped the influence of these lower frequency dipoles and their supporting towers was minimal. However, lower height coverage at the Alice Springs and Sydney sites using the same system, was superior, suggesting that background influences were limiting the system

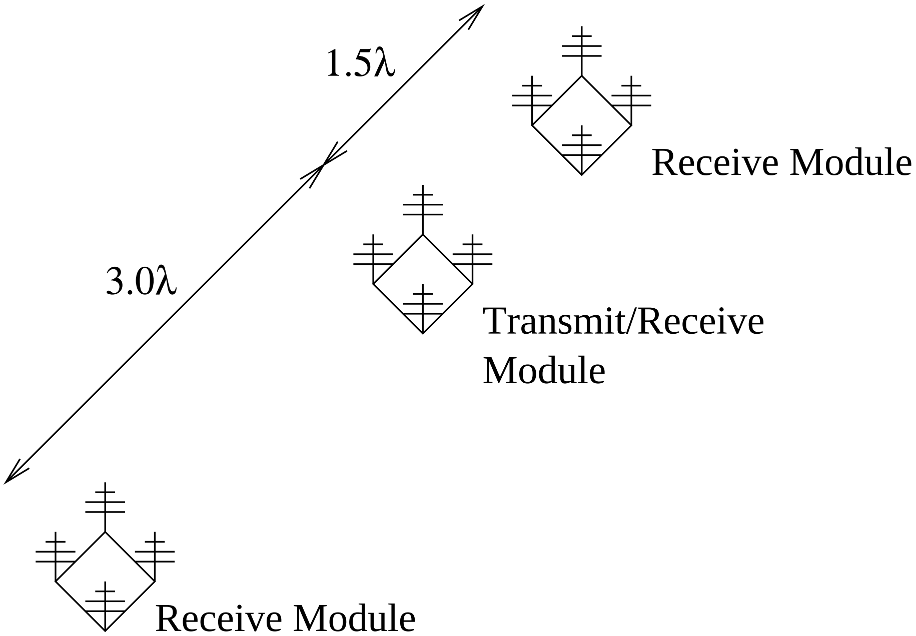

Figure 3.8: Configuration of antenna modules for determining pattern scales in the lower atmosphere (From *Dullaway* [1999])

at Buckland Park and the surrounding MF system was likely to be the source of this. The feed cable length used was 31.4 m or 8.5λ for RG213-MIL which has a velocity factor of 66%. The array was orientated so that it had an East-West baseline. As illustrated in Figure 3.2, the Yagis were all orientated such that the elements were aligned with the baseline.

3.3 Second generation array

The first generation array proved to be very reliable and robust. However, there were areas that could be improved, leading to the development and construction of the second generation array. These included increasing the gain, reducing the effect of side-lobes in the radiation pattern, increasing the power handling capability of the antenna array and simplifying the total design of the array.

Increasing the number of antennas in the array should increase the gain and hence increase the coverage of the radar, especially in conditions where the signal strength had previously been too low. A reduction in the spacing between antennas should decrease the side-lobes. Increasing the amount of transmitted power with the first generation array would have resulted in exceeding the maximum voltage rating on many of the components, especially the tuning capacitors. The spacing between the centres of the receiving array, however, should not greatly exceed 1.5λ. As the relative complexity of the original baluns and splitter boxes resulted in significant construction time and cost, a simpler method was desired. However, any changes to this section of the antenna array would need to replicate the wide bandwidth characteristics obtained with the first generation array to be a viable alternative.

3.3.1 Gamma-matched Yagis

The antennas chosen were three element Yagis (see Figure 3.9), which were slotted inside Oz-Post supports embedded in the ground in the desired position. This base provided enough stability and rigidity that additional guy wires were not necessary.

A gamma-match system was chosen to tune the antennas to the desired input impedance. The principle of the gamma-match can be understood via Figure 3.10. The outside of the coaxial cable is attached to the centre of the driven elements as the RF voltage at the centre of a $\frac{1}{2}\lambda$ dipole is zero. The centre conductor of the coaxial cable taps into one side of the driven element. The input impedance increases as the tap moves away from the centre of the element. Any inductive reactance is tuned out via a series capacitor. The capacitor and tap were combined together into one assembly to simplify the design as well as provide a higher input power rating. The position of the tap was varied via a sliding clamp arrangement, joining the driven element and a smaller aluminium tube positioned parallel to the element. A smaller diameter rod attached to the centre conductor of the coaxial cable was inserted in the aluminium tube, while remaining insulated from it, therefore forming a capacitor. By varying the amount the rod was inserted, the capacitor's value could be altered. To waterproof the gamma-match, heat-shrink tubing was placed around the junction of the rod and the arm.

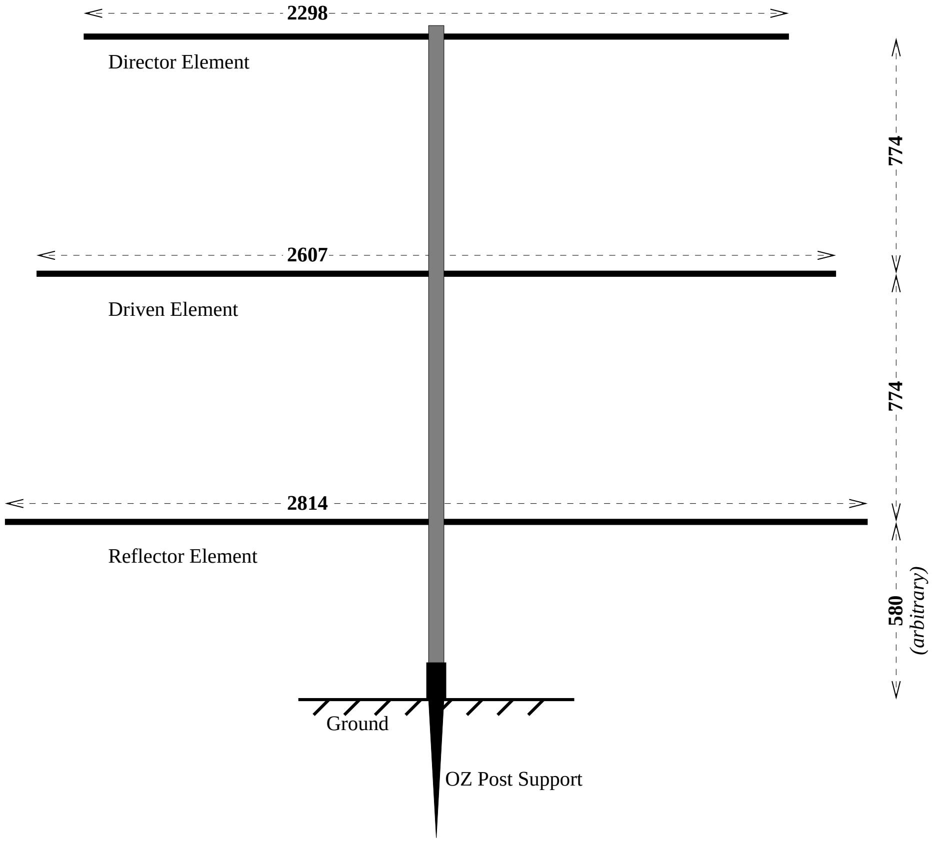

Figure 3.9: Three element Yagi, suitable for 54.1MHz - Elevation, (measurements in mm)

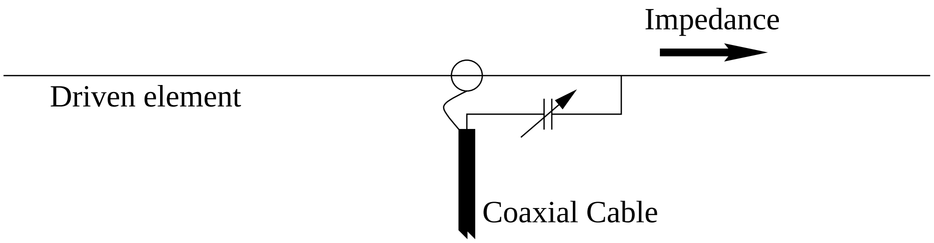

Figure 3.10: Gamma-match method

3.3.2 Layout and final tuning

The number of antennas in each receiving array was increased from four to nine. To limit the increase in physical size this would create and to reduce the effect of side-lobes, the distance between antennas was reduced to 0.5λ, thus giving a geometric area size of $1\lambda \times 1\lambda$ compared with $0.7\lambda \times 0.7\lambda$ for the older array. Due to the reflector elements being slightly longer than 0.5λ the antennas were rotated 45°. This arrangement also helped to decrease coupling between the antennas. The final layout of the array is shown in Figure 3.11 with the baseline chosen to be east-west.

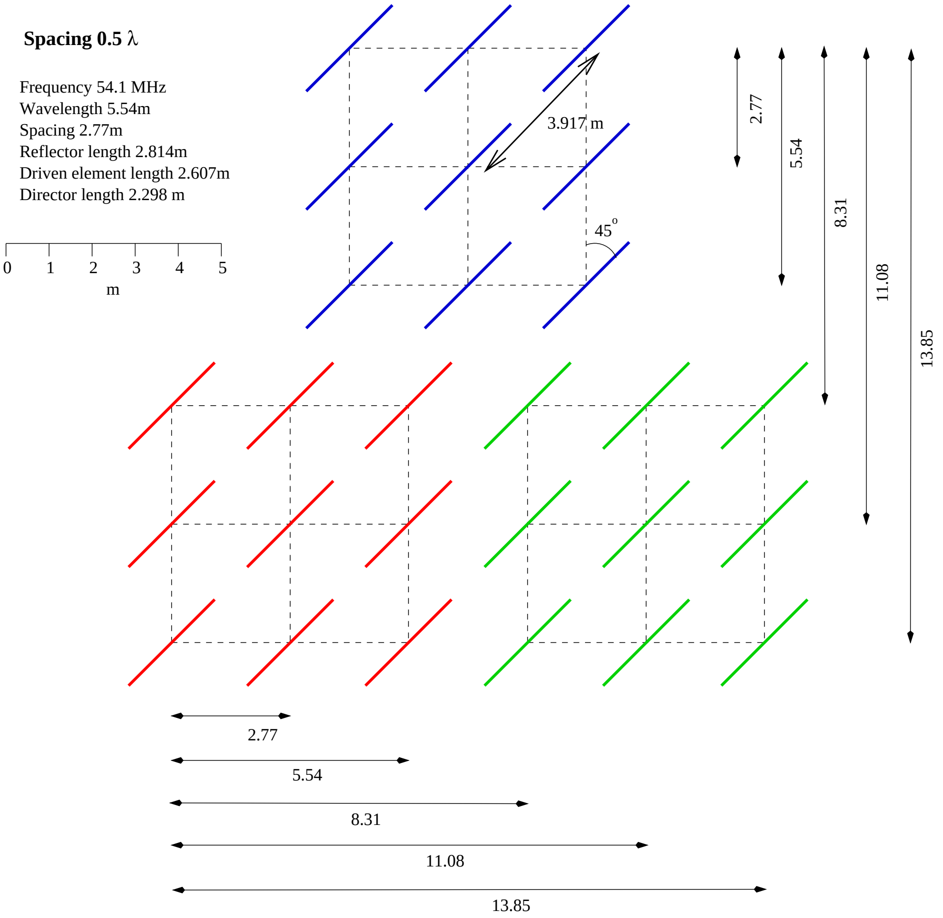

Figure 3.11: Second/Third Generation Boundary Layer Radar Antenna Setup - Plan arrangement, (measurements m)

The impedance of each receiving array needed to be 50Ω, so a method of combining the nine antennas in each group was developed using quarter-wavelength transformers.

The feed to the antennas was split into nine parallel sections, which required the input impedance of each of these sections to be $50\Omega \times 9 = 450\Omega$. Each of these sections consisted of a $\frac{5}{4}\lambda$ long 75Ω coaxial cable connected to an antenna. To maintain a matched system, the input impedance Z_L of the antenna is given by the quarter-wave transformer equation, [*ARRL*, 1994]

$$Z_L = \frac{Z_O^2}{Z_i} \tag{3.6}$$

where Z_O is the characteristic impedance of the line (50Ω) and Z_i is the impedance at the input end of the line (450Ω), so that the antennas had to be tuned to 12.5Ω. Close proximity of objects, even a human body, can affect the measured impedance of the antennas, therefore a $\frac{5}{4}\lambda$ long 75Ω cable was constructed to assist in the tuning of the antennas. This length would duplicate that used in the combiner harness described above. The harness was constructed by an external company[1] and provided as a sealed unit.

It was found that the sliding capacitor arrangement on the gamma-match was extremely sensitive to very minor adjustment. The allowed deviation in the impedance after tuning was $\pm 0.1\Omega$ for the magnitude and $\pm 1.0°$ for the phase. As the combining harness was a sealed unit, tuning of the antennas was performed without the harness attached. Initial attempts at tuning the array were unsuccessful, with the combined impedance of a receiving group being $\sim 84\Omega$ and $10°$. This error was found to be due to a manufacturing fault, which was rectified. A T-section, similar to that used in the first generation array ("section E" in Figure 3.6), was attached to the output of the harness to aid in tuning. However, this reduced the power rating of the antenna array, effectively making it the same as the original array.

The first generation Yagi's balun boxes had proven to be robust and any tuning remained relatively stable for long durations. The gamma-match, due to its exposure, had a greater chance of being affected by environmental changes. The sensitivity of the capacitor, observed during tuning, implied any slight changes could drastically

---

[1] Broadband Propagation

affect the impedance. A summary of the results of a crude trial conducted over several hours and including the effects of moisture on the gamma-match are summarized in Tables 3.1 and 3.2. The variation in impedance observed when surface water was added was negligible compared with the variation noticed when no water was added but observations were taken several hours apart. The effects of adding water are given in Table 3.2.

Date	Impedance
26.6.1999	$12.14\Omega, -2.0°$
6.7.1999	$12.49\Omega, +6.1°$
(re-tuned)	$12.61\Omega, -0.6°$
(two hours later)	$12.78\Omega, -3.3°$

Table 3.1: Temporal Variation of Impedance

Action	Impedance
Dry.	$12.78\Omega, -3.3°$
Water on connections between gamma-match and driven element.	$12.80\Omega, -3.7°$
Water on Gamma-match capacitor.	$12.87\Omega, -2.9°$
Water on all components.	$12.93\Omega, -1.3°$

Table 3.2: Effect of Water on Impedance

The bandwidth of the second generation receiving array was found to be relatively narrow ($\sim 1MHz$) when compared with the first generation receiving array ($> 2MHz$, see Figure 3.12), requiring a careful analysis of the individual sections which made up the array: the gamma-match; $\frac{5}{4}\lambda$ section; and final combining section with attached T-section. As shown in Figure 3.12, the T-Section in this case only shifted the position of the bandwidth relative to frequency. It has negligible effect on the actual bandwidth's broadness. The bandwidth of a single 2nd generation Yagi antenna is greater than 2 MHz, which indicates how the $\frac{5}{4}\lambda$ section restricts the bandwidth.

The input impedance along a transmission line is given by [*ARRL*, 1994],

$$Z_{in} = Z_o \frac{Z_L cosh(nl) + Z_O sinh(nl)}{Z_L sinh(nl) + Z_O cosh(nl)}, \tag{3.7}$$

where Z_{in} is the complex impedance at the input of the line, Z_L is the complex load impedance, Z_o is the characteristic impedance of the line, l is the electrical length of

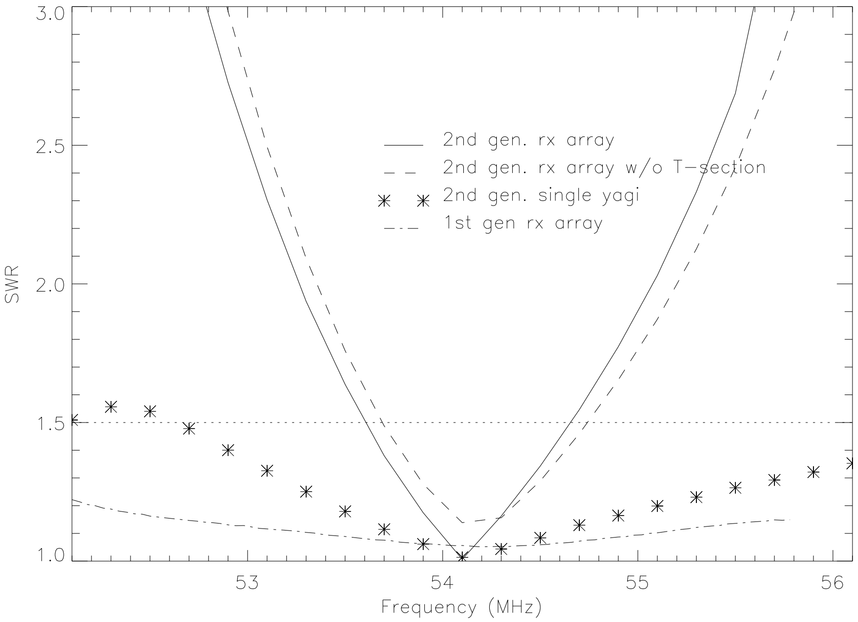

Figure 3.12: SWR vs frequency

the line, n is the complex loss coefficient $(\alpha + j\beta)$, α is the matched line loss attenuation in nepers/unit length [2] and β is the phase constant of the line in radians/unit length. Using Equation 3.7 the bandwidth of a $\frac{1}{4}\lambda$, $\frac{3}{4}\lambda$ and $\frac{5}{4}\lambda$ long transmission line with a load impedance of 12.5Ω can be calculated, see Figure 3.13. The coaxial cable used for the transmission line is Belden 1617a.

Two things to be noted in Figure 3.13 are the reduction in the bandwidth and the increase in SWR at 54.1 MHz, as the cable length increases, both of which are due to cable attenuation. Comparisons of Figures 3.12 and 3.13, show that the major contributing factor to the narrow bandwidth of the second generation receiving array are the $\frac{5}{4}\lambda$ sections.

---

[2] 1 neper = 8.688dB

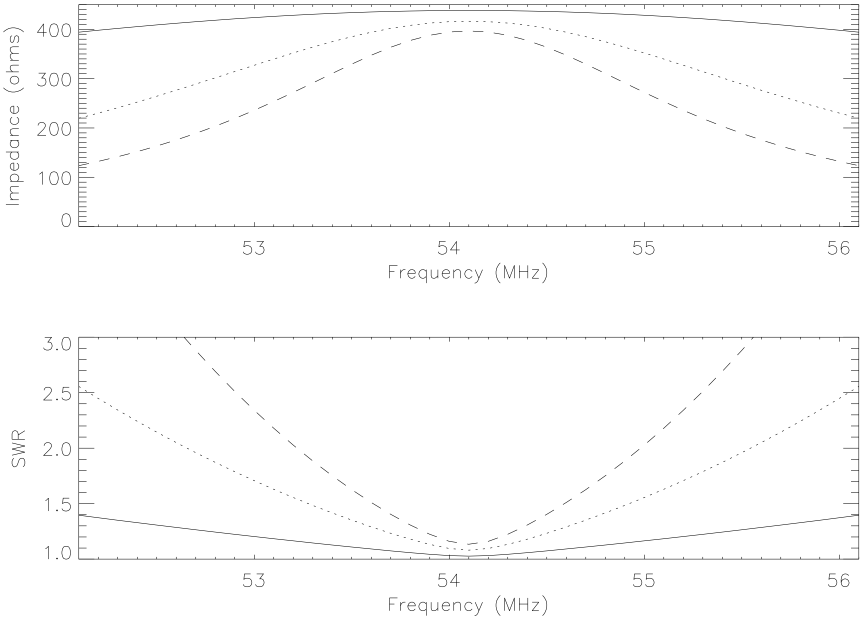

Figure 3.13: Quarter wavelength sections using 75Ω coaxial cable (Belden 1617a) and a 12.5Ω load. Cable lengths $\frac{1}{4}\lambda$ (solid), $\frac{3}{4}\lambda$ (dotted), $\frac{5}{4}\lambda$ (dashed). Ideal impedance is 450Ω.

3.4 Third generation array

The combiner harness of the antenna array was redesigned in order to increase the bandwidth and give a value comparable with that obtained with the first generation array. The final design chosen consisted of each Yagi being tuned to be 50Ω. Three such Yagis were then combined in parallel to give an input impedance of $\frac{50}{3}\Omega$, which was then fed via a $\frac{1}{4}\lambda$, 50Ω transmission line, to give an input impedance of 150Ω. Combining three of these arrangements in parallel gives an input resistance of 50Ω (Figure 3.14). The change in input impedance required a modification to the dimensions of the gamma-match. A single such gamma match was initially constructed and attached to a Yagi. The frequency response of this modified Yagi was measured, thus giving it's bandwidth. By modelling the effect of the proposed combining section, a theoretical response could be obtained. This is shown in Figure 3.15.

The bandwidth of the modelled array is comparable with that of the first generation

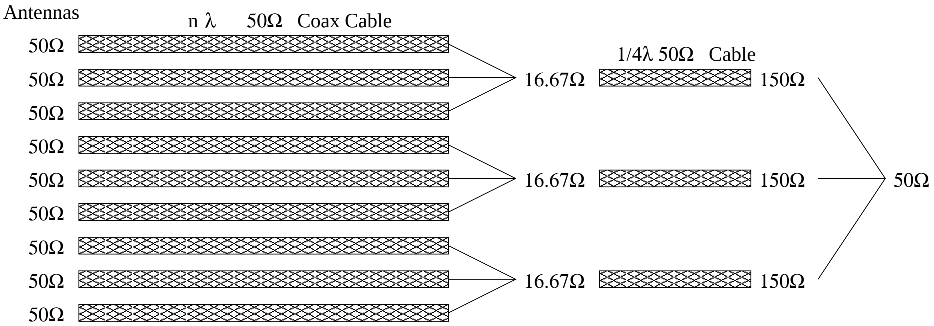

Figure 3.14: Schematic of the third generation array combination.

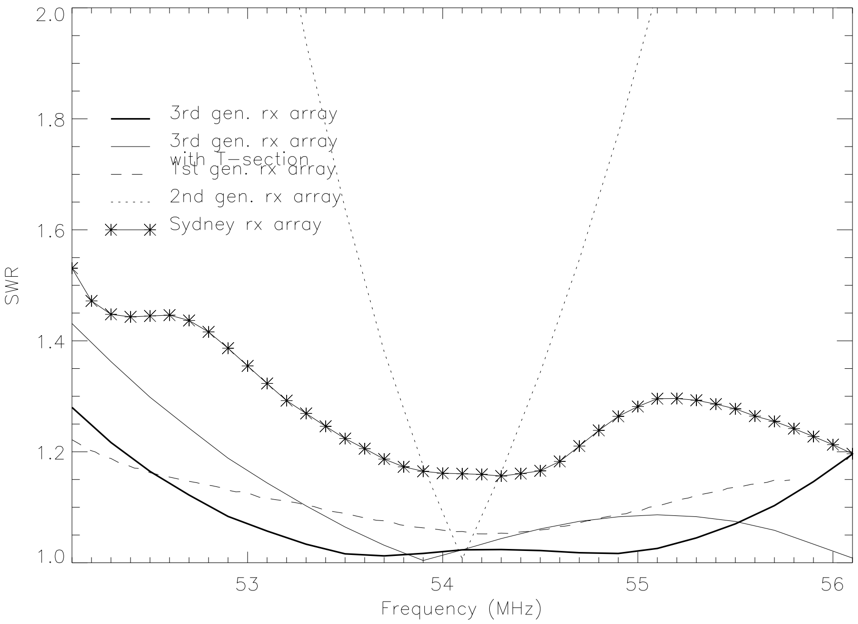

Figure 3.15: Third generation array, bandwidth modelling results are shown along with actual measurement from 1st and 2nd generation arrays as well as measurements obtained from the Sydney Airport Installation (9/99) using a third generation array.

array. Actual measurements obtained from the Sydney Airport installation are shown for comparison. A T-Section was not included in the design of the array as it had negligible effect on the actual bandwidth and would only reduce the maximum possible power that could be driven through the arrays without damaging its components.

The third generation array is equivalent or superior in most aspects to the first and second generation array. It has the wide bandwidth of the first generation array and the relative simplicity of construction of the second generation array, along with a higher input power limit than either of the previous two designs. However, the tuning of a gamma-match is a sensitive process and due to exposure to the weather it has greater potential for deterioration than the first generation baluns. Regular maintenance of the array was found to be necessary, with the time between tunings being as short as two months (depending on the care taken with the previous tuning). The deviation in the impedance away from optimal 50Ω, before re-tuning, has been observed to be much greater with the third generation array than it was with the first generation array. The amount of adjustment required with both antenna designs is dependent upon the care taken during the previous tuning, thus implying tuning is susceptible to the abilities (and patience) of those doing the maintaining.

3.5 Summary

The evolution of the VHF Boundary Layer Radar antenna array has been discussed. The performance of each stage of development and individual section was examined. The focus of the evaluation of the arrays centred around the bandwidth and minimizing any mismatch between components.

The first generation array was found to be robust and tunable with a wide bandwidth. To improve the performance of the system and obtain measurements from greater ranges, the number of antennas and hence, the gain, was increased. To simplify the array and reduce the construction costs a simpler antenna design was implemented concurrently. The relative complexity of the toroid-wound baluns with three-element

Yagis and folded driven element was replaced by simpler (and less expensive) gamma matched three-element Yagis. The combining harness was similarly modified to be simpler and cheaper to construct. However, this second generation design was found to have an extremely narrow bandwidth and needed to be redesigned, hence the third generation array was conceived and constructed. The use of a T-section in the final tuning stage was excluded as it was found the bandwidth of the array was the crucial factor and not the minimization of mismatching. In addition the T-section would reduce the power handling capabilities of the array.

The third generation array has comparable bandwidth to the first generation and hence a similar level of ringing would be expected with both systems. However the susceptibility of the third generation array to de-tuning, due to the sensitivity and exposure of the gamma match, may result in the requirement of an increase in the frequency of maintenance.

Most of the design criteria have been met. The array sizes for all three arrays given were small enough to ensure that the diffraction pattern was in the far field. The point where the near field and far field meet was calculated to be as low as ~ 40 m. A limited number of antennas has been used in the array, to limit the size of the array. An increase in the number of antennas was accomplished with very minor increase in total antenna size, with the implementation of the second and third generation arrays. By reducing the spacing between antennas the effect of ground clutter entering through side-lobes was reduced.

The following chapter deals with the calibration of the radar, which requires knowledge of the antenna beam pattern. Using numerical models the beam-width and gain of the arrays presented in this chapter are calculated, thus enabling comparisons of the different generation's beam patterns to be performed. The numerical modelling is then extended to calculate the theoretical coupling within the arrays.

Chapter 4

Radar Calibration

Preliminary discussion on the characteristics of the antenna systems used was given in Chapter 3. However, to be able to accurately describe the entire system, further analysis is required. Some of the atmospheric parameters, (i.e. reflection coefficients, rain rates), that can be measured with the radar, require the absolute received signal power to be measured. Thus a number of the radar characteristics and properties need to be determined, including the gain of the array (transmitting and receiving), losses in the feeder cables and combining harnesses, effective noise of the receivers, and coupling between antennas.

The work presented in the following chapter highlights the motivation behind obtaining the above estimates of the relevant parameters as well as the methods used to obtain them. Through the use of electromagnetic modelling programs, such as Numerical Electromagnetic Code (NEC), part of the information about the actual antenna array can be obtained without the need to perform time consuming, difficult and in some cases impossible, measurements with the available equipment. Where possible, measurements were attempted for comparison.

4.1 Modified Radar Equations

A fully calibrated radar system makes it possible to determine the absolute power received by the system. If the transmitted power is accurately known then the backscattering cross section σ can be determined. A value more commonly used is the reflectivity $\eta(r)$ or the expected backscattering cross section per unit volume. The weather radar equation which relates the signal at the receiver's output $\overline{P}(r_0)$ to radar parameters and $\eta(r)$ can be written as [*Doviak & Zrnić*, 1993],

$$\overline{P}(r_0) = \frac{P_t g^2 g_s \lambda^2 \eta c \tau \pi \theta_1^2}{(4\pi)^3 r_0^2 l^2 l_r 16 ln(2)}, \tag{4.1}$$

where r_o is the range to the center of the scattering volume (metres), P_t is the transmitted peak power, g is the axis antenna power gain with no feed-line loss, g_s is the system gain, λ is the radar wavelength (m), τ is the transmitted pulse length (s), θ_1 is the one way half-power antenna beam-width (radians), l is the one-way atmospheric attenuation and l_r is the receiver loss factor.

Equation 4.1 is for a mono-static radar system[1] , as the BLR is effectively bi-static, modifications to the equation are required. Instead of g^2 we will use $(g_t \times g_r)$, where g_t and g_r are the axis antenna power gains for the transmitting and receiving arrays, respectively. Similarly for θ_1^2 we will use $(\theta_t \times \theta_r)$ where θ_t and θ_r are the respective one-way half-power antenna beam-widths for the transmitting and receiving arrays. Instead of P_t we will use $\epsilon_{tx} P_t$, where ϵ_{tx} is the transmission line loss, P_t will be measured at the output of the transmitter. The loss due to atmospheric attenuation can be considerable when using higher frequency radars, but at VHF this can be considered negligible (i.e. $l = 1$).

The reflectivity can be expressed as,

$$\eta(r) = \frac{1024 \pi^2 r_0^2 l_r ln(2) \overline{P}(r_0)}{\epsilon_{tx} P_t g_t g_r \lambda^2 c \tau \theta_t \theta_r g_s}. \tag{4.2}$$

The majority of the rest of this chapter will be devoted to the determination of the variables given in the above equation.

---

[1] Same antennas are used for transmitting and receiving

4.2 Calibration parameters

The receiver calibration is discussed first, with the receivers total gain being calculated by comparisons with a noise source substituted in place of the antenna inputs. The transmitter efficiency is then determined by measuring the losses in the feeder cables. The following section deals with obtaining the antenna gain and beam-width values, which will be the final values required in order to use Equation 4.2 to measure reflectivity.

4.2.1 Receiver calibration

In order to measure the absolute received power, we first need to establish the relationship between the signal at the antenna's output and the record signal at the output of the receivers, whose amplitude is given by A_t. This relationship will include the effects of amplification of the signal before and after demodulation, (see Figure 2.2), and any losses in the receiving path, excluding antennas. In order to do this the antenna is substituted with a known power source.

The output of the antennas was replaced by a noise generator which created an accurately known level of power, given by,

$$P_{ng} = kBT_{ng}, \tag{4.3}$$

where k is Boltzman's constant, 1.3805×10^{23} JK^{-1}, B is the bandwidth of the receiver and T_{ng} is the noise temperature of the generator. The recorded signal at the output of the receivers due to the noise generator is given by

$$\overline{A^2}_{noise} = N_c {V_f}^2 P_{ng} + \overline{A^2}_{extra}, \tag{4.4}$$

where N_c is the number of coherent integrations, V_f is the voltage conversion factor of the system and $\overline{A^2}_{extra}$ is the additional noise of the system often given in terms of the effective noise temperature of the receiver, T_{rx}. From Equation 4.4 , T_{rx} is given by

$$T_{rx} = -\frac{\overline{A^2}_0}{kBN{V_f}^2}, \tag{4.5}$$

where $\overline{A^2}_0$ is the recorded noise level when no power is present at the antenna outputs, (i.e. noise generator is switched off, T_{ng} is zero). Equations 4.4 and 4.5 were solved by varying T_{ng} followed by the application of a linear fit to the results, as shown in Figure 4.1. The noise levels were calculated using the Hildebrand-Sekhon algorithm [*Hildebrand & Sekhon*, 1974].

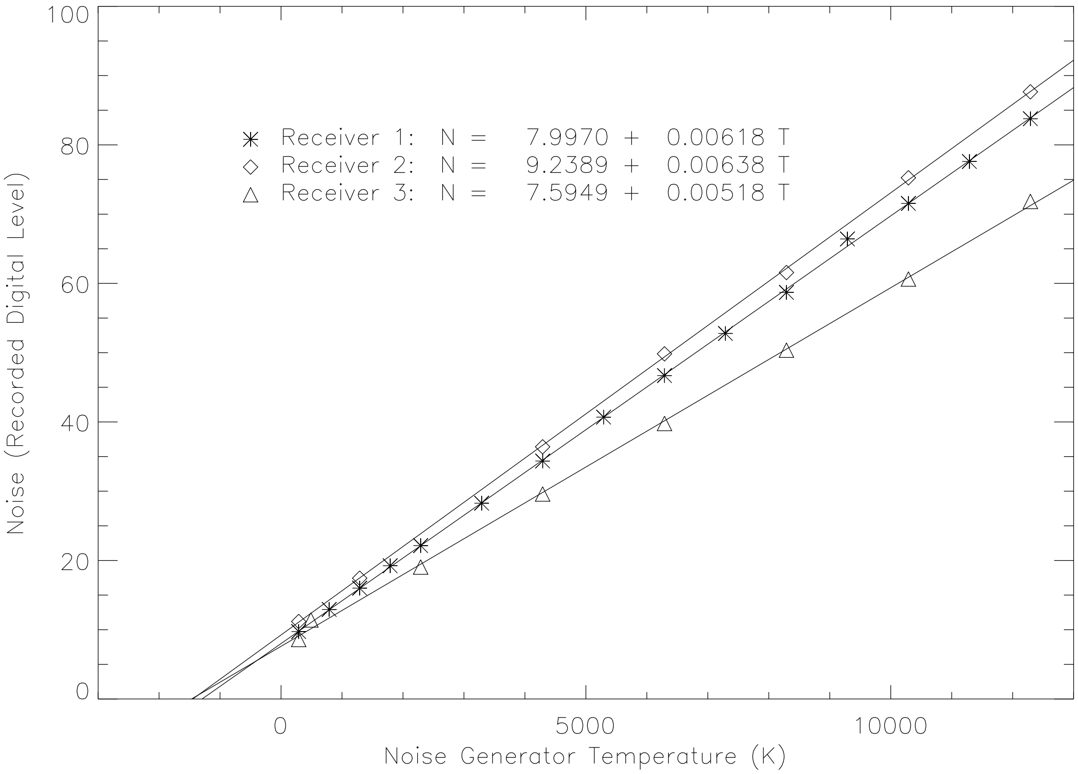

Figure 4.1: Noise generator calibration from 5th June 2000. The calculated linear fit for each receiver is shown. The offset in noise at 0K is due to the receiver noise contribution. The noise recorded digital level is in units of A_t^2.

The values obtained for T_{RX}, V_f and N_{offset} are given in Table 4.1.

The software selectable receiver gain was fixed at 83 dB during the calibration process, which is the same level as used during normal spaced antenna operations. Any modification in this level will result in a subsequent change in V_f that will need to be taken into account when determining received power.

Receiver	Rx. Temperatures, T_{RX}	Noise offset, N_{offset}	Voltage amplification factor, V_f
1	1400 K	8.00	2.09×10^{-16}
2	1450 K	9.24	2.13×10^{-16}
3	1470 K	7.59	1.91×10^{-16}

Table 4.1: Receiver temperatures, noise offset due to receivers and voltage amplification factor for the BLR system. Bandwidth and gain of the receivers were fixed at 1 MHz and 83 dB, respectively, 5th June 2000.

For a coherent signal the power at the output of the antennas is given by

$$P_{signal} = \frac{\overline{A^2}_{signal}}{l_r N_c^2 {V_f}^2} \tag{4.6}$$

where l_r is the finite bandwidth loss of the receiver. This loss factor is a function of both the shape of the transmitted pulse and the frequency response of the receiver and is given by,

$$l_r = \frac{c\tau/2}{\int_0^\infty \mid W(r) \mid^2 dr} \tag{4.7}$$

where c is the speed of light, τ is the transmitted pulse width and $W(r)$ is the range-weighting function of the receiver. For an ideal receiver whose filter is perfectly matched to a rectangular pulse, the loss of signal power is 1.8 dB, while for a receiver with a Gaussian frequency response, the loss is approximately 2.3 dB [*Nathanson & Smith*, 1972]. Butterworth filters are used in the present system and can be approximated by Gaussian filters, hence a value of 2.3 dB is used.

The power at the receiver's output can hence be given by,

$$\overline{P}(r_0) = g_s l_r P_{signal} = g_s \frac{\overline{A^2}_{signal}}{N_c^2 {V_f}^2} \tag{4.8}$$

For validation of the measurements in Table 4.1 the sky noise was measured by running the radar in a purely receptive mode (i.e. transmitter switched off). Using the calibration relationship derived previously, the sky noise temperatures wer measured. The results are compared with radio astronomy observations, conducted at 45 MHz from 1982 till 1984, shown in Figure 4.2 [*Alvarez et al.*, 1997]; the expected transit of the BLR's antenna beam along with its effective beam-width is illustrated.

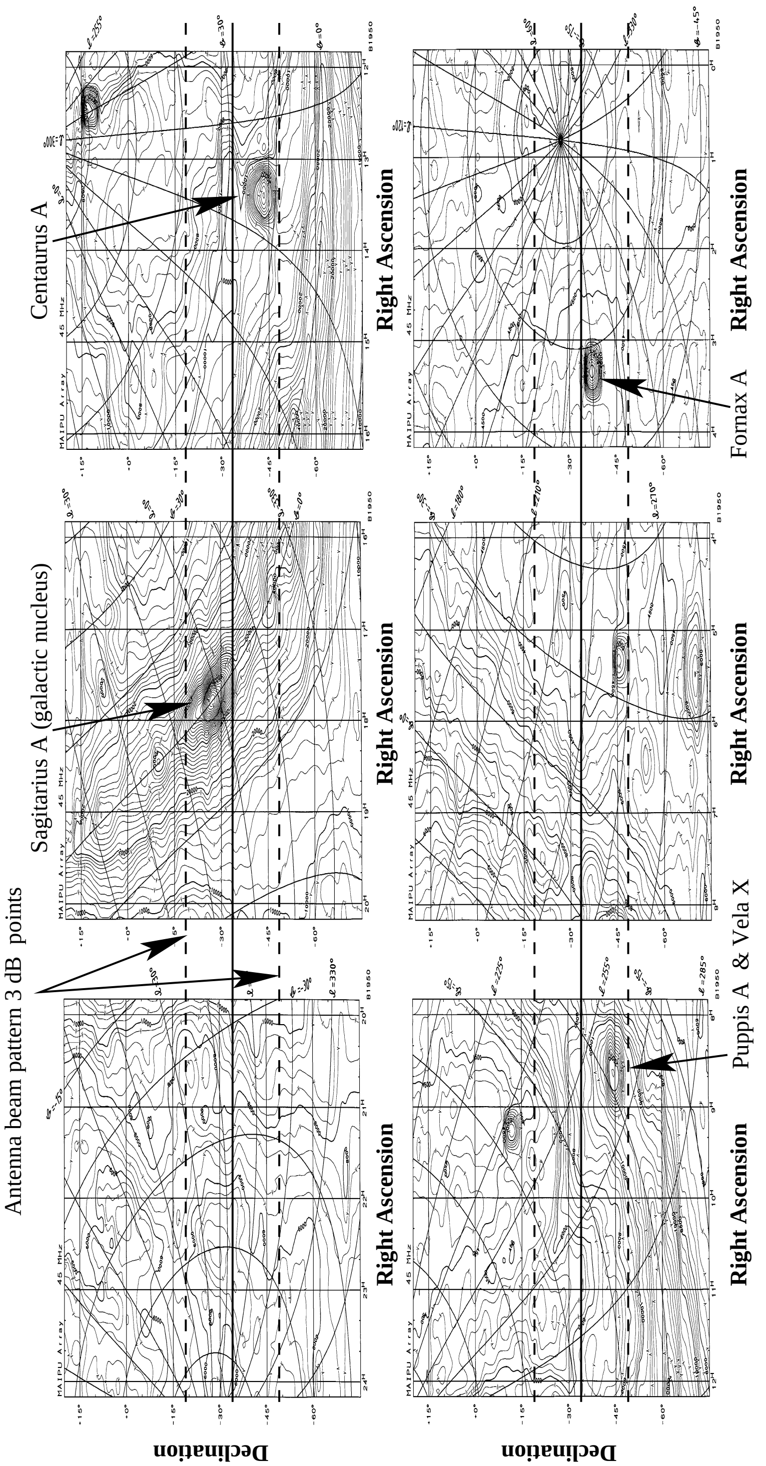

Figure 4.2: Maps of a 45 MHz continuum survey of the southern hemisphere in equatorial coordinates (Epoch 1950) obtained using the Maipu Radio Astronomy Observatory. Each map covers declination range $-75° \leq \delta \leq +19°$ and 4 hours in right ascension. Galactic coordinates are superposed to each map. The transit of the centre of the BLR beam pattern is shown (solid line) along with the beam-width marked by the position of the 3 dB points. Potentially discernible radio sources are labelled. (Adapted from *Alvarez et al.* [1997]).

Observations given in Figure 4.2, were made with the 45-MHz array of the University of Chile at the Maipu Radio Astronomy Observatory (33°30′05″S, 70°51′28″W). The Maipu array has a beam-width of 4.6° × 2.4°, full width half maximum. The sky noise temperature values, obtained from the transit of the centre of the antenna beam in Figure 4.2, are shown in Figure 4.3, along with the sky noise temperature values measured by the BLR, over a 24 hour period centred on 0600 UTC 19th July 2000, (Note: the results from Maipu were scaled in order to fit on the same plot as the BLR results).

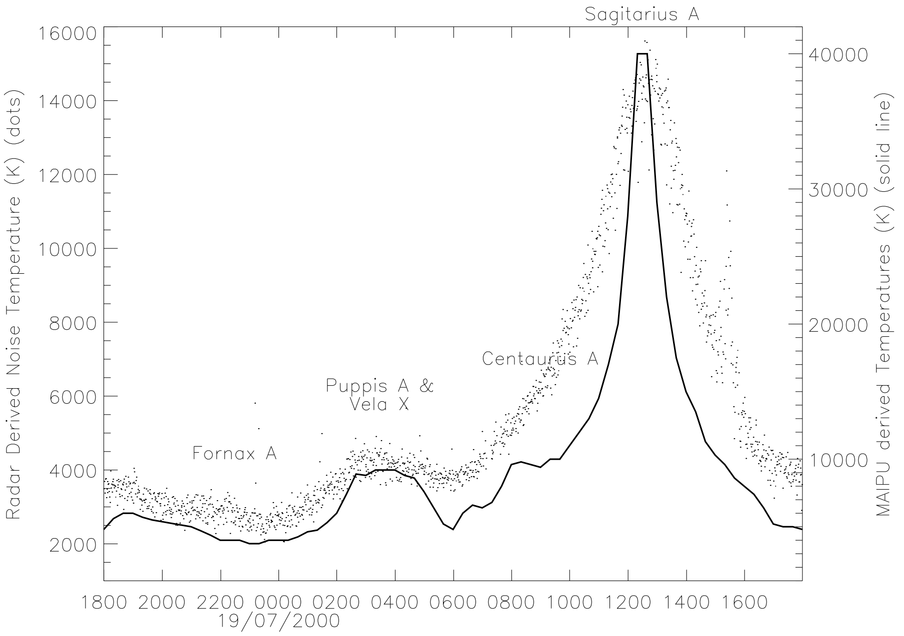

Figure 4.3: Sky noise temperatures obtained by the BLR from 1800 UTC 18th July 2000 to 1800 UTC 19th July 2000 (dots left-scale) together with values obtained by the Maipu Radio Astronomy Observatory (solid line right-scale) [*Alvarez et al.*, 1997].

As both the BLR and Maipu array have finite beam-widths the sky noise temperatures obtained are actually a convolution of the antenna pattern with the actual sky noise. The wide bandwidth of the BLR compared with the Maipu array results in a coarser resolution of radio sources and sky noise (Figure 4.3). The convolution effect is apparent in the broadening and reduction of the galactic centre peak, Sagittarius A, (Figure 4.3), transecting the beam just after 1200 UTC. The maximum value measured during the Maipu campaign was over 40000 K, while the maximum measured using the BLR was ∼15000 K. The BLR observations were not able to resolve the signal from Centaurus A, and despite Fornax A being within the beam, no discernible signal was detected from it. A direct comparison of the two sets of measurements would require a two-dimensional convolution of the antenna beam pattern with the Maipu observations. This was not feasible as the initial values used to create the continuum survey were not available.

The minimum values obtained by the Maipu system and the BLR were, ∼3500 K and ∼3000 K, respectively. The agreement in the minimum sky noise temperature values was expected, because the spatial extents of regions with low noise temperature are relatively large when compared with the localized peaks of high noise temperature. The minimum sky noise value is comparable with the value obtained using the SOUSY 53.5 MHz radar which was ∼3000 K [*Hocking et al.*, 1983].

4.2.2 Transmission calibration

The transmission coefficient, ϵ_{TX} is the attenuation due to the passive network of feeder cables and combiners. The length of the feeder cables between the transmitter and antenna combining harness is 8.5λ, thus the attenuation can be defined as [*Terman & Pettit*, 1952],

$$\alpha l = 8.688\sqrt{\frac{Z_{SC}}{Z_{OC}}}, \tag{4.9}$$

where α is the attenuation constant (dB), l is the cable length (m), Z_{SC} and Z_{OC} are the measured impedances with the cable short- and open-circuited respectively. The total attenuation in the cables (one way) can be obtained by simply measuring the open and short circuit impedances of the cable. The values obtained for the three cables A, B and C were 1.528 dB, 1.506 dB and 1.513 dB, respectively, which agrees with the theoretical value of attenuation of 1.53 dB for 8.5λ of RG213-MIL cable. The symmetric and balanced nature of the combining section means that its attenuation is equivalent to a single cable (RG213-MIL) with a length comparable with the shortest distance between the beginning of the combination harness and a single antenna input (i.e. 1.25λ), giving an attenuation of 0.225 dB. Hence the transmission coefficient[2] is -1.755 dB i.e. -(1.53 + 0.225).

All the losses between the array output and receiver output have been either measured or calculated. The loss due to the actual antennas was not measured, although attempts at calibration by comparison with a *perfect* dipole were carried out by past users. However, these resulted in efficiency values of greater than 1.0, implying a less than *perfect* dipole was actually being used for reference. Therefore, for simplicity, the efficiency of the individual antennas is taken to be 1.0, (i.e. lossless).

The loss due to the cabling in the combining harness is the same for reception and transmission, hence for the receiving arrays an additional loss of 0.225 dB must be included. This is due to the receiver calibration not being able to take into account the losses associated with the combining harness and the antennas.

4.3 Antenna Modelling

Numerical Electromagnetic Code (NEC-2) [*Burke & Poggio*, 1977] was used for modelling the array. "Moment of method" procedures are used to solve numerically the integral equations for the currents induced on a structure by sources or incident fields. An input file contains the physical specification for the structure along with the method of excitation. The output may include current and charge density, electric, magnetic and radiated fields.

The original NEC-1 code was written in 1977, when computer memory and CPU speeds were relatively small, thus limiting the maximum number of segments that could be used to model the elements making up an antenna. The maximum number of segments allowed under the next version of the code, NEC-2, is 600. The number of words allowed in core storage was also restricted, forcing virtual memory to be used. By using virtual memory, on-going calculations were constantly written to and read

---

[2] A negative sign is used as attenuation is a loss

from the hard drive, thus increasing the run time. A copy of the sources code was obtained and modified to allow 3000 segments, together with an increase in the amount of RAM allowed to be used. This enabled the entire array to be completely analyzed to a sufficient degree of accuracy, with the whole calculation having a duration of less than 10 minutes. A brief description of the changes made can be found in Appendix E.

The resolution that can be used in modelling the structure is limited by numerical inaccuracies that can occur when the segment length becomes too small compared with the wavelength. For accurate results the segment lengths should be less than 0.1λ but greater than 0.001λ. The segment lengths used for this work were of the order of 0.05λ. Another limitation of NEC-2 occurs when elements of dissimilar diameter are parallel and in close proximity, (*private communication, L. B. Cebrik*[3]*)*. Care is required in the interpretation of results when modelling a gamma match. The driven element, the gamma rod and the elements between them have different diameters which can yield inaccurate results. For calculation of antenna pattern and gain, the model consisting of Yagis without gamma matches attached was therefore used. The input code for a third generation array can be found in Appendix F. The supporting boom is included in the model, although it was found this had negligible effect, providing the number of segments in the elements attached to the boom were either all even or all odd. Examples of power patterns obtained from NEC-2 are shown in Figures 4.4 and 4.5.

The half-power beam-width describes the spread or concentration of the beam, where the power has fallen to half of the maximum power. The maximum calculated gain and beam-width for the array is given in Table 4.2. Most antennas are not symmetrical about the vertical axis, so when representing the solid pattern of an antenna, cross-section or plane diagrams are often used. The cross-section containing the axis of the antenna is called the *E-plane pattern*, while the one perpendicular to the axis of the antenna is called the *H-Plane pattern*, both of which are shown in Figure 4.4(b) and Figure 4.5(b). These two diagrams are usually sufficient to fully

---

[3] *L. B. Cebrik, W4RNL, w4rnl@arrl.org*

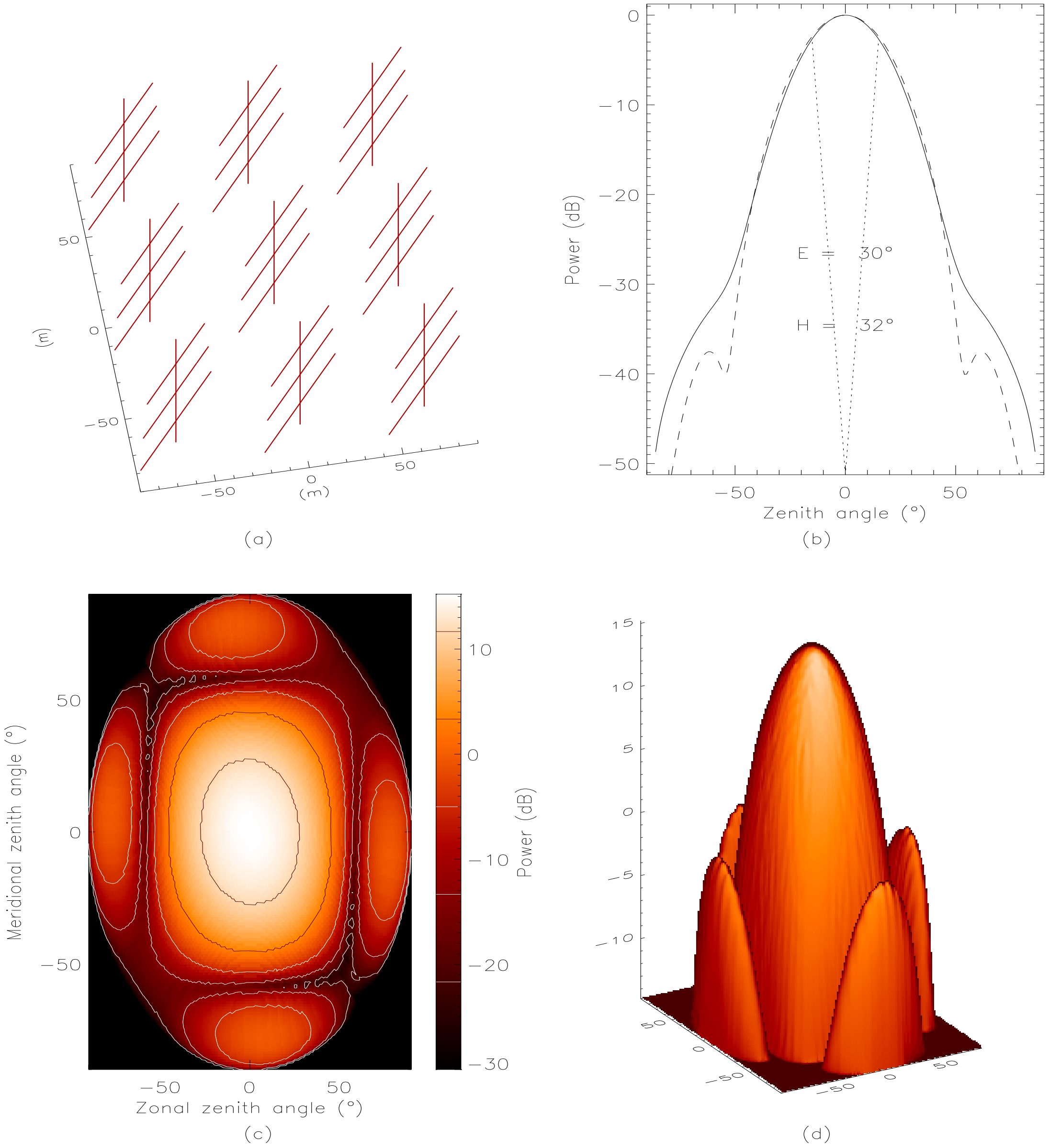

Figure 4.4: Third generation receiving array power patterns. (a) is the NEC-2 input structure, (b) is the normalized power in the E-Plane (solid) and H-Plane (dashed), beam-widths are shown for both planes, (c) is a contour plot of the power pattern, (d) is a three dimensional view of the power pattern.

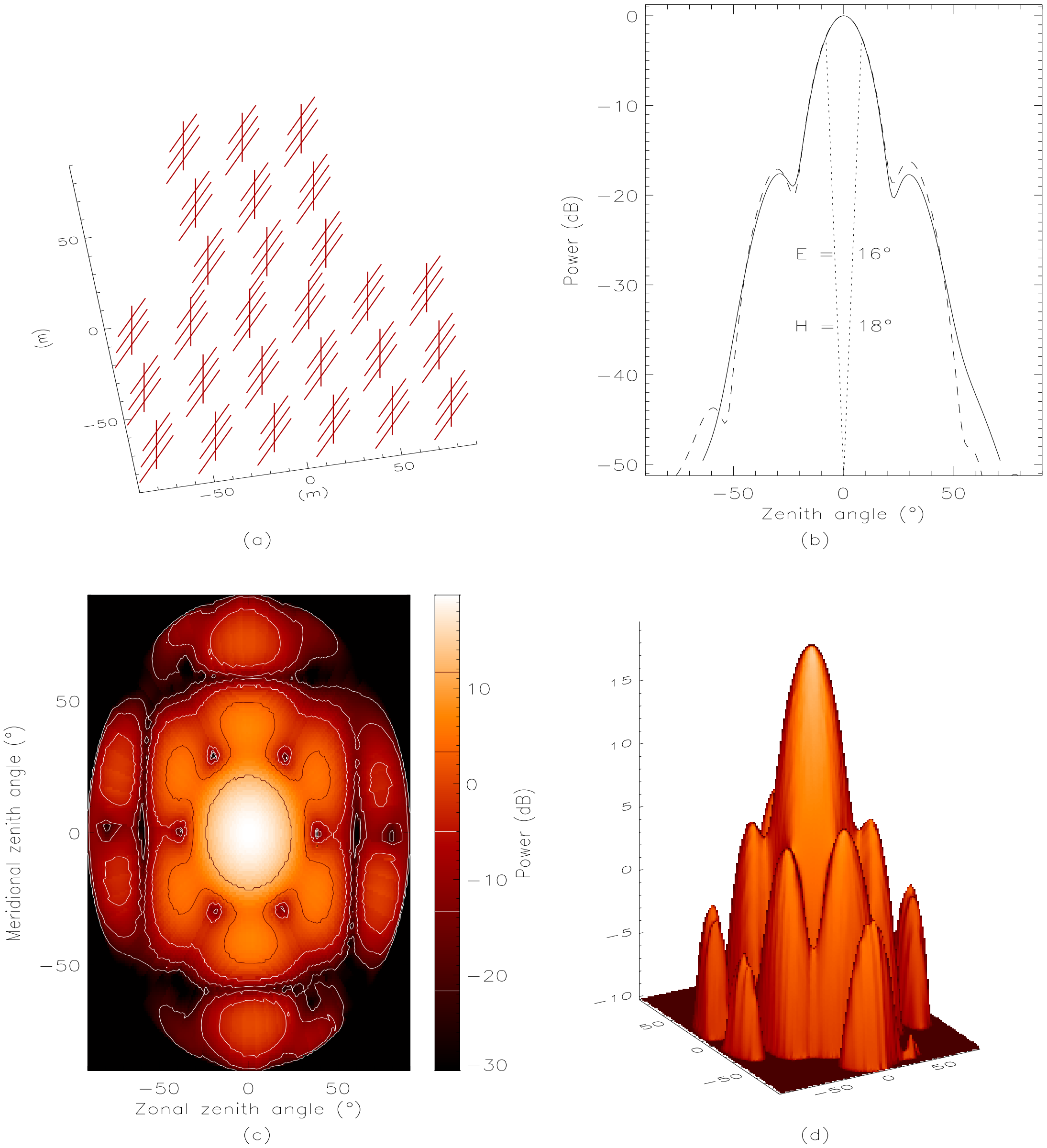

Figure 4.5: Third generation transmitting array Power Patterns. (see Figure 4.4 for full description)

describe the power pattern of an antenna, although this is not the case for an array with its elements orientated 45° with respect to the baseline. For the second and third generation arrays, the field pattern could be approximated via pattern multiplication, where the pattern of a single antenna is multiplied by the pattern of an array of point sources, although this method would not include the effect of coupling between antennas.

For a square based symmetrical array (similar to the receiving array) of point sources, the side-lobes would be greatest along the axes, (North-South and East-West for arrays used). Due to the orientation of the antennas, the *E-Plane* and *H-Plane* are not along these axes but 45° to them. To examine the position and strength of the side-lobes for each array the cross-section parallel and perpendicular to the array's axes need to be examined instead. However, the asymmetry of the transmitting array results in a slightly more complex radiation pattern. The peaks of side-lobes occur at places other than on the coordinate axes or the E-Plane or H-Plane axes. The positions and relative strengths of the side-lobes are thus estimated by considering the maximum power at each zenith angle for all azimuthal angles and then locating local maxima. The calculated side-lobe's strength and position angle are shown in Table 4.2 for the first and third generation transmitting and receiving arrays.

Measurement	First Generation Receiving Array	First Generation Transmitting Array	Third Generation Receiving Array	Third Generation Transmitting Array
Max Gain	13.07 dBi	17.96 dBi	15.22 dBi	19.74 dBi
Beam-width	36 - 42°	20 - 22°	30 - 32°	16 - 18°
side-lobe: Gain	5.42 dBi	6.78 dBi	-0.54 dBi	0.93 dBi
side-lobe: Angle	68°	65°	60°	53°
Vestigial lobe: Gain	-	6.0 dBi	-	7.13 dBi
Vestigial lobe: Angle	-	31°	-	26°

Table 4.2: Gain and beam-width for first and third generation transmitting and receiving arrays.

The improvement in maximum gain, reduction of the width of the main beam and reduction in the gain of the side-lobes of the third generation array compared with the first generation array can be seen from the values in Table 4.2 and Figure 4.6. The symmetry of the receiving arrays can be seen with the single side-lobe, compared with the multiple lobes for the transmitting array. The vestigial lobe is the shoulder where a side-lobe has joined to the main beam, as a result of the grating lobe effect caused by the triangular nature of the transmission array's layout. The effects of ground clutter were reduced when using the third generation array as opposed to the first generation with a relative gain reduction, at the higher zenith angles, of greater than 10 dB in transmission and reception.

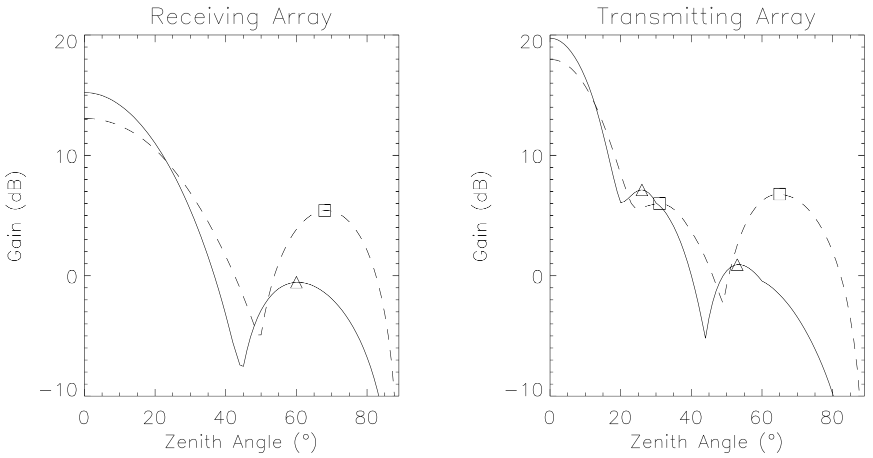

Figure 4.6: Maximum gain vs zenith angle. First generation array (dashed), third generation array (solid)

4.4 Coupling

Spaced antenna analysis, which involves three or more antennas, assumes that any coupling between signals does not affect the measurements. Any significant signal coupling may result in an underestimation or overestimation of the actual wind speed [*Fedor & Plywaski*, 1972]. In this section, the coupling between antennas is determined. Coupling could still occur in the transmission lines, T/R switches, pre-amplifier front ends and the receivers. Signal coupling can result in velocity errors of up to 50 per cent [*Fedor & Plywaski*, 1972].

4.4.1 Theoretical calculation of Coupling

To calculate the expected coupling coefficients, the entire array was modelled with NEC2. Using the computer model, two of the antennas were excited firstly in an even mode (+1 volt, +1 volt) and then in an odd mode (+1 volt, -1 volt) of excitation. By considering the two antennas which were excited, the voltage V_1 measured at the terminals of antenna 1 can be written,

$$V_1 = Z_{11}I_1 + Z_LI_1 + Z_{12}I_2, \tag{4.10}$$

where Z_{11} is the self impedance of antenna 1, Z_L is the load impedance of antenna 1, Z_{12} is the mutual impedance between antenna 1 and antenna 2 and I_1 and I_2 are the respective currents in antennas 1 and 2.

Solving the two simultaneous equations (i.e. odd and even) and using the values of Z_{11} and Z_L, the value of Z_{12} can be determined. The self impedance was calculated by modelling a single antenna using NEC and assuming all antennas in the array would behave the same. The result is $Z_{11} = 34.3391 + j6.13452\Omega$, with a load impedance of 50.0Ω being used. However, the value of Z_L was found to be arbitrary as different loads produced the same mutual impedance. The mutual impedance is determined by,

$$Z_{12} = \frac{-(I_{1o} - I_{1e})(Z_{11} + Z_L)}{(I_{2o} - I_{2e})}, \tag{4.11}$$

where I_{1o} and I_{2o} are the currents in antennas 1 and 2 for the odd mode of excitation and I_{1e} and I_{2e} are the currents for the even mode of excitation. The impedance matrix Z_{ij} can be obtained by repeating this procedure for all possible antenna pairings. The calculations can be reduced by assuming that the relative dielectric constant and conductivity of the ground do not vary beneath the entire array, thus $Z_{12} = Z_{21}$.

Coupling between the three receiving arrays can now be calculated using this matrix, as long as any effect of the cables, combining sections, T/R switches, receivers, etc. is of lower order. The effect of the impedance transformation is assumed to be negligible, other than changing what the effective load the antenna “sees”. The load impedance for each array was 50.0Ω.

The equivalent circuit for a receiving array is shown in Figure 4.7

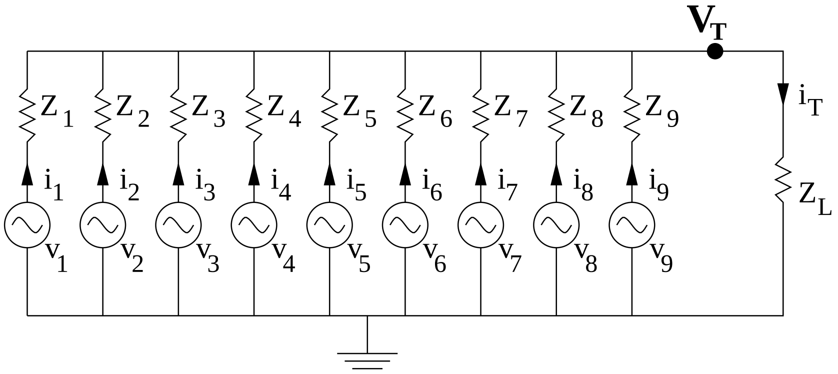

Figure 4.7: Equivalent circuit for a receiving array of 9 Yagis. Where Z_i is the effective impedance of antenna i taking into account self and mutual impedances, I_i is the current flowing from antenna i, v_i is the voltage induced in antenna i by the incident EM field, I_T is the total current from the combination of all the antennas in the array and Z_L is the effective load impedance of the array.

The induced voltage in an antenna i belonging to array A is hence given by

$$v_{iA} = \sum_{j=1}^{27} Z_{ij} I_j + \sum_{j=1}^{9} I_j Z_{LA} \tag{4.12}$$

similarly for antennas in array B and C

$$v_{iB} = \sum_{j=1}^{27} Z_{ij} I_j + \sum_{j=10}^{18} I_j Z_{LB} \tag{4.13}$$

and

$$v_{iC} = \sum_{j=1}^{27} Z_{ij} I_j + \sum_{j=19}^{27} I_j Z_{LC} \tag{4.14}$$

respectively. Z_{LA}, Z_{LB} and Z_{LC} are the effective load impedance for each array. Equations 4.12, 4.13 and 4.14 can be reduced to the following matrix equation,

$$\mathbf{v} = \mathbf{ZI} \tag{4.15}$$

where

$$\mathbf{v} = \begin{pmatrix} v_1 \\ \vdots \\ v_{27} \end{pmatrix} \tag{4.16}$$

$$\mathbf{I} = \begin{pmatrix} I_1 & \dots & I_{27} \end{pmatrix} \tag{4.17}$$

$$\mathbf{Z} = \begin{pmatrix} Z_{1,1}+Z_{LA} & \dots & Z_{1,9}+Z_{LA} & \dots & Z_{1,19} & \dots & Z_{1,27} \\ \vdots & \ddots & \vdots & \ddots & \vdots & \ddots & \vdots \\ Z_{9,1}+Z_{LA} & \dots & Z_{9,9}+Z_{LA} & \dots & Z_{9,19} & \dots & Z_{9,27} \\ \vdots & \ddots & \vdots & \ddots & \vdots & \ddots & \vdots \\ Z_{19,1} & \dots & Z_{19,9} & \dots & Z_{19,19}+Z_{LC} & \dots & Z_{19,27}+Z_{LC} \\ \vdots & \ddots & \vdots & \ddots & \vdots & \ddots & \vdots \\ Z_{27,1} & \dots & Z_{27,9} & \dots & Z_{27,19}+Z_{LC} & \dots & Z_{27,27}+Z_{LC} \end{pmatrix} \tag{4.18}$$

The current from each antenna given an excitation voltage can now be created by rearranging 4.15 to give

$$\mathbf{I} = \mathbf{Y}\mathbf{v} \tag{4.19}$$

where $\mathbf{Y} = \mathbf{Z^{-1}}$. The voltage measured for each array is just the sum of currents coming from the antennas in that array, multiplied by the load impedance. For example the voltage V_A for array A is given by,

$$V_A = \left(\sum_{i=1}^{9} I_i\right) Z_{LA}, \tag{4.20}$$

and similarly for B and C.

The excitation voltage at each antenna is produced by an induced EMF created by the incident electro-magnetic wave, which takes the form of a diffraction pattern. Each antenna's voltage would vary depending upon its position in this pattern. To calculate the effect on a single antenna, the diffraction pattern is required. A simpler concept of excitation is used to approximate the degree of interaction between arrays.

Assuming that each array is excited uniformly, an expression for the coupling between receiving arrays can be obtained.

Using Equations 4.19 and 4.20 the voltage from array A can be written as,

$$V_A = \sum_{i=1}^{9}\sum_{j=1}^{9} Y_{ij} v_A Z_{LA} + \sum_{i=1}^{9}\sum_{j=10}^{18} Y_{ij} v_B Z_{LA} + \sum_{i=1}^{9}\sum_{j=18}^{27} Y_{ij} v_C Z_{LA}. \tag{4.21}$$

Let

$$\alpha_{AA} = \sum_{i=1}^{9}\sum_{j=1}^{9} Y_{ij} Z_{LA}, \tag{4.22}$$

$$\alpha_{AB} = \sum_{i=1}^{9}\sum_{j=10}^{18} Y_{ij} Z_{LA}, \tag{4.23}$$

$$\alpha_{AC} = \sum_{i=1}^{9}\sum_{j=19}^{27} Y_{ij} Z_{LA}, \tag{4.24}$$

where α_{xy} is the coupling coefficient between array x and array y. Equations 4.21, 4.22, 4.23 and 4.24 can be similarly written for arrays B and C. Hence the measured voltage at the output of each array in terms of the excitation voltages of all the arrays is given by,

$$V_x = \alpha_{xA} v_A + \alpha_{xB} v_B + \alpha_{xC} v_C, \tag{4.25}$$

where v_A, v_B and v_C are the excitation voltages for arrays A, B and C respectively.

Let $\mathbf{V}$ be the voltages at the output of the three arrays,

$$\mathbf{V} = \begin{pmatrix} V_A \\ V_B \\ V_C \end{pmatrix} \tag{4.26}$$

and $\mathbf{v}'$ be the excitation voltages for the three arrays,

$$\mathbf{v}' = \begin{pmatrix} v_A \\ v_B \\ v_C \end{pmatrix} \tag{4.27}$$

Equation (4.25) can therefore be reduced to the matrix equation,

$$\mathbf{V} = \alpha \mathbf{v}', \tag{4.28}$$

where α is the coupling coefficient,

$$\alpha = \begin{bmatrix} \alpha_{AA} & \alpha_{AB} & \alpha_{AC} \\ \alpha_{BA} & \alpha_{BB} & \alpha_{BC} \\ \alpha_{CA} & \alpha_{CB} & \alpha_{CC} \end{bmatrix}. \tag{4.29}$$

Using NEC to model the third generation array and then applying the procedure described above α was determined to be

$$\alpha = \begin{bmatrix} 0.8188 - 0.0465j, & 0.0006 - 0.0028j, & -0.0005 - 0.0032j \\ 0.0006 - 0.0028j, & 0.8167 - 0.0523j, & -0.0004 - 0.0018j \\ -0.0005 - 0.0032j, & -0.0004 - 0.0018j, & 0.8127 - 0.0505j \end{bmatrix}. \tag{4.30}$$

The diagonal symmetry in Equation 4.30, is representative of the assumption that the relative dielectric constant and conductivity of the ground are constant under the whole antenna array.

4.4.2 Experimental measurement of Coupling

The calculated values can be compared with measured values made in April 2000, using a Network Analyzer. The measurements were made over a 10 MHz range centred on 54.1 MHz. Figure 4.8 shows the pairings used to measure the coupling between individual antennas. These measurements are summarized in Table 4.3.

Pair	Antennas Used	Measured coupling	Description
a	27 24	-18dB	0.5λ echelon (edge)
b	27 23	-25dB	0.71λ collinear
c	27 21	-26dB	1.0λ echelon (edge)
d	27 20	-44dB	1.12λ -
e	16 13	-18dB	1.0λ echelon (inside)
f	14 23	-26dB	1.67λ between centre of groups

Table 4.3: Individual antenna pairs: Measured coupling

The coupling between all antennas can be understood using these measurements. Pairs a,b,c and d show the coupling with regard to antennas on the edge of the array.

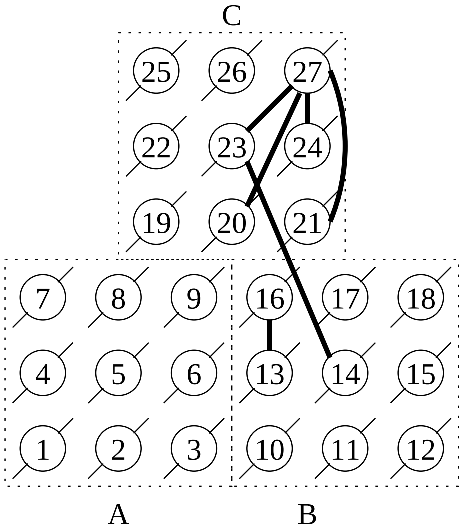

Figure 4.8: Pairing used for measurement of coupling between individual antennas

As expected, the effect reduces as the antennas become more collinear and the distance between them increases. No beam forming (enhancement) or extreme shadowing was observed due to antenna pairs having antennas situated between them (i.e. pair c). Coupling between antennas nearer the centre of the array was no different than between antennas on the edge (i.e. pairs a and f) implying higher order coupling effects were negligible. Coupling between antennas in different groups was of the order of antennas in similar orientation within the same group. Pair d (antennas 27 and 20) had an extremely low level of coupling (i.e. $\sim$ 44dB), which was probably due to movement of the connecting cable during recording of the data; note the sharp dip in the magnitude and jump in the phase of the coupling, as shown in Figure 4.9. The results given in Table 4.3 imply any coupling between antennas is a function of distance and orientation with respect to each other and not dependent upon the position of other antennas.

Coupling may occur between the cables feeding the antenna system. To take into account any such effect, the measurements between each receiving array were carried out at the end of the cable runs inside the radar hut. These results are shown in Figure 4.10. The variation of the coupling with frequency complicates consideration of the effects of coupling on received signals, as discussed in Section 6.6. For short duration

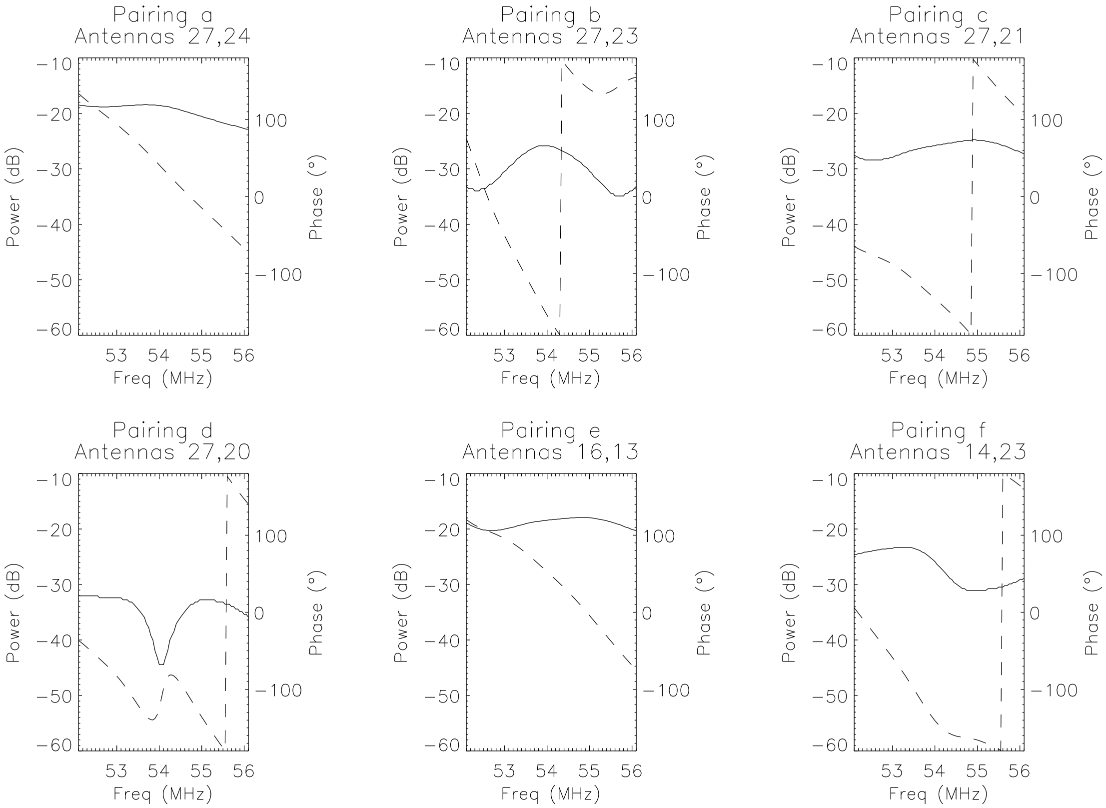

Figure 4.9: Coupling measurements for the individual antenna pairs. Solid line is the coupling magnitude, while the dashed line is the phase. Of particular interest is the variation of magnitude and specifically, phase with frequency.

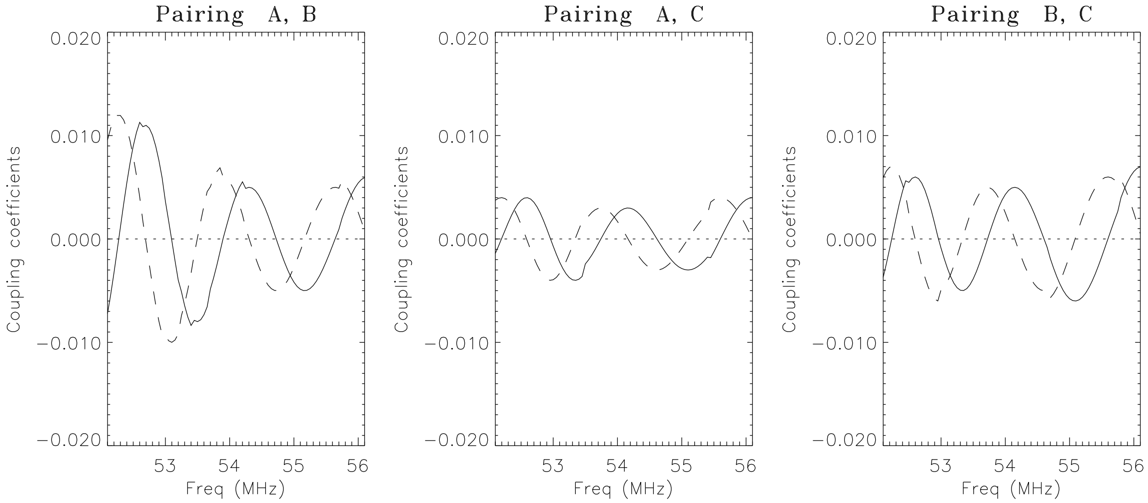

Figure 4.10: Coupling coefficients between the three receiving arrays as a function of frequency. Real part (solid) line, Imaginary part (dashed) line.

transmitted pulses, receivers must use a relatively wide bandwidth ($\sim 1 - 2$ MHz). It can be seen from Figure 4.10 that the oscillatory nature of both real and imaginary components of the coupling coefficient complete a cycle in less than 2 MHz. Therefore a range of values instead of a single value must be used for the coupling coefficient. For comparison with the modelled values, the average magnitude of the coefficients over a 2 MHz range around the operating frequency will be used. The magnitude of the coupling matrix Equation 4.30 will be used to represent modelled values. The results are given in Table 4.4. The modelled and measured values agree for pairings AB and AC, However, for BC the measured value was 5 dB higher, most likely due to the simplification of the model. Two assumptions in particular are that the cables and combining harness have negligible contribution to the coupling and the self impedance of each antenna is the same. Measurements suggest that the latter assumption may not be valid since during array tuning, the self impedance of each antenna was found to be slightly affected by the presence of the other antennas, requiring minor re-tuning after all antennas had been setup.

Yagi pairs	Modelled values	Measured Values			
		@54.1 MHz	Mean*	Max*	Min*
AB	-44 dB	-44 dB	-44 dB	-40 dB	-46 dB
AC	-49 dB	-50 dB	-50 dB	-48 dB	-50 dB
BC	-51 dB	-46 dB	-46 dB	-44 dB	-46 dB

Table 4.4: Coupling magnitudes. Measured vs modelled. (* over 2MHz range centred on 54.1MHz)

4.5 Summary

In this chapter the gain of the system was determined using a noise generator. A comparison between the sky noise temperatures obtained with the BLR and a detailed continuum map was attempted. The broad convolution of the antenna beam pattern made a direct comparison problematical. However, the shape and behaviour of the temporal variations in the sky noise had excellent agreement between the two data sets. Good agreement was found between the two sets of data when considering the minimum noise temperature recorded, with $3000K$ for the BLR systems and $3500K$ for the Maipu measurements.

The polar diagrams of the transmitting and receiving arrays were calculated using a numerical electromagnetic code (NEC). The subsequent calculations regarding the shape and behaviour of beam-patterns enabled a comparison between the first and third generation arrays. The third generation array has superior gain, with an increase of over 2 dB during reception and just under 2 dB when transmitting. The beam-width of the third generation array was found to be $\sim 20\%$ narrower compared with the first generation array. The side-lobes were greatly minimized with the third generation array, with a reduction from 5.24 dBi to -0.54 dBi on reception and from 6.78 dBi to 0.93 dBi on transmission.

The same code was used to analyze the level of coupling within the array. Comparisons of these simulated coupling values and measured values agreed. The measurements of the coupling coefficients did reveal the variation in phase of coupling within a relatively narrow bandwidth. This implies any consideration of coupling must include the variation found in a bandwidth centre on the operating frequency.

With the information regarding beam-widths and the calibration of the receivers, the BLR is now fully calibrated. Observations and results obtained from the BLR are discussed in the next Chapter, along with measurements obtained using the calibrated radar. Appendix G contains a summary of the calibration values obtained in this chapter.

Chapter 5

Results

In this chapter the selection of operating parameters and subsequent development of differing modes of operation are presented. The coverage of the BLR is examined. Firstly the performance of the first generation array (Chapter 3) in three different locations (Buckland Park, Alice Springs and Sydney Airport), with different background atmospheric conditions and using a number of different operating modes is discussed. The performance of the radar at BP while using each of the three different antenna arrays is presented.

A study of the statistics of atmospheric parameters obtained over an eight month period using the third generation array is given. This gives a measure of the average background conditions which are observed with the BLR. Comparisons of radar derived winds with radiosonde and aircraft wind measurements are presented, along with similar comparisons by other authors. A brief presentation showing the ability of the radar to distinguish radar and precipitation echoes is given.

Using the radar calibration values from Chapter 4 measurements of reflectivity are obtained. These radar measurements are used in conjunction with preliminary simultaneous aircraft measurements to briefly investigate observed scattering irregularities.

The final section in this chapter deals with measurements of the turbulent refractivity structure constant C_N^2. A method for differentiating isotropic and anisotropic scatter, as the determination of C_N^2 requires the backscatter to be isotropic, is presented. The range of values obtained for C_N^2 with the BLR are compared with values obtained by other authors.

5.1 VHF BLR Operation

In order to maximize the performance of the BLR it was necessary to optimize the operational parameters, although at times this would involve a compromise in the values selected. However, obtaining good coverage from the lowest levels and the highest levels simultaneously was not possible, while only using one mode of operation. This lead to the development of several modes of operation. The choice of how many and which modes would be implemented was dependent upon the average background conditions of the atmosphere that the radar would be operating in, and the level of resolution required, both vertically and temporally. These concerns are discussed in the following sections.

5.1.1 Operational Considerations

How the operating and acquisition parameters of the radar affected the acquired time-series and subsequent chosen analysis technique was discussed, in Sections 2.1 and 2.2, respectively. Discussed below are the considerations and compromises required in the selection of operating parameters in order to obtain useful measurements with the BLR.

The PRF must be as low as possible in order to reduce the possibility of range aliasing. However, this reduces the mean power and hence the SNR. Increasing the number of coherent integrations increases the detectability, albeit at the cost of increased sampling time. Long sampling times may result in the correlation functions and spectra not being sufficiently resolved, resulting in errors in wind measurement, as discussed in Section 6.2. Long sampling times also result in increased frequency resolution and a reduction in the Nyquist frequency, with increased frequency aliasing. Increasing the length of the time-series improves the frequency resolution, but increases the sampling period of wind measurements.

The overall sensitivity of the system is improved by increasing the average transmitted power P_a. Increases in P_a can be achieved either by increasing the duty cycle d and/or transmitter peak power, P_p. In order to increase d, either τ_{tx} or the PRF must be increased. Increasing the PRF would be counter-productive, as it would reduce the maximum height range. The remaining two options involve either increasing the transmitted pulse length or increasing the peak power of the transmitter. The transmitter peak power is fixed with the BLR system, so the only way of increasing the SNR without complications is to increase the transmitted pulse length. However, this will result in an increase in the range resolution ΔR, and an increase in the minimum height obtainable.

5.1.2 Operational Modes

The fundamental goal of the BLR was to obtain measurements for as low a height as possible. However, to enable the BLR to be a flexible tool for observing the lower troposphere, coverage to at least several kilometres was also desired.

The variation in conditions required consideration of the variability of the dynamic range of the time-series that were observed both in time and height. The gain needed to be set sufficiently low to avoid saturation of the receivers at the lowest heights. However, this meant the signal output for echoes from the higher heights would be very weak. The weak signals resulted in coarse digitization and poor coverage from the upper levels. To achieve coverage over the widest possible range, different operating modes were implemented. The three main modes were *normal*, *high* and *extra-high*.

During initial experiments at Buckland Park (BP), with the BLR, only the *normal* mode was implemented. This mode used a 150 m transmitted pulse with the gain of the receivers optimized, for lower height coverage while still obtaining measurements up to 3 km. Further trials at Buckland Park focussed on trying to obtain results from the lowest possible heights. The use of a 100 m transmitted pulse, to minimize ringing in the antennas, while also minimizing the receiver gain was trialed. It was found this led to an increase in coverage at the lowest heights of only $\sim 2-3\%$, compared with the *normal* mode, while no coverage was achieved above $700 - 800$ m. This showed that the lower height limitation was not due to operational parameters, but was dependent upon the hardware.

While being protected during transmission by the T/R switch, the receiver is also simultaneously "blanked". This involves cutting off any possible input into the receiver during, and for a short period after, transmission of the pulse. It was found that the removal of the blanking was not instantaneous, causing an attenuation of the received signal. The length of the blanking section, which is software selectable, was minimized while still being sufficiently long enough to protect the receiver, however, no significant improvement in the lower height coverage was evident.

Subsequent trials at BP, Alice Springs and Sydney airport involved attempts to increase the maximum height coverage and to fill in gaps in the data due to low SNR when using the normal mode. Two additional modes were developed, the *high* and *extra high* modes (Table 5.1). Both of these modes used longer transmit pulses of 300 m and 600 m, respectively. However, as an extension of the maximum height coverage was desired, a decrease in PRF was required, which limited the increase in average power that would be achieved by using the *high* and *extra high* modes. The *high* mode's main function was to fill the gaps in the *normal* mode data, to maintain lower height coverage, so the same receiver gain as used for the *normal* mode was applied. Alternatively, the receiver gain for the *extra high* mode was increased by 24 dB, as this mode's main purpose was to increase the maximum height range, although it would be at a cost of saturation of the receivers at the lower heights.

With the use of the high and extra-high modes, coverage was improved, as can be seen by comparing the normal and high modes at Alice Springs (see Figure 5.1) and Sydney (see Figure 5.2).

The temporal variation in background conditions which could be encountered when

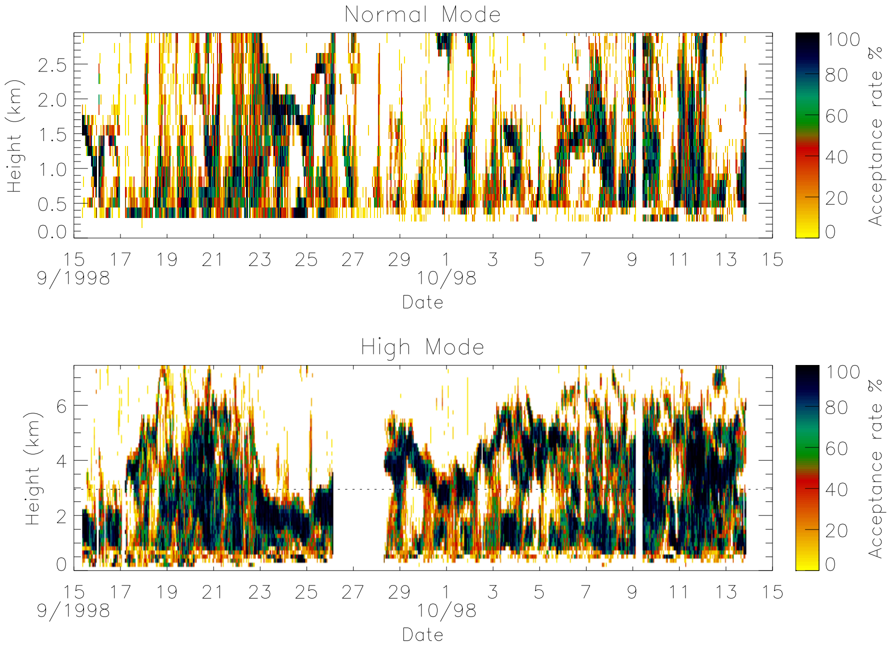

Figure 5.1: Hourly coverage for the *Normal* and *High Modes* from CAFE experiment at Alice Springs. No data was taken in the high mode on 27th September 1998.

using a single mode at a single site is illustrated by the coverage achieved during the Alice Springs campaign, see Figure 5.1. Sharp contrasts in the height coverage achieved by the normal mode can be seen in the data acquired between 22nd and 30th September 1998. Earlier in the period, coverage was obtained from 400 m to 3000 m, while later on, the coverage did not exceed even 1000 m at times. The cause of this sharp difference was due to the humidity contribution to the vertical gradient of the potential refractive index M (Equation 1.20). The humidity observed at Alice Springs during the campaign was at times extremely low, resulting in poor coverage. However, during periods of increase cloud cover and humidity, coverage improved dramatically.

The increase in height coverage and subsequent reduction in range resolution observed using different modes can be see in Figure 5.3. Where comparisons of wind measurements obtained for the normal, high and extra high modes obtained during the CAFE campaign are shown. The loss of range resolution is especially noticeable around regions of wind shear, as can be seen at 800 m in Figure 5.3. At this range,

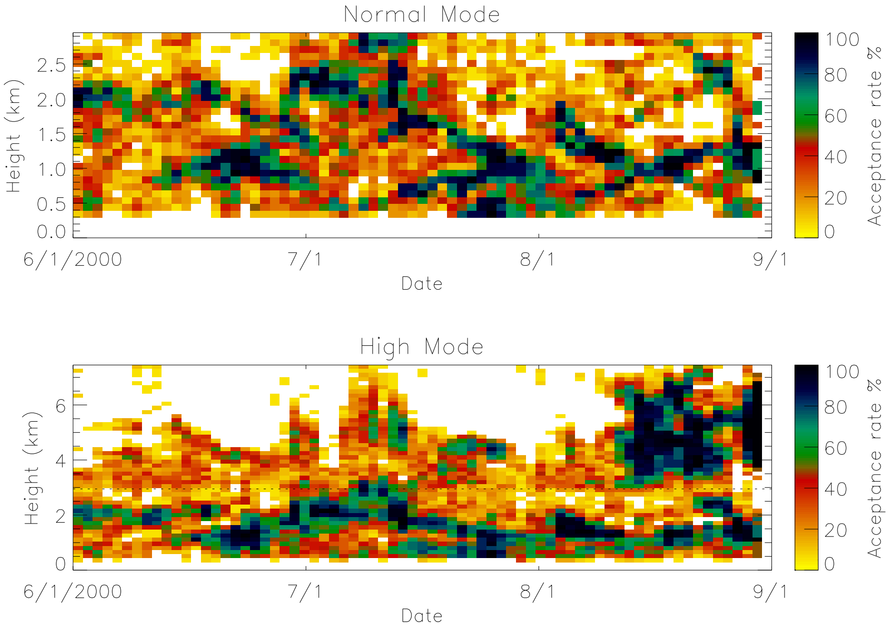

Figure 5.2: Hourly coverage for normal and high modes from trials at Sydney Airport.

an underestimation in the zonal component of $\sim 20\%$ is observed when using the *extra high* mode as opposed to the *normal* mode. However, the improvement in height coverage can be seen by the differing acceptance rates.

Under normal situations wind profilers measure a reflectivity-weighted average of the radar volume. However, at the lowest heights, the receiver's blanking-delay attenuates the echoes, resulting in measurements being weighted towards the top of the radar volume. Therefore the effective sampling volume will not be a symmetrical triangle as shown in Figure 2.1. Lower height wind measurements will be incorrect when using the longer transmitted pulses, as they will be biased towards the velocities from the top of the radar volume. This effect will also give the impression of increased coverage at the lower heights when using a longer pulse, as can be seen in the high acceptance rate ~50 % at 300 m when using the extra-high mode (Figure 5.3). However, the wind measurements do not agree with those obtained by the normal and high modes, implying they are incorrect.

The loss of resolution can also be clearly seen in the power profiles shown in Figure

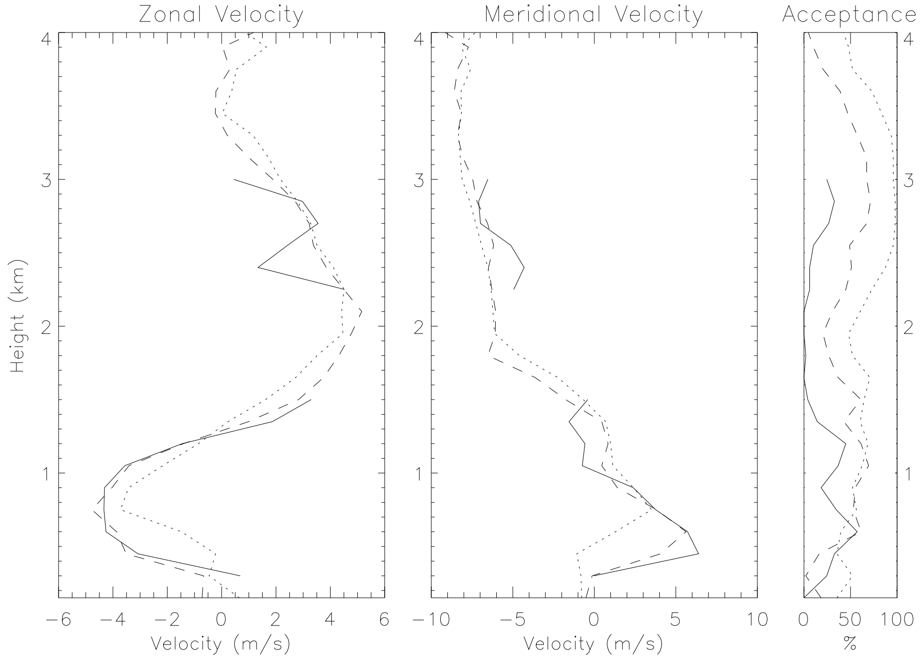

Figure 5.3: Profiles of Zonal and Meridional wind components for normal (solid line), high (dashed line) and extra high (dotted line) modes. The data represents 2 hours of averaged winds, centred 1200 UTC 19 September 1998, (CAFE98 campaign).

5.4. The layer at 3.0 km, has a vertical extent of ∼400 m when measured using the normal mode, while measurements using the extra-high mode give a vertical extend of ∼1000 m. The extra-high mode is unable to resolve the peaks at 1500 m, 2300 m and 3500 m. Similar losses of resolution were observed in vertical velocity, pattern scale and fading time measurements.

While the use of the *high* and *extra high* modes enable an improvement in height coverage at the expense of the lower heights, the normal mode, due to its superior range resolution, is the preferred operating mode. The use of multiple modes also reduces the time resolution of each mode. This problem is emphasized at BP, when the BLR and VHF ST radars have to be multiplexed as they transmit on the same frequency, hence halving the available operating time of the BLR.

Consideration of the desired performance of the system is thus required, with the number and type of modes being used dependent upon the coverage, height and time resolution needed. In situations where hourly averages are required and the acceptance

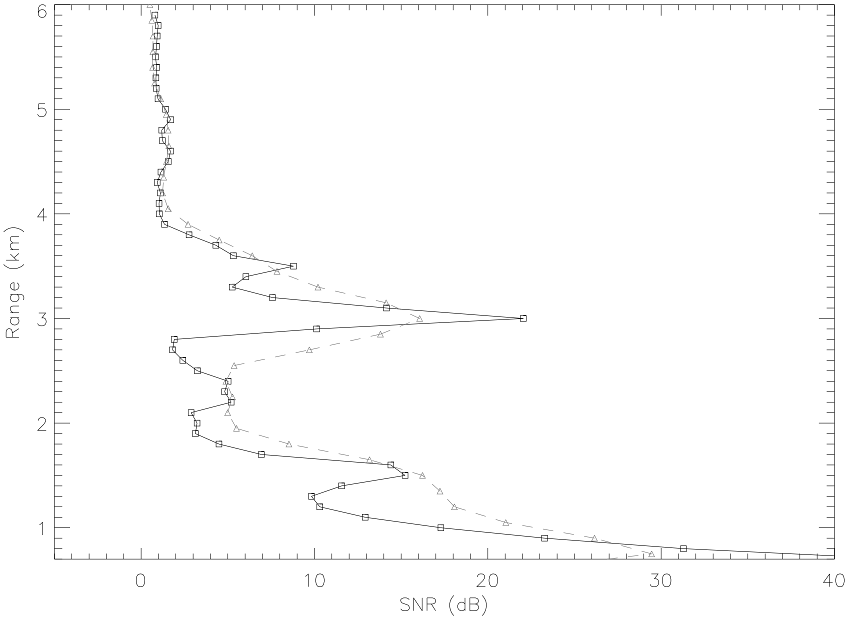

Figure 5.4: Signal to noise average profiles from 1500-1600 UTC, 14 October 2000. Normal mode (solid line) and extra high mode (dashed line).

rate > 10% over the range required, it would be sufficient to use the normal mode only. If the acceptance rate is low or zero within the desired range then use of a longer pulse will be required to fill the gaps. If high temporal resolution of atmospheric parameters is required then the use of several modes will provide a compromise between minimizing range and time resolution. The variability of conditions with time will influence the type and number of modes. In conditions where coverage will vary dramatically, (i.e Alice Springs) two to three modes will be required. Alternatively, in an environment where the coverage is higher with only moderate variation, two modes should be sufficient (i.e. Sydney and BP). A summary of the three main modes and their corresponding parameters can be found in Table 5.1.

Parameter	Normal	High	Extra High
Tx. Pulse width	1 μs	2 μs	4 μs
Receiver bandwidth	1 MHz	500 kHz	250 kHz
Pulse repetition frequency	20480 Hz	15000 Hz	10000 Hz
Duty Cycle	2%	3%	4%
Average power	20 W	30 W	40 W
Number of coherent integrations	1024	1024	1024
Number of data points per sample	1024	760	512
Height Coverage: Minimum	100 m	100 m	150 m
Height Coverage: Maximum	5900 m	7500 m	13350 m
Range resolution	150 m	300 m	600 m
Sampling Height	100 m	100 m	150 m
Receiver amplification	83 dB	83 dB	107 dB
Record length	51.2 s	51.9 s	52.4 s
Nyquist frequency, N_f	10 Hz	7.3 Hz	4.8 Hz
Frequency resolution, Δf	0.02 Hz	0.02 Hz	0.02 Hz

Table 5.1: Typical operating parameters for different modes of operation, (i.e. *Normal*, *High* and *Extra High*).

5.2 Performance and Coverage

In the previous section, the requirements of differing modes and coverage obtained under different conditions was discussed. In this section we will focus on results obtained over three and a half years at the Buckland Park field site. The majority of the discussion will use results obtained with the normal mode, the default operating mode.

The coverage of the VHF BLR while situated at BP is shown in Figure 5.5. The dates where the antenna array modifications took place are marked on the diagram. The radar began running in a campaign type mode on 10th July 1997, using the first generation array. For a full description of the different generations of array development, see Chapter 3. The radar ran intermittently till 4th September 1998, while the VHF ST radar would sometimes be running continuously, thus causing the gaps in the data observed during this period. The radar was relocated to Alice Springs for the CAFE98 campaign, where it operated continuously from 15th September 1998 to 13th October 1998, see Figure 5.1. Following CAFE98 the radar was relocated to Sydney

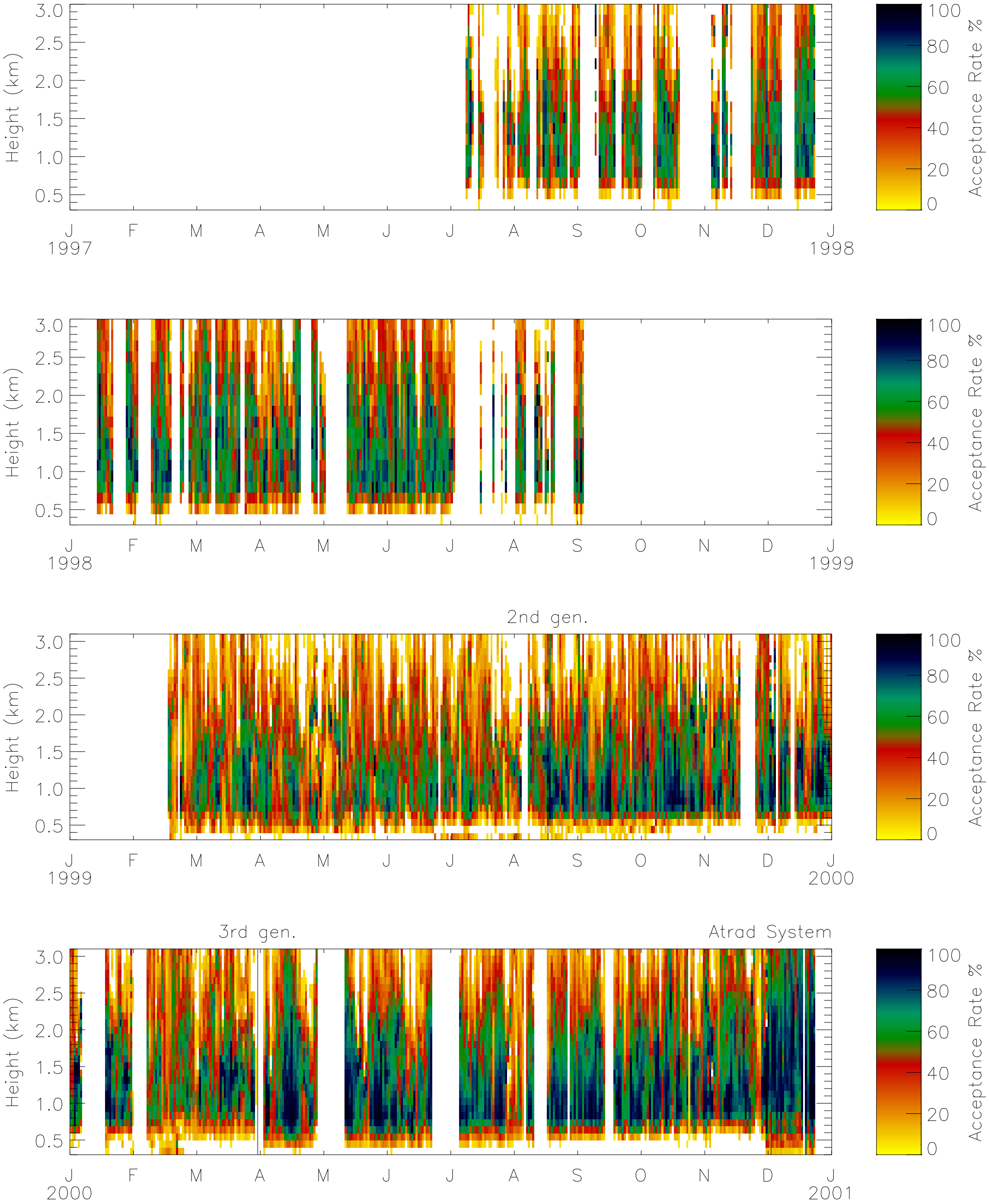

Figure 5.5: Daily Averages of the coverage at the Buckland Park Field Site. Gaps in the data are from periods when the radar was not operating. The change over dates when the second and third generation arrays were introduced are marked. From 4th December 2000, a commercial Boundary Layer Radar (ATRAD) was installed, although the third generation antenna array was retained.

airport, for a one month trial, beginning December 1998. Due to power supply problems, the radar only acquired data continuously from 5th January 1999 to 7th January 1999, see Figure 5.2. The radar was relocated back to the Buckland Park field site where it resumed operation on 17th February 1999 until 17th August 1999.

The average coverage (or acceptance rate) obtained over this period is shown in Figure 5.6. The lack of coverage above 3.0 km with the first generation array is an artifact caused by maximum height range sampled during 1997-1998 being only 3.0 km. Realistically the coverage should show the same decrease with height as shown in Figure 5.6 with the second and third generation arrays.

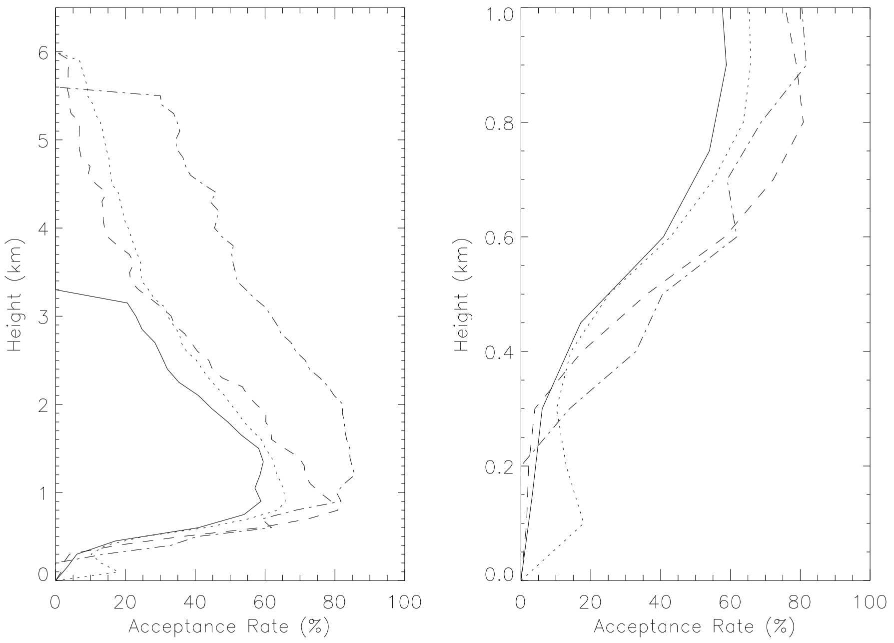

Figure 5.6: The average coverage of the *normal* mode as a function of height for the first generation array (solid line), the second generation array (dotted line), the third generation array (dashed line) and the ATRAD transmitter and data acquisition system using the third generation array (dashed-dotted line). The plot on the right shows the lower heights magnified.

On 17th August 1999, the second generation array was completed and the radar began transmission and reception using this array. The increase in gain due to the greater number of antennas, is apparent by the increase in acceptance rate above

500 m. From Figure 5.6 it would appear that the lower height coverage also improved. However, from Figure 5.5 we can see these lower points are actually erroneous sporadic measurements. The inconsistency of these points is highlighted by the atmospheric parameters derived from the time-series obtained at these heights, which were often random and several orders of magnitude larger than those obtained from one to two range gates higher. These false measurements were most likely due to interference, which had become noticeable in time-series from the lower heights.

Noise spikes began to appear with increasing regularity in all receivers simultaneously, and often in several adjacent heights. During sky-noise observations, when the transmitter was disconnected, spikes were still observed. This implied the equipment, in particular the RDAS, was the source of the interference. A pre-FCA median filter was incorporated to remove the spikes.

The second generation array performance was deemed to be unsatisfactory, (see Section 3.3), as the lower height coverage was less than that achieved with the first generation array. This was deduced to be due to the narrow bandwidth of the second generation array.

On 3rd April 2000, the third generation array was installed. The improvement in lower height coverage can be seen in both Figures 5.1 and 5.6. However, the deterioration in the RDAS resulted in jumps appearing in the time-series, along with an increase in the number of spikes. The median filter was no longer sufficient for the removal of all the internal interference. The increase in the minimal obtainable height was observed from April 2000 to December 2000, (Figure 5.6). During this period the antennas were less well maintained, which may have added to the loss in lower heights as ringing increased.

Examples of the typical horizontal wind measurements obtained with the third generation array running in the normal mode, from 22nd September 2000, are shown in Figures 5.7. Both plots in Figure 5.7 show the height-time cross-section of the wind velocity[1] from 0-2.5 km, however, the top plot shows from 0615 UTC to 2400 UTC,

---

[1] Note: Velocity vectors point in the direction that the wind is blowing to

while the bottom plot only shows 1330 UTC to 1530 UTC.

The Mean Sea Level (MSL) pressure chart, from 1200 UTC 22nd September 2000, Figure 5.8, shows a high pressure system near the radar site. Mesoscale features associated with the high can be observed in the top plot of Figure 5.7, around $\sim$0900 UTC 22th September 2000 at 400-900 m and $\sim$1400 UTC at $\sim$1.0-1.6 km. The bottom plot in Figure 5.7 is the magnified view of the feature observed at the latter time. Very light winds are associated with the centre of the feature in Figure 5.7, which is emphasized by the lack of measurements at the actual centre, as the FCA analysis will break down for very light winds.

Of particular importance is the significant spatial and temporal variation in the measured wind. In less than an hour, the wind direction changed by 180° (i.e. 1.5 km in the bottom plot of Figure 5.7), and within 400 m a wind shear of 180° was observed (i.e. $\sim$1430 UTC). This has particular importance when considering the effects of temporal averaging and altitude averaging due to using multiple modes and longer transmit pulses.

The results from Figure 5.7, show the capability of the radar to be used to probe events from a daily, hourly and even shorter perspective. The ability to gain temporal resolution of the order of minutes is particularly important when attempting to observe localized events, i.e. now-casting.

On 30th November 2000, the RDAS and Transmitter were replaced with a commercial system [2]. Using the same antennas (i.e. third generation array), the lower height coverage was greatly increased, with successful measurements at 400 m occurring greater than 30% of the time, compared with the previous success rate of $\sim$ 15%. It should be noted that the ATRAD system shaped the transmitted pulse, which reduced the effect of ringing in the antennas, helping to improve the lower height coverage. The transmitter peak power is 7.5 kW compared with 1 kW for the original transmitter, which explains the marked increase in coverage above 1.0 km.

The improvement in coverage has been outlined and was obtained by modifications

---

[2] Atmospheric Radar Systems Pty Ltd (ATRAD), BLR3 radar

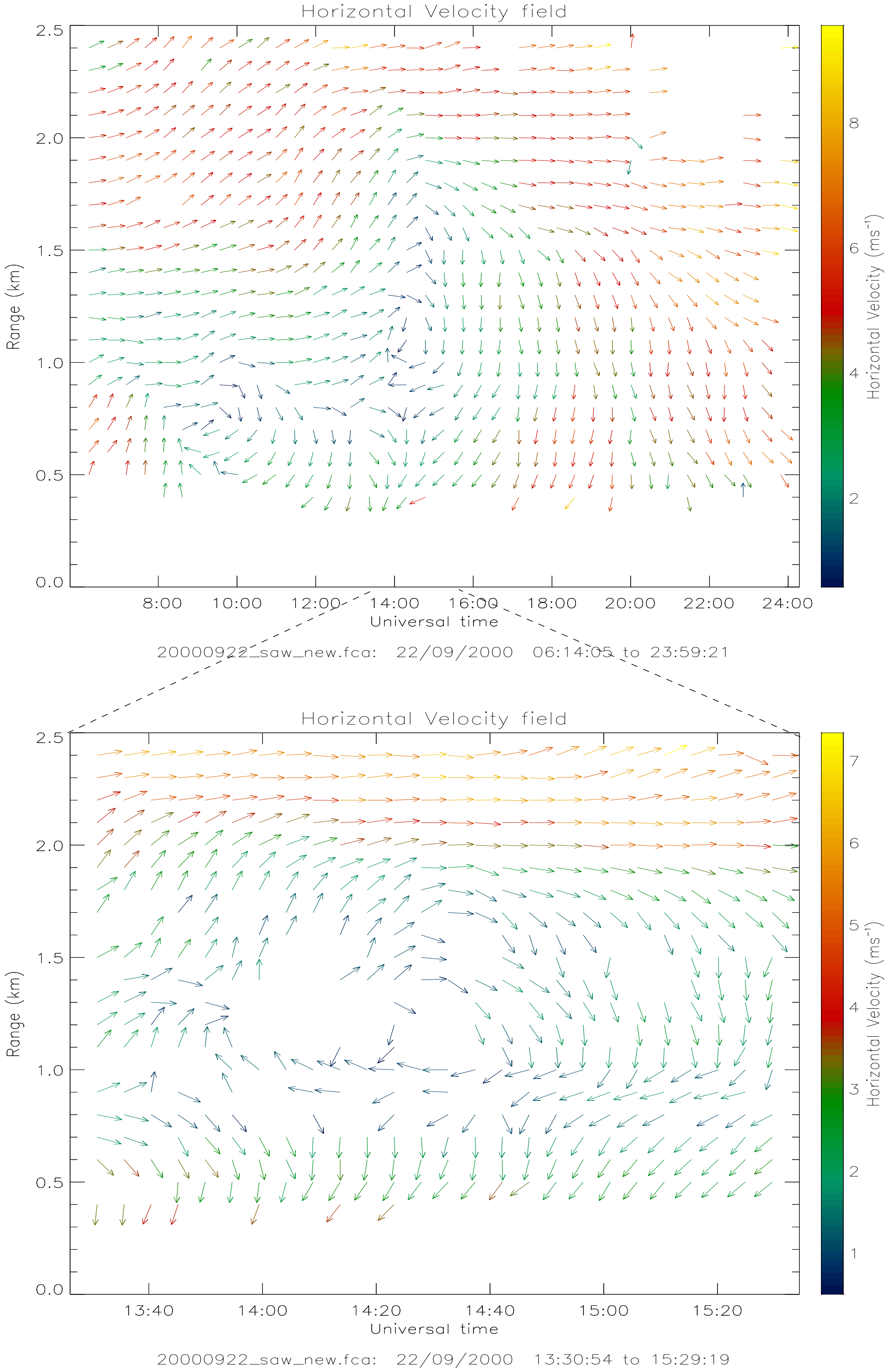

Figure 5.7: Horizontal velocity wind-fields from 22nd September 2000, for heights from 0 km to 2.5 km. Top plot is from 0615 UTC to 2400 UTC, while the bottom plot is from 1330 UTC to 1530 UTC

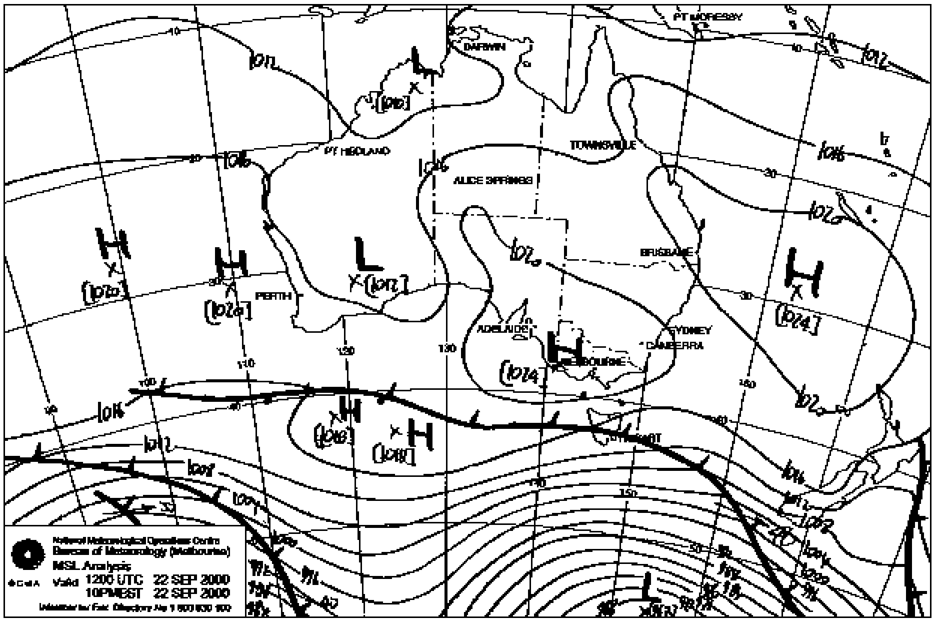

Figure 5.8: Mean Sea Level (MSL) pressure analysis chart for 1200 UTC 22nd September 2000 (obtained from the Bureau of Meteorology's web page, *www.bom.gov.au)*

to the antenna array. The effect of the deteriorating RDAS was observed. With a fully dedicated and well maintained system, measurements from 300 m to greater than 5 km can be achieved. In situations of high humidity, measurements have been obtained from greater than 8.0 km.

5.2.1 Atmospheric parameter measurements

The following discussion deals solely with measurements made using the third generation array, (i.e. 1st April 2000 to 30th November 2000). A full description of the parameters which can be obtained from FCA is given in Chapter 6, namely: pattern scale; random velocity; zonal velocity; meridional velocity and vertical velocity. The time-height cross-section of daily averages and distributions of FCA derived parameters are shown in Figures 5.9 and 5.10, respectively.

From Figure 5.9 we find no apparent seasonal biasing in any of the parameters shown. The high correlation between acceptance rate and SNR is a result of the strong dependence of FCA on the SNR. A gradual increase in the lowest height at which a

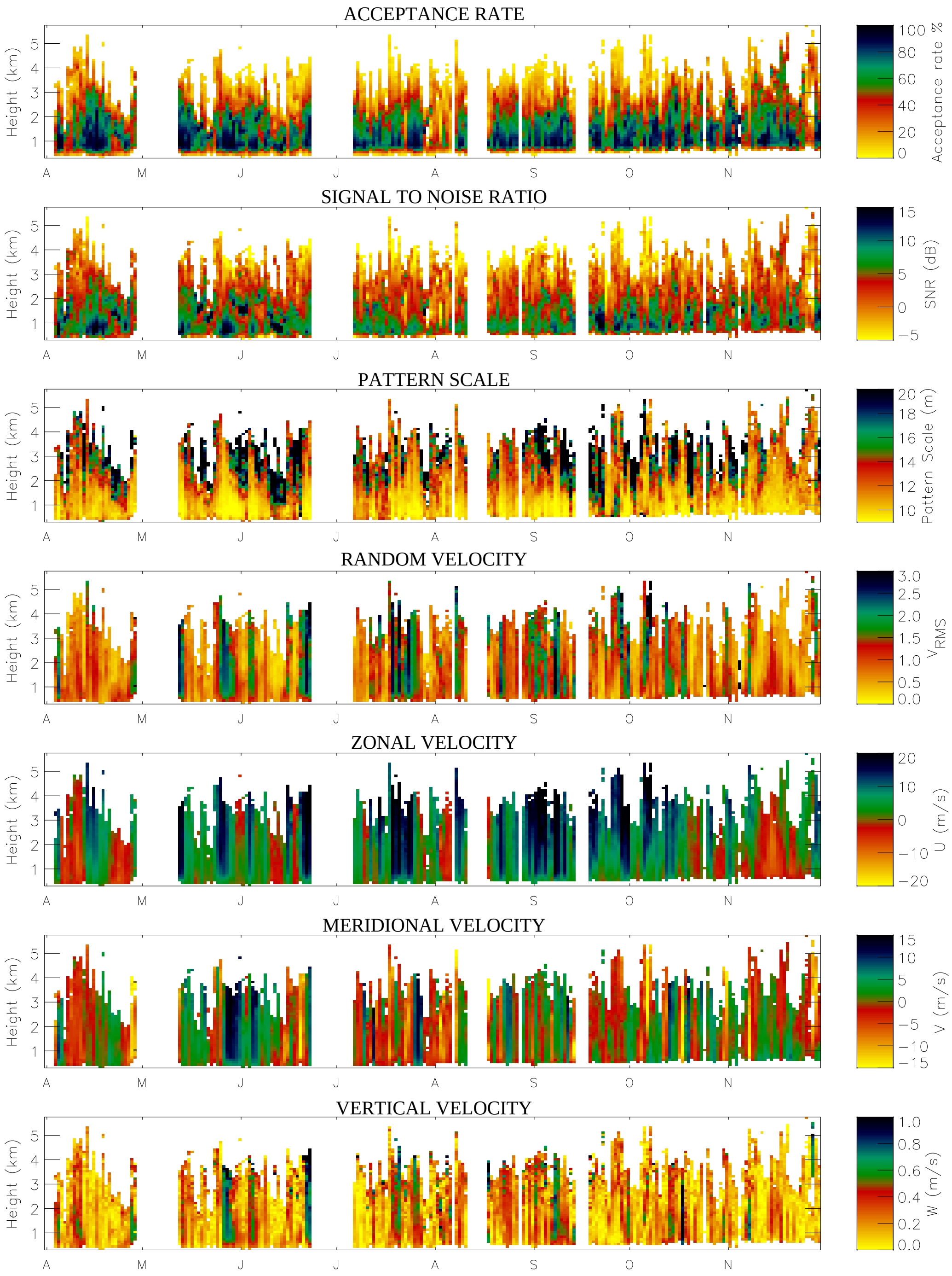

Figure 5.9: Time height cross-section of daily averages of FCA derived parameters from 1 April 2000 to 30 November 2000 (i.e. third generation array). The parameters are (from the top) coverage rate , SNR , pattern scale, random velocity (v_{RMS}), zonal velocity (u), meridional velocity (v) and vertical velocity (w), respectively.

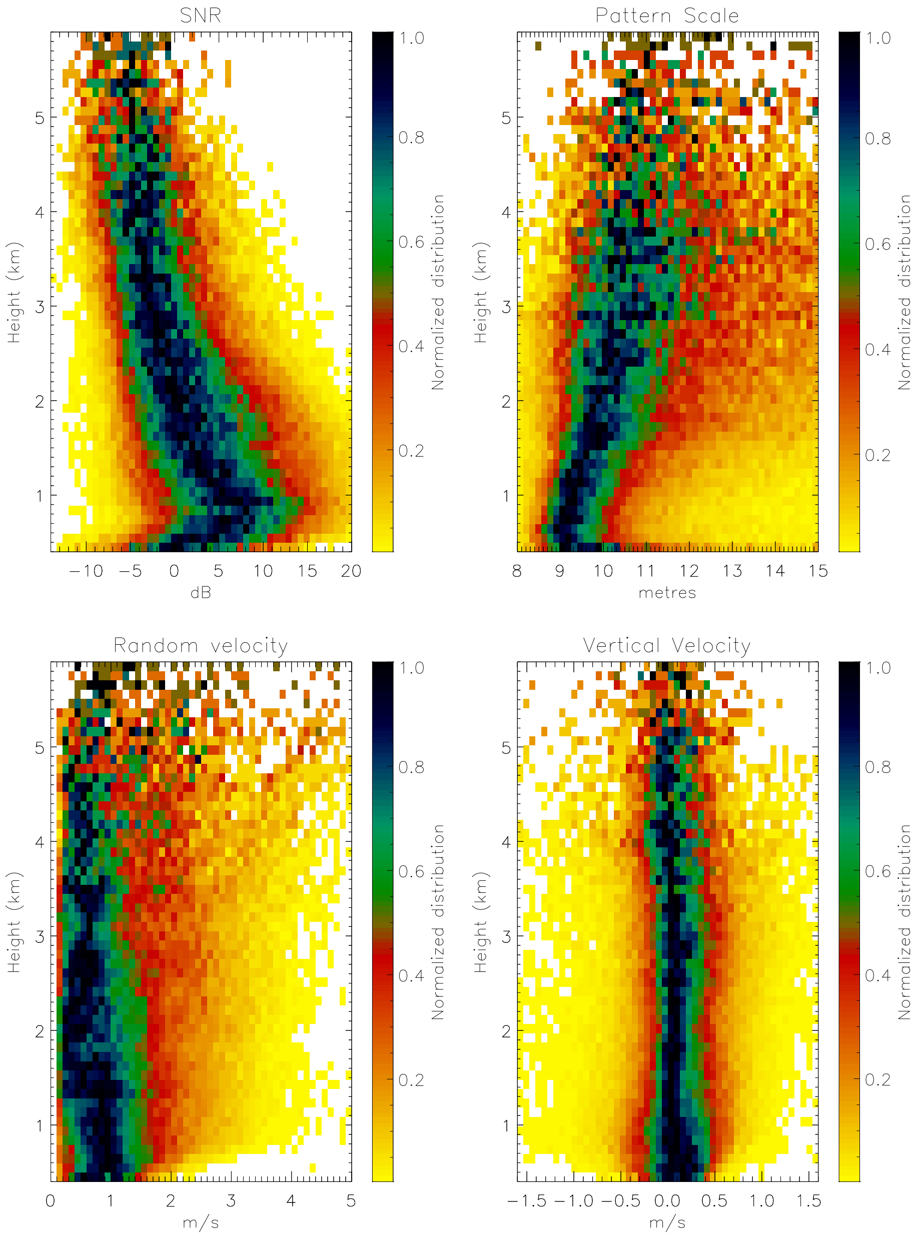

Figure 5.10: Distributions for Signal to Noise Ratio (SNR); pattern scale; random velocity and vertical velocity from 1st April 2000 to 30 November 2000. Distributions have been normalized by the maximum at each height.

successful measurement is made during the period, can be seen in all parameters in Figure 5.9. As explained in Section 5.2, this is an artifact of the deterioration of the RDAS and possible degradation of the antennas with time.

The increase in pattern scale with height implies the scatterers become more anisotropic with height, see Section 5.5.2. The optimal spacing for the antennas, to correctly determine the "true" velocity of the wind, is where the spatial correlation is ~ 0.5 [*Briggs*, 1984], or where the antenna spacing is equal to the pattern scale. If the antenna's spacing is too small, the "true" velocity may underestimate the actual wind, which is known as the *Triangle size effect*, and is discussed in Section 6.5. The antenna spacing used in the third generation array is either 8.31 or 9.29 metres, depending on which antenna pairing is being considered. From Figure 5.10 it can be seen that the pattern scale above 1.0 km is typically larger than the antenna spacing. This implies the present setup is susceptible to underestimations in the derived wind velocities, due to *triangle size effect*, which is the case as shown in Section 5.3.

Typical values obtained for the random velocity, derived from the corrected fading time via FCA (using Equation 6.34), are $\sim$1 ms^{-1}, although values as large as 4 ms^{-1} were observed. From Figure 5.9, it can be seen such large values are localized in time and correspond to periods where the horizontal velocity is relatively strong. The distribution plot of the random velocity (Figure 5.10) shows a general decrease in the random velocity with height, although, there are periods where the random velocity may increase with height (Figure 5.9).

The vertical velocity distribution shown in Figure 5.10 is not symmetrical about 0 ms^{-1}. A slight shift of $\sim$ 10 cm^{-1}, independent of height, was observed.

Contamination of the vertical winds by the horizontal winds can occur if the antenna beam is not directed vertically, [*Low*, 1996]. However, no correlation was found between the vertical and meridional and zonal velocities, implying this was not occurring. The average meridional velocity was $\sim$0 ms^{-1} for all heights, while the average zonal velocity profile was dependent upon height, increasing in magnitude with height. The implication is that the average vertical velocity over the eight months is actually slightly positive (upward), with no horizontal wind contamination.

5.3 Horizontal Velocity Comparisons

Comparisons between winds obtained from the BLR with in-situ measurements were accomplished with a variety of differing instrumentation.

Thirty radiosondes were launched from the Buckland Park field site, between 31st July 1997 and 26th September 1997. These included, eleven fitted with GPS receivers and nineteen fitted with Omega VLF receivers. A scatter-plot comparison of zonal velocity, meridional velocity and velocity magnitude, using 10 minute averaged radar velocities centred around the launch time is shown in Figures 5.11a, 5.11b and 5.11c, respectively.

Radiosondes are launched twice daily from Adelaide Airport (AAP), $\sim$ 36 km to the south of Buckland Park, by the Bureau of Meteorology. Scatter-plot comparisons of the wind components from 174 flights, from June 2000 to October 2000, with 20-min averaged profiler observations, are shown in Figures 5.11d, 5.11e and 5.11f.

A Grob G109B aircraft obtained wind measurements using GPS, on 18th July, 31st July, 12th October and 20th October 2000, between 200 m and 3000 m. Comparisons of 10-min averaged profile measurements, centred on the aircraft flight time, are given in Figures 5.11g, 5.11h and 5.11i. Depending on which particular atmospheric feature was being probed, individual soundings could consist of a full sounding from $\sim$ 300 m to 3000 m, a short descent or ascent over $\sim$ 500 m or a fixed height observation for the duration of the sounding.

The calculated radar averaged velocity values were required to fulfill several criteria before they were included in the comparisons. Only measurements with a SNR greater than 5 dB were used. At least three values were necessary in order to obtain an average, with any value greater than five standard deviations away from the mean being removed. When comparing this average value with the sonde or Grob aircraft measurements further rejection criteria were applied. Comparisons which had a difference

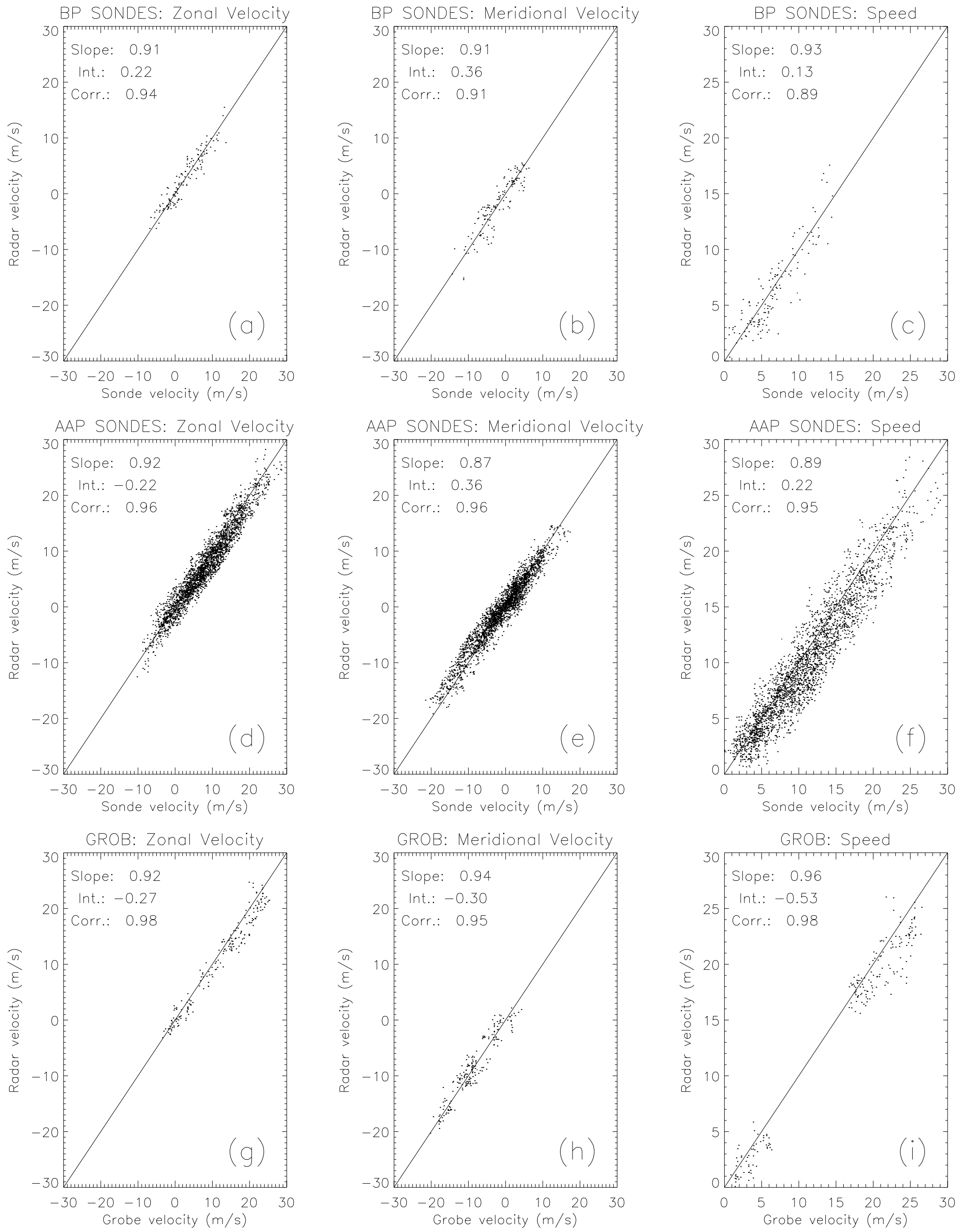

Figure 5.11: Scatter-plot comparison, of radar derived zonal velocity, meridional velocity and velocity magnitude, with measurements from radiosondes launched from: Buckland Park (a), (b), (c); Adelaide Airport (d), (e), (f) and measurements obtained from the Grob G109B aircraft operating near Buckland Park (g), (h), (i). Lines of unit slope are shown. Calculated values for the slope and intercept of a weighted least squares fit straight line to the scatter-plot and values for the correlation between the two sets of values are given.

	Statistic	BP sondes	AAP sondes	Grob
	Correlation	0.94	0.96	0.98
	Intercept (ms^{-1})	0.22	-0.22	-0.28
u	Slope	0.91	0.92	0.92
(Zonal)	Mean Difference, $\overline{\Delta V}$ ms^{-1}	-0.12	0.76	1.09
	$\sigma_{\Delta V}$, ms^{-1}	1.56	1.87	1.73
	rms, ms^{-1}	1.25	1.64	1.65
	σ_{rms}, ms^{-1}	0.94	1.19	1.20
	Correlation	0.91	0.96	0.95
	Intercept (ms^{-1})	0.36	0.36	-0.30
v	Slope	0.91	0.87	0.94
(Meridional)	Mean Difference, $\overline{\Delta V}$ ms^{-1}	-0.18	-0.44	-0.23
	$\sigma_{\Delta V}$, ms^{-1}	2.03	1.81	1.78
	rms, ms^{-1}	1.60	1.47	1.50
	σ_{rms}, ms^{-1}	1.22	1.15	0.98
Number of profiles		29	174	68
Number of samples		131	2648	191
Radar averaging period, min..		10	20	10

Table 5.2: Statistics of comparisons of BP sondes, AAP sondes and Grob measurements with Profiler observations, for Zonal (u) and Meridional (v) wind components. The slope is obtained via a least-squares fit to the scatter-plots shown in Figure 5.11. The rms values indicate root-mean-square differences between sonde or Grob and radar data, while σ_{rms} is the standard-deviation in the rms values.

of greater than 10 ms^{-1} were rejected as it was assumed that at least one instrument was in error or they were measuring completely different wind environments [*Weber & Wuertz*, 1990]. If either of the horizontal components of any of the wind measurements were greater than 30 ms^{-1}, the measurement was excluded. By applying both these criteria, any interference from sources such as aircraft echoes was minimized.

A summary of the statistics of the comparisons of the sonde and Grob measurements with the radar is given in Table 5.2.

Comparing the results in Table 5.2, with values obtained by other authors is complicated by the lack of consistency in which statistical parameters are used for the comparison. Hence, the main statistical values used are: the correlation, root-mean-square difference, the standard deviation of the difference and the slope of a linear fit to a scatter-plot.

The values of correlations obtained for all the comparisons were greater than 0.9; for the AAP sondes comparison, a value of 0.963 was obtained for both v and u. This correlation value compares favourably with values obtained by other authors using radiosondes and 915 MHz profilers (i.e. 0.96 to 0.97 [*Weber & Wuertz*, 1990]) and 0.92 to 0.93 [*Martner et al.*, 1993]), radiosondes and ∼400 MHz profilers (i.e. 0.91 to 0.93 [*Weber et al.*, 1990; *Martner et al.*, 1993], radiosonde and 50 MHz ST-profilers (i.e. 0.82 to 0.94 [*Martner et al.*, 1993]) and 405 MHz profiler with 50 MHz profiler (i.e. 0.94 to 0.95 [*Weber et al.*, 1990]).

The velocity rms values obtained for u and v were 1.64 ms^{-1} and 1.47 ms^{-1}, respectively. These values also agree favourably with those obtained by other authors. *May* [1993] obtained rms values of 1.5 ms^{-1} using radiosondes and a 50 MHz profiler, *Angevine & MacPherson* [1995] obtained rms values ∼0.9 ms^{-1} using a 915 MHz profiler and an aircraft, although this was for the magnitudes and not the individual components. Significantly larger values have been obtained by *Vincent et al.* [1987] (i.e. 3-4 ms^{-1}) and *Kessler et al.* [1986] (i.e. 2.5-3.5 ms^{-1}). Although, these larger values could be due to large spatial separation between the radiosonde and the radar [*Vincent et al.*, 1987] or inability to correct for the influence of vertical velocity [*Kessler et al.*, 1986]. Values of rms of ∼1 ms^{-1} were obtained using different pairs of beam directions of a 405 MHz profiler, with the results taken over 1 month, thus implying for a wind profiling radar, rms values ∼1 ms^{-1} can be due to measurement error alone.

The standard deviation $\sigma_{\Delta V}$, values obtained were ∼1.5-2.0 ms^{-1}, which compares exceptionally with other author's values. The smallest value *Martner et al.* [1993] obtained was ∼3.0 ms^{-1} for the comparison with a 915 MHz profiler and radiosonde, with other values for comparisons with a 404 MHz and 50 MHz radar being 4-6 ms^{-1}. Although, values of $\sigma_{\Delta V}$ obtained in a comparison of 405 MHz and 50 MHz radars, which were closer to values obtained with the BLR, measured $\sim 2.2\text{ms}^{-1}$ [*Weber et al.*, 1990]. These small values of $\sigma_{\Delta V}$ suggest that any effect of spatial separation between the two set of measurements is minor. This is not surprising considering the local topography of the Adelaide Plains, which is flat between and surrounding AAP and Buckland Park.

The slopes of the least-squares fit applied to the scatter-plots in Figure 5.11 are all less than 1.0 (i.e 0.87 to 0.94), implying that the BLR measurements underestimate the wind velocity, compared with the sonde and aircraft winds. *Weber et al.* [1990] observed similar underestimations in a comparison of a 405 MHz Doppler beam swinging profiler with radiosonde measurements; they obtained slopes of 0.84 - 0.86. However, in comparisons between a 405 MHz and a 50 MHz profiler they found slopes of 0.90 and 1.03 for u and v, respectively.

The height, time and wind speed dependency of the apparent underestimation of the BLR wind measurements compared with sonde and Grob measurement was investigated. Figure 5.12 shows the difference between radar and sonde measured u (top left), v (top right) and $|V|$ (bottom left), along with the difference as a function of wind velocity (bottom right).

It can be seen in Figure 5.12, a, b and c, that the underestimation occurred at all heights. It should be noted that in Figure 5.12, points above 3500 m may consist of only a few values and hence will be susceptible to large variations. Measurement from these heights will occur during meteorologically interesting events which tend to have predominantly strong easterly winds associated with them. This behaviour is shown by the large variation in zonal differences above 3700 m.

The implication is that the observed differences are appreciable compared with what would be expected. The increase of magnitude differences with height, seen in Figure 5.12, agrees with the measurements of slope obtained from the scatter-plots (Figure 5.11). The underestimation is dependent on the actual wind velocity and the height of the measurement.

To determine if the underestimations had any temporal dependencies, the differences in velocities were plotted as a function of time, (Figure 5.13). Although there is scatter amongst the values plotted, there appears to be a slight trend. The differences from days 170 to 180 appear to be smaller and more evenly distributed around

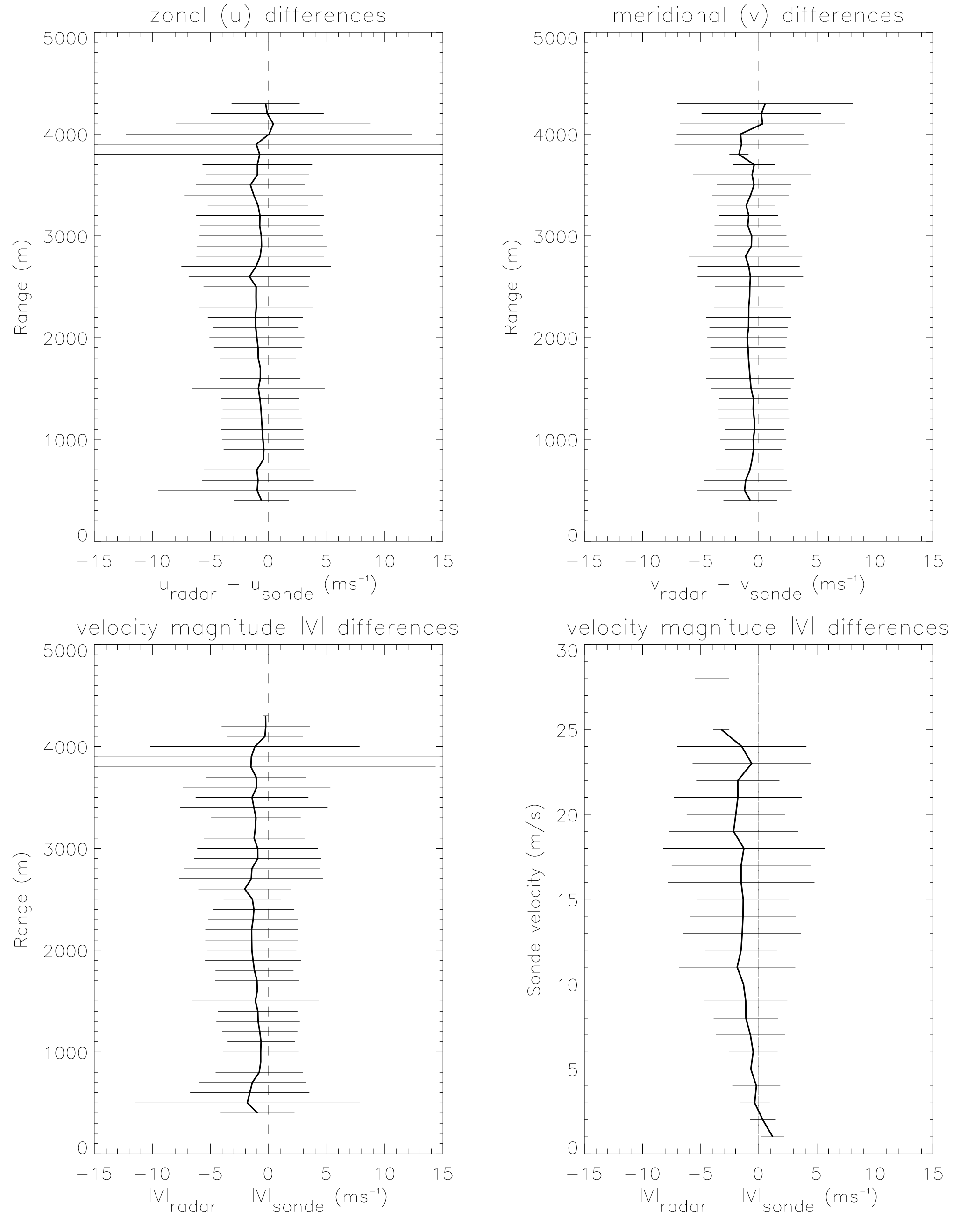

Figure 5.12: Velocity differences between AAP sondes and BLR measured velocities for (a) zonal component u (top left), (b) meridional component v (top right) and (c) velocity magnitude $|V|$ as a function of range. (d) Velocity magnitude differences as a function of sonde measured speed are also shown (bottom right).

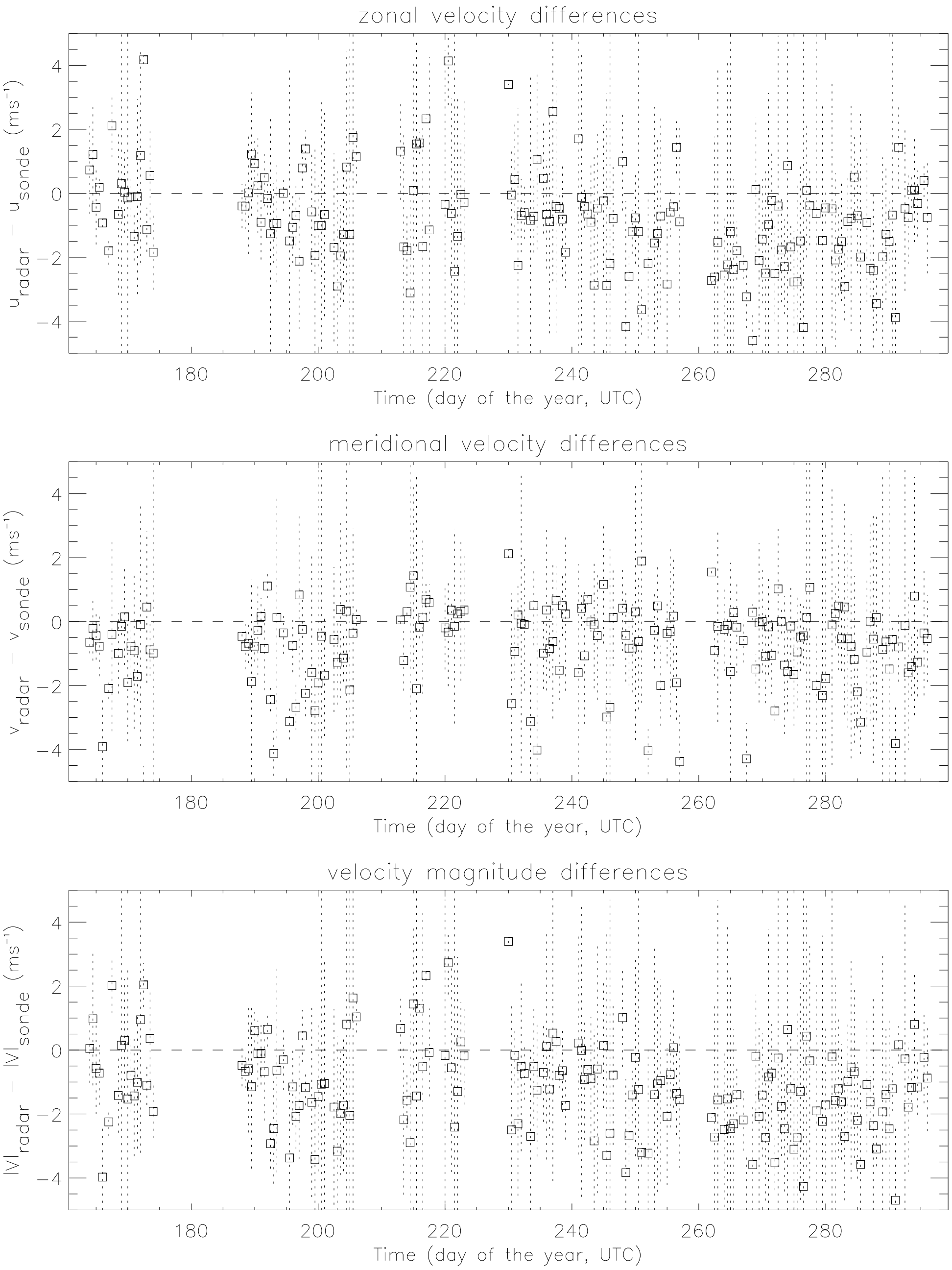

Figure 5.13: Velocity differences between AAP sondes and BLR measured velocities, given as a function of time, (i.e. Julian Day for 2000). The velocity differences are given in terms of radar measurements - sonde measurements. Components shown are zonal u (top), meridional velocity v and velocity magnitude $|V|$ (bottom).

zero difference, than values obtained from day 280 to 300. Two possible reasons for this decreasing performance could be antenna de-tuning or some characteristic of the receivers deteriorating with time.

In summary, comparisons of radar derived winds and alternative measuring techniques implied radar winds were underestimations of the actual wind. The underestimation is dependent upon background wind velocity and appears to be increasing very slightly with time. At heights below 700 m, the underestimation is larger than expected, when considering the usual background wind and values obtained from slightly higher altitudes. To put the underestimations into perspective, the correlation values obtained were still very high ~ 0.96 for the AAP sonde comparison.

5.4 Rain Detection

One of the advantages of operating at VHF as opposed to UHF is the ability to distinguish the clear air echo (CAE) from the precipitation echo during periods of rain.

In Figure 5.14 an example of the Doppler spectrum obtained from a 20 minute period centred at 0830 UTC on 2nd October 1999, is shown. Eleven 52 s time-series, with a one minute gap between each time-series, were averaged together to obtain the spectra shown. The CAE echo, which is at $\sim$0 ms^{-1}, is well defined and separated in the spectra from the precipitation (or rain) echo, which can be seen below 1.8 km around $\sim$-8 to -9 ms^{-1}.

Profiles of temperature and dew-point obtained from a sonde flight, launched from Adelaide Airport at 1100 UTC on the 2nd October 1999, are also shown in Figure 5.14 (on the right). From the sonde measurements the freezing layer was determined to be at $\sim$2.6 km, with a highly saturated region above. A region of enhanced echoes with increasing downward velocity was observed below the freezing layer and above 1.8 km, which was determined to be due to melting snow.

The terminal velocity $w(D)$ (ms^{-1}) of water droplets can be related to the drop-size

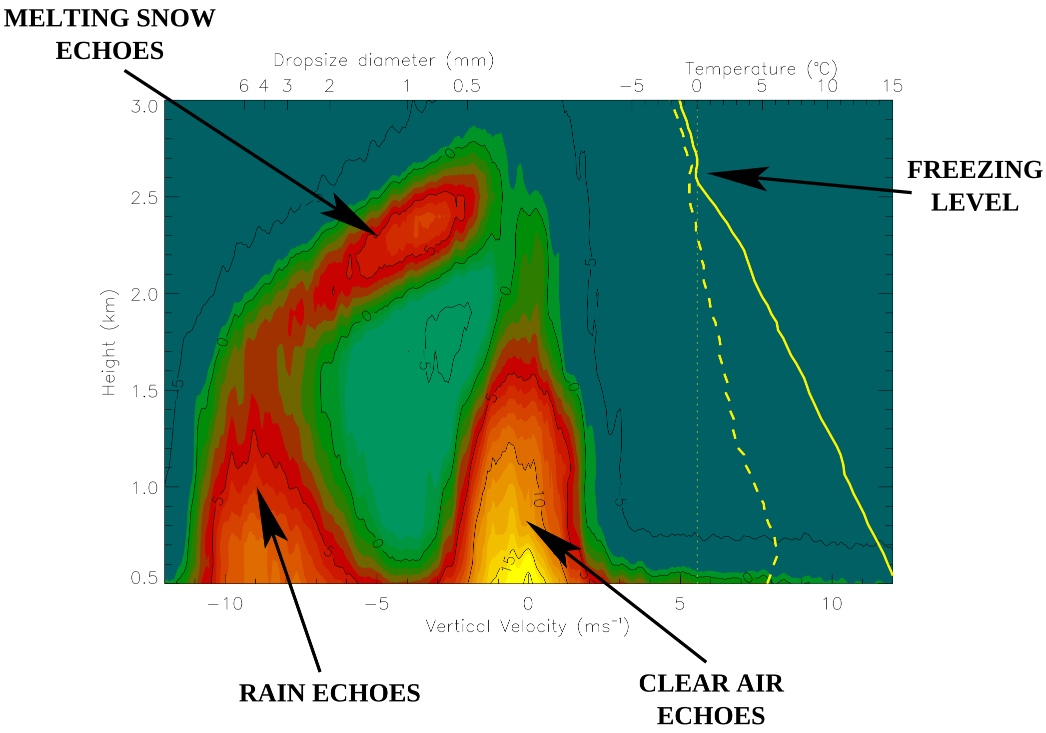

Figure 5.14: Velocity-height cross section obtained between 0820 UTC and 0840 UTC on 2nd October 2000. Vertical velocity is positive for upwards motion. The clear air echoes (CAE) and rain or precipitation echoes are labelled. An axis for conversion from the terminal velocity of water droplets to drop-size is given at the top of the plot. Shown on the right are the temperature (solid) and dew-point (dashed) profiles measured by a sonde launched from AAP at 1100 UTC on 2nd October 1999.

diameter D (mm) by [*Foote & duToit*, 1969; *Atlas et al.*, 1973]

$$w(D) = 9.65 \;-\; 10.3\; \exp(-0.6D) \left(\frac{\rho}{\rho_0}\right)^{-0.4} \tag{5.1}$$

where ρ is the air density and ρ_0 is the air density at a pressure of 1013 hPa and a temperature of 20°C. The effective drop-size values, calculated as if at ground level (i.e. 1013 hPa), are shown along the top of Figure 5.14.

If the precipitation spectra can be sufficiently isolated and the effects of spectral broadening and the background vertical wind velocity removed, it is possible to obtain the drop-size distribution $N(D)$ and a measure of the rainfall rate. The precipitation echo $P(w)$ can be given by [*Rajopadhyaya et al.*, 1993],

$$P(w) = \frac{1}{Z} N(D) D^6 \frac{dD}{dw}, \tag{5.2}$$

where Z is the radar reflectivity due to the precipitation given by,

$$Z = \frac{\eta \lambda^4}{\pi^5 |K_w|^2}, \tag{5.3}$$

where $K_w = (m^2 - 1)/(m^2 + 2)$, $m = n - jn\kappa$ is the complex refractive index of water and the reflectivity η is given by Equation 4.2.

With a fully calibrated radar it is possible to determine $N(D)$ and hence the rainfall rate R given by [*Doviak & Zrnić*, 1993],

$$R = (\pi/6) \int_0^\infty D^3 N(D) w(D) dD. \tag{5.4}$$

Preliminary results comparing rainfall rates measured by a rain gauge located next to the radar and radar derived rainfall rates have been promising [*C. Lucas, 2000, private communication*]. However, while the rain gauge measures the rainfall rate at the surface, the radar is only able to measure the rainfall above ~500 m. These initial comparisons have not included the calibration values to derive Z, instead only the general shape of the DSD has been determined unambiguously. Rain rates between 0600 and 1200 UTC on 2nd October 1999, from the profiler and the rain gauge are shown in Figure 5.15 [*Lucas et al.*, 2000]. It is clear from these preliminary results that the BLR has great potential for rain studies.

5.5 Calibrated Measurements

The calibration values obtained in Chapter 4 can be used to determine the absolute received power. Using this information the reflectivity η, which is the backscattering cross section per unit volume, can be determined. The reflectivity can be directly related back to the cause of the scatter. As shown in Section 5.4, if precipitation is present, it is possible to obtain a measure of the rainfall rates.

In the next section, reflectivity observations will be related back to the atmospheric conditions present at the time via in-situ measurements. This will highlight the ability of the radar to observe relatively thin layers of strong reflectivity which occur in the

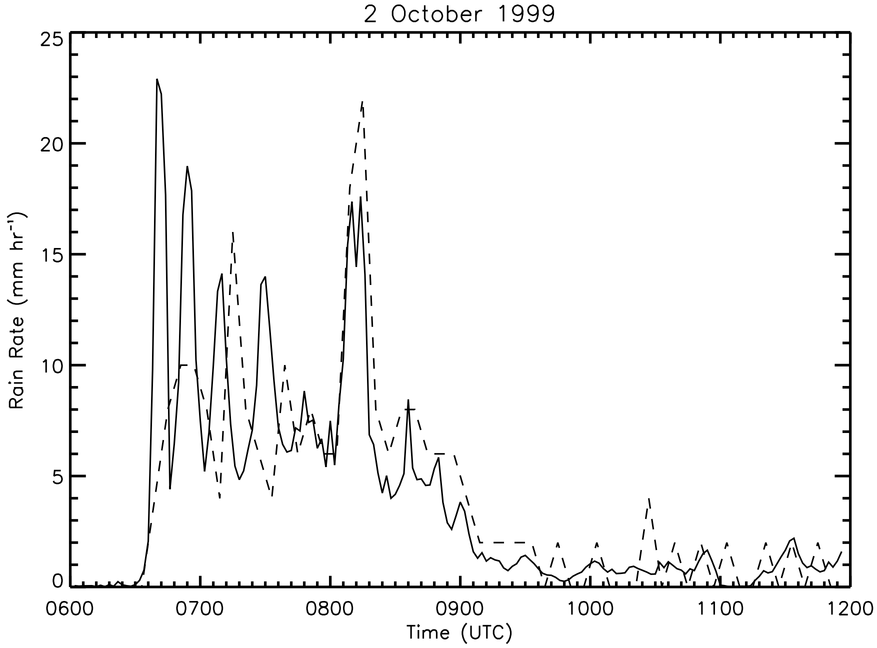

Figure 5.15: Rain rate between 0600 and 1200 UTC on 2nd October 1999. Shown are rates from co-located gauge (dashed) and from drops > 1mm from the profiler retrieval (from *Lucas et al.* [2000]).

atmosphere. Following this will be the determination of the turbulent refractive index structure, C_N^2. This can be directly related back to the η provided the scatter is isotropic, therefore a method for determining the isotropy of the scattering mechanism is derived first. A comparison between C_N^2 values obtained from BLR measurements and C_N^2 values obtained by other authors is discussed.

5.5.1 Reflectivity observations

Values of reflectivity were obtained using Equation 4.2 and the calibration values discussed in Chapter 4. Figure 5.16 shows the "reflection coefficient" or reflectivity values from 20th October 2000 between 00 UTC and 07 UTC and 0.5 and 3.5 km altitude. Also shown in Figure 5.16 are the temperature, dew-point temperature, relative humidity and M^2 profiles obtained between 0352-0415 UTC from a sounding made by a Grob G109B Aircraft, (see Section 1.5).

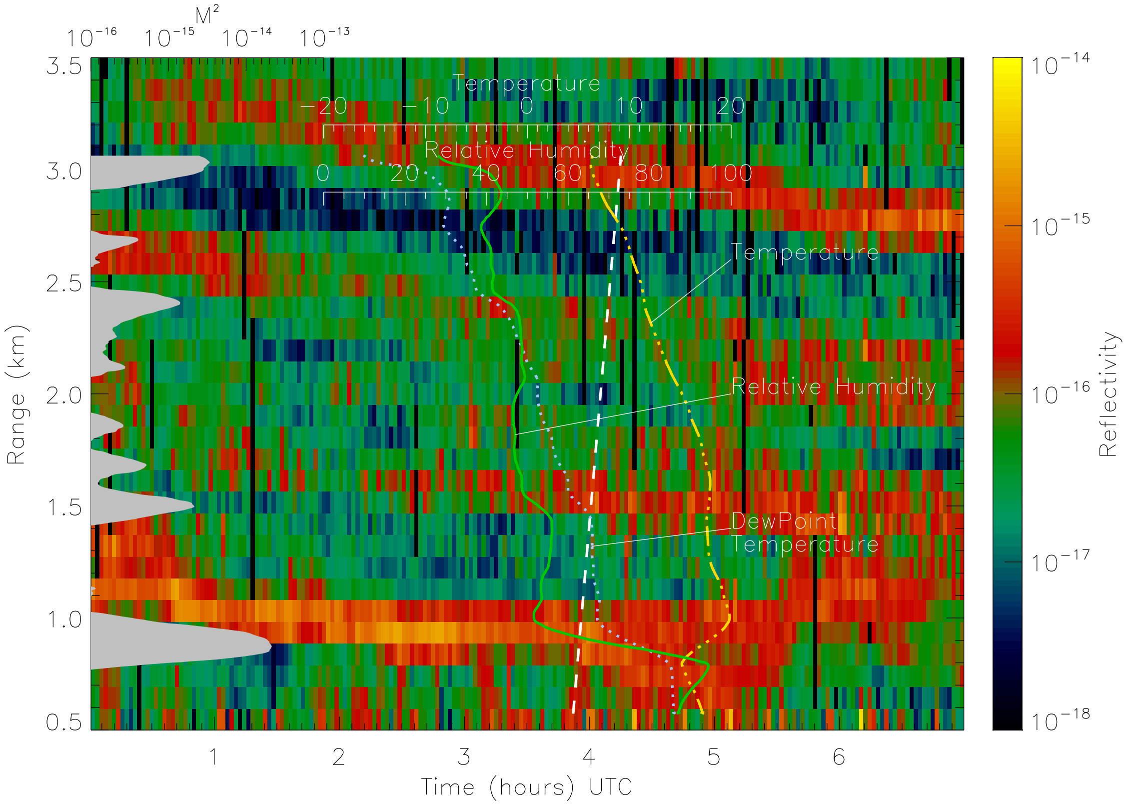

Figure 5.16: Time-height cross section of reflection coefficient for 20th October 2000 between 00 UTC and 07 UTC and 0.5 and 3.5 km altitude. Also shown are temperature (dash-3 dot), dew-point (dotted), relative humidity (solid) and M^2 (solid shaded area on left). These measurements were obtained via a sounding by a Grob Aircraft. The ascent of the aircraft, 0352-0415 UTC is represented by the dashed line. (see text for further description)

The Grob G109B acquired a sounding by slowly ascending (or descending) at a rate of $\sim$1 ms^{-1}, over the range 500-3000 m. The aircraft at the time of the sounding was located within 5-10 km of the radar site, being close enough that spatial variation between the two sets of measurements would be minimized, but far enough away to avoid spurious reflections from the aircraft. In order to calculate M^2, (Equation 1.20), the temperature, dew-point temperature and pressure profiles were interpolated at regular heights (i.e. 1.0 m), then smoothed[3] over 50 m. The smoothing was applied to remove the effects of minor fluctuations, which occur with small time or height

---

[3] Radiosonde measurements have significant smoothing applied, with typical smoothing period for a GPS sonde is $\sim$60 seconds which with an ascent rate of 4 ms^{-1} corresponds to $\sim$240 m.

increments and to smooth digitizing effects caused by the extremely high sampling rates. Without accounting for these minor fluctuations, the height derivatives in (1.20) became appreciable, causing large values of M^2. The effective sampling resolution of the BLR is 150 m, resulting in a smearing within the radar volume. A smoothing value of 50 m was chosen arbitrarily to make comparisons possible with radar reflectivities and maintain the superior height resolution of Grob measurements.

One of the goals of the campaign involving the Grob was to gain insight into the nature of horizontal layers observed in the reflections. The campaign was continuing as this thesis was being completed so an in-depth discussion into various observations is beyond the scope of this thesis. Only a brief summary of the single sounding shown in Figure 5.16 will be given.

In order to understand Figure 5.16, all the observations shown must be referenced back to the time of ascent of the Grob, given by the dashed line. This caution can be understood by noting the descent, during the seven hours of observations, of the layers initially observed at ∼3.5 km, ∼2.6 km and ∼2.0 km. The reflectivities shown represent values obtained for every radar profile obtained during the period.

The profile of M^2 and values of reflectivity obtained during the sounding show good agreement. The layers at ∼1.0 km and ∼3.0 km have well pronounced peaks in the M^2 profiles. The smaller peaks between 1.5 km and 2.7 km, in M^2, are indicative of the broad poorly defined layers in the reflectivity within this region. From the thermodynamic traces, further understanding of the characteristics of the layers observed can be obtained. The layer at 1.0 km is associated with a temperature inversion at the top of the boundary layer, with moist well mixed air trapped below. Above this inversion, the air is relatively warm and dry up to ∼1.5 km, where another inversion was observed. This inversion is accompanied by a further decrease in humidity. The poorly defined layers in M^2 in the region from 2.0 to 2.5 km are associated with subtle increases in moisture. The final layer at ∼3.0 km, is associated with a sharp reduction in humidity.

It should be noted that the 50 m smoothing filter applied to the Grob measurements was to enable relatively simple comparisons with the reflectivities obtained by the radar. One of the goals of the Grob campaign is to observe the finer scale structure of the layers, thus such smoothing may be deemed inappropriate for such observations. Further discussion of observations of layers is presented in Section 5.5.3.

5.5.2 Isotropic scatter discrimination

The turbulent refractivity structure parameter can be calculated if the back-scatter is due to isotropic turbulence by [*Kropfli et al.*, 1968],

$$C_n^2(r) = \frac{0.38\eta(r)}{\lambda^{1/3}}, \tag{5.5}$$

where $\eta(r)$ is given by Equation 4.2

Measurements of C_n^2 in homogeneous, isotropic turbulence are related to the temperature and humidity fluctuations as given by [*Tatarskii*, 1971],

$$C_n^2 = a^2\alpha' M^2 L_o^{\frac{4}{3}}, \tag{5.6}$$

where a^2 is a universal constant taken to be 2.8 [*Ottersten*, 1969], α' is a ratio of eddy diffusitivities which is often taken to be unity [*VanZandt et al.*, 1978], L_o is the outer scale length of the turbulence spectrum and M is the gradient of the generalized potential index of refraction given by Equation 1.20.

In order to use (5.5) a method is needed to determine if the backscatter is from isotropic turbulence. The following discussion on isotropic scatter determination is based upon the theory given in *Briggs* [1992]. For simplification, assume that the aspect sensitivity (or angular dependence of the scatterer) $\sigma(s)$, is only dependent upon the zenith angle θ, where $s = sin(\theta)$, therefore restricting the discussion to vertically pointing radars.

The angular power spectrum $W(s)$, is determined by a combination of the antenna polar diagrams and the aspect sensitivity of the scattering cross-section. If the transmitting and receiving antenna polar diagrams and angular dependence (or aspect sensitivity) of the scatterer are of Gaussian form, they can be written as,

$$\begin{aligned} \sigma(s_T) &\propto exp(-\frac{s^2}{s_T^2}) \\ \sigma(s_R) &\propto exp(-\frac{s^2}{s_R^2}) \\ \sigma(s_a) &\propto exp(-\frac{s^2}{s_a^2}) \end{aligned} \tag{5.7}$$

where

$$\begin{aligned} s_T &= sin(\theta_T), \\ s_R &= sin(\theta_R), \\ s_a &= sin(\theta_a). \end{aligned} \tag{5.8}$$

θ_T, θ_R are the e^{-1} half-widths for the polar diagrams of the transmitting and receiving arrays and θ_a is the e^{-1} half-width for the polar diagram of the scatterer. Hence the angular power spectrum is,

$$W(s) \propto exp(-\frac{s^2}{s_0^2}), \tag{5.9}$$

where

$$\frac{1}{s_0^2} = \frac{1}{s_a^2} + \frac{1}{s_T^2} + \frac{1}{s_R^2}. \tag{5.10}$$

The spatial correlation function $\rho(r)$ is given by,

$$\rho(r) = exp(-\pi^2 s_0^2 r^2), \tag{5.11}$$

where r is in wavelengths. The pattern scale $r_{0.5}$ is a measure of the average radius of the spatial correlation characteristic ellipse (i.e. where $\rho(r_{0.5}) = 0.5$), see section 6.2 for more detail. Substituting $r_{0.5}$ in Equation 5.11 enables a relationship between the pattern scale r_o calculated via FCA and the angular dependence of the scattering cross-section to be obtained, providing values for s_T and s_R are known (Figure 5.17).

For the BLR third-generation array $\theta_T = 10.2$ and $\theta_R = 18.6$, hence $r_{0.5} = 9.57$ m is the predicted value of the pattern scale for isotropic scatter, i.e. $\theta_a = 90°$. Hence, providing the pattern scale can be measured, the level of isotropy of the scatter can be determined. If the scatter is isotropic, values for C_N^2 can be calculated.

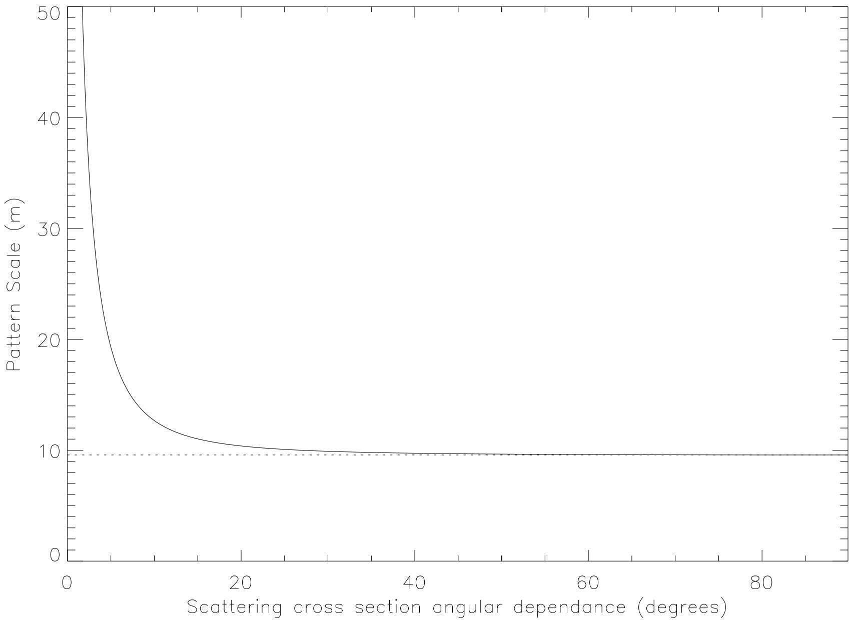

Figure 5.17: Relationship between pattern scale of the diffraction pattern for the BLR and angular dependence of the scattering cross-section. The pattern scale of isotropic scatter (i.e. 90^o) is shown by the dotted line.

5.5.3 Refractive Index Structure Parameter

The radio refractive index structure parameter C_N^2, depends on the level of turbulence and the gradient in the temperature and humidity. Detailed presentation of the characteristics of scatterers at VHF is outside the scope of this thesis, but measurements from 1800 UTC 4th September 2000 to 0900 UTC 5th September 2000, are shown in Figure 5.18 as examples.

A layer of enhanced reflectivity at ~ 2 km was present during the whole period of observation, (Figure 5.18). The random velocity V_{RMS} increased with height within the layer, with the layer having a thickness of three range gates (~ 300 m). The pattern scale of scatterers within the layer decreased with height, implying an increase in isotropy. Similar relationships between increasing turbulence and smaller horizontal correlation lengths have been reported by other authors [*Chau et al.*, 2000].

By limiting measurements to regions where the pattern scale was of the order of

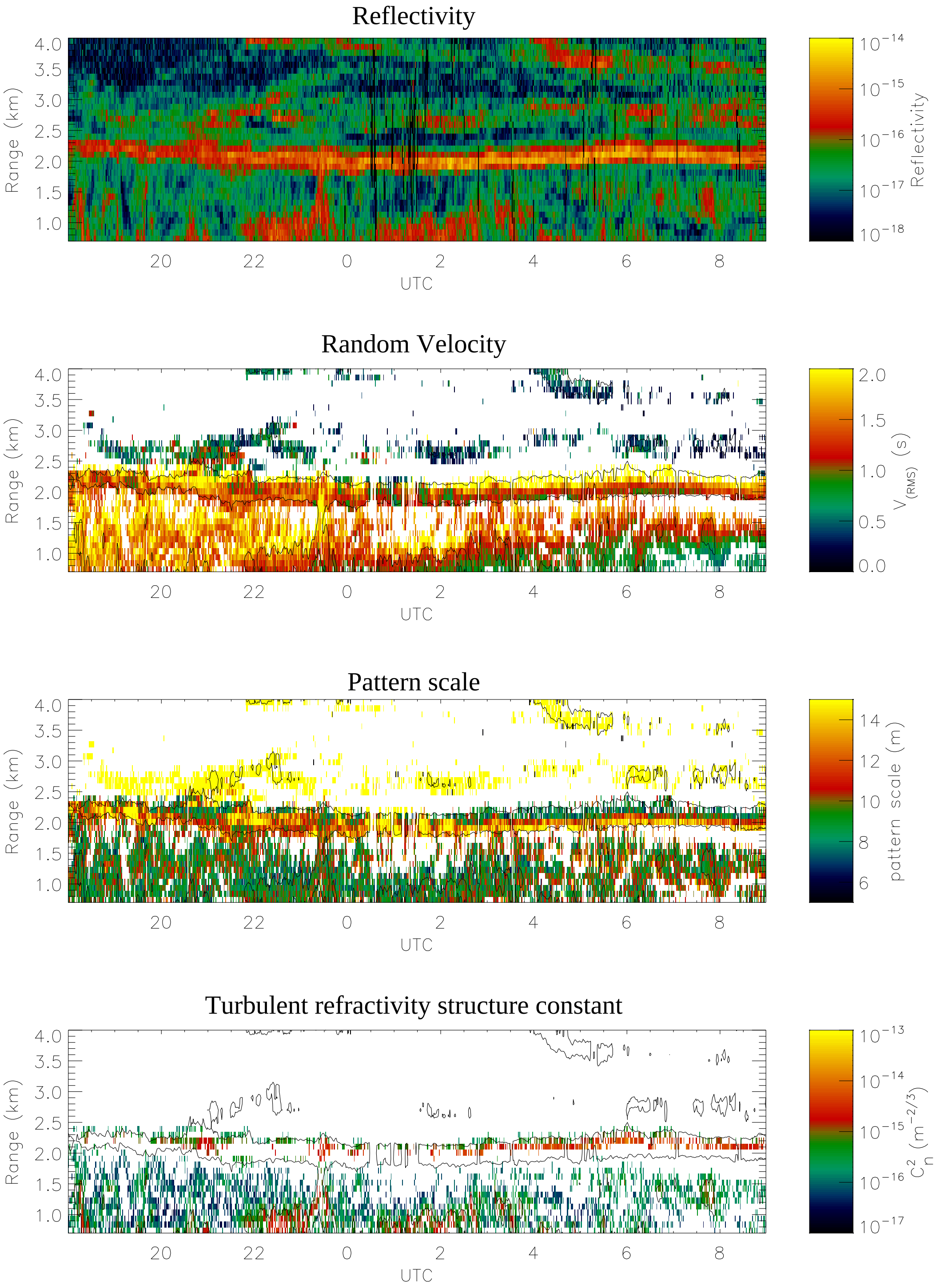

Figure 5.18: Time-height cross-sections of (from the top) reflectivity, random velocity, pattern scale and turbulent refractivity structure constant. Taken from 1800 UTC 4th September to 0900 UTC 5th September 2000. Contours of reflectivity are overlayed on the bottom three plots to show regions of enhancement.

10 m, (i.e. isotropic turbulence), estimations of C_N^2 were obtained using Equation 5.5. An enhancement of C_N^2 at the top of the layer can be seen, when compared with values obtained from the region below the layer. In the region below the layer, values of C_N^2 and V_{RMS} obtained were, $\sim 10^{-16}$ to 10^{-15} $\mathrm{m}^{-2/3}$ and 1 to 2 ms^{-1}, respectively. At the top of the layer, similar values of V_{RMS} were associated with values of C_N^2 in the range $\sim 10^{-15}$ to 10^{-14} $\mathrm{m}^{-2/3}$.

Measurements of temperature, dew-point temperature and potential temperature from radiosondes launched from Adelaide Airport, at 1115 UTC and 2315 UTC on 4th of September 2000, are shown in Figure 5.19.

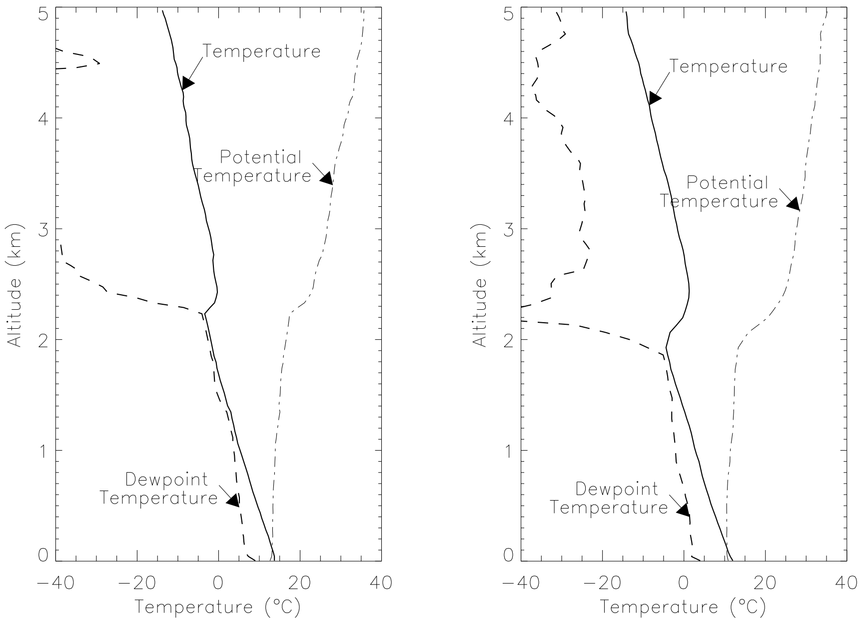

Figure 5.19: Temperature, dew-point temperature and humidity profiles from Adelaide Airport radiosondes launched 4th September 2000 at 1115 UTC (left) and 2315 UTC (right)

The top of the Cloud Topped Boundary Layer (CTBL) is marked by a temperature inversion, which strengthened, deepened and descended during the 12 hours between sonde launches. The height of the inversion coincides with the layer observed with the radar at 2 km, with a similar thickness of $\sim$ 300 m as determined from the second sounding. This highlights the ability of the VHF radar to give a good measure of the height of the top of the boundary layer.

The influence of q (behaviour of q can be characterized by the dew-point temperature) and its derivative on M^2 (1.20) can be seen by the enhanced regions of reflectivity in Figure 5.18. The inversion layer at 2 km is characterized by a strong gradient in q from its bottom. The CTBL is moderately well mixed, as θ is relatively constant within it. In Figure 5.19 a saturated region[4] is observed to exist, below the inversion, between ~1 km and 2.2 km However by 2300 UTC the vertical extent of this saturated region had decreased considerably. Observations of cloud cover over this period ranged from mostly cloudy with scattered showers during 4th September 2000, to partly cloudy on the 5th September 2000, which agrees with the radiosonde measurements. The effect of the higher values of q below the inversion, compared with above the inversion, results in greater values of M^2, and hence greater coverage below the inversion. The coverage of the radar can be quantified by considering where measurements of pattern scale were obtained.

In Figure 5.18, layers corresponding to regions of weakly turbulent velocity and highly anisotropic scatter were noted at ~3 km, and descending from around 4.0 km to 3.5 km. These layers are associated with variations in the dew-point or q and hence increased values of M^2.

Values of C_N^2 calculated over fourteen consecutive days, commencing on 14th October 2000, are shown in Figure 5.20. The top plot in Figure 5.20 includes the isotropic scatter determination (ISD) procedure described in Section 5.5.2. The bottom plot retains all values, including the contribution of anisotropic scatter. Anisotropic scatter will produce an increase in reflectivity [*Hocking et al.*, 1986], resulting in an overestimation of C_N^2 values. This overestimation can be seen between 1 km and 2.5 km, in the bottom plot of Figure 5.20. This region corresponds with the height range over which specular reflections from layers were observed, see Figure 5.18. The decrease in C_N^2 up to 3 km is behaviour common to profiles of C_N^2 [*VanZandt et al.*, 1978], [*Doviak & Zrnić*, 1993] and [*Hocking & Mu*, 1997]. The increase above 3 km is a result of the

---

[4] In a fully saturated region the temperature and dew-point temperature are equal.

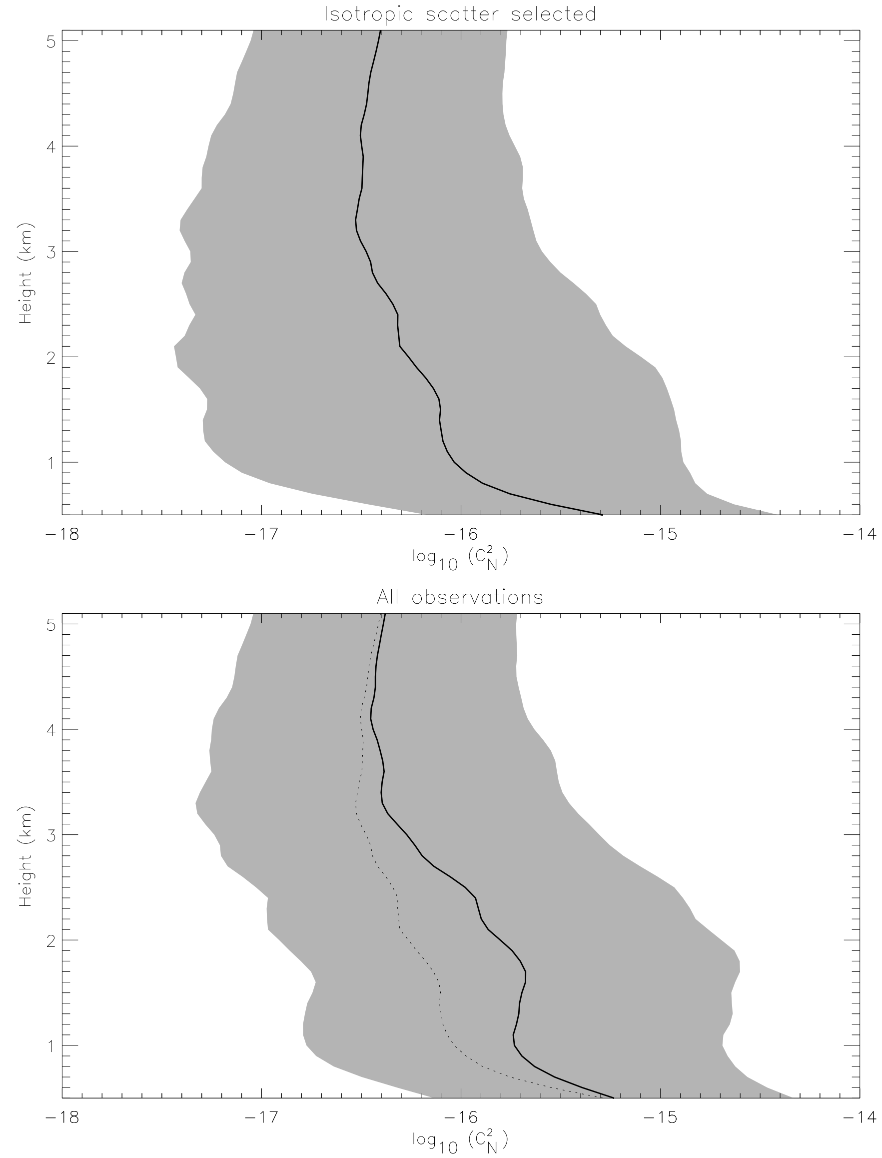

Figure 5.20: Vertical profiles of C_N^2 from 1st October 2000 to 14th October 2000. Mean values (solid line) along with the standard deviation (shaded area) for each height are shown. The top plot contains values where the pattern scale was less than 10m (i.e. isotropic), while the bottom plot has no restrictions showing all values. For comparison the mean values from isotropic measurements are also shown in the bottom plot (dotted line)

limit of detectability of the signal at those heights (see fig.3 in *Hocking et al.* [1986]).

In order to obtain the top profile in Figure 5.20, the following assumptions were made. Small values of SNR, which cause a failure in FCA, often correspond to regions of low reflected power. As anisotropic scatter causes an increase in power [*Tsuda et al.*, 1988], the regions of low SNR were assumed to be due to isotropic scatter. However, measurements of pattern scale show an increase in pattern scale and hence anisotropy with height, with very few measurements being of isotropic scatter (Figure 5.10). This implies that measurements of C_N^2 obtained from above 3 km will be contaminated with anisotropic influences and will be overestimations.

Many estimates of the refractive index structure have been made by numerous authors. Care must be made in interpretation and comparison of measurements made by differing systems, especially in the lower troposphere.

In the lower troposphere the humidity term q dominates. Many observations of C_n^2 measured the optical refractivity structure constant, which is independent of q. To distinguish between radar and optical refractive index structure, the radar refractive index structure is labeled C_N^2 [*Gossard*, 1977]. In the middle to upper troposphere and stratosphere the humidity term is often assumed to be negligible and it is possible to directly compare the radar and optical refractive index structures [*Hocking et al.*, 1986].

The values and variations obtained here for C_N^2 compare favourably with those of other authors, although there is some suggestion of possible underestimation. Measurements of C_N^2 were observed to alter by an order of magnitude within an hour. Similar fluctuations have been observed by other authors [*VanZandt et al.*, 1978; *Luce et al.*, 1996].

An extensive study by *Gossard* [1977] determined the distribution of optical and radio refractive index structure constants for a variety of air masses. Observations of the same mass of air in different conditions gave a range of values for C_N^2 in the lowest 3 km ranging from less than 10^{-16} $\mathrm{m}^{-2/3}$ to $\sim 10^{-14}$ $\mathrm{m}^{-2/3}$. This range of values is represented in the height distribution of C_N^2 given in Figure 5.20. The variability shown in the profiles in *Gossard* [1977] (Figure 5.21) where the magnitude of C_N^2 varies by several orders of magnitude over several hundred metres, highlights the validity of the width of the calculated distribution.

Measurements at a height of 805 m from a year-long C_N^2 measurement program using a Frequency Modulated Continuous Wave (FM-CW) Doppler radar in several locations in Colorado gave values ranging between 10^{-17} and 10^{-15} $\mathrm{m}^{-2/3}$ [*Chadwick & Moran*, 1980]. Values of C_N^2 greater than 10^{-15} $\mathrm{m}^{-2/3}$ were measured, but these values were questioned due to suspected contamination by aircraft, rain, snow, birds and insects. Comparisons between the Millstone Hill 440-MHz turbulence scatter radar and a stellar scintillometer found values of C_n^2 in the lowest five kilometres ranging from 10^{-15} to 10^{-17} $\mathrm{m}^{-2/3}$ [*Good et al.*, 1982], However these values were for the optical refractive index structure. The differences between C_n^2 and C_N^2 can be up to a few orders of magnitudes. C_N^2 is predominately greater than C_n^2, but at times the opposite condition occurs [*Gossard*, 1977; *Good et al.*, 1982]. Any comparisons with previous optical refractive index structure measurements and C_N^2 will only be approximations, dealing with orders of magnitude only. Measurements of the optical refractive index structure range from $(10^{-15} - 10^{-16} m^{-2/3})$ at the ground to $(10^{-16} - \sim 10^{-18} m^{-2/3})$ at around 5 km, [*Brown & Good*, 1984*a*; *Brown & Good*, 1984*b*; *Bufton et al.*, 1972; *Barletti et al.*, 1976; *Ochs & Lawrence*, 1972; *Vernin et al.*, 1979].

Distributions of C_N^2 taken with 50 MHz radars at Poker Flat and Platteville over a period of approximately 11 months at a height of 3.8 km [*Nastrom et al.*, 1986], show excellent agreement with the distribution shown in Figure 5.20. However, other authors have reported C_N^2 values significantly larger than those shown in Figure 5.20. *Hocking & Mu* [1997] using the Buckland Park VHF ST radar in May 1991 recorded measurements between 2 km and 5 km being greater than $10^{-14}\mathrm{m}^{-2/3}$, these values were several orders of magnitude greater than the typical range measured by the BLR during the October 2000 campaign.

Using a vertical beam to estimate C_N^2 depends upon the nature of the scatterers.

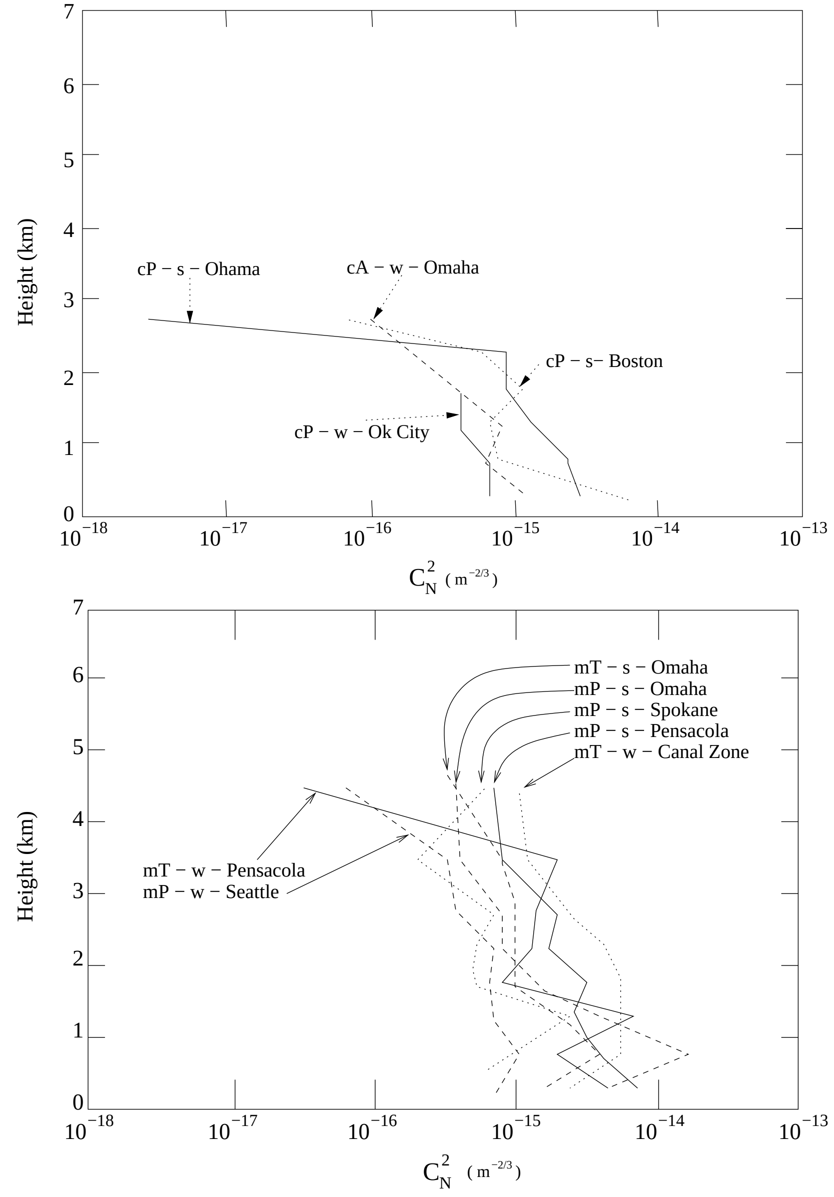

Figure 5.21: The height distribution of radio refractive index structure constant in some continental *c* (top) and maritime *m* (bottom) air masses at the locations indicated. Winter and summer seasons indicated by *w* and *s*. Continental, polar and tropical air masses are designated *c*, *p* and *t*. (From *Gossard* [1977] Figures 15 and 16)

Restricting our measurements to only isotropic measurements results in a large proportion of the data being unusable. To avoid anisotropy, normal VHF measurements of C_N^2 involve the use of oblique beams pointing to zenith angles greater than 10° [*Luce et al.*, 1996]. The BL radar in its present configuration is unable to do this.

It is hoped that the Grob campaign, which was continuing while this thesis was being written, will provide in-situ measurements of C_N^2 for comparison with the radar derived values. Such comparisons will enable the validity of the assumptions with regard to the isotropic scatter determination method to be tested. The comparisons could also be used to check the accuracy of the calibration values obtained in Chapter 4, as some of the assumptions made in determining the calibration terms may be inaccurate. The assumption made in Section 4.2, that the antenna was lossless will not be true, resulting in an underestimation of the received power and hence C_N^2.

5.6 Summary

In this chapter the considerations for selection of the radar operating parameters were presented. The three main operating modes *normal*, *high* and *extra high* were detailed. The latter two modes were developed to increase coverage of the radar, along with filling "gaps" in the *normal* mode data. Comparisons between different modes showed the superior coverage of the longer transmitted pulse modes, although at a cost of a loss of range resolution.

The difference in coverage achieved when using the different generations of antenna array was presented. The lower height coverage of the second generation array was worse than the coverage of the first generation array. However, an increase in lower-level coverage was observed when the third generation array was installed. Unfortunately deterioration in the RDAS began to affect the quality of measurements at the lowest height, with a reduction in the lower-level coverage, which increased with time. The minimum height from which the BLR obtained measurements was 300 m, while at times measurements from up to 8 km were obtained while using the extra high mode.

A statistical evaluation of the atmospheric parameters measured with the radar, using the third generation array, over the range 500 m to 5900 m, was presented. From these measurements we can determine the average characteristics we should expect from observations made with the BLR. The average profile of the pattern scale increased with height, implying increasing anisotropy, while the random velocity was predominantly less than 1 ms^{-1} and decreased slightly with height. The vertical velocity showed a slight bias of $\sim$10 cms^{-1}, which showed no correlation with the horizontal velocities, thus implying it was real and not due to leakage of the horizontal velocity in the vertical values.

The radar derived wind values were compared with in-situ wind measurements obtained from radiosondes launched from Buckland Park, radiosondes launched from Adelaide airport and wind measurements obtained by aircraft (Grob) flying near Buckland Park. All three different comparisons had correlation values between 0.91 and 0.98 and RMS values between 1.25 ms^{-1} and 1.65 ms^{-1} for the zonal and meridional components. The values for the slopes of least-squares fits to the data were between 0.87 and 0.94, implying that the radar wind observations are underestimations compared with measurements from the radiosondes and Grob. Further analysis showed this underestimation was independent of range, but was dependent upon the background wind velocity and appeared to increase over the five months of observations.

The distinguishability of rain echoes and clear air echoes observed with the BLR was shown. The calibration values obtained in Chapter 4 were used to calculate values for reflectivity. Simultaneous aircraft measurements of atmospheric parameters showed excellent correlation between M^2 values derived from the aircraft measurements and the reflectivity vertical structure observed with the radar. Using the calibrated radar, values of the turbulent refractivity structure parameter were also obtained. However, this required the filtering out of anisotropic data, leaving a relatively small amount of data. Comparisons of the range of values obtained with values obtained by different authors were favourable, although there was a hint of underestimation. To be able to verify the values of C_N^2, a comparison with a co-located apparatus will be required.

The effect of the underestimation in the radar derived wind measurements is investigated in the next chapter. Potential sources of error in the wind measurements derived by using FCA are replicated using simulated data.

Chapter 6

Spaced Antenna Winds Analysis

Full Correlation Analysis (FCA) [*Briggs et al.*, 1950] is a method of analyzing the diffraction pattern produced by scatter from moving irregularities in the atmosphere and sampled at a number of spaced receivers. The underlying assumption of FCA is the concentric ellipsoid form of the spatial-temporal correlation functions of the diffraction pattern. By sampling the diffraction pattern at different locations the ellipsoid's parameters may be estimated by calculating the auto- and cross-correlation functions of the received signals. The apparent velocity v_a can be determined via the time-displacements of the cross-correlation functions. The true velocity v_t takes into account any effects of anisometry or change in the diffraction pattern and requires additional calculation of the auto-correlation functions.

FCA is the standard method adopted in this thesis for extracting winds with the VHF BL radar. In this chapter the background theory of FCA and parameters which can be obtained are discussed. In Section 5.3 comparisons between radiosonde-measured winds and the VHF BL radar derived FCA winds have shown an underestimation in the FCA true velocity. A simplified one-dimensional model and a more complex radar backscatter model, which gives time-series depending on the input parameters, are discussed. These models are used to explore the possible sources of error in FCA, in particular wind velocity underestimation. Application of the two models, using parameters and conditions which represent those used and observed by the VHF

Boundary Layer radar and the subsequent analysis is presented. The output from the models is used to determine possible causes for the observed wind underestimation by the VHF BL radar, shown in Section 5.3.

6.1 FCA Theory

In this section and the following section, the discussion of FCA is based on the theoretical details presented in *Briggs* [1984]. Let $f(x, y, t)$ be the complex voltage of the diffraction pattern measured by an antenna at time t and position (x, y). For simplicity the following discussion will deal with a fixed height, hence the absence of z. The spatial-temporal correlation function as a function of x-direction separation ξ, y-direction separation η and lag τ is given by,

$$\rho(\xi, \eta, \tau) = \frac{\langle f^*(x, y, t) f(x + \xi, y + \eta, t + \tau\rangle}{\langle\mid f(x, y, t) \mid^2\rangle}. \tag{6.1}$$

To begin with, we will assume the diffraction pattern is stationary, non-changing and isotropic, therefore the correlation function would depend only on the magnitude of spatial displacement and not the orientation and would be given by,

$$\rho(\xi, \eta, \tau) = \rho(\xi^2 + \eta^2), \tag{6.2}$$

thus consisting of concentric circles centred around $(0, 0, \tau)$, see Figure 6.1a.

To include the effect of anisotropy, we simply stretch the correlation function in a particular direction, therefore giving concentric ellipses in the (ξ, η) plane, given by

$$\rho(\xi, \eta, \tau) = \rho(A\xi^2 + B\eta^2 + 2H\xi\eta), \tag{6.3}$$

see Figure 6.1b. The ellipse given by $\rho(\xi, \eta) = 0.5$, is referred to as the "characteristic ellipse", which is a measure of the scale of the pattern.

To include the effect of random motion of the irregularities, we extend the above principles to include the time axis. The temporal correlation function, for a fixed but randomly changing pattern, would de-correlate with increasing time lag, similar to the

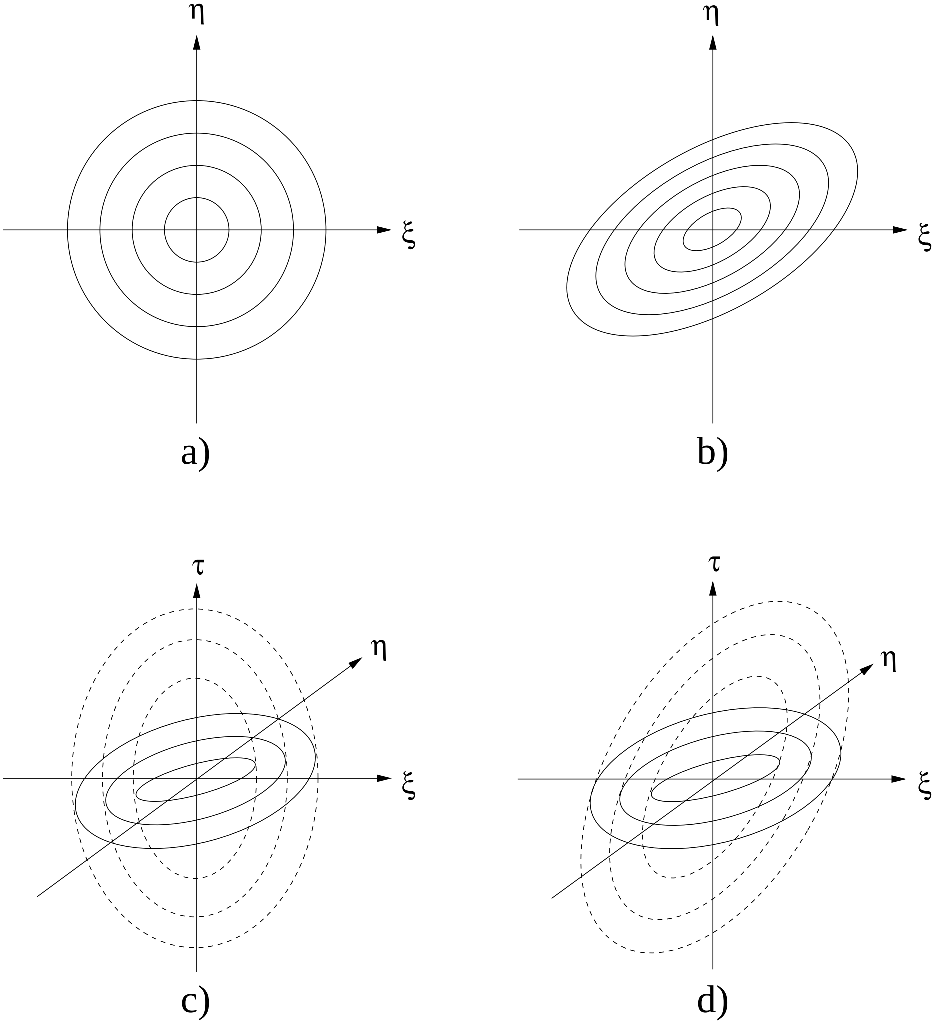

Figure 6.1: Contour plot of correlation functions for various diffraction patterns. a) stationary, non-changing, isotropic pattern, b) stationary, non-changing, anisotropic pattern, c) stationary, randomly changing, anisotropic pattern, d) moving, randomly changing, anisotropic pattern

decrease in spatial correlation function with increasing separation. Hence Equation 6.3 can be extended to give,

$$\rho(\xi, \eta, \tau) = \rho(A\xi^2 + B\eta^2 + K\tau^2 + 2H\xi\eta). \tag{6.4}$$

The correlation function is now a family of ellipsoids in (ξ, η, τ) space, (see Figure 6.1c). There is no tilt with respect to the τ axis as this would imply the pattern was non-stationary. By using Equation 6.4, we assume that the temporal and spatial correlation have the same functional form, although we do not assume what the actual form is. This assumption regarding the temporal and spatial correlation is considered the weak point of FCA. *Baker* [1980] found solutions using spaced sensor measurements that gave non-ellipsoidal results for the spatial-temporal correlation function, implying that the temporal and spatial correlation functions were not always the same.

For a moving and randomly changing pattern we will consider the frame of reference moving with the pattern, with coordinate system given by (ξ', η', τ'). The correlation function of the pattern $f(\xi', \eta', \tau')$, is thus

$$\rho(\xi', \eta', \tau') = \rho(A\xi'^2 + B\eta'^2 + K\tau'^2 + 2H\xi'\eta'), \tag{6.5}$$

If the pattern is moving with a velocity $\vec{V} = (V_x, V_y)$ with respect to the coordinate system (ξ, η, τ), then the two coordinate systems are related by the transformation

$$\xi = \xi' + V_x t \tag{6.6}$$

$$\eta = \eta' + V_y t \tag{6.7}$$

$$\tau = \tau' \tag{6.8}$$

The spatial-temporal correlation function in the stationary frame of reference (i.e (ξ, η, τ)) can be written as

$$\rho(\xi, \eta, \tau) = \rho(A(\xi - V_x t)^2 + B(\eta - V_y t)^2 + K\tau^2 + 2H(\xi - V_x t)(\eta - V_y t)) \tag{6.9}$$

This is of the form

$$\rho(\xi, \eta, \tau) = \rho(A\xi^2 + B\eta^2 + C\tau^2 + 2F\xi\tau + 2G\eta\tau + 2H\xi\eta). \tag{6.10}$$

The inclusion of factors involving $\xi\tau$ and $\eta\tau$, results in the ellipsoids being tilted with respect to the τ-axis, (see Figure 6.1d). The coefficients A, B, C, F, G, H fully describe the situation, along with the form of ρ.

To determine the two-dimensional horizontal wind we require a minimum of three antennas. The use of additional antennas would give over-determination of the parameters, which may improve overall accuracy and minimize errors. By calculation of the auto- and cross-correlation functions of the time-series, we are able to determine

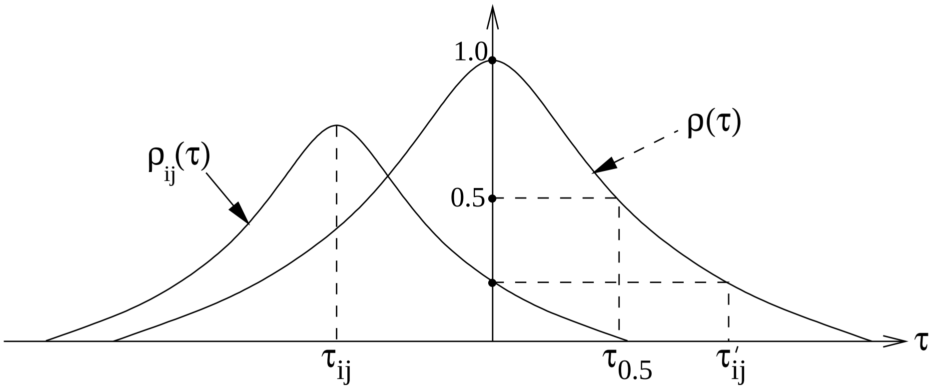

Figure 6.2: Representation of the auto- and cross-correlation functions, $\rho(\tau)$ and $\rho_{ij}(\tau)$, used for determination of the FCA ellipsoid parameters. $\tau_{0.5}$ is the fading time, τ'_{ij} is the lag where the cross-correlation function is a maximum and τ_{ij} is the lag where the auto-correlation function is equal to the zero-lag cross-correlation function.

the ellipsoid parameters using Equation 6.10. See Figure 6.2 for a representation of the correlation functions.

The auto-correlation function for the time-series obtained from antenna i is given by,

$$\rho_i(\tau) = \rho(0,0,\tau) = \rho(c\tau^2), \tag{6.11}$$

while the cross-correlation function for the time-series obtained from antennas i and j with spatial separation (ξ_{ij}, η_{ij}) is given by,

$$\rho_{ij}(\xi_{ij}, \eta_{ij}, \tau) = \rho(A\xi_{ij}^2 + B\eta_{ij}^2 + C\tau^2 + 2F\xi_{ij}\tau + 2G\eta_{ij}\tau + 2H\xi_{ij}\eta_{ij}). \tag{6.12}$$

The auto-correlation function for each antenna is theoretically identical, although there are some statistical differences, hence the mean of the auto-correlation functions are used, denoted by $\rho(\tau)$. For ease in calculating the ellipsoid parameters, we define the following,

$$a = \frac{A}{C}, b = \frac{B}{C}, f = \frac{F}{C}, g = \frac{G}{C}, h = \frac{H}{C}\, and\, k = \frac{K}{C}. \tag{6.13}$$

The parameter τ'_{ij} defines where the cross-correlation function is a maximum,

$$\frac{\partial \rho_{ij}(\tau'_{ij})}{\partial \tau} = 0. \tag{6.14}$$

From (6.12) this can be written,

$$\tau'_{ij} = -f\xi_{ij} - g\eta_{ij}, \tag{6.15}$$

thus giving one solution for each antenna pairing. Due to the over-determination of f and g, a least-squares formulation is applied to obtain optimum values as well as estimates of errors. τ_{ij} defines the temporal lag where the auto-correlation function equals the cross-correlation function at zero lag,

$$\begin{aligned} \rho(\tau_{ij}) &= \rho_{ij}(\xi_{ij}, \eta_{ij}, 0) && (6.16) \\ \rho(C\tau_{ij}^2) &= \rho(A\xi_{ij}^2 + B\eta_{ij}^2 + 2H\xi_{ij}\eta_{ij}) && (6.17) \end{aligned}$$

Thus τ_{ij} is given by,

$$\tau_{ij}^2 = a\xi_{ij}^2 + b\eta_{ij}^2 + 2h\xi_{ij}\eta_{ij}. \tag{6.18}$$

The three cross-correlation functions each give a solution to (6.18), enabling determination of a, b and h. In practice, τ_{ij} is not calculated directly, instead τ''_{ij}, the lag where the auto-correlation function is equal to the maximum of the cross-correlation function, is calculated and τ_{ij} is given by [*Briggs et al.*, 1950],

$$\tau_{ij}^2 = \tau_{ij}'^2 + \tau_{ij}''^2. \tag{6.19}$$

From (6.13) all that is required to determine the ellipsoid parameters is the scale of the parameters (i.e. C), although this is somewhat arbitrary. The *fading time*, $\tau_{0.5}$, is defined to be where the mean auto-correlation function equals 0.5,

$$\rho(0, 0, \tau_{0.5}) = \rho(C\tau_{0.5}) = 0.5 \tag{6.20}$$

6.2 Physical parameters obtained from FCA

We now have a way, via the auto- and cross-correlation functions, to parameterize the spatial-temporal correlation function. The ellipsoid parameters can be used to determine several physical parameters including true and apparent velocities, a spatial description of the pattern (i.e. axial-ratio, axial-rotation and pattern scale) and mean lifetime of the pattern due to turbulence. These physical parameters can then be used to gain further knowledge about the form and type of scatter that produces the diffraction pattern.

The apparent velocity $\vec{V_a}$, which does not take into account any change or anisometry in the diffraction pattern, is calculated via the cross-correlation maximum time lags, τ'_{ij}, where the magnitude V_a and direction θ_a are given by

$$V_a = \sqrt{f^2 + g^2} \tag{6.21}$$

$$\theta_a = arctan(\frac{g}{f}). \tag{6.22}$$

The true velocity of the pattern includes the effect of random changes and anisometry in the diffraction pattern. BY equating coefficients of $\xi\tau$ and $\eta\tau$ in Equations 6.9 and 6.10

$$aV_x + hV_y = -f \tag{6.23}$$

$$bV_y + hV_x = -g, \tag{6.24}$$

the zonal and meridional pattern velocity V_x and V_y are obtained:

$$V_x = \frac{hg - bf}{ab - h^2} \tag{6.25}$$

$$V_y = \frac{hf - ag}{ab - h^2}. \tag{6.26}$$

The true velocity of the scatterers, and hence background wind, is given by

$$\vec{V_t} = \frac{1}{2}(V_x, V_y). \tag{6.27}$$

The factor of $\frac{1}{2}$ is due to the point source effect [*Briggs*, 1980].

6.2.1 Properties of the diffraction pattern

The spatial properties of the pattern can be described using the characteristic ellipse of the spatial correlation function, (i.e. where the correlation function equals 0.5). By using (6.20) the characteristic ellipse can be written as,

$$A\xi^2 + B\eta^2 + 2H\xi\eta = C\tau_{0.5}^2. \tag{6.28}$$

The minor axis r_{minor} of the characteristic ellipse, the axial ratio R_{ax} and the axial-orientation θ_{ax} of the major axis are given by (e.g. [*Holdsworth*, 1995]),

$$r_{minor} = \sqrt{\frac{2\tau_{0.5}^2}{a+b-r}}, \tag{6.29}$$

$$R_{ax} = \frac{a+b+r}{a+b-r} \tag{6.30}$$

and

$$\theta_{ax} = 0.5\, arctan\left(\frac{2h}{b-a}\right), \tag{6.31}$$

where

$$r = \sqrt{(a-b)^2 + 4h^2}. \tag{6.32}$$

The pattern scale $r_{0.5}$ is a measure of the average “radius” of the characteristic ellipse

$$r_{0.5} = \frac{r_{max}}{\sqrt{R_{ax}}}. \tag{6.33}$$

Since the diffraction pattern and the angular power spectrum form a Fourier transformation pair, the spatial properties of the diffraction pattern can be directly related to the angular spectrum of the returned energy (e.g. [*Briggs*, 1992]). Taking into consideration the beam patterns of the transmitting and receiving array, it is possible to extract the aspect-sensitivity function of the scatterers and hence deduce the degree of anisotropy of the scatter. A brief description of the theory and application of isotropic scatter determination is given in Section 5.5.2.

If there is no mean wind, or we are in the frame of reference moving with the background wind, then the width of the auto-correlation function $\tau_{0.5}$ is related to the turbulent motion by [*Briggs*, 1980],

$$v_o = \frac{\lambda\sqrt{2ln2}}{4\pi\tau_{0.5}}, \tag{6.34}$$

where v_o is the root mean square (RMS) velocity or random velocity of the scatterers. If there is a mean wind present, then the 'width' of the auto-correlation function is reduced, or the spectral width is larger (beam broadening). To account for the effect of the background wind we use the corrected fading time $T_{0.5}$, which is calculated from the auto-correlation function in the frame of reference moving with the background wind, i.e from Equation 6.4,

$$\rho(0,0,T_{0.5}) = \rho(KT_{0.5}^2) = 0.5. \tag{6.35}$$

Comparing (6.20) and (6.35), gives

$$\tau_{0.5} = T_{0.5}\sqrt{k}, \tag{6.36}$$

where

$$k = 1 - aV_x^2 - bV_y^2 - 2hV_xV_y. \tag{6.37}$$

Inserting $T_{0.5}$ in place of $\tau_{0.5}$ in (6.34) gives an estimate of the isotropic RMS velocity of turbulent motions.

In summary, the FCA uses the auto- and cross-correlation functions obtained from a minimum of three non-collinear antennas, which sample the diffraction pattern produced by scatterers in the atmosphere, to obtain a variety of measurements regarding the scatterers. A list of rejection criteria for applying FCA experimentally is given in *Briggs* [1984], with further refinements presented in *Holdsworth* [1995].

The selection of experimental parameters must be chosen such that a realistic range of measurements is achievable. Incorrect choice of parameters can result in biased results. The sampling time of the data set is particularly crucial when attempting to measure high-velocity winds. If the sampling time is too long, then the correlation functions will not be sufficiently resolved to allow precise measurements, resulting in an underestimation of the velocities when large velocities are present [*Holdsworth & Reid*, 1995*a*]. This underestimation of the velocities is in the form of a cut-off velocity. If no turbulence is present, this is given by [*Holdsworth & Reid*, 1995*a*],

$$V_{max} = \frac{4.8\lambda}{\delta t}\left(arcsin\left(\frac{1}{sin^2\theta_s} + \frac{1}{sin^2\theta_b}\right)^{-1/2}\right)^{-1}, \tag{6.38}$$

where δt is the sampling time, θ_s is the aspect sensitivity in degrees and θ_b is the beam-width in degrees. The inclusion of turbulence results in a decrease in V_{max}. This velocity cut-off behaviour was observed by other authors when the sampling time was too long, creating an artificial limit to the velocities that could be measured [*Low*, 1996].

FCA theory assumes that the signals and hence correlation functions are noiseless. In most operational situations this will not be the case, hence a method for removing the effect of the noise is required. The effect on the auto-correlation function will be to create a spike at zero-lag which must be removed by interpolation. The cross-correlation function will also have a spike at zero-lag if noise is present simultaneously in all receivers, (i.e. this would occur if lightning discharges are detected by the receivers). This spike will similarly need to be removed. After removal of the spikes, both the auto- and cross-correlation function will need to be re-normalized by the same factor. The factor used for normalization is chosen such that the auto-correlation function will be unity at zero-lag. The effect of noise is examined further in Section 6.5.

The method of zero-lag interpolation and the number of lags over which it is performed must be considered carefully. A four-lag sixth-order polynomial is considered optimal [*Holdsworth & Reid*, 1995*a*]. The use of greater than four lags provides no significant improvement, while the sixth-order polynomial fit minimizes any potential underestimation in the value of the correlation maxima. To derive the cross-correlation maxima ρ_{0ij} and corresponding lag times τ'_{ij}, a Gaussian is fitted to the cross-correlation function. The Gaussian fit should be limited to lags within the main lobe of the cross-correlation function, thus restricting the effect of the tails of the correlation function.

6.3 One Dimensional Model

Computer modelling can provide insight into the limitations of analysis techniques and associated assumptions within a controlled environment. Through systematic evaluation, differences in analysis techniques can be obtained under a variety of conditions.

The model described below simulates the one-dimensional random pattern of complex amplitude $E(x,t)$ produced by radar returns from atmospheric scatterers moving along the x-axis, with a systematic velocity v together with random motions. Following the assumptions of *Briggs* [1984], we assume that the conditions required for full correlation analysis (FCA) hold. Thus given the velocity of diffraction pattern V, the antenna spacing ξ_o, the pattern scale ξ_1 and turbulence (RMS velocity) v_o within the scatterers, the pattern at the antennas can be modelled. The technique used follows the one-dimensional model described in *Briggs & Vincent* [1992] for spaced antenna analysis in the frequency domain.

Since this method used a Gaussian correlation function the pattern lifetime is defined as where the auto-correlation function falls to a value of e^{-1} when $V = 0$, is given by

$$\tau_1 = \frac{\lambda}{2^{\frac{1}{2}} 2\pi v_o} \tag{6.39}$$

where λ is the radar wavelength. The observed fading period, defined as the lag where the auto-correlation function falls to e^{-1}, is given by

$$\tau_o = \left[\frac{V^2}{\xi_i^2} + \frac{1}{\tau_1^2}\right]^{-\frac{1}{2}} \tag{6.40}$$

The power spectrum, which is the Fourier transform of the auto-correlation function, is

$$W_{11}(f) = \frac{1}{\sqrt{\pi} f_o} exp\left[\frac{-f^2}{f_o^2}\right] \tag{6.41}$$

where

$$f_o = \frac{1}{\pi}\left[\frac{V^2}{\xi_1^2} + \frac{1}{\tau_1^2}\right]^{\frac{1}{2}} \tag{6.42}$$

The cross spectrum can be calculated by considering that the cross-correlation is a real symmetrical function centred on a time shift τ' and is given by

$$W_{12}(f) = W_{12} exp\left[\frac{-f^2}{f_o^2}\right] exp\left[i\phi_{12}(f)\right] \tag{6.43}$$

where

$$W_{12} = \frac{1}{\sqrt{\pi} f_o} exp\left[-\frac{\xi_o^2}{\pi^2 \xi_1^2 \tau_1^2 f_o^2}\right] \tag{6.44}$$

and $\phi_{12}(f)$ is the phase factor given by

$$\phi_{12}(f) = -\frac{2\pi\xi_o f V}{(V^2 + \frac{\xi_1^2}{\tau_1^2})} \tag{6.45}$$

The initial time-series is given by

$$x_1(t) = \int_{-\infty}^{\infty} A_1(f) exp(-i2\pi t f) df \tag{6.46}$$

where $A_1(f)$ is the amplitude spectrum given by

$$A_1(f) = \sqrt{W_{11}(f)} e^{i\phi_1(f)} \tag{6.47}$$

and $\phi_1(f)$ is random phase, $\phi \in [0, 2\pi]$, included because the power spectrum only contains information about the magnitude of the amplitude spectrum.

The second time-series is given by

$$x_2(t) = \int_{-\infty}^{\infty} F_2(f) exp(i\phi_{12}(f)) exp(-i2\pi t f) df \tag{6.48}$$

where $A_2(f)$ the amplitude spectrum for the second time-series is given by [*May*, 1988],

$$A_2(f) = \rho_m A_1(f) + \sqrt{1 - \rho_m^2} \sqrt{W_{11}(f)} e^{i\phi_2(f)}, \tag{6.49}$$

where $\phi_2(f)$ is random phase and ρ_m is the maximum value of the cross-correlation,

$$\rho_m = exp\left(\frac{-\tau_o \xi^2}{\xi_1^2 \tau_1^2}\right). \tag{6.50}$$

This gives a method to generate two time-series which represent sampling of a 1-dimensional diffraction pattern at two points, separated by distance ξ_o, which would be observed from specified parameters. The addition of random phase enables generation of a large number of time-series with the same parameters for the statistical evaluation of the retrieved parameters.

τ' can be calculated by fitting a Gaussian to the cross-correlation, giving the apparent velocity

$$V_a = \frac{\xi_o}{\tau'}. \tag{6.51}$$

A Gaussian fit to the mean of the auto-correlation functions is then used to calculate the time-lag τ_x where the auto-correlation function is equal to the zero-lag cross-correlation function. The true velocity of the diffraction pattern is thus given by

$$V = \frac{\xi_o \tau'}{\tau_x^2}. \tag{6.52}$$

6.4 Radar Backscatter Model

The "radar backscatter model" of *Holdsworth & Reid* [1995*a*] was used for generating model data where more than two receivers were desired. Only a rudimentary description of the model is provided. For a more in-depth discussion, the reader is directed to *Holdsworth* [1995], *Holdsworth & Reid* [1995*a*] and *Holdsworth* [1999*b*]. The actual modelling program which has undergone significant upgrades in the period from 1995 to 2000, was supplied by D. A. Holdsworth [1]. The only modifications made here were to the code for the initialization menus.

The model is based upon a volume scatter situation, where the volume containing atmospheric scatterers is illuminated by a transmitted radar pulse and the subsequent backscatter is sampled. The scatterers represent an aspect-sensitive region of refractive index and are advected by the background wind with contributions from turbulence and gravity wave motions. The model allows the inclusion of the effects of anisometric scatterers, velocity shear and variable lifetimes.

The geometry of the model is shown in Figure 6.3. The complex signal from all the scatterers are combined at each sampling point d_i. The signals at the ground incorporate the effect of transmitter and receiver polar diagrams, aspect-sensitivity of the scatterer and shape of the transmitted radar pulse. The "radar volume" is defined according to the "effective beam-width" θ_{max}, the width of the range gate δR_{max} and the range of the volume with respect to the antennas, R. The scatterers are situated in an "enclosing volume" with their positions initially random. With each iteration of the model, a sample of the resultant diffraction pattern occurs and the

---

[1] dholdswo@atrad.com.au

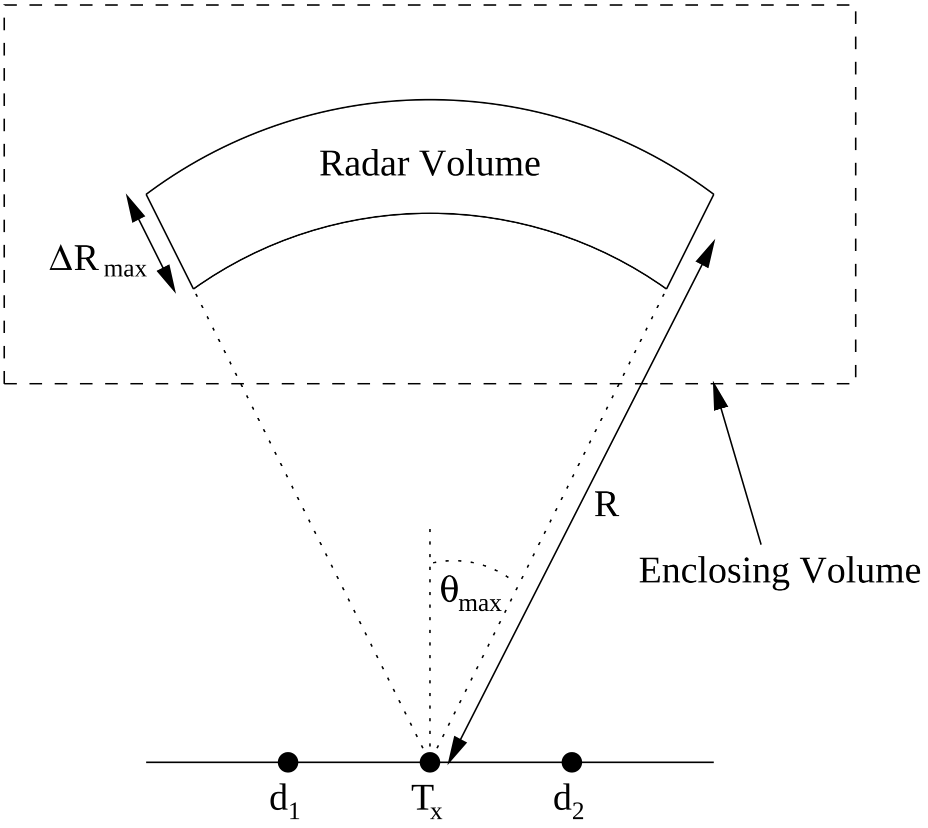

Figure 6.3: Illustration of the principles used in the *Radar Backscatter Model*, see text for description of parameters.

position of each scatterer is updated according to the effect of the background wind, turbulent motions and gravity wave perturbations. As individual scatterers exit the enclosing volume they are allowed to reappear on the opposite side in order to maintain a constant number of scatterers.

This model has been shown to simulate the characteristics of radar backscatter extremely well at a range of frequencies from MF to VHF [*Holdsworth & Reid*, 1995*a*]. Application of FCA to model data gives results in excellent agreement with the input parameters. The radar backscatter model has been used to investigate a number of practical aspects of FCA including the sampling time interval; interpolation and fits used in the analysis; noise [*Holdsworth & Reid*, 1995*a*]; and coarsely digitized data and receiver characteristic differences [*Holdsworth*, 1999*a*]. Application of other analysis techniques to the model data has been accomplished, enabling the ability to investigate and compare various spaced antenna (SA) techniques, a number of imaging interferometry techniques [*Holdsworth & Reid*, 1995*b*] and spatial correlation analysis (SCA) [*Holdsworth*, 1999*b*].

6.5 Sources of errors in Full Correlation Analysis

In Section 6.2 the effects of incorrect sampling parameters and fitting procedures on FCA were briefly discussed. In addition to these factors a number of other influences need to be considered.

Comparisons between the FCA derived "true" velocity magnitudes and those obtained via alternative techniques or alternative measuring devices have at times shown an underestimation in the FCA true velocity over a range of radar frequencies. At MF/HF *Golley & Rossiter* [1970] observed a decrease in FCA true velocity with decreasing antenna separation. Similar behaviour was observed earlier by *Kelleher* [1966] and became known as the "triangle size effect". Underestimations in the wind derived by the spaced antenna technique have been found in comparisons between VHF ST spaced antenna (SA) radars with radiosonde velocities [*Vincent et al.*, 1987; *Sharp & Reid*, 2000]; VHF Doppler beam swinging technique with spaced antenna observations [*Van Baelen et al.*, 1990]; a VHF meteor radar with nearby MF SA radar [*Cervera & Reid*, 1995]; VHF SA Boundary Layer Radar with radiosonde [*Vincent et al.*, 1998] and VHF SA Boundary Layer Radar with UHF wind profiling radar [*Baltink & Reid*, 2000]. Recent comparisons from an anemometer, measured winds with velocities from a UHF Spaced-Antenna array at 300 m showing an underestimation in the zonal-component [*Cohn et al.*, 2000]. It should be noted that comparisons of alternative techniques and apparatus with FCA have shown no apparent underestimations in wind measurements, demonstrating the validity of FCA and suggesting experimental equipment or other external causes for previous underestimations [*May*, 1993; *Sheppard et al.*, 1993].

The triangle size effect (TSE) previously mentioned, describes the decrease in FCA true velocity with a decrease in spacing between antennas, together with a decrease in corrected fading time $T_{0.5}$, pattern scale $r_{0.5}$ and a possible elongation in the characteristic ellipse along the long side if a non-equilateral triangle antenna arrangement is used. FCA attributes any decrease in correlation to time delay or spatial separation between measurements. Therefore, any additional attenuation of the calculated correlation functions may be incorrectly interpreted, causing an underestimation in the true velocity.

There are a number of suggested causes of TSE. Digitization noise and differing receiving channel characteristics were found to cause spatial correlation function to be extrapolated below unity at zero lag, thus causing TSE [*Golley & Rossiter*, 1970; *Brown & Chapman*, 1972]. Antenna coupling was also proposed as a cause of TSE. However, care should be taken as the sense of the bias is dependent upon the real component of coupling between the antennas. A positive real component will reduce the velocity while a negative component will result in an increase [*Fedor & Plywaski*, 1972].

The effect on the true velocity measurement if noise is not accounted for, is given by [*Meek*, 1990],

$$\frac{V_t'}{V_t} = 1 + \frac{2r_{0.5}' ln(N)}{d^2 ln(2)}, \tag{6.53}$$

where V_t is the underestimated measured true velocity, V_t' and $r_{0.5}'$ are the correct true velocity and pattern scale respectively, d is the antenna spacing and N is the noise factor.

Equation 6.53 can be extended to any situation where the cross-correlation functions are attenuated by a factor ρ_0, where N is now given by [*Holdsworth*, 1999*a*],

$$N = \frac{-\rho_0}{1-\rho_0}. \tag{6.54}$$

Previous investigations using the "radar backscatter model" have confirmed or introduced the following sources of TSE: receiver characteristic differences; antenna coupling; non-application of noise correction to correlation functions; coarse digitization; receiver saturation and antenna characteristic differences [*Holdsworth*, 1999*a*]. In many situations it may not be possible to isolate individual causes.

Coarse digitization and receiver saturation can be detected and, by modifying the operating parameters, they can in principle be eliminated. However, the large variability in echo dynamic range, which can be observed with changes in altitude, usually mean that a compromise is required (see Figure 6.4).

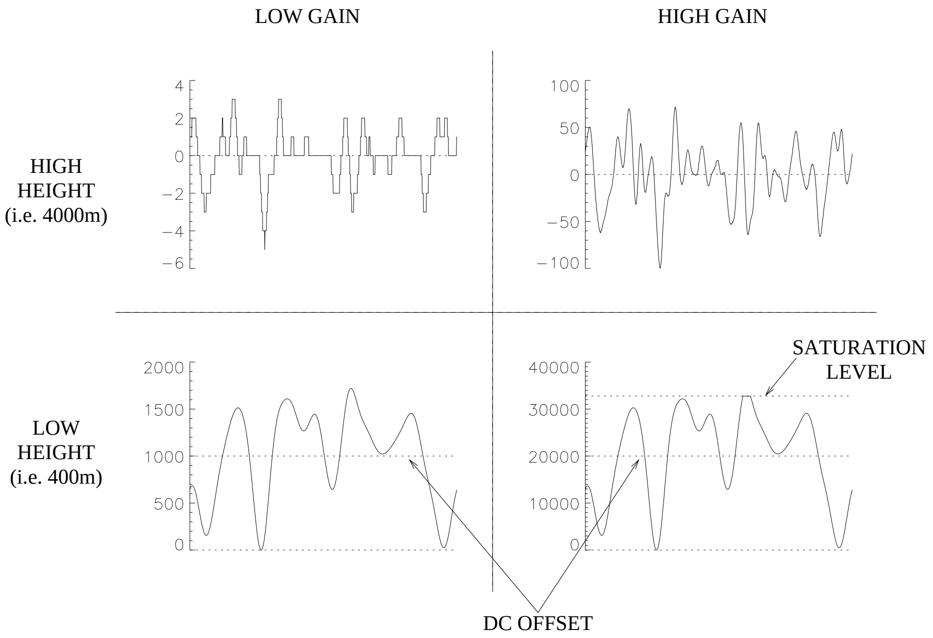

Figure 6.4: Gain effect on time-series with low dynamic range (high height) and large dynamic range with a DC offset (low height). Saturation level is the receiver's dynamic range limit. For simplicity only the real part (in-phase) of the time-series is shown

In order to obtain successful measurements from higher heights, the gain of the receivers must be set sufficiently high. However, this may cause the receiver to be saturated at the lower heights. Alternatively, a background DC-offset in the receivers, due to slow fading ground clutter, can be present at the lower heights. Therefore any increase in gain will increase the level of offset and decrease the dynamic range available before saturation occurs.

Correct application of the noise correction to the correlation functions will remove noise as a source for TSE, except in cases of small SNR, where an overestimation can occur [*Holdsworth*, 1995]. The remaining sources of TSE are related to differences between receiving paths (i.e. antennas, receivers, cable lengths, etc.). While consideration in planning, construction and tuning of components can initially reduce or eliminate the source, long term variability can become a concern as individual components age and deteriorate. One obvious example is the tuning of the antennas of the arrays, which are not only dependent to conditions at the time of tuning (i.e. moisture, temperature, etc.), but may deteriorate over time due to exposure to the elements.

Receiver-characteristic differences can be estimated by calculating the mean time-series at a specific height over a large period of time (see Section 6.6.2), however this is susceptible to any temporal variations in receiver characteristics.

Coupling between the receiver paths can be measured (see section 4.4.2) or modelled (see section 4.4.1). However, the complexity of coupling within an antenna array means that, even with this information, it would not be possible to counteract the coupling. By careful minimization of coupling between antennas during design and construction, the removal of coupling as a source of TSE should be possible.

Underestimation of the velocity by FCA can be due to processes other than the causes of TSE. Instrumental low-pass filters can cause an underestimation due to the loss of high-frequency information. A low-pass filter function can be written,

$$|Y(f)|^2 = \exp\left(\frac{-f^2}{f_o^2}\right), \tag{6.55}$$

where f_o is the cut-off frequency. The true velocity after filtering is given by [*Chandra & Briggs*, 1978],

$$V_{t(\text{filtered})} = V_t \left(1 + \frac{1}{\pi^2 f_o^2 T_{0.5}^2}\right)^{-1}. \tag{6.56}$$

The effect of the low-pass filter can be considered negligible if

$$f_o \gg \frac{1}{\pi T_{0.5}}, \tag{6.57}$$

(i.e. it is only significant if filtering removes the fading component with periods of the order of the corrected fading lifetime). Typical values for the corrected fading time obtained with the VHF BLR are $\sim$ 1s, therefore for low-pass filtering to be negligible it is required that,

$$f_o \gg 0.3\text{Hz}. \tag{6.58}$$

For the BLR, the Nyquist frequency used is typically 10 Hz, although values as low as 4.8 Hz are sometimes used (see Table 5.1). However, as both of these values are much greater than 0.3 Hz, low-pass filtering is negligible for the BLR.

High-pass filtering causes an overestimation of the velocity. It is only mentioned here for completeness; the reader is directed to *Chandra & Briggs* [1978] for more detail.

6.6 Instrument effects on BLR FCA

As shown in Section 5.3, comparisons between FCA true velocity obtained from the VHF BLR and radiosondes launched from Adelaide Airport show an underestimation in the radar velocities. The small antenna spacing implies TSE may be a cause of this underestimation.

The "One Dimensional Model" (see Section 6.3) and "Radar Backscatter Model" (see section 6.4) can be used to create time-series upon which the effects of antenna coupling, spatial averaging of the diffraction pattern and receiver-differing characteristics on FCA with differing parameters can be observed. The following analysis mainly deals with the BP Boundary Layer Radar with the antenna spacing remaining fixed, although other input parameters to the model, namely pattern scale, horizontal velocity, turbulence and aspect sensitivity are varied.

6.6.1 Coupling effects on FCA

Coupling between antennas depend upon their respective orientation. In general, the strength of the coupling increases with a reduction in antenna spacing, hence the potential for it being a source of TSE. The effect of coupling on FCA is dependent on the sign of the real component of the coupling coefficients. A positive component will result in a decrease in the measured true velocity, while a negative component will result in an increase [*Fedor & Plywaski*, 1972], where the coupling coefficient is given by,

$$\alpha = A + jB. \tag{6.59}$$

The coupling coefficients between antennas of the third generation array were determined via modelling (see Section 4.4.1), although actual measurements showed considerable variation in a narrow bandwidth around the operating frequency of 54.1 MHz, (see Figure 4.10). Due to the finite length of the transmitted pulse and subsequent finite receiver bandwidth, a range of frequencies centred around the operating frequency must be included into the coupling modelling. The largest coupling coefficient magnitude measured in the 4 MHz bandwidth, centred on the operating frequency, was 0.012, for the pairing of Yagi A and Yagi B, see Figure 4.10. Any value of coupling within the desired frequency range will therefore have a coefficient with magnitude less than 0.012. This limit can be used to gain a measure of the maximum possible effect coupling will have on the FCA true velocity.

Results from application of the one-dimensional model are shown in Figure 6.5, with values expressed as a percentage difference between the calculated FCA true velocity with coupling and the velocity calculated without coupling.

Velocity and turbulent velocity parameters were varied during the investigation, with ten cycles being performed for each combination of parameters. Using these ten values, the mean value for each particular combination was calculated after any outlying points were removed. The number of successful measurements for low velocities (i.e. 5 ms^{-1}) and high turbulent velocities (i.e 1 ms^{-1}) was low due to the large variance created by a relatively large turbulent velocity compared with the background velocity. This low success rate can be seen in Figure 6.5, where the distribution of coupling coefficients for a velocity of 5 ms^{-1} and turbulent velocity of 1 ms^{-1}, is significantly broader than the remaining distributions.

The trend of the values agree with results obtained by *Fedor & Plywaski* [1972]. The imaginary component has negligible effect, while the calculated velocity decreases for a positive real component and increases for a negative real component. For the VHF BLR, the maximum effect of coupling between antennas on the FCA true velocity

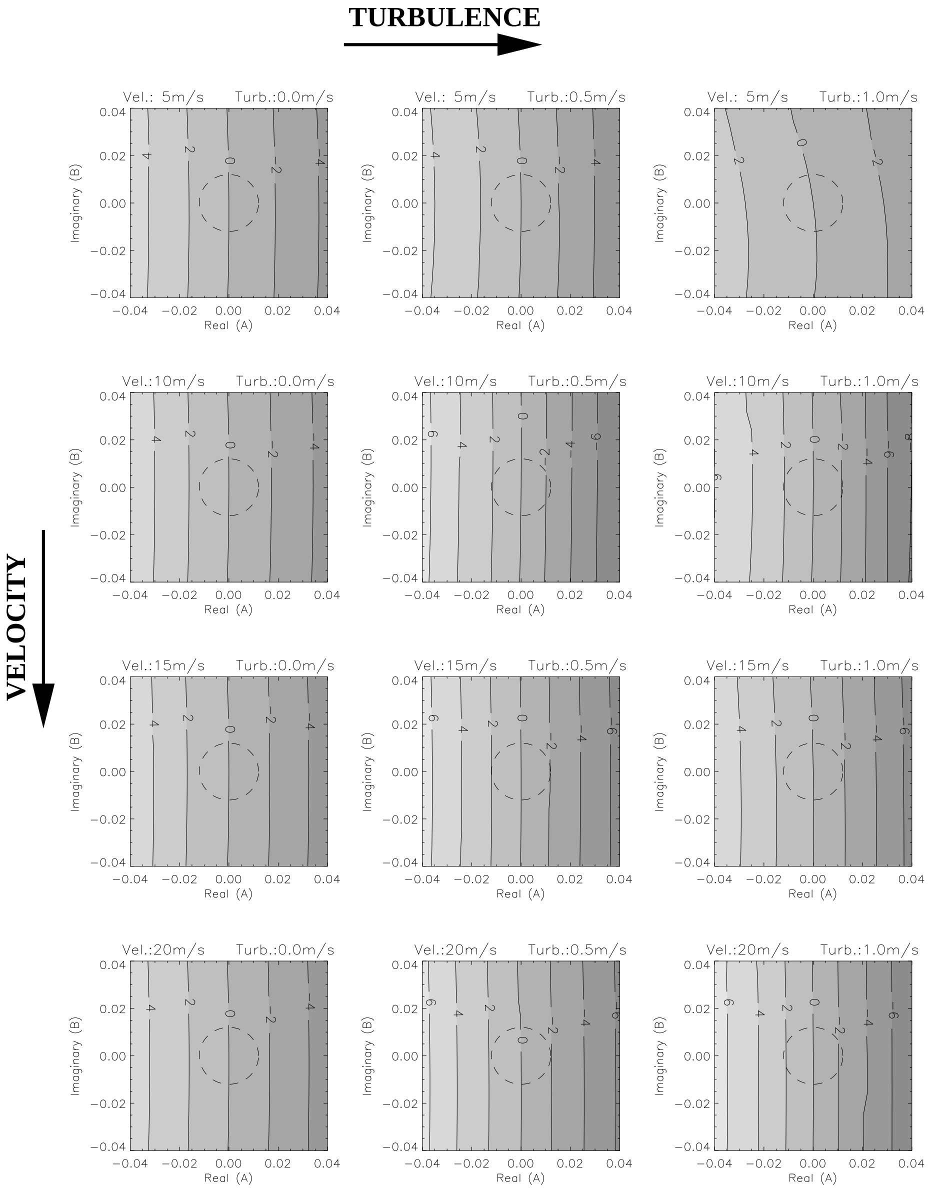

Figure 6.5: The effect of coupling on FCA true velocity. Values shown are the percentage differences from the actual velocity. The behaviour as a function of real and imaginary components of the coupling coefficient is shown for various velocities and levels of turbulence. The dashed circle represents the maximum expected level of coupling for the VHF Boundary Layer Radar.

will be $\sim 2\%$, and is independent of the actual velocity or level of turbulence.

6.6.2 Receiver characteristics effect on FCA

A very slow fading background signal had been observed at the lowest heights since the initial inception of the system in 1997. To remove this background signal, a first-order polynomial, which was fitted to the data, was removed from the time-series. The application of higher-order polynomials was tried, but this often introduced undesirable behaviour, especially at the edges of the time-series. The first-order polynomial fit was chosen as a compromise, although it should be realized at times this fit will not be sufficient to remove the background signal and at other times it may introduce additional background signal.

The source of the background signal was interpreted to be due to either ground clutter or a non-constant DC offset in the receivers. As any constant DC offset is removed by phase-flipping alternate transmitting pulses [*Röttger*, 1989].

In order to determine the source and strength of the background signal, a daily average of the time-series at each height and each receiver was calculated, (Figure 6.6). If ground clutter was the only source of the background signal then the average time-series would be zero. However, as is shown in Figure 6.6, the in-phase and quadrature components exhibit non-linear characteristics (i.e. in-phase component of receiver 3 at 300 m), thus implying the addition of a non-linear trend (or offset) to the time-series was occurring.

The importance of this trend depends upon the relative magnitudes of the dynamic range of the time-series, compared with the magnitude of the trend. Typical dynamic ranges for the BLR, (measured in digitized units), obtained from 300 m and 500 m are $\sim 100 - 300$, compared with offset values of $\sim 20 - 40$ (ie $\sim 10\% - 40\%$).

The stability or consistency of the trend over time has two major consequences. If it is indeed very stable, it would be possible to remove its effect via simple subtraction of a known background behaviour. Conversely, if it does vary with time, the averages shown in Figure 6.6 will be underestimations of the offset, due to averaging.

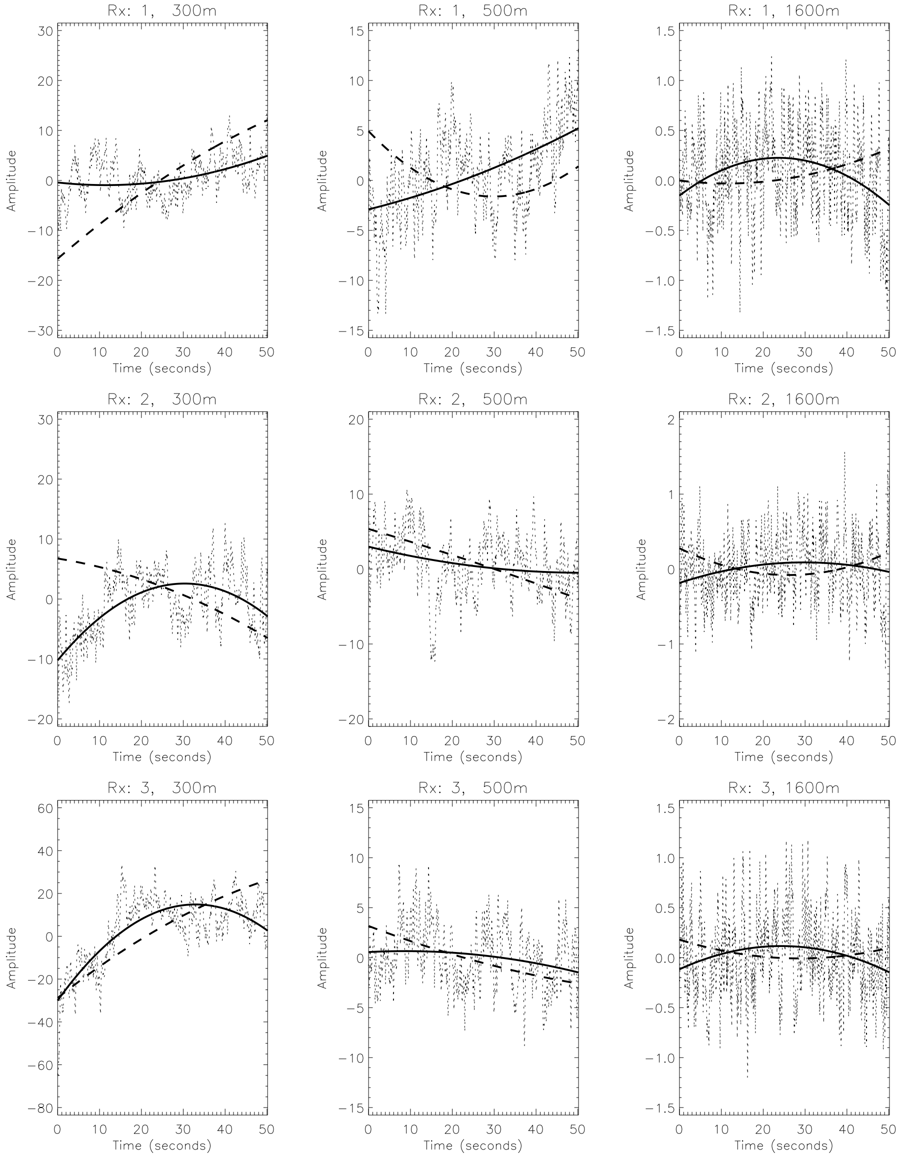

Figure 6.6: Average time-series for each receiver for the entire day of 14 October 2000. In-phase component of time-series and a second-order polynomial fit are shown in the solid line, the dashed line is a similar fit to the quadrature component (quadrature component not shown). Heights shown are 300, 500 and 1600 m

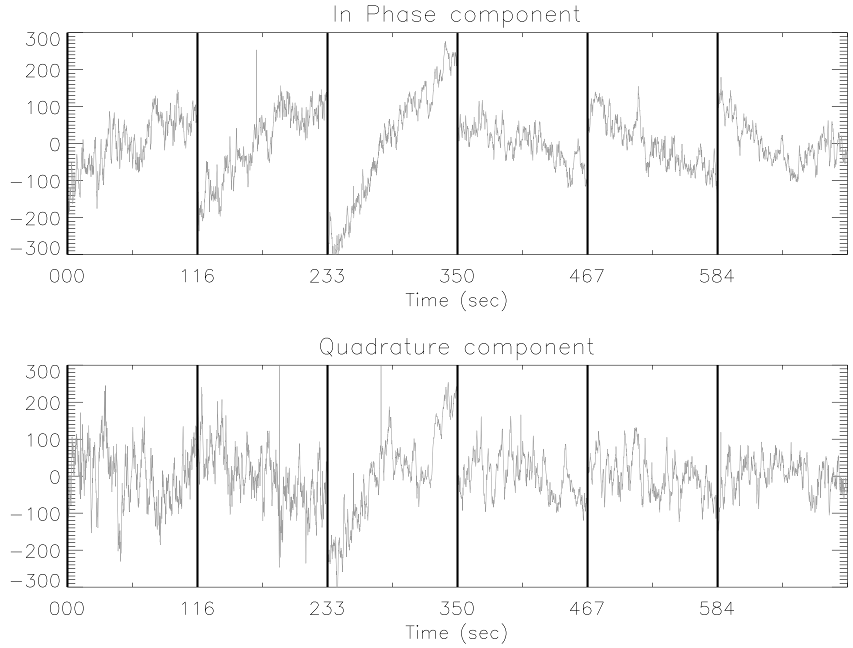

Figure 6.7: Six consecutive time-series from 300 m starting 0259 UTC, 14 October 2000. In-phase (top) and quadrature (bottom) components shown separately.

Observations of six consecutive time-series, shown in Figure 6.7, imply the offset can vary dramatically with time. The third times-series in Figure 6.7 has an offset several times greater than the dynamic range of the actual time-series (once the offset is removed). Hence, the trend varies with time and can be very substantial compared with the times-series. This implies attempts to remove its effects will require a different fit applied to each time-series.

Using the one-dimensional model, the effect of the addition of a background trend to the time-series was simulated and results quantified. Even though the receiver magnitude characteristics, shown in Figure 6.6, can be non-linear, only linear offsets were considered for two reasons. Firstly, by using only a linear trend it is possible to gain a qualitative feel for the more complex offset effect. Secondly, to remove very slow fading clutter, a linear fit has been applied to the data in the past. In certain situations this may contaminate and bias the time-series. The basic concept of the linear fit used is shown in Figure 6.8, where the trend δ is given as a fraction of the dynamic range of the initial time-series.

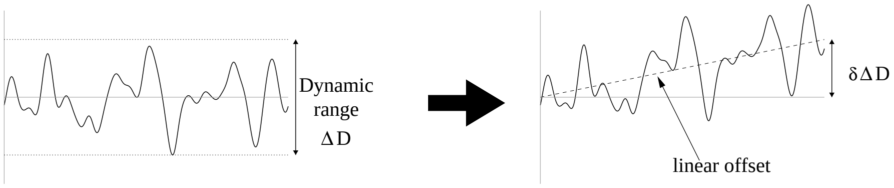

Figure 6.8: Illustration of the addition of a linear fit to a time-series. Where the actual height of the offset slope is $\delta\Delta D$

The effect of varying δ on the correlation functions is shown in Figure 6.9. The offset can be considered as adding a very slow fading contribution to the time-series. As the "magnitude" of the offset increases, the width of the auto-correlation function increases and a "floor" is added to the auto-correlation. The addition of the "floor" is especially apparent as δ increases and the attenuation of the cross-correlation increases.

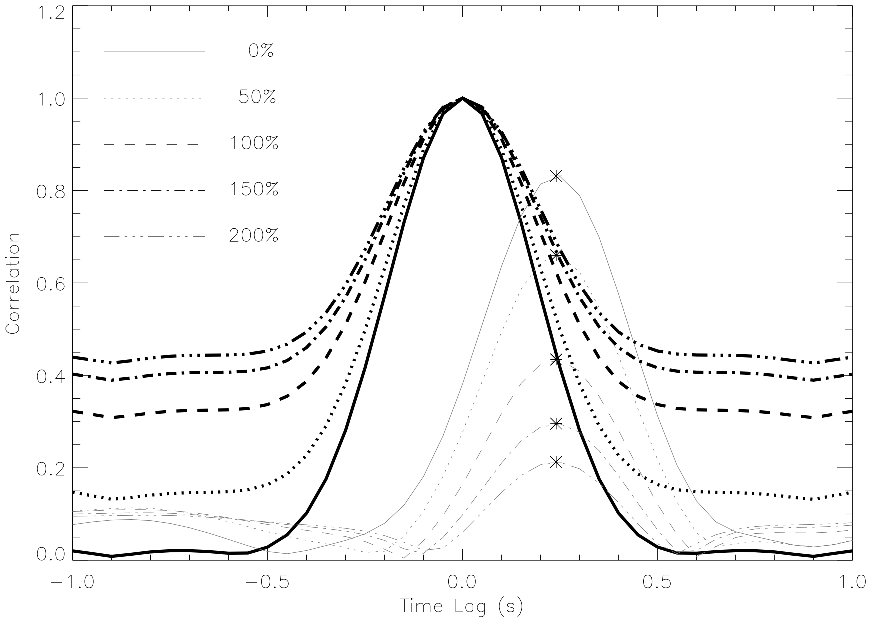

Figure 6.9: The effect of receiver differences on auto-(black) and cross-correlation (grey) functions due to the linear offset δ. The cross-correlation function peak is denoted by (*)

The effect of the δ is illustrated in Figure 6.10, where the error in velocity as a function of δ, is given for a range of initial velocities. The results imply the underestimation will increase with an increase in background velocity, along with an increase in δ.

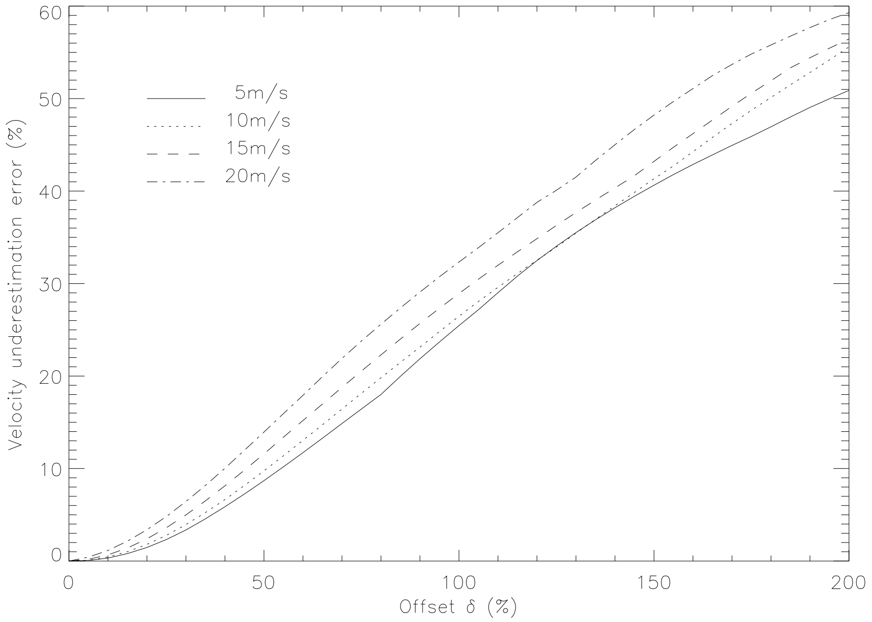

Figure 6.10: Effect of linear offset applied to one of the time-series used in application of FCA to model data, with model input velocities of 5, 10, 15 and 20 ms^{-1}.

From Figure 6.10 it can be seen that underestimations of $\sim$10% require values of δ being $\sim$ 50%, although as the background velocity increases, smaller values of δ are required. It should be noted, that as a first-order polynomial is fitted to the data, it is extremely unlikely such high values of δ would occur in analysis of real data.

6.6.3 Effect of spatial averaging on FCA

FCA treats the measurement made by each array as if it was a sample of the diffraction pattern made at a single point. However, with an array of antennas, the measurement is actually a combination of samples made at multiple points, which are electronically combined. To observe the effect of spatial average on FCA, the time-series initially obtained at each of the 27 Yagi positions (see Figure 3.11), were created via modelling. A linear combination of the nine time-series corresponding to a single receiving array was employed, thus giving a final output of three time-series representing each receiving array. The time-series representing the Yagis at the centre of each receiving array were used to represent the non-spatially average time-series (labelled *normal*).

However, the one-dimensional model can not be extended to more than two antennas as it assumes statistical behaviour to create the second time-series with respect to the first. Any additional time-series created, using the one-dimensional model, would have the desired correlation with the primary time-series, but may have very little correlation with other secondary time-series, despite the potential for them to be spatially close. Hence for modelling spatial averaging effects the "radar backscatter model" was used. FCA was performed on both time-series and the results were compared.

Comparisons between normal and spatially averaged FCA output parameters are given in Figures 6.11, 6.12 and 6.13, where the effects produced by different input parameters (i.e. velocity, turbulence and aspect sensitivity θ_S) are illustrated. The input values were 5, 10, 15, 20 ms^{-1} for velocity, 0.0, 0.5, 1.0, 1.5 ms^{-1} for turbulence and 10°, 20°, 30° for aspect sensitivity, with each possible combination of input values repeated ten times.

Examining Figures 6.11, 6.12 and 6.13, shows that there is no bias in the FCA true velocity for all variations of input parameters. A very slight bias was observed in the apparent velocities for all input velocities, which increased with increases in the turbulent velocity. The dependence of corrected fading time on input velocity (see Figure 6.11) and pattern scale (see Figure 6.13) was unexpected as the corrected fading time should only be dependent upon the degree of turbulence, (see Equation 6.39). Simulations using the one-dimensional model where the input-velocity and turbulence were varied, found no bias (see Figure 6.14). Neither did simulations where input-velocity and pattern scale/aspect sensitivity were varied (see Figure 6.15).

The discrepancies between the two models arise from the differences in methods used to create the simulated time-series. The one-dimensional model assumes certain

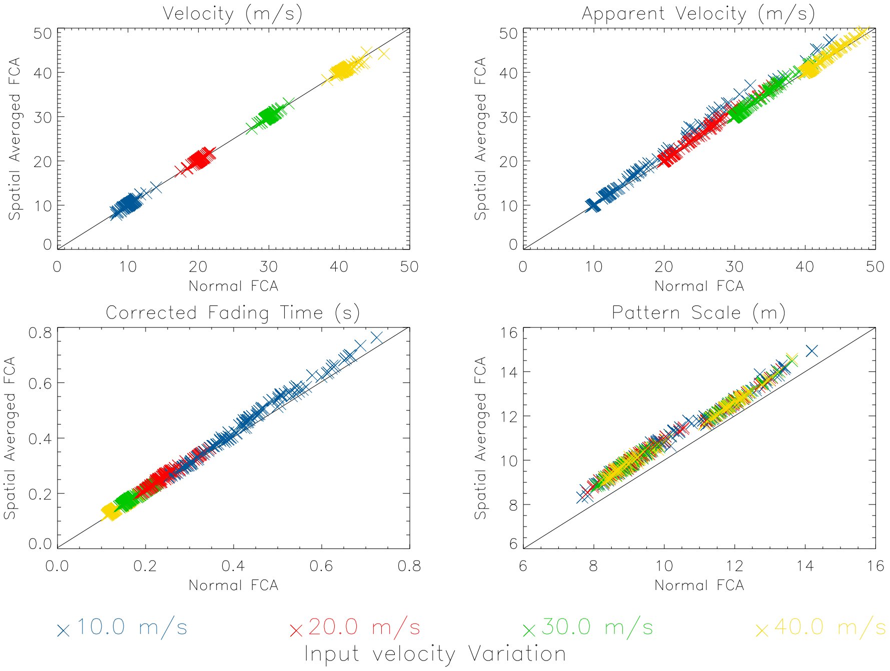

Figure 6.11: Spatial averaging effect on FCA derived parameters (i.e true velocity, apparent velocity, corrected fading time and pattern scale) from modelled data created using the “radar backscatter model” (see text). Parameters used in model were 10, 20, 30, 40 ms^{-1} for velocity, 0.0, 0.5, 1.0, 1.5 ms^{-1} for turbulent velocity and 10, 20, 30° for aspect sensitivity θ_S. All combinations of these input parameters are shown with emphasis on velocity input parameters (i.e. 10 ms^{-1} (blue), 20 ms^{-1} (red), 30 ms^{-1} (green) and 40 ms^{-1} (yellow))

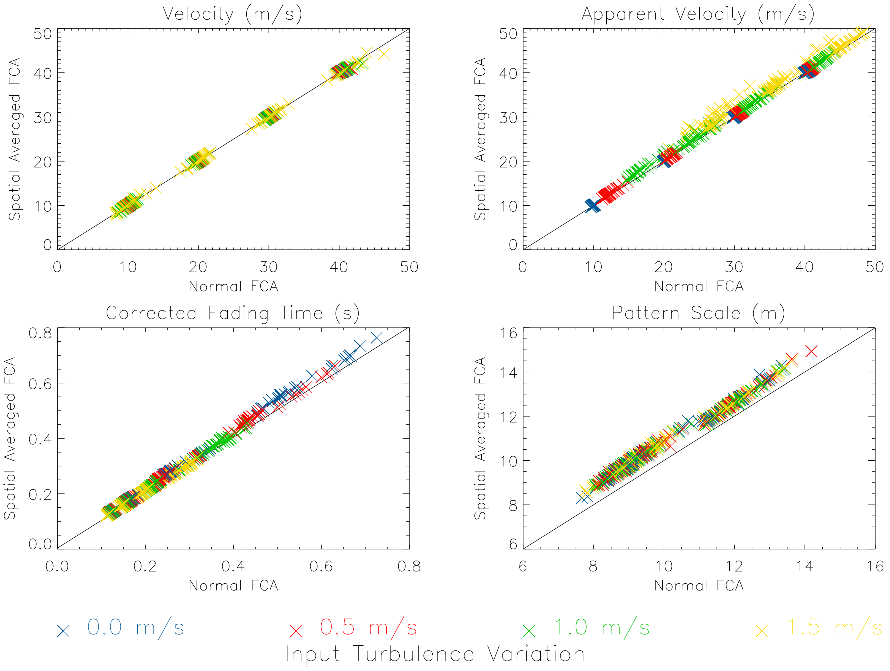

Figure 6.12: Same as Figure 6.11, except for varying turbulent velocity input parameters. (i.e. 0.0 ms^{-1} (blue), 0.5 ms^{-1} (red), 1.0 ms^{-1} (green) and 1.5 ms^{-1} (yellow))

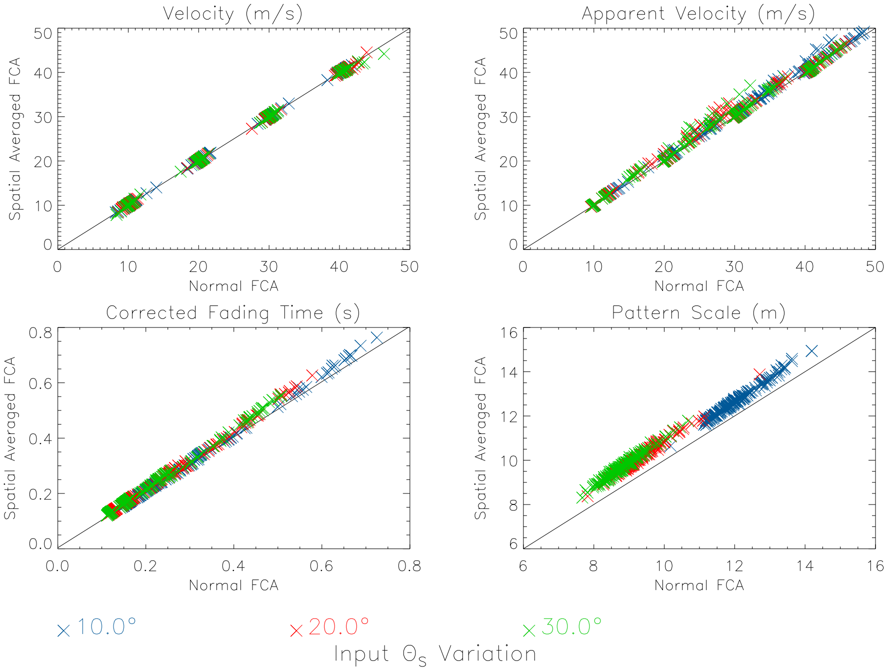

Figure 6.13: Same as Figure 6.11, except for varying aspect sensitivity input parameters. (i.e. 10° (blue), 20° (red) and 30° (green))

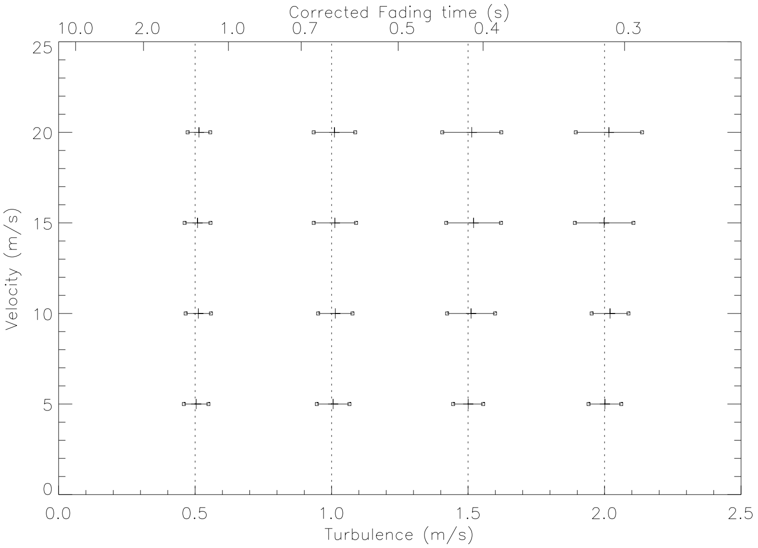

Figure 6.14: One-dimensional model results showing variation of measured turbulence (or corrected fading time) with input parameters being 0.5, 1.0, 1.5 and 2.0 ms^{-1} and background wind velocities of 5, 10 ,15 and 20 ms^{-1}. Corrected fading time was calculated from FCA principle. Error bars represent standard deviation found from 100 model runs for each combination of turbulence and velocity.

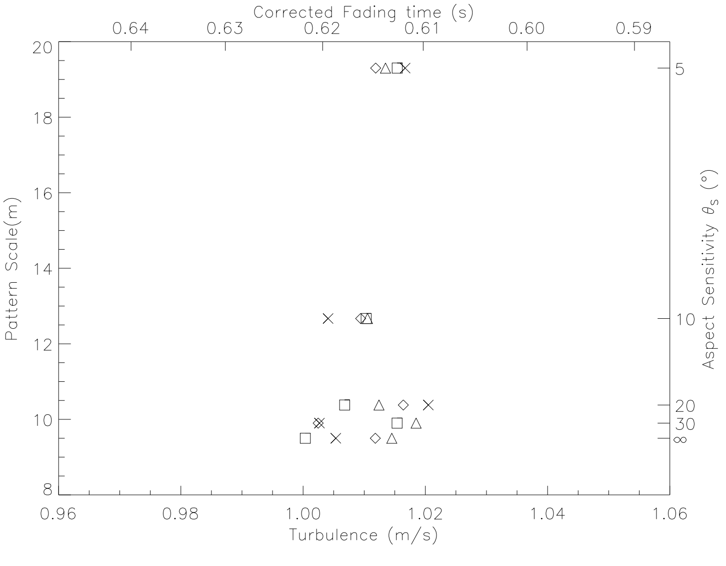

Figure 6.15: Turbulence (or corrected fading time) calculated via FCA from the one-dimensional model with fixing input turbulent velocity of 1 ms^{-1}, aspect sensitivities of 5°, 10°, 20°, 30° and ∞°, and background wind velocities of 5 ms^{-1} (diamond), 10 ms^{-1} (triangle), 15 ms^{-1} (square) and 20 ms^{-1} (cross).

statistical properties concerning the time-series with the fundamental concepts of the model based upon Full Spectral Analysis (FSA), which is the frequency equivalent of FCA. Any results would therefore be expected to comply with FCA theory, hence the absence of any bias in Figures 6.14 and 6.15. The "radar backscatter model" does not assume any properties based upon FCA (or any other analysis technique), but simulates the behaviour of the scatterers combined with the radar parameters (i.e. beam-width). The overestimation of turbulent velocities when using data from the "radar backscatter model" is most likely due to changes in the amplitude of the returns from individual scatterers due to the spatial power variation of the transmitting polar diagram [*Holdsworth*, 1995].

In Figure 6.16, a similar interdependence between velocity and turbulence with observations of data obtained using the BP VHF Boundary Layer Radar is presented. The simplicity of the direct comparison and the lack of consideration of other parameters implies its validity may be weak; however it is included for completeness.

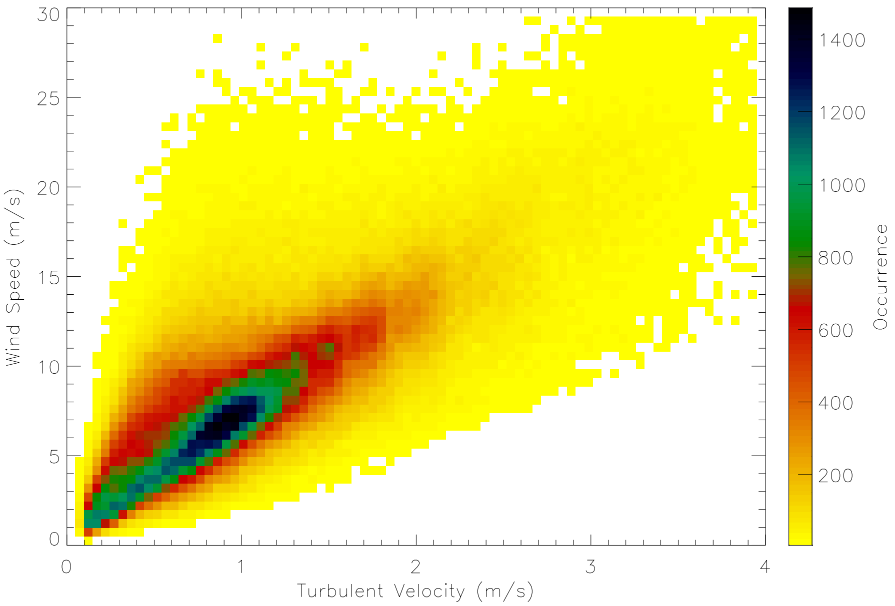

Figure 6.16: Histogram of wind speed and turbulent velocities from FCA analysis of data taken by the BP VHF Boundary Layer Radar during October 2000

The observed underestimation in pattern scale is not dependent upon velocity, turbulence or aspect sensitivity. The pattern scale is used to estimate the isotropy of scatter (see Section 5.5.2) thus, any underestimation in this parameter may result in incorrect assumption about the nature of the scattering mechanism being observed. Further investigation about the effect of spatial averaging upon the pattern scale is beyond the scope of this thesis.

6.7 Summary

In this chapter, the theory of Full Correlation Analysis and parameters obtained have been reviewed. Two methods of modelling time-series which are dependent on initial parameters were given. The application of the two models provided methods to observe the effect of potential sources of error in FCA derived parameters.

Antenna coupling, which can cause underestimation of FCA true velocities, was found to be negligible for the VHF BLR. Although the actual values of the coefficients are hard to quantify, a qualitative analysis found errors in the velocity would be at the most ∼2% and could be either underestimations or overestimations.

The effect of receiver characteristic differences upon FCA was also investigated. The addition of linear-offsets was found to cause underestimations in the radar derived wind velocity. The underestimation was amplified by increases in the background velocity or the slope of the linear-offset. The fitting and removal of a first-order polynomial to the time-series will remove the effect if the offset is purely linear, however, for non-linear trends some underestimation will still occur.

Spatial averaging, due to the combining time-series for a number of points, sampling the diffraction pattern at different locations, was found to have no effect on the FCA true velocity determination. However spatial averaging appeared to give an overestimation of the turbulent velocities, an effect that depended on the background wind. This overestimation was only present in the “radar backscatter model”, which was due to the inability of the one-dimensional model to account for the polar diagram of the antennas.

The results presented in this chapter emphasize the care and consideration required in designing, manufacturing and maintaining a VHF Boundary Layer Radar. Poor design or lack of maintenance can lead to differences in the receiving paths, which will cause increasing inaccuracies and underestimations in the FCA true velocity determination.

Chapter 7

Radio Acoustic Sounding System

As noted in Section 2.4.1 there are significant advantages in using RASS in conjunction with a VHF radar. A 'Radio Acoustic Sounding System' (RASS) consists of a wind profiling radar and an acoustic source used together to obtain the temperature profile of the atmosphere. The sound waves generated by the acoustic source modulate the atmospheric refractive index and produce artificial irregularities that scatter or reflect radio waves. Depending on the form of the acoustic excitation, the received echoes from the perturbations are Doppler shifted, to either the transmitted acoustic frequency, the Bragg frequency corresponding to the speed of sound or a combination of the two.

In this chapter, a brief overview of the history of RASS is presented together with the background theory and underlying principles. Potential sources of error in the temperature determination are detailed.

RASS observations were carried out with the BLR, with mixed results. It is shown that advection of the acoustic wavefront can severely limit the coverage obtained with a BLR RASS when only a few acoustic sources are used. In order to validate the methods and procedures being used in the BLR RASS, several trials involving larger VHF radars were performed. The larger radars were less susceptible to advection of the acoustic wave, which simplified investigations into the techniques being applied to the smaller BLR RASS.

Underestimations were observed in the temperatures derived using the BLR RASS, especially at the lower heights. However, comparisons with measurements of temperatures obtained using the large VHF radar/RASS and radiosondes were extremely good. The potential sources of the underestimations observed at the lower heights using a BLR RASS is discussed.

7.1 RASS Theory and Implementation

With a RASS, a radar measures the speed of propagation of acoustic disturbances created by a nearby acoustic source. The speed of sound measured at each height can be used to calculate the profile of virtual temperature, T_v.

Under the ideal gas law assumption the speed of sound c_s, through a standard dry atmosphere is given by [*North & Peterson*, 1973],

$$T = \frac{M_m}{\gamma R} c_s^2, \tag{7.1}$$

where T (K) is the temperature, M_m is the molecular weight of moist air, γ is the ratio of specific heats (≈ 1.4), and R is the universal gas constant ($= 8314.44$ J mol^{-1} K^{-1}). The molecular weight for moist air is given by,

$$M_m = M\left(1 - 0.378\frac{e}{p}\right), \tag{7.2}$$

where M is the molecular weight of dry air and e (hPa) is the partial pressure of water vapour. Replacing T with T_v in 7.1 gives,

$$T_v = \frac{M}{\gamma R} c_s^2 = \frac{c_s^2}{401.94}. \tag{7.3}$$

The RASS virtual temperatures can be derived using Equation 7.3, provided c_s is known.

Once the Doppler shift of the received signal has been measured, Equation 2.3 is used to determine c_s. However, the Doppler shift corresponds to the apparent measured acoustic velocity $\vec{c}_a$ which is the vector sum of the true sound velocity $\vec{c}_s$, and the motion of the ambient atmosphere $\vec{v}$,

$$\vec{c}_a = \vec{c}_s + \vec{v} \tag{7.4}$$

The measured Doppler shift c_a of the RASS echo is therefore the projection of $\vec{c}_a$ onto the antenna beam direction $\vec{n}$,

$$c_a = \vec{n} \cdot \vec{c}_s + \vec{n} \cdot \vec{v} \tag{7.5}$$

In order to determine the true acoustic velocity, the radial velocity of the atmosphere must be measured and accounted for. A radial velocity of 1 ms^{-1} will increase the inferred temperature by 1.7 K. Accounting for the vertical (radial) velocity has shown to improve the accuracy of derived temperature measurements [*May et al.*, 1989; *Angevine*, 1991; *Moran & Strauch*, 1994]. However, if substantial ground clutter is present and contaminates the vertical velocity estimate, improvement may not be possible for a RASS using radar beams pointed vertically [*Baltink*, 1998]. Computational limits in the past wind profilers have used a frequency offset to shift the RASS echo to near zero-frequency. This meant simultaneous measurements of acoustic velocity and radial wind velocity were not easily obtained. However, advances in computing power and signal processors means that time-series that have large Nyquist frequencies can now be obtained. This enables simultaneous measurements of clear air echoes (hence radial velocities) and rass echoes [*Angevine et al.*, 1994]. The increase in Nyquist frequency also reduces the amount of noise and interference that are folded into the clear air and acoustic spectral peaks, thus quality and accuracy of measurements is improved.

The upper limit of coverage of temperature profiles obtained with a RASS is predominately due to two effects. Firstly, if the acoustic wavelength λ_a is one half the RF wavelength λ_e, the energy reflected from each acoustic wavefront adds coherently at the receiver, thus the signal strength is increased. This is known as the *Bragg* effect,

$$\cos^{-1}(\vec{k_a}.\vec{k_r}) \approx 0, \tag{7.6}$$

where $\vec{k_a}$ is the acoustic wave number and $\vec{k_r}$ is the radial direction of the radar beam [*Matuura et al.*, 1986*b*]. For the Bragg effect to be satisfied at as many heights (and temperatures) as possible, a range of acoustic frequencies is required. Examples of the acoustic frequencies required for different radar frequencies are shown in Table 7.1.

Radar Frequency (MHz)	Acoustic frequency (Hz) -60°C (213 K)	0°C (273 K)	40°C (313 K)
44.75	87	99	106
54.1	106	120	128
400	781	884	947
1000	1953	2211	2367

Table 7.1: RASS acoustic frequencies required for different radar operating frequencies, for different atmospheric temperatures.

Secondly, the curvature of the acoustic waves create a focusing effect, that causes the reflected electro-magnetic waves to be concentrated into a small spot [*Clifford et al.*, 1978]. The size of the focussed 'spot' is determined by whichever beam of the acoustic source and radar is the narrower. [*Clifford et al.*, 1978]. If the radar beam-width θ_e, is smaller than the acoustic beam-width θ_a, then the spot size (3-dB points) ρ is equal to the effective antenna radius a_e. If the $\theta_a < \theta_e$ then $\rho = 2a_a$, where a_a is the effective acoustic source radius.

RASS techniques were first attempted in the early 1960's using a $\sim$ 10 GHz radar. However the high acoustic frequencies (22 kHz) suffered from strong attenuation, which limited the maximum height of observations to less than 30 m [*Marshall et al.*, 1972]. The first successful measurements using the RASS technique occurred in the early 1970's, where a 36.8 MHz radar designed for observations of ionized meteor trails in the upper atmosphere was used, [*Marshall et al.*, 1972; *North & Peterson*, 1973]. Temperature profiles up to ~3.0 km were obtained using the above system in very light wind conditions, however, stronger winds limited the maximum height coverage to ~800 m. The maximum range at which temperature profiles can be obtained with a RASS has been greatly extended with the use of beam steering techniques, with measurements to altitudes greater than ~20 km being obtained by the MU radar in Japan [*Matuura et al.*, 1986*b*; *Takahashi et al.*, 1988] (see Figure 7.1).

The maximum range is significantly less for typical wind profilers, which utilize a vertical beam for RASS measurements. The maximum altitude achieved for large

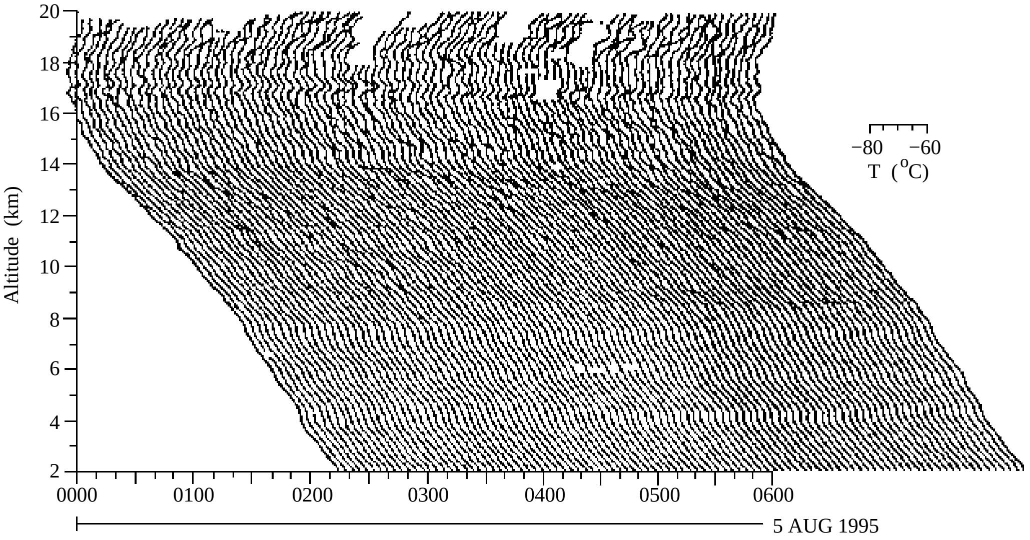

Figure 7.1: Temperature profiles obtained by MU radar-RASS observations for six hours on August 5, 1995. The observation interval was 3.6 min. (Adapted from *Arikawa et al.* [1998])

VHF arrays used for stratosphere-troposphere observations is 5-9 km, although this depends upon background atmospheric conditions [*May*, 1988]. A high frequency (HF) radar/RASS operating at 18.8 MHz has achieved measurements of temperatures up to 6.0 km, with good agreement in comparisons with temperatures obtained by nearby radiosonde soundings [*Rapoport et al.*, 1996].

7.1.1 RASS Limitations

The performance of a RASS is restricted by atmospheric conditions and operating parameters. The higher acoustic frequencies used for UHF RASS are strongly attenuated by the atmosphere ($\sim$10 dB km^{-1}), therefore measurements are limited to 1.5 - 2.5 km for $\sim$400 MHz radars and 0.7 - 1.5 km for $\sim$1 GHz profilers [*May*, 1988], while the acoustic frequencies corresponding to a VHF RASS have negligible attenuation.

The acoustic wavefront is advected by the background wind and distorted by turbulence and vertical gradients in the wind, humidity and temperature. Horizontal advection of the wavefront means that the ‘spot’ will move with respect to the antennas. This is the main restriction on the height coverage of VHF RASS [*Peters et al.*, 1983], although this effect can be reduced by steering the radar beam so that it follows the effective backscatter region [*Matuura et al.*, 1986*b*].

Turbulence, especially in the boundary layer, acts to distort the acoustic wavefront, causing the spot to broaden [*Lataitis & Clifford*, 1996]. At UHF, the broadening of the spot results in measurements being obtained from double the range expected by simple ray tracing calculations alone [*May et al.*, 1996]. Evidence of increased relative power away from the centre of the main lobe of the antenna pattern, with an increase in height, has been observed [*May et al.*, 1996]. The spot consists of an intense echo region, approximately half the size of the transmitting array, surrounded by a region of weaker intensity [*May et al.*, 1996]. Errors as large as 1°C can occur if the RASS spot is displaced off the radar centroid; this effect is especially important at lower heights [*Peters & Kirtzel*, 1994].

Temperature gradients (and humidity gradients to a lesser extent) alter the shape of the acoustic wavefront as it propagates. If the temperature gradient and horizontal velocity shear are constant, then the acoustic wavefronts are ellipsoids, with the major axis tilted leeward[1] [*Takahashi et al.*, 1988]. The dependence of the maximum height coverage r_{max}, on the acoustic velocity (or temperature) gradient C', wind velocity gradient U', and effective antenna diameter D, is defined as [*Masuda*, 1988],

$$r_{max} = 0.36\left(D\left|\frac{C'}{U'}\right|\right)^{\frac{1}{2}} \tag{7.7}$$

Horizontal velocity ‘leakage’ can create further complications. If $U' < C'$ then the effective backscatter region is produced upwind of the antennas, slanted from the vertical direction [*Masuda*, 1988] (Figure 7.2).

If the radar used has a large beam-width then a substantial component of the horizontal velocity from upwind will contribute to the apparent measured acoustic velocity (Equation 7.5). This effect is analogous to the effect of tilted refractivity

---

[1] On or toward the side to which the wind is blowing.

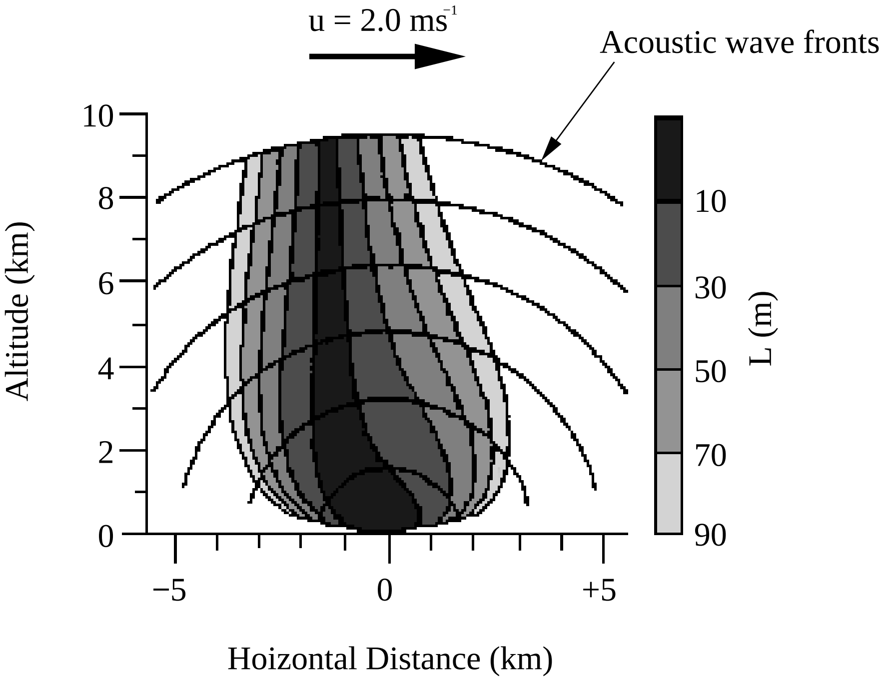

Figure 7.2: Vertical cross-section of effective backscatter region, where $U' < C'$ (here a constant background wind of 2 ms^{-1} is shown). The regions are shown by shaded contours as a function of L (m), the distance between the centre of the radar antenna and the intersection of the normal to the acoustic wavefront and the ground (adapted from *Adachi* [1996])

.

surfaces on standard Doppler measurements [*Palmer et al.*, 1991]. To correct for this effect, the apparent beam direction, $\vec{n}_a$, must be used in place of the actual beam direction in Equation 7.5.

An underestimation in the acoustic speed and temperature will occur if this contribution is unaccounted for. In the lower troposphere the lapse rate is typically $\sim$ 6 K km^{-1} [*Houghton*, 1986], therefore if U' is less than 3.5 $\mathrm{ms}^{-1}\mathrm{km}^{-1}$ temperatures will be underestimated.

The RASS-measured temperature at a given range gate represents the mean value of the sampling volume, which is weighted by the reflectivity [*Angevine & Ecklund*, 1994]. This effect is especially apparent at the lowest heights, where the recovery of the receivers can create a significant gradient in the reflectivity profile [*Görsdorf &*

Lehmann, 2000] (Figure 7.3).

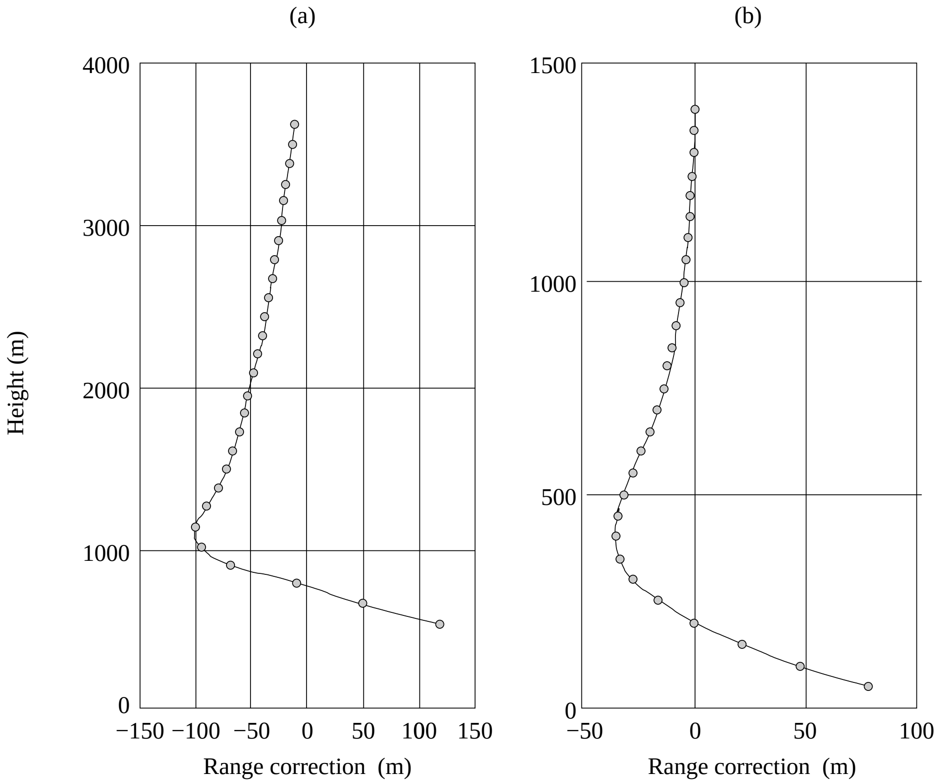

Figure 7.3: Mean range correction due to the reflectivity weighting for wind profiling radar/RASS operating at (a)482 MHz and (b)1290 MHz (adapted from *Görsdorf & Lehmann* [2000])

7.1.2 Acoustic excitation

Either fixed frequency or frequency modulated acoustic sources are used, as summarized below. For further information refer to *May et al.* [1990].

For fixed-frequency excitation the length of the acoustic pulse relative to the radar pulse, determines the frequency of the reflected signal. If a continuous-wave (CW), acoustic source is used (Figure 7.4(a)), then the signal reflected only contains the frequency of the initial acoustic source. If a short acoustic pulse is used (Figure 7.4(b)) then the signal will consist of the Bragg (acoustic velocity) frequency. A long-acoustic pulse, which overlaps the radar sampling volume (Figure 7.4(c)), will produce two peaks; one at the acoustic frequency and the other at the Bragg frequency. Modulation of a range of frequencies (Figure 7.4(d)), produces a sharp peak at the Bragg frequency, provided the correct sweep parameters are chosen .

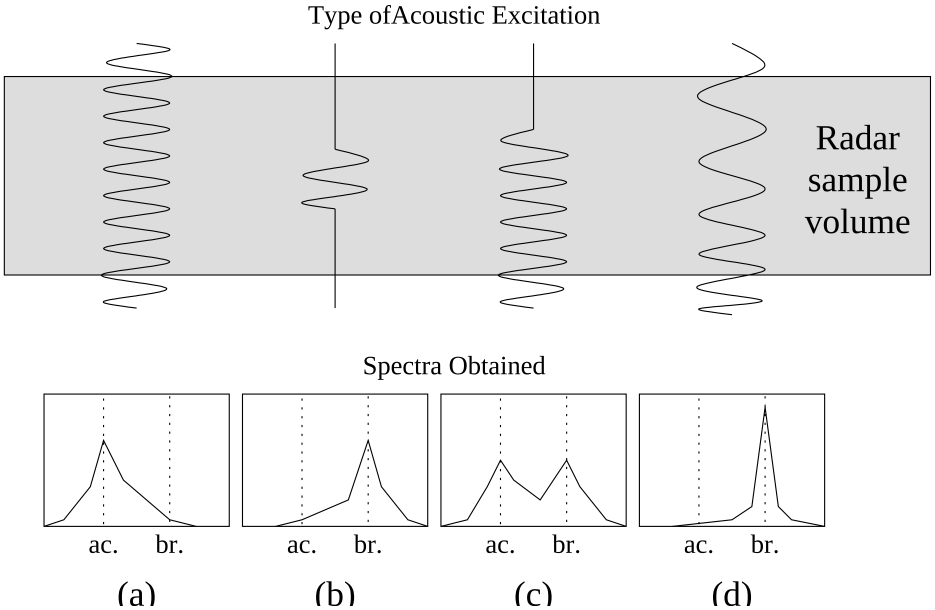

Figure 7.4: Illustration of the different acoustic excitation used within the radar sample volume and the resultant spectra obtained. Where 'ac.' is the transmitted acoustic frequency and 'br.' is the Bragg frequency. The different excitation methods are (a) continuous acoustic source, (b) short pulse, (c) long pulse, (d) frequency modulated continuous wave

The behaviour of the long pulse (Figure 7.4(c)) will be closer to either the continuous acoustic source (Figure 7.4(a)) or the short pulse (Figure 7.4(b)), depending upon its length. The short pulse is optimized if the ratio of the acoustic pulse length to radar pulse length is ∼0.2, but as the acoustic pulse length decreases so does the SNR [*Adachi et al.*, 1993].

Although the frequency modulated pulse shown in Figure 7.4(d) is a chirped pulse, different modulations can be used. Some examples of modulation sequences used include: sawtooth [*Angevine et al.*, 1994]; comb of frequencies [*Peters et al.*, 1983]; band-limited white noise [*May et al.*, 1990]; pseudo random sequences [*Klaus et al.*, 2000] and chirped [*Masuda et al.*, 1992].

Sawtooth excitation can be considered as a coarse chirped wave, especially when the frequency steps and dwell times are reduced towards zero. The use of single frequency, short duration pulses has declined in favour of the more accurate, frequency modulated acoustic excitation [*Masuda et al.*, 1992]. The optimal chirped acoustic pulse satisfies the following inequality,

$$\frac{\Delta r}{L_{fm}\sqrt{(2)}} \gg 1, \tag{7.8}$$

where Δr is the radar pulse length, and L_{fm} correspond to the length of the effective scattering volume for RASS;

$$L_{fm}(r) = \frac{c_a(r)}{|\Delta F_x|^{1/2}}, \tag{7.9}$$

where $c_a(r_B)$ is the acoustic velocity at range r, ΔF is the rate of the acoustic sweep (Hz s^{-1}) and x is given by,

$$x = 1 + \frac{\Gamma k_d^2}{\Delta F \lambda_e}, \tag{7.10}$$

where λ_e is the radar wavelength.

Several acoustic excitation techniques were trialed with the BLR RASS. The use of a random hop was investigated, but spectral analysis of the acoustic source showed biasing toward the centre of the frequency range being used. The biasing was determined to be due to the selection of frequencies being only 'pseudo random'.

Triangle sweeps were also trialed. However, the repetition of frequencies when the sweep reversed, caused over-representation of these frequencies which resulted in non-uniformity of the spectra for individual time-series. However, if enough time-series were incoherently integrated, this effect was averaged out.

A sawtooth excitation was found to be the most effective, as it approximated a chirped wave and was relatively easy to produce. The acquisition of RASS measurements with the BLR are discussed in the next section.

7.2 VHF BLR RASS

A single acoustic source was used for the initial attempts at implementation of a BLR RASS. An Electro-Voice MH4020C horn speaker mounted in a trailer for mobility was used. The long wavelengths of the acoustic frequencies used meant the beam-width of the acoustic source was substantially larger than the radar beam-width, so the spot size had a similar diameter to the transmitting array (i.e. $\sim$15 m).

The Nyquist frequency (see Section 2.2.1) for RASS observations needs to be large enough to account for the large Doppler shift of the RASS echo ($\sim$ 120 Hz). A value of $\sim$ 160 Hz was chosen for the Nyquist frequency, which is large enough that any windowing effects on the RASS echo are negligible. This Nyquist frequency is sixteen times greater than the Nyquist frequency used for spaced antenna wind measurements (10 Hz).

A RASS dataset of the same duration (i.e. 52 seconds) as a spaced antenna dataset, would be sixteen times as large, requiring a substantial amount of transfer time between the RDAS and control computer (Section 2.4.3). In order to minimize the gap between datasets, while still obtaining usable datasets, a record length of 6.4 s and a maximum height observation of 3.0 km, were chosen. This resulted in a transfer time of $\sim$ 5 s, such that adata-set was obtained every $\sim 11 - 12$ s.

The most significant restriction in measurements obtained with a VHF BLR/RASS was the size of the spot. A light to moderate wind of 5 ms^{-1}, results in the spot being advected horizontally by 15 m after propogating for 3 s (i.e. 3 s $\approx$ 1 km range coverage). Because the BLR is not capable of beam-swinging careful positioning of the acoustic source upwind of the antenna array was required. Wind profiles obtained from FCA measurements were used in order to estimate the required position of the speaker. The position of the centre (highest point) of the acoustic wavefront was calculated via integration of the wind profiles (u, v). In order to obtain RASS echoes from height r_o, the approximate position of the speaker (x, y), is given by,

$$x = -\int_0^{r_0} u(r)\, dr \tag{7.11}$$

$$y \;=\; -\int_0^{r_0} v(r)\,dr \tag{7.12}$$

Because wind measurements did not extend to the ground a linear interpolation between the velocity at the lowest observed range and 0 $\mathrm{ms^{-1}}$ at the ground level, was applied (Figure 7.5).

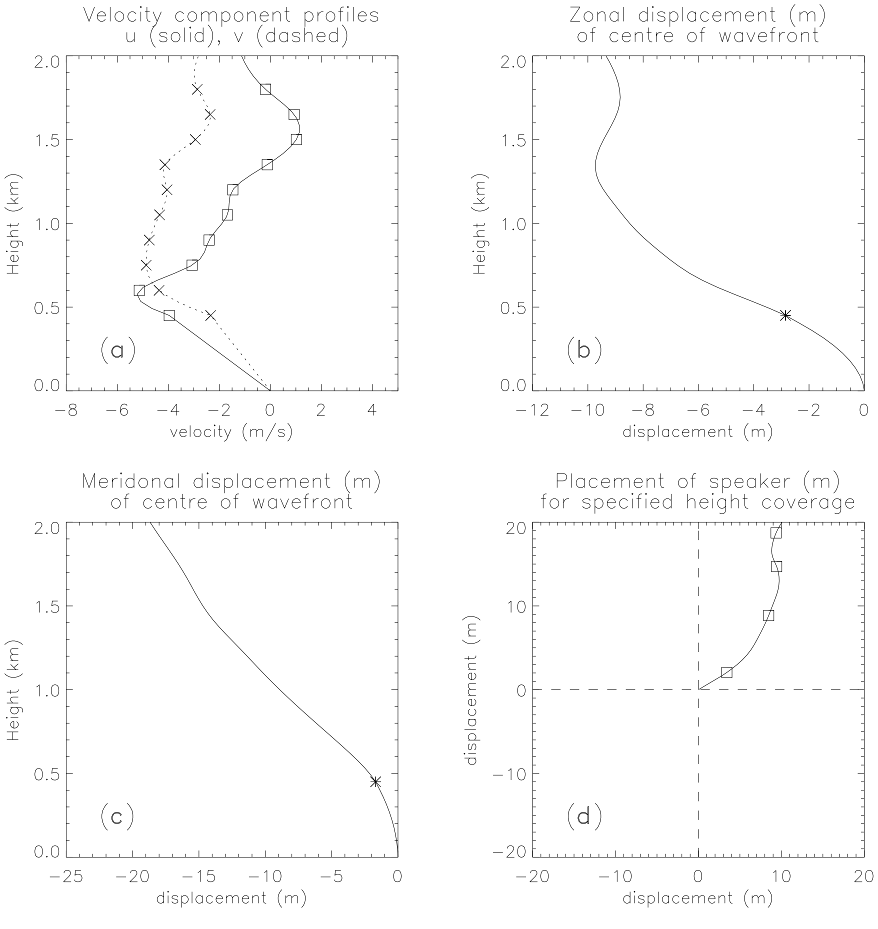

Figure 7.5: Illustration of the determination of the ideal speaker placement, using FCA derived wind profiles from 1630 UTC to 1700 UTC on 23rd September 1997. (a) The zonal u (solid line) and meridional v (dashed line) profiles, (b) and (c) are the zonal and meridional displacement of the centre of the acoustic wave, assuming that the acoustic source and radar are co-located and (d) the placement of the speaker in order to gain measurements for different heights, (each 500 m increment is represented by a square).

This is a simplistic determination of the wavefront position since it does not take into account the modification of the wavefront due to temperature gradients, wind velocity gradients and turbulence [*Matuura et al.*, 1986*b*]. Application of ray-tracing techniques was beyond the scope of this thesis, but it would improve the initial placement of the speakers [*Takahashi et al.*, 1988]. However, the absence of measurements in the lowest ranges (below 300 m), and subsequent assumptions regarding the form of the wind profiles need to be carefully considered, as they affect any ray-tracing results.

Once the speaker was placed at the pre-determined position, a brief trial was performed using a fixed frequency CW acoustic wave. A continuous frequency creates a backscattered signal at that frequency (Figure 7.4(a)). Observation of a narrow band centred around the acoustic frequency enabled determination of whether or not a measurement from each height could be obtained for given background wind conditions and placement of the acoustic source. A further refinement in the position of the speaker for optimal coverage was accomplished through examination of the relative strength of the single frequency as observed in the three individual receiving arrays.

Changes of only 2-3 metres in the position of the speaker were found to have substantial effects on coverage. The coverage could change from no coverage at all to a height coverage of over 800 m being obtained. The complications of trying to locate the spot were further compounded by constantly changing winds. This trial-and-error method was time-consuming and often not very successful. Eventually some measurements were obtained, which were then be compared against virtual temperatures measured by radiosondes.

If the single-frequency-acoustic-excitation test showed that it was possible to obtain measurements from a range of heights, then a complete RASS observation was performed. The acoustic source was allowed to run non-stop, sweeping through a given range of frequencies. A typical acoustic excitation involved stepping from 118 Hz to 123 Hz, with 0.05 Hz steps and a dwell time of 100 ms with each step. At 54.1 MHz, these frequencies would cover the range from -11°C to 15°C. With a lapse rate of 7°C km^{-1} and a ground temperature of 17°C, this corresponds to a height range from 500 m to 4200 m. One complete sweep took $\sim$ 5 s to complete. To obtain statistically reliable spectrum it was necessary to incoherently average spectra, from 5 s data sets accumulated over a period of five minutes.

Intermittent interference was often detected. Isolation of this interference was complicated, as its frequency was not fixed. The strength of the interference would decrease with height which suggested the source of the interference was internal to the RDAS. The presence of the interference at the highest heights enabled a filter to be designed and then applied to the lower ranges. However, if the interference was at the same frequency as the RASS echo, then corruption of the data was unavoidable, although the filtering did reduce the effect.

Figure 7.6 shows the RASS-derived temperature profiles obtained on 15th September 1997, together with temperature observations from two radiosonde flights launched from Buckland Park just prior to, and after, the RASS acquisitions. A pronounced underestimation in the RASS derived temperatures, compared with the sonde temperatures, is apparent.

The underestimation observed (Figure 7.6), suggested that frequencies less than the Bragg frequency were enhanced in the spectra.

It was discovered that the acoustic sweep reset at the start of each data acquisition, hence the sweep was locked to the acquisition cycle. This synchronization resulted in a bias toward the frequencies at the start of the sweep (Figure 7.7). This effect was highlighted by running the sweep forwards (i.e. 122 Hz to 117 Hz) and then backwards (i.e. 117 Hz to 122 Hz), where a difference of $\sim 2°\mathrm{C}$ was observed between the two different sweeps.

Unfortunately, this was not enough to account for all of the underestimation, although it reduced it by half. The RASS control, which was initially an integrated part of the RDAS, was removed and isolated in a separate computer running a Linux operating system. Although, this enabled total isolation of the start of the data acquisition cycle and acoustic excitation sweep, it complicated attempts at unattended operation. The remaining underestimation suggests than an over-representation of the lower frequencies of the sweep was still a factor.

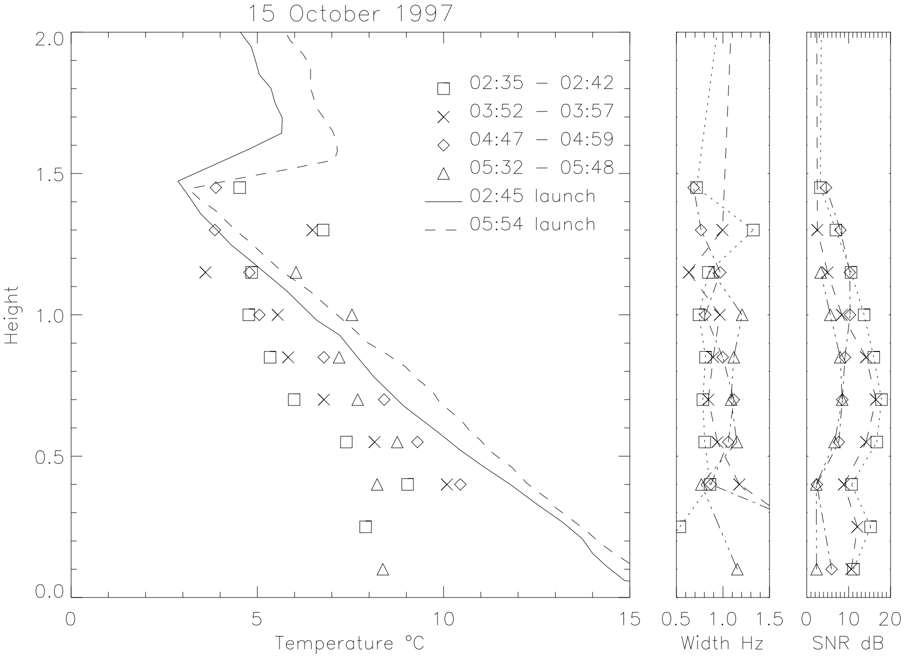

Figure 7.6: RASS measurements made on 15th of September 1997. Virtual temperature measurements from co-located sonde launches at 0245 UTC (solid line) and 0554 UTC (dashed line) are shown. Rass measurements were obtained from 0235 - 0242 (squares), 0352-0357 (cross), 0447 - 0459 (diamonds) and 0532-0548 (triangles)

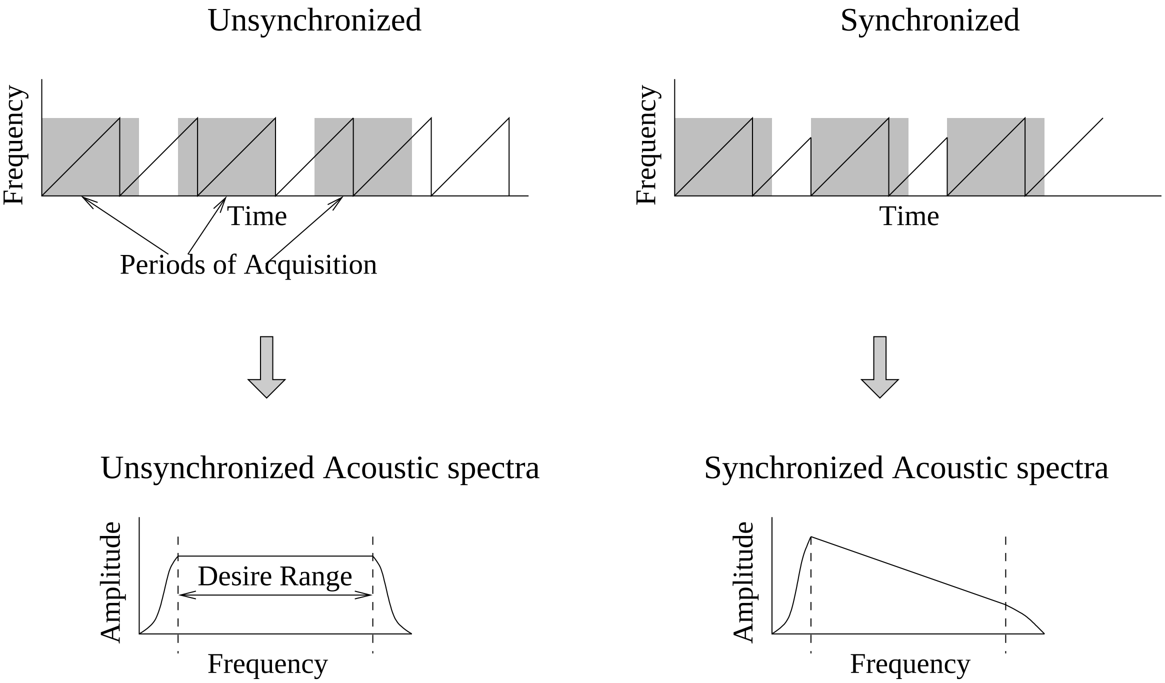

Figure 7.7: Illustration of the effect of synchronization of acquisition and acoustic sweep start times.

The specifications of the speaker showed that the frequency response was not flat around 110-130 Hz (Figure 7.8). The variability in the frequency response, suggested that the speaker was not optimal for RASS measurements for a radar operating at VHF. Although the frequency response suggests an enhancement would actually occur at the higher frequencies not the lower, thus an overestimation would occur (Figure 7.8).

Additional sources, located at different positions relative to the radar antenna would increase the occurrence of a 'spot' being observed by the radar and hence extend the height coverage. This along with the need for optimal sound sources, motivated the purchase of four new speakers from VAF Pty Ltd [2].

The speakers were specifically designed so that they could also be used with the large VHF ST radars located at Buckland Park and Mt. Gambier, which operate at

---

[2] VAF: www.vaf.com.au

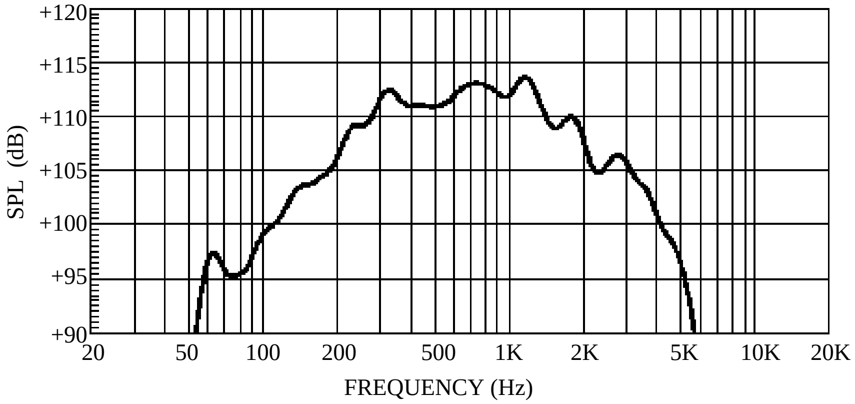

Figure 7.8: Axial frequency response of Electro-Voice MH4020C horn.

54.1 MHz and 44.75 MHz, respectively. The design specifications included: portability; flat response over the range 80 Hz to 130 Hz (which corresponds to ∼-90°C @ 44.75 MHz and ∼50°C @ 54.1 MHz, respectively); relatively high power ∼140 dB (for upper troposphere measurements using the larger VHF arrays); and durability in harsh environmental conditions. The specifications of the speaker, which was designed and manufactured by VAF, are given in Appendix I. All the design goals for the new speaker were met, although deterioration of the speakers has been observed due to exposure to the weather.

A campaign with three of the speakers, (the fourth speaker was sent to Mt. Gambier), occurred at Buckland Park during December 1999. The campaign took place from the 10th December 1999 to 12th December 1999. The main purpose of the campaign was too attempt to simulate an unattended operational situation. Fifty data-sets (∼ 9 minutes) of RASS measurements were taken every hour. These fifty data-sets were incoherently averaged together to produce a representative spectrum for each height and each hour during the campaign.

Synoptic chart forecasts before the trial period predicated a large, slow moving, high pressure system would direct south to south westerly winds at the surface level, over the field site. Therefore, to maximize coverage, the speakers were placed on the

Figure 7.9: VAF E-115 RASS speaker at Buckland Park

NW, SW and SE corners of the antenna array. However, post analysis of the campaign data highlighted the restrictions involved in the use of only a few sources with a small antenna array. At the start of the observations, coverage was obtained up to 1.5 km, see Figure 7.10. This was a result of light winds and a vertical shear in the zonal wind component at 1 km, which effectively advected the spot back over the antenna array. Several hours into the campaign the shear weakened until the lowest 3 km of the atmosphere consisted of south-westerly winds, with a magnitude of 10 ms^{-1} above 1 km. This meant only one of the speakers was actually upwind of the antenna array. The advection of the spot was very pronounced with such large velocities . In Figure

7.10, the reduction and eventual loss of height coverage of the RASS echo is shown by 1125 UTC.

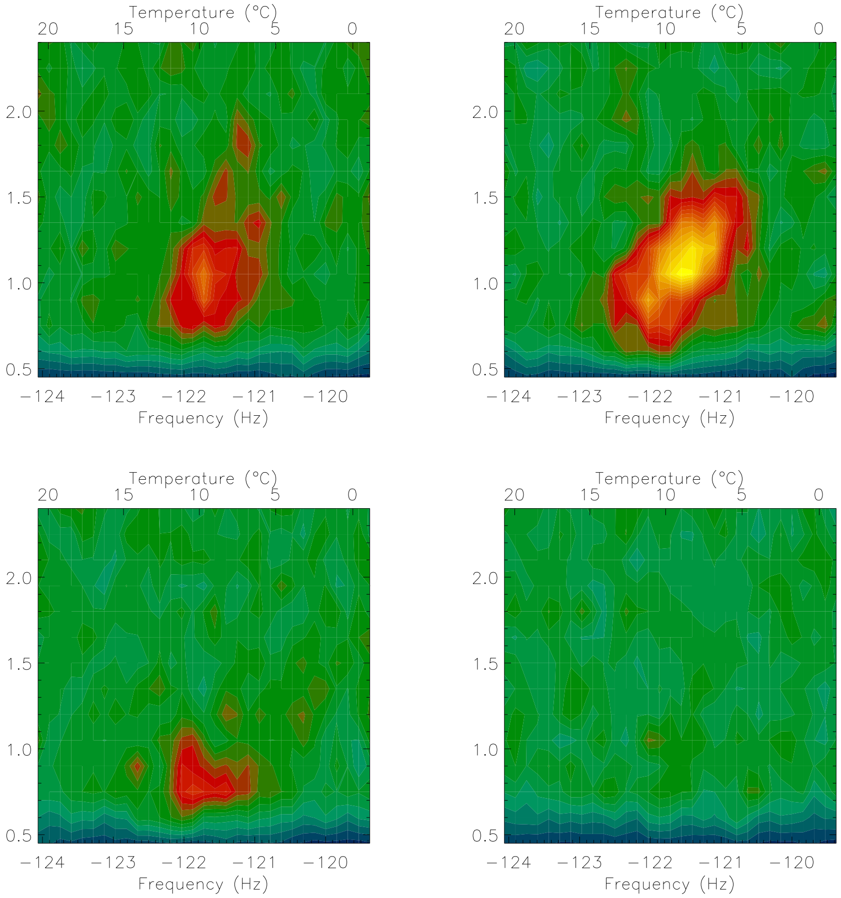

Figure 7.10: Frequency-height cross-sections from the RASS campaign to test operational conditions, 10-12th December 1999, at Buckland Park field site. Each cross-section consists of the combined spectra acquired during ∼ 10 minutes of acquisition time (i.e. 50 data sets), the data shown was acquired on 10th December 1999 at 0810 UTC (top left), 0915 UTC (top right), 1020 UTC (bottom left) and 1125 UTC (bottom right)

A comparison between the few temperature profiles obtained and measurements from radiosondes launched from Adelaide Airport, showed the same underestimation as previously noted. Investigation of the potential source of underestimation was hampered by the difficulty in obtaining the spot. Attempts at observing the effects of different acoustic excitation techniques were unsuccessful, with the continual repositioning of the speakers required. It was not possible to definitely determined whether a change in performance of the BLR RASS was due to different operating parameters or a change in atmospheric conditions, without continual repetition of earlier results for validation of every minor change made.

The RASS was applied to the larger VHF arrays at Mt. Gambier and at Buckland Park, in order to check that neither the RASS analysis techniques, operating parameters or the acoustic sources that were being used, were the source of the underestimation.

7.3 RASS with ST Radars

After the difficulties associated with finding the 'spot' using the small VHF BLR array, the large array of the Mt. Gambier system provided a superior platform to obtaining RASS temperature measurements. The large array of the system produced a spot size comparable in size to the array and was easily observed. There were two campaigns involving the application of RASS to the Mt. Gambier system. The first campaign was a brief "proof of concept" trial on the 10th August 1998. The second trial involved simulating an operational situation and took place from 20th to 21st December 1999. The following discussion is based solely upon the second trial.

The Mt. Gambier array has six receivers. Different combinations of antennas can be used, depending upon the type of experiment being performed. However, for the RASS campaign the array was broken into six groups, (Figure 7.11).

For simplicity, the acoustic source was placed at the centre of the array. The campaign was run on a similar basis to the BLR campaign, with RASS measurements attempted once every hour. However, the data transfer rate between the RDAS and the control computer was substantially slower than the BLR transfer rate. Hence, in a five minute period only 10 data-sets were obtained. However, due to the large antenna (and spot) size, measurements were easily obtained and incoherent averaging of the

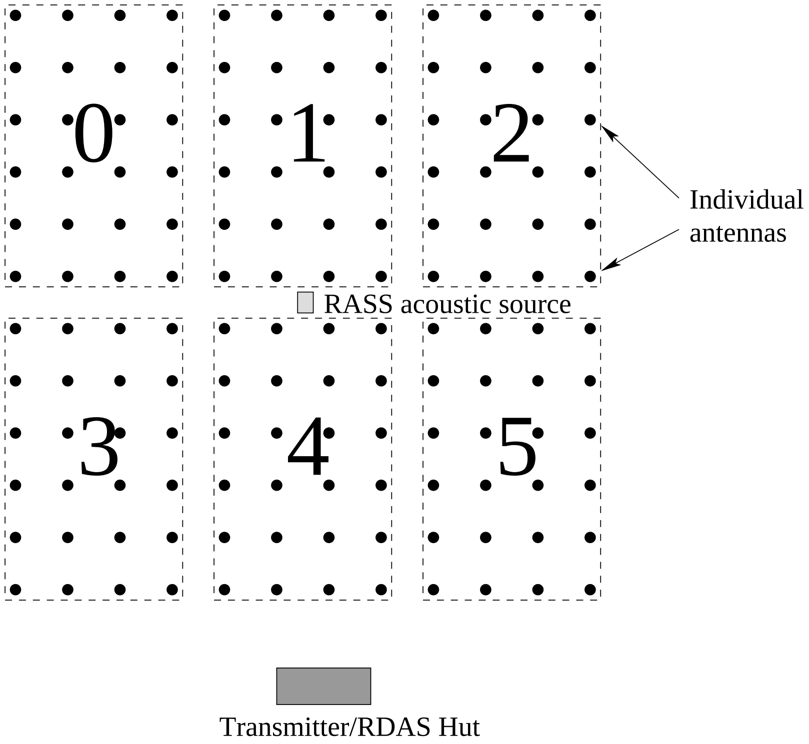

Figure 7.11: The layout of the Mt. Gambier ST radar/rass. The configuration of the six antenna sub-arrays are shown. The position of the acoustic source for trials on 20th to 21st December 1999 is shown.

spectra was not required.

The acoustic excitation was controlled via a sound card in an additional computer. The type of excitation used was a sawtooth modulation, sweeping from 103 Hz to 93 Hz, with a step size of 0.1 and dwell time of 60 ms.

An example of the rass echo obtained by the six receiving arrays of the Mt. Gambier VHF radar is shown in Figure 7.12. The movement of the spot can be clearly seen in Figure 7.12, where strong echoes at the lower heights ∼1 km, were received by antenna group 0. While the strongest echoes received by antenna group 5 were at ∼4 km, therefore it was deduced that the spot was eventually advected to the east-south-east out of the observation range of the antenna array.

The Mt. Gambier radar is located adjacent to a meteorological observation stations, which launches a single radiosonde each day at ∼2300 UTC. Comparisons between RASS derived temperatures and radiosondes were excellent, Figure 7.13. A

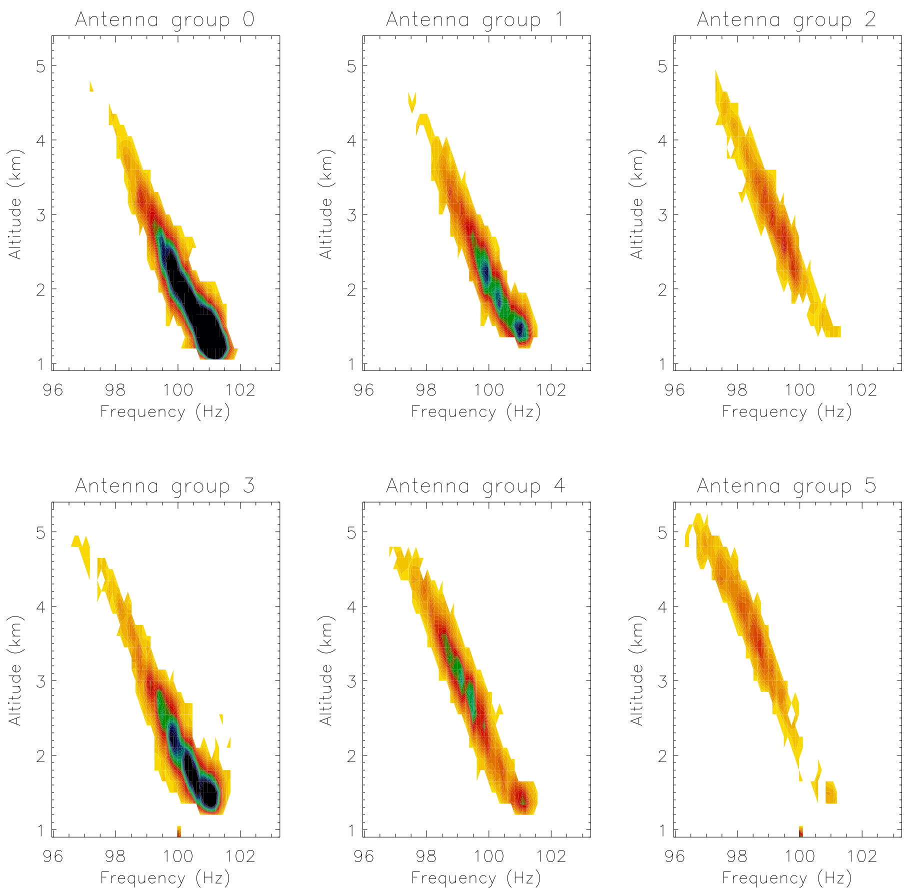

Figure 7.12: Frequency-height cross-sections of the RASS echo obtained from 0108 UTC to 0113 UTC on 21st December 1999, using the Mt. Gambier ST radar. The orientation of the antenna groups with respect to the centre of the array was NW, N, NE, SW, S and SE for antenna groups 1 - 6 respectively

consensus averaging algorithm was applied to the RASS data to help accurately determine the Bragg frequency at each specific height.

This algorithm consisted of several steps designed to eliminate spectral interference created by internal and external sources. Firstly, the spectra from all six receivers at each height was incoherently combined together. In order to isolate any potential RASS peaks, a Gaussian fit was applied to the six most prominent peaks in the spectra that were within the range of possible Bragg frequencies. Any peaks that had insufficient SNR, or a width that was too large or small were rejected. At each height it was found that typically only one peak satisfied the above requirements. Using the

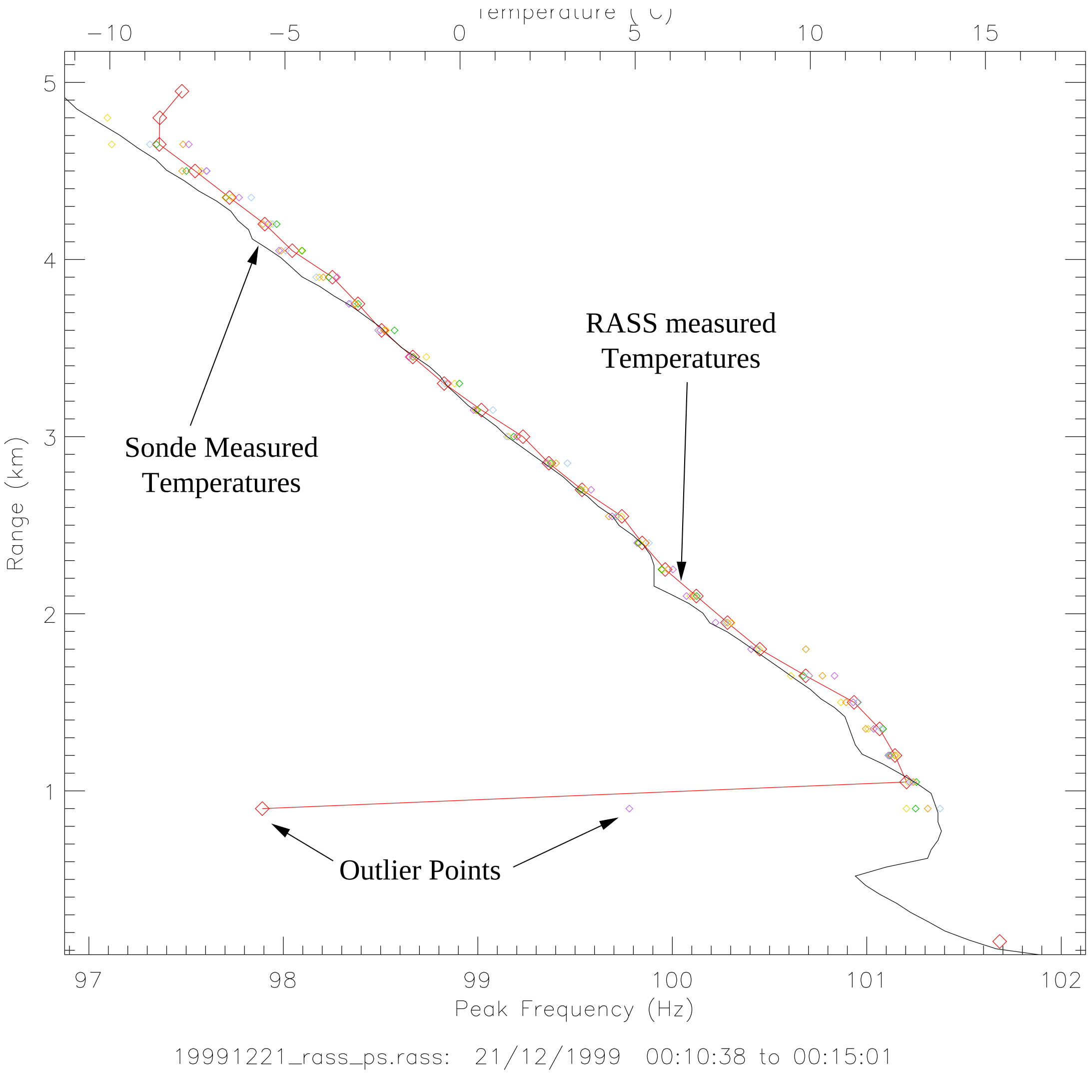

Figure 7.13: A comparison of temperatures between a radiosonde launched 2316 UTC on 20th December 1999, (black line) and RASS derived virtual temperatures (red line), obtained from 0010 UTC to 0015 UTC on 21st December 1999. The six best estimates of the Bragg frequency are given at each height, (where possible). The value with the largest SNR is used to plot the temperature profile, (see text for further description).

values obtained from all the times-series within the observation period, the mean and standard deviation of the peak distribution was calculated for each height. Any peaks that were several standard deviations away from the mean value were rejected. The peak with the largest SNR in the remaining distribution, was taken to be representative of the Bragg frequency at that height.

The coverage of the Mt. Gambier VHF ST radar/RASS compares well with the coverage obtained with the INSU/Météo radar at CNRM/Toulouse, operating at 45 MHz, when a single acoustic source at the centre of the array was used [*Klaus et al.*, 2000].

During the Mt. Gambier RASS campaign, no complaints of noise pollution were received, even when night time observations were being conducted. This was due to the local topography of the land, with the radar situated in a slight depression and no residential properties being nearby. However, the trials at Buckland Park, where night time operation was similarly performed, did produce some complaints from nearby residents. The local topography of BP is extremely flat with the noise of the RASS being audible at distance over 1 km away from the acoustic source in quiet conditions. In addition, the isolation of the surrounding area near BP results in any anomalous background noise being extremely noticeable.

Two brief campaigns were run to temporarily implement a RASS to the large VHF ST radar at Buckland Park. The campaigns occurred on 24th August 1998 and 22nd October 1999. Measurements from the 22nd October 1999 campaign are shown in Figure 7.14. In the second campaign, up to three speakers were used as acoustic sources. During observations from 0819 UTC to 0847 UTC, two of the sources were situated on the NW and SW corner and the third source was in the centre of the array (Figure 7.14(a)). The second set of measurements, taken from 0851 UTC to 0903 UTC, used only a single acoustic source, situated in the middle of the south edge of the array (Figure 7.14(b)).

Although no simultaneous radiosonde soundings were available during the VHF ST radar campaign, the results obtained still provided insight. Comparisons between

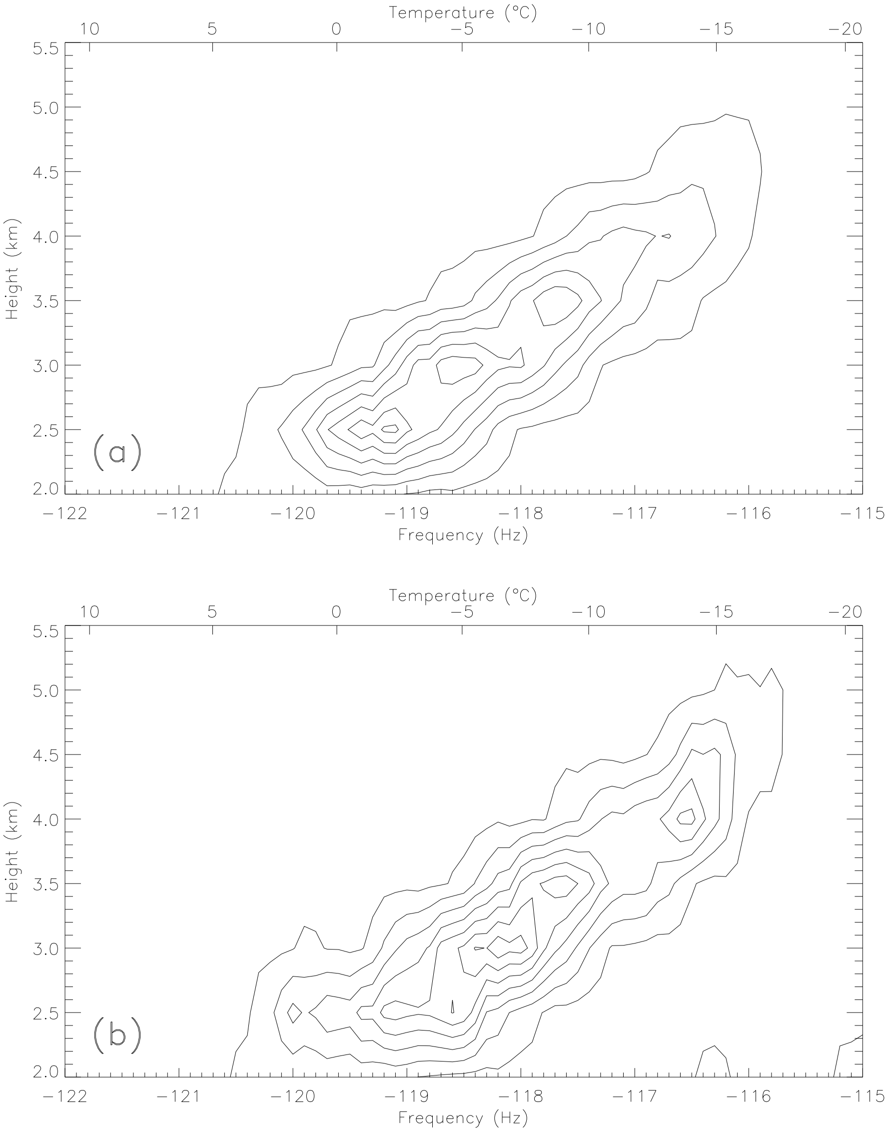

Figure 7.14: Frequency-height cross-section showing the RASS echo obtained with the Buckland Park ST VHF radar. The entire array was combined together, and connected to a single receiver. The relative strength of the echo as a function of height and frequency is given by the evenly spaced contour levels, (with arbitrary units). The observation periods from 22nd October 1999, were (a) 0819 UTC - 0847 UTC and (b) 0851 UTC - 0903 UTC.

the two set of measurements show very similar behaviour. This is despite the different observation periods used, with the duration of the first set being more than twice the duration of the second set. Hence, with a large antenna system such as that of the BP VHF ST radar, the spectra of the RASS echo will be fully resolved within a relatively short period. Once the peak is fully resolved, additional measurements will not improve the measurements and may even cause spreading of the peak due to temporal variations and evolution.

Additionally, the use of extra sources in the first set did not give any obvious advantage over the second set of measurements. The implication of this result is that careful consideration of the position of the sources is required in order to improve the coverage.

7.4 Discussion

The temperature underestimations found with the BLR RASS, were not due to operational parameters or the acoustic source. Accurate measurements of temperature profiles were obtained with a larger VHF radar, using exactly the same techniques and acoustic sources.

Two possible causes of the underestimation were discussed briefly in Section 7.1. When the horizontal velocity gradient is less than the acoustic velocity gradient the effective backscatter region is on the windward side of the array. Consequently the broad beam of the BLR means that returns occur from off-zenith in the windward direction (Figure 7.2). The influence of the horizontal velocity would therefore act to reduce the apparent speed of sound, and reduce the inferred temperature. This effect only occurs during conditions of low wind shear, which are often associated with light winds. Light winds are required for good height coverage when using a RASS. It is probably that during periods of excellent RASS coverage, the likelyhood of temperature underestimation at the lowest heights is increased.

The second potential source of underestimation is due to the profile of the reflectivity and the range-weighting function of the receiver. The combination of these two effects will usually result in a positive gradient in signal power at the lower heights and a negative gradient in the upper height [*Görsdorf & Lehmann*, 2000]. The overall effect leads to an underestimation of temperatures at lower ranges and an overestimation at upper ranges. Measurements of temperatures using the BLR RASS from the upper heights were too few to even qualitatively suggest an overestimation was occurring.

Two potential sources of the observed underestimation in the temperature profiles using a BLR RASS have been presented. However, further investigation is beyond the scope of this thesis.

7.5 Summary

The application of RASS to the BLR and larger VHF radars highlights several difficulties that can occur when trying to operate a BLR RASS.

Even when using the large array, the position of the acoustic source relative to the radar antenna array has a marked effect on the height coverage. It was observed than even moderate horizontal winds of 5 ms^{-1} advected the spot by ∼15 m horizontally, within the time it took for the acoustic wavefront to propagate to an altitude of 1 km. Despite this problem, with the use of larger arrays (∼ 100 m) it was possible to accurately obtain temperature measurements up to 5 km.

Ideally, RASS observation using a small-array radar would require many acoustic sources spread around the profiler, instead of a few large sources. While the acoustic sources built by VAF Pty Ltd, were suitable for coverage of the middle troposphere using a VHF ST radar/RASS, they were not suitable for obtaining good coverage using a BLR, with its associated wide beam. However, the area over which the acoustic sources would need to be spread, would be several times larger than that required for the antenna array. Phased arrays of acoustic sources could be used to steer the acoustic wave windward, however the quality of the acoustic beam would be extremely sensitive to the turbulence within the boundary layer.

Two potential sources of underestimation in the temperature profiles were presented, with both possibly occurring simultaneously. Further analysis is required in order to determine if the range-weighting effects are appreciable. The effects of horizontal contamination when the region of effective backscatter was off-zenith and windward were also noted. It may be possible to determine the extent of this effect by using in-beam interferometry to determine the angle-of-arrival and this remains to be investigated.

Chapter 8

Summary

This thesis has covered the basic development, refinement and modifications to a prototype Very High Frequency (VHF) Boundary Layer Radar (BLR).

This summary will bring together some of the main aspects of this research with suggestions for further work.

In Chapter 2, The design goals of a portable, flexible and easily transportable BLR were presented. Two fundamental questions were asked and then answered, namely 'Whether to use VHF or ultra high frequencies (UHF)?' and 'Whether to use spaced antenna (SA) or Doppler beam steering (DBS) techniques'. There is no absolute answer to these two questions, as all possible combinations of these choices have advantages with respect to each other. For a number of reasons the final design consisted of a radar operating at VHF using a spaced antenna configuration.

UHF echoes are usually dominated by precipitation reflects, making simultaneous determination of the clear air vertical velocity often not possible, At VHF however, precipitation and clear air echos can be seperately distinguished. VHF radars, unlike UHF radars, do not suffer interference from birds, bats and insects. Additionally acoustic frequencies required for UHF RASS application are heavily attenuated, compared with acoustic frequencies for VHF RASS, so in principle the temperature can be measured over a greater range.

SA operation was chosen over DBS for several reasons. The need for a small far field results in a small-scale array and hence wide beam-width at VHF. Aspect sensitivity will reduce the side-lobes contributions for SA. However, for DBS techniques aspect sensitivity combined with the wide beam-width of the radar, will require a large oblique angle to be used. This will increase ground clutter and cause significant height smearing in the measurements. The use of a simple vertical beam removes the complications of beam steering. Superior time resolution is obtained with SA as only a single measurement of an area is required as opposed to three measurements of different regions needed for DBS. The use of multiple receiving antennas enables the spatial structure of the scatterers to be determined. Interferometry techniques can be used to determine the angle of arrival of signals.

In Chapter 3, the evolution of the antenna array was considered, with three generations of development detailed. The initial simple design of the array provided a wide bandwidth necessary for lower height, small transmitted pulse width operation. A desire for an increase in gain, minimization of the side-lobes and simpler construction resulted in two further modifications to the array. The number of antennas used increased from 12 to 27. However, the spacing between antennas was reduced from 0.7λ to 0.5λ, so that the overall size of the array only increased slightly, but with an increase in gain. The final layout of the array consisted of three arrays of nine three-element Yagis, with individual reception on each group and all three groups used for transmission.

Further investigation of the system was continued in Chapter 4, where calibration values were measured and/or calculated. Using a noise generator the absolute received power was determined. Numberical modelling enabled various important aspects of the system to be investigated. These included not only the beam pattern of the array and gain, but also the coupling between array elements. The third generation array has a gain of 15 db with a beam-width (3-dB point) of $30 - 32^\circ$ for each array on reception, and 19 dB and $16 - 18^\circ$ for the whole array on transmission. The modelled and measured values of coupling agreed well, with values of less than -44 dB obtained.

The performance and coverage of the system was assessed in Chapter 5 . Improvements to the antenna array were reflected in improved performance of the system. The BLR was operated in a variety of conditions that can affect the height coverage of the system. This motivated the development of different modes of operation to maximize height coverage, albeit at the cost of temporal and height resolution. Measurements from 300 m up to over 8 km have been observed with the BLR.

Expoitation of the SA technique enables a number of important atmospheric parameters to be studied. The range of pattern scales obtained on average ranged from 9 to 12 m. Measurements of the random horizontal velocity (turbulence) were typically less than 1 ms^{-1} although they could be as large as 4 ms^{-1}. The average vertical velocity was determined to be $\sim$ 10 cms^{-1}. No influence of the horizontal winds was detected in these measurements, implying this was not an artifact caused by the antenna beamed pointing off zenith. Further investigation of the vertical velocities is required.

A detailed evaluation of the accuracy of wind measurements was accomplished by comparisons with *in-situ* measurements obtained from radiosonde launches from Buckland Park and Adelaide Airport, and measurements obtained by aircraft near the field site. Comparisons of velocity measurements were very good, with the results similar to those obtained by other authors. Correlation values were $\sim$0.96, with horizontal velocity RMS values in the range 1.25 to 1.65 ms^{-1}. A least-squares fit to scatter-plots gave values for the slope of $\sim$0.9, implying SA winds were underestimating horizontal velocities by $\sim$10%. Further investigation of the underestimation showed a potential dependence with time, perhaps implying a long-term deterioration of the system (eg antennas) may be a case.

Calibrated measurements of reflectivity and C_N^2 showed the ability of the BLR to accurately resolve the fine structure of the atmopshere, with layers that had vertical extent of only 100 m or less, being a feature. Detection of the top of the BL is particularly clear using the BLR.. In order to determine the value of C_N^2, a method for determining isotropic scatter was presented. The values of C_N^2 obtained in the lowest 1-2 km were typically $10^{-14.5}$ to $10^{-16.5}$ $\mathrm{m}^{-2/3}$. These values compare favourably with measurements obtained by some authors, but showed an underestimation with respect to the values obtained by others. Comparisons with *in-situ* measurements are required to fully validate the techniques used here. It should be noted that in order to accurately obtain measurements of C_N^2 at a given height a successful FCA results must be obtained and the scatter must be isotropic. The combination of these two requirements resulted in limited coverage of measurements.

Observations of rain echoes highlighted the ability of the BLR to discriminate clear-air echoes from echoes due to precipitation. Investigation of the rainfall rates using calibrated measurements is on-going [*Lucas et al.*, 2000].

The velocity underestimation motivated an investigation of possible causes. Two models were used to provide artificial time-series that enabled simulation of the effects of antenna coupling, receiver characteristics, and spatial averaging on the FCA. It was found that coupling either caused an underestimation or an overestimation of the velocity, depending on the coupling-coefficient values. Whatever the situation, the effect on the BLR was determined to be at most ~2%. Differing receiver characteristic can cause underestimation of horizontal velocities. Significant offsets were observed in the time-series at the lower heights, suggesting this may be one cause of velocity underestimation. Although pre-analysis detrending of the data generally minimized the effect, in certain situations it introduced further underestimations. The final potential cause examined was spatial averaging; this was found to produce no overall bias.

Chapter 7 dealt with operating a RASS system using a BLR. Several problems specific to a BLR RASS were observed. The small antenna size resulted in moderate background winds advecting the acoustic wave away from the radar in a relative short time, hence the height coverage was limited. When measurements were obtained, a height dependent temperature underestimation was observed. Observations using larger VHF radar did not show this bias, in fact excellent agreement was obtained in comparisons with co-located radiosonde measurements. Hence, the underestimation was deduced to be due to an artifact of the BLR. Two potential sources of underestimation were considered. The wide antenna beam in certain situations can cause measurements to be obtained obliquely, thus introducing horizontal wind leakage into the sound velocity. Secondly, the weighting of measurements by the background power profile, which is an artifact of the atmosphere and receiver recovery is also a factor at the lowest heights.

This thesis has detailed the development of a BLR that has been successfully applied to observations of the lower atmosphere. The performance of the system is comparable to that obtained by UHF radars at a similar stage of development. Measurements at the moment are possible from as low as 300 m up to occasionally as high as 8 km . Further refinement of the system will only improve the height coverage and the data acceptance rate at all heights. As this is a new tool for observing the lower atmosphere the areas of future research are boundless, with a few examples given in the next section.

8.0.1 Further Work

The potential uses of the BLR in observing the lower atmosphere are numerous. The further work presented here can be broken into two categories; applications of the BLR and improvements to the system.

The BLR is an ideal platform for observing meteorological events. Already it has shown potential for studying frontal passages and the development of the boundary layer, to give just two examples. In particular cold fronts (cool changes) which cross South Australia in the summer are very shallow with a depth of $\sim 1-2$ km. Further study of the development of the boundary layer and in particular the formation of nocturnal jets and interaction of frontal passage with inversions is possible.

Using the BLR for precipitation studies has only just begun at the time of writing; with encouraging results [*Lucas et al.*, 2000]. The development of the sea breeze is an ideal area for studies, especially considering the close proximity of the field site to the ocean. Basically almost any dynamical process within the lowest few kilometres is a prime candidate to be observed and investigated with the BLR.

Further investigation of the temperature underestimations observed using the BLR RASS is required. Calculation of the range-weighting of the power profile is necessary to determine the effect that this has on the derived temperature profiles. Analysis of the angle-of-arrival of the RASS signal will enable removal of the effects of the horizontal and vertical background winds. The use of multiple smaller acoustic sources will assist in maintaining a RASS spot within the antenna array. The use of a large acoustic array is one area of investigation which could be examined. If a large enough acoustic array is used then the spot size would increase in proportion to the size of the acoustic array.

With further improvements to the system, the accuracy and range of measurements will be increased. Further validation of the calibration technique is required. Continued comparison with *in-situ* measurements of C_N^2 provide one source of validation. Measurement of rainfall rates is another method for calibration. Phase calibration of the receivers using Galactic sources, provide a method for daily checks on the stability of the receiver characteristics.

Pattern scales typically observed by the system were typically larger than the receiving array spacing, thus suggesting the antenna spacing may be slightly too small. However, careful calculation of the effect on the antenna beam pattern, in particular the side-lobes, is required before any changes to the array are implemented.

One of the first areas which needs to be looked at are the T/R switches, with all three presently used being different from each other. Minimization of ringing and rapid recovery of the receiver are crucial for lower height coverage, hence the T/R switches must be optimized.

Saturation of the receivers at the lower heights imposed a restriction on the gain used, which in turn reduced coverage from the upper heights. Increasing the dynamic range of the receivers will allow an increase in the gain, hence allowing an improvement in upper height limit while still maintaining the lower height coverage. This would reduce the need for different operational modes and allow better time resolution.

Investigation into filtering of the data using the model is required to help improve the quality of data. Application of wavelet analysis would help in the detection and removal of reflections from aircraft, without having to reject either part or all of the time-series.

Finally, application of consensus averaging to measurements would help improve the quality of the data, introducing comparisons with adjacent heights and times may help to detect outliers. However, the large variability observed in the lower heights means such comparisons may produced large difference, when the measurements are real.

Appendix A

Glossary

a^2	universal constant taken to be 2.8
a_a	effective acoustic radius
a_a	effective antenna radius
A_e	effective antenna area
$A_1(f)$	amplitude spectrum
$A_2(f)$	amplitude spectrum for the second time series
$\overline{A^2}_{noise}$	recorded signal at the output of the receivers due to the noise generator
$\overline{A^2}_{extra}$	additional noise of generator
$\overline{A^2}_0$	recorded noise level when no power is present at antenna outputs
A_t	amplitude of record signal at the output of the receivers
A_z	eddy exchange coefficient
B	bandwith of the receiver
c	speed of light
c_a	apparent speed of sound
c_s	speed of sound
C_p	specific heat at a constant pressure
$C_n^2(r)$	turbulent refractivity structure parameter
C'	acoustic velocity gradient
d	duty cycle
d	antenna spacing
d_i	sampling point
D	diameter of antenna
e	partial pressure of water vapor (hPa)
f	Coriolis parameter
f_D	position of Doppler shifted scattered signal
f_o	operating frequency of the radar
f_o	cut-off frequency

$f(x, y, t)$	complex voltage of the diffraction pattern measured by an antenna
g	acceleration of gravity
g	gain of system including effect of T/R switches, preamplifier front ends, receivers and cables
$G(dBi)$	gain as measure of the response of the antenna as a function of direction
g	axis antenna power gain with no feed-line loss
g_s	system gain
g_t	axis antenna power gains for transmitting arrays
g_r	axis antenna power gains for receiving arrays
h	offset height; height of the slope
h	boundary layer depth
h	CBL depth
I_1	currents in antenna 1
I_2	currents in antenna 2
I_{1o}	currents in antenna 1 for odd mode of excitation
I_{2o}	currents in antenna 2 for odd mode of excitation
I_{1e}	currents in antenna 1 for even mode of excitation
I_{2e}	currents in antenna 2 for even mode of excitation
I_i	current flowing from antenna i
I_T	total current from combination of all antennas in the array
k	Boltzman's constant
k	von Karman's constant (= approximately 0.4)
k_a	acoustic wave number
k_r	radial direction of radar beam
K_w	complex refractive index of water
l	electrical length of the line
l	cable length (m)
l	one-way atmospheric attenuation
l_r	finite bandwidth loss of receiver
l_r	receiver loss factor
L_{fm}	effective scattering volume for RASS
L_o	outer scale length of turbulence spectrum
M	number of points or samples in the time-series
M	molecular weight of dry air
M_m	molecular weight of moist air
M_n	n-th classical spectral moment
M	gradient of generalized potential index of refraction
n	refractive index of air
n	complex loss coefficient
N_e	number density of electrons
N_c	critical plasma density
N_c	number of coherent integrations

N_f	Nyquist frequency
$N(D)$	drop-size distribution
$\overline{N}$	noise level
$< N >$	noise power
N	amplitude
n	complex loss coefficient
N	noise factor
N_{offset}	noise offset due to receivers
p	amplitude reflection coefficient of the discontinuity
p	pressure
p	atmospheric pressure (hPa)
p_o	pressure
P_a	average transmitted power
$P(f)$	typical power spectrum
P_{ng}	noise generator power
P_p	peak pulse power
P_r	reflected power
$P(r_0)$	signal at the receiver's output
$\overline{P}(r_0)$	weather radar equation which relates the signal at the receiver's output
P_S	height of Doppler shifted scattered signal
P_{signal}	coherent signal; power at output of antenna
P_t	transmitted power
P_t	transmitted peak power
$P(w)$	precipitation echo
q	specific humidity
Q	heat input
r_B	Bragg height
r	range
R	range
R	rainfall rate
R	universal gas constant
R_a	impedance of load
R_{ax}	axial ratio
r_{minor}	minor axis of the characteristic ellipse
R_m	gas constant for moist air
$R^{[n]}$	n-th derivative of the auto-covariance/auto-correlation function
R_o	characteristic impedance of line used to feed the antenna
$r_{0.5}$	pattern scale; measure of the average "radius" of the characteristic ellipse
$r'_{0.5}$	pattern scale
r_0	range to the centre of scattering volume (metres)
r_o	boundary between far field and near field

s	sin (θ)
$< S >$	signal power
$< SNR >$	signal to noise ratio
t	time
t	temperature
T	sampling time
T	sampling interval
T	absolute temperature (K)
T_{ng}	noise temperature of the generator
T_{rx}	effective noise temperature of receiver
T_R	time between transmission and reception of the pulse
$T_{0.5}$	corrected fading time
T_v	virtual temperature
u	wind
u	zonal velocity
u_*	frictional velocity
u_g	geostropic wind component in the x direction
U_i	radiation intensity from a lossless isotropic source with same power input
U_m	maximum radiation intensity
U'	wind velocity gradient
v	systematic velocity
v	meridional velocity
v_a	apparent velocity
v_A	excitation voltage for array A
v_B	excitation voltage for array B
v_C	excitation voltage for array C
v_{iA}	induced voltage in an antenna i, belonging to array A
v_{iB}	induced voltage in an antenna i, belonging to array B
v_{iC}	induced voltage in an antenna i, belonging to array C
v_i	voltage induced in antenna i by the incident EM field
v'	excitation voltages for the three arrays
v_o	root mean square (RMS) velocity
v_o	turbulence (RMS)velocity
v_{RMS}	random velocity
v_t	true velocity
V	velocity
V	velocity of diffraction pattern
V	scatterer's velocity
$\mathbf{V}$	voltages at the output of the three arrays
V_a	magnitude
V_A	voltage measured for array A

V_B	voltage measured for array B
V_C	voltage measured for array C
V_f	voltage conversion factor of the system
V_1	voltage measured at the terminals of antenna 1
V_t	underestimated measured true velocity
V_t'	correct true velocity
$V_{t(filtered)}$	true velocity after filtering
V_x	zonal pattern velocity
V_x	measured voltage at the output of each array in terms of the excitation voltages of all the arrays
V_y	meridional pattern velocity
w	vertical velocity
$w(D)$	terminal velocity
W_f	width of Doppler shifted scattered signal
W_τ	width of auto-correlation function
$W(r)$	range-weighting function for receiver
$W(s)$	angular power spectrum
X_a	reactance of load
$x_1(t)$	initial time series
$x_2(t)$	second time series
(x, y)	position
z	height or altitude
z_i	auto-covariance function of a M-point complex time series
z_i	top of the CBL, the inversion height
z_0	aerodynamic roughness length
Z	radar reflectivity due to the precipitation
Z_i	impedance at the input end of the line
Z_{ij}	impedance matrix
Z_i	effective impedance of antenna i taking into account self and mutual impedances
Z_{in}	complex impedance at the input of the line
Z_L	input impedance of the antenna
Z_L	effective load impedance of array
Z_L	load impedance of antenna 1
Z_L	complex load impedance
Z_{LA}	effective load impedance for array A
Z_{LB}	effective load impedance for array B
Z_{LC}	effective load impedance for array C
Z_O	characteristic impedance of the line
Z_o	characteristic impedance of the line
Z_{OC}	measured impedances with cable open-circuited
Z_{SC}	measured impedances with cable short-circuited
Z_{11}	self impedance of antenna 1

Z_{12}	mutual impedance between antenna 1 and antenna 2
α	efficiency loss factor
α	matched line loss attenuation in nepers/unit length
α	attenuation constant (dB)
α	coupling coefficient
α	surface wind angle
α'	ratio of eddy diffusitivities, often taken to be unity
α_{xy}	coupling coefficient between array x and array y
β	phase constant of the line in radians/unit length
γ	ratio of specific heats
Γ	environmental lapse rate
Γ_d	dry adiabatic lapse rate
δ	trend
δt	sampling time
$\delta \Delta D$	actual height of the offset slope
ΔF	acoustic rate sweep
ΔR	radar pulse length
ΔR	range resolution
δR_{max}	width of range gate
ϵ_{TX}	transmission coefficient
ϵ_{tx}	transmission line loss
η	volume reflectivity
$\eta(r)$	reflectivity or expected backscattering cross section per unit volume
θ	potential temperature
θ_a	direction
θ_a	e$^-$1 half-width for polar diagram scatterer
θ_a	acoustic beam-width
θ_{ax}	axial orientation
θ_b	beam width in degrees
θ_{HP}	half-power beam widths in the θ plane
θ_{max}	effective beam width
θ_r	one-way half-power antenna beam-widths for receiving array
θ_R	e$^-$1 half-width for polar diagram receiving array
θ_s	aspect sensitivity in degrees
θ_S	aspect sensitivity
θ_t	one-way half-power antenna beam-widths for transmitting array
θ_T	e$^-$1 half-width for polar diagram transmitting array
θ_v	virtual potential temperature
θ_1	one-way half-power antenna beam-width (radians)
λ	radar wavelength (m)
ξ	scattering cross section

ξ_o	distance
ξ_o	antenna spacing
ξ_1	pattern scale
ρ	voltage reflection coefficient
ρ	magnitude force correlation
ρ	air density
ρ	amplitude reflection coefficient of the discontinuity
ρ_m	maximum value of the cross correlation
ρ_o	factor
ρ_o	air density
$\rho(r)$	spatial correlation function
ρ_{0ij}	cross-correlation maxima
σ	backscattering cross section
$\sigma(s)$	aspect sensitivity
σ_N	standard deviation of noise level
$\sigma_{\delta V}$	standard deviation
σ_{RMS}	standard deviation in the root mean square values
τ	lag
τ	surface stress
τ_x	vertical stress due to motion in the x direction
τ_y	vertical stress due to motion in the y direction
τ	width
τ	transmitted pulse length (s)
τ	transmitted pulse width
τ_{ij}	lag where the auto-correlation function is equal to the zero lag cross-correlation function
τ_x	time lag
τ'	time shift
τ'_{ij}	lag where the cross-correlation function is a maximum
$\tau"_{ij}$	lag where the auto-correlation function is equal to the maximum of the cross correlation function
τ_{tx}	ratio of transmitted pulse length
$\tau_{0.5}$	fading time
ϕ	phase
ϕ	phase shift
ϕ	latitude
ϕ	half-power beam widths in the ϕ planes
$\phi_{12}(f)$	phase factor
$\phi_1(f)$	random phase

ACRONYMS

AAP	Adelaide airport
AoA	angle of arrival
BL	boundary layer
BLR	boundary layer radar
BP	Buckland Park
CTBL	cloud topped boundary layer
FCA	full correlation analysis
FSA	full spectral analysis
IP	in-phase
IPP	inter-pulse period
ISD	isotropic scatter determination
MST	Mesospheric Stratospheric Tropospheric
PRF	pulse repetition frequency
QP	quadrature
RASS	radio acoustic sounding system
SA	spaced antenna
ST	stratospheric troposphere (radar)
SNR	signal to noise ratio
SWR	standing wave ratio
T/R	transmit/receiver
TSE	triangle size effect
UHF	ultra-high frequency
VHF	very-high frequency
VSWR	voltage standing wave ratio

Appendix B

Passive T/R switch

The T/R switch protects the sensitive receivers from being damaged by the high-powered transmission pulse. T/R switches used in VHF radars generally use PIN (P-Instrinsic-N) diodes as the switching device. These diodes are short-circuited by an application of a large DC bias current [*Reid*, 1995]. However, in the BP BLR *passive T/R switches* are used. These employ special P-N junction diodes which are switched by the presence of the RF transmitter pulse. Passive T/R switches enable precise switching when necessary, virtually instantaneous recovery and no introduction into the system of switching transients.

A simplified circuit of a passive T/R switch is shown in Figure B.1. When a transmit pulse is present all the diodes switch on, thus 'short circuiting' the receiver to ground, while presenting a high impedance path to the transmitter. Upon reception all the diodes are switched off, therefore the antenna is connected to the receiver.

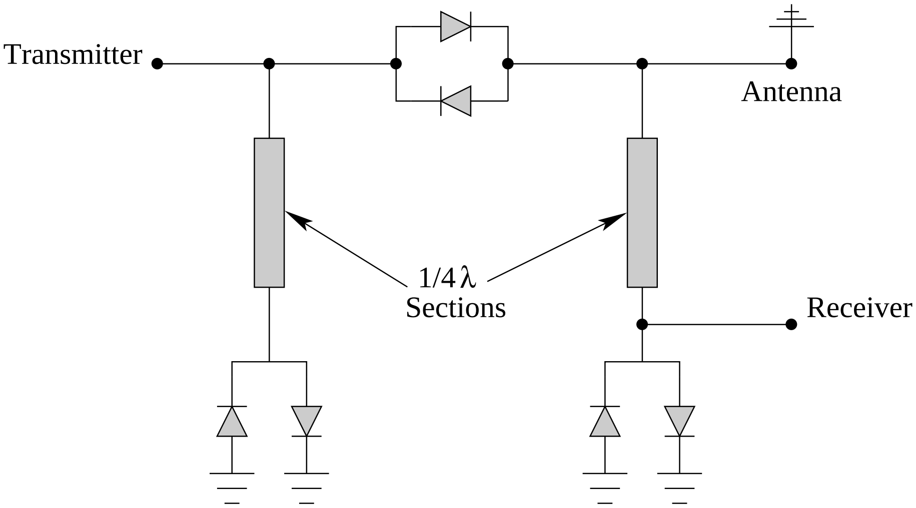

Figure B.1: Simplified circuit of a passive T/R switch

Appendix C

Vector Impedance Meter Control Program

The following program, written in Pascal was used to control a Hewlett Packard Vector Impedance Meter model 4193A. A computer is connected via a IEE488 card to the GPIB bus on the Vector Impedance Meter. The user is prompted to give a start frequency, end frequency, frequency resolution, output filename and a trigger delay which determines the amount of time between successive measurements for the VIM to stabilize before recording the value.

The output data is of the form [magnitude, phase, frequency].

```
program VIM;


uses tpdecl,crt ;
const vimname: nbuf = ’vim    ’;
      bdname: nbuf =’GPIB0  ’;
var bd: integer;
    spr: integer;
    st: string;
    freq: string;
    startfreq: string;
    stopfreq: string;
    sweepend: string;
    sweepstep: string;
    result: text;
    filename: string;
```

```
    triggdelay: integer;

{=======READING DATA========================}
function readstr(bd: integer): string;
var buf: cbuf;
    i  : integer;
    s  : string;
begin
  ibrd(bd,buf,sizeof(buf));
  i := 1;
  while (i<=ibcnt) and (buf[i] <> #10) and (buf[i] <> #13) do
  begin
    s[i] := buf[i];
    inc(i);
  end;
  s[0] := char(i-1);
  readstr := s;
end;

{=======SENDING PARAMETERS===================}
procedure sendstr(bd: integer; cmd: string);

var buf: cbuf;
    i  : integer;
begin
  for i:= 1 to length(cmd) do
    buf[i] := upcase(cmd[i]);
  ibwrt(bd,buf,length(cmd));
end;

{=======MAIN===============================}
begin
     triggdelay:= 1000;
     sweepstep:= '1';
{locating and clearing Card and Device}
     bd:=ibfind(bdname);
     ibclr(bd);
     ibonl(bd,0);
     bd:=ibfind(vimname);
     delay(100);
     ibclr(bd);
     delay(2000);
     writeln(iberr); }
```

```
{=======SETTING OUTPUT FORMAT==============}
     sendstr(bd,'FMT2T2');

{=======SETTING SWEEP RANGE================}
     writeln('PARTIAL SWEEP MEASURING USING Vector Impedence Meter (VIM)');
     writeln('---------------------------------------------------------');
     write('Starting frequency in Mhz ?');
     readln(startfreq);
     write('Stopping frequency in Mhz ?');
     readln(stopfreq);
     writeln('Sweep steps WARNING 2,3 take lots of time');
     writeln('1. 100 steps');
     writeln('2. 1000 steps');
     writeln('3. HIGH RESOLUTION');
     readln(sweepstep);
     write('What is the filename i.e. Antenna2.dat?');
     readln(filename);
     writeln('Trigger delay in ms?');
     write('(1000 is usually adequate increase if you have blank lines in data)');
     readln(triggdelay);

{=======MEASURING AND RECORDING DATA=======}
     writeln('BEGINNING MEASURING AND RECORDING PRESS A KEY TO STOP AND EXIT');
assign(result,filename);
rewrite(result);


     sendstr(bd,'TF'+startfreq+'ENPF'+stopfreq+'ENP'+sweepstep+'W1');
     repeat
       sendstr(bd,'EX');
       delay(triggdelay);
       st:=readstr(bd);
       writeln(result,copy(st,9,7),' ',copy(st,19,6),' ',copy(st,34,5));
       writeln(st);
       sweepend := copy(st,27,1);
     until (sweepend = '3') or KeyPressed;
close(result);
     writeln(spr);}
     delay(200);
     writeln('Clearing VIM')      ;
     ibclr(bd);
     delay(2000);
     writeln('Taking VIM offline');
     ibonl(bd,0);
end.
```

Appendix D

T Section calculations

The following is a brief outline of the calculation of the components used in the T-Section following [*Bowick*, 1982], pg 69 *Impedance Matching.* First consider a simple L-Section which transforms 50Ω to 200Ω (see Figure D.1). To obtain the value of the components the circuit's series Q (Q_S) and the circuit's parallel Q (Q_S) must be determined.

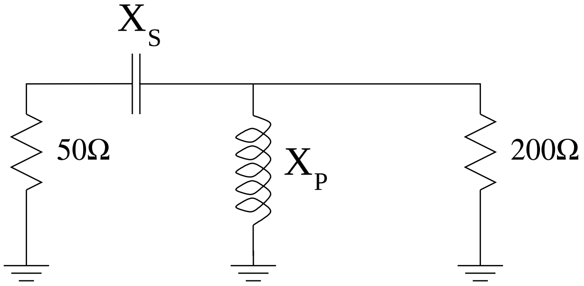

Figure D.1: L Section

$$Q_S = \frac{X_S}{R_S} \tag{D.1}$$

$$Q_P = \frac{R_P}{X_P} \tag{D.2}$$

$$Q_P = \sqrt{\frac{R_P}{R_S} - 1} \tag{D.3}$$

where X_S, X_P are the reactive series and parallel components respectively, and R_S, R_P are the series and parallel resistances. Let

$$Q_S = Q_P \tag{D.4}$$

and 50Ω and 200Ω be the values of R_S and R_P, hence giving,

$$\begin{aligned} Q_S &= \sqrt{\frac{200}{50} - 1} = \sqrt{3} && \text{(D.5)} \\ X_P &= \frac{R_P}{Q_P} = \frac{200}{\sqrt{3}} = 115.5\Omega && \text{(D.6)} \\ X_S &= Q_S R_S = \sqrt{3}50 = 86.6\Omega && \text{(D.7)} \end{aligned}$$

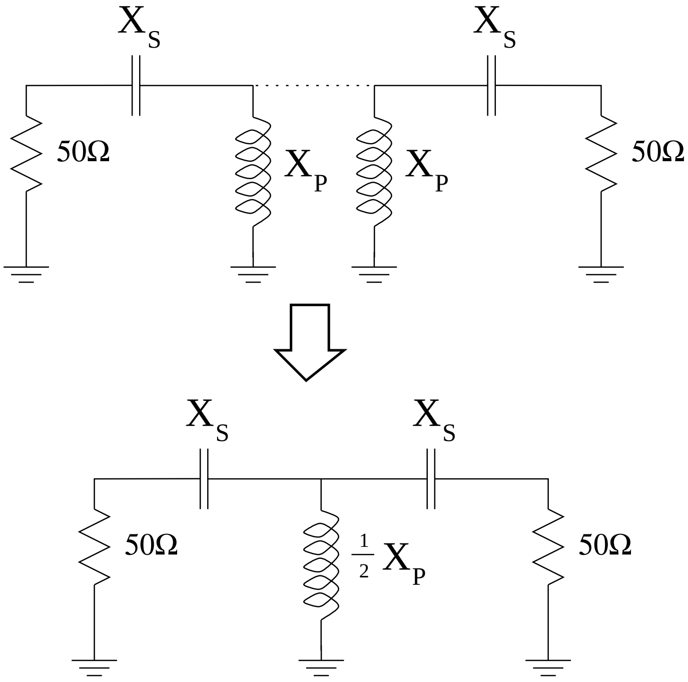

Figure D.2: Two L-Sections combined together to form a T-Section

Combine two of these L-circuits back to back to obtain the 50Ω : 50Ω T-Section transformer. Where capacitor's and inductor's values are given by,

$$C = \frac{1}{\omega X_S} = \frac{1}{2\pi 54.1E0686.6} = 34pF \tag{D.8}$$

$$L = \frac{\frac{1}{2}X_P}{\omega} = \frac{57.75}{2\pi 54.1E06} = 169.5nH. \tag{D.9}$$

Appendix E

Modifications to NEC-2 Code

The following modifications were applied to the Numerical Electromagnetic Code, thus increasing the number of segments and amount of memory used by the program, for calculation of large arrays consisting of many elements. If the computer executing the program has to use disk space as virtual memory the execution times grows rapidly, hence the need to use as much RAM as possible before resorting to virtual memory[1].

The changes shown are for the Fortran version of the code, which consists of two files, *nec2a.f* and *secnds.f*. Only modifications to *nec2a.f* are required.

Variable Name	Original Value	Altered value	Purpose
LD	300	3000	Max. Number of segments and surface patches
IRESRV	8100	9000000	Number of words in core storage
NETMX	30	150	Maximum number of
NDIMN	30	150	non radiating networks
NDIMNP	31	151	NETMX, NDIMN and NDIMNP must all be specificed.
NSMAX	30	150	Maximum number of voltage sources
LOADMX	30	200	Maximum number of load.

---

[1] Virtual memory involves using disk space as if it was memory, hence required reading and writing to the disk, which can be time consuming

Appendix F

NEC-2 Input code

The following input code for NEC-2 model a transmitting array consisting of 27 three-elements Yagis. This type of array was using for the Boundary Layer Radar. The model includes the driven elements, reflector, director, boom and an imperfect ground. No attempt was made to model the gamma match, antenna feeds, transmission lines, or combining circuitry.

```
CM      Array of 27 3-element yagis
CM      Elements are aligned 45 degrees against the baseline, counterclockwise
CM                     / / /
CM                     / / /
CM                     / / /
CM                  / / / / / /
CM                  / / / / / /
CM                  / / / / / /
CM      extended thin wire kernel
CM      imperfect ground, dielectric constant 13, conductivity 0.006
CM Aluminium conductivity 3.7e7 mhos/meter
CE
GW  1   11   -0.8125   -0.8125   2.128     0.8125    0.8125    2.128    .0254
GW  2   11   -0.9221   -0.9221   1.354     0.9221    0.9221    1.354    .0254
GW  3   11   -0.9949   -0.9949   0.58      0.9949    0.9949    0.58     .0254
GW  4   11   0.        0.        0.        0.        0.        2.800    .05
GM  4    2   0.        0.        0.        2.77      0.        0.       1.0
GM  12   2   0.        0.        0.        0.        2.77      0.       1.0
GM  36   1   0.        0.        0.        8.31      0.        0.       1.0
GM  36   1   0.        0.        0.        -4.155    8.31      0.       37.
GM  0    0   0.        0.        0.        -6.925    -6.925    0.       1.0
```

```
GE  1
EK
FR  0    1    0    0   54.1
EX  0    2    6    0   1.
EX  0    6    6    0   1.
EX  0    10   6    0   1.
EX  0    14   6    0   1.
EX  0    18   6    0   1.
EX  0    22   6    0   1.
EX  0    26   6    0   1.
EX  0    30   6    0   1.
EX  0    34   6    0   1.
EX  0    38   6    0   1.
EX  0    42   6    0   1.
EX  0    46   6    0   1.
EX  0    50   6    0   1.
EX  0    54   6    0   1.
EX  0    58   6    0   1.
EX  0    62   6    0   1.
EX  0    66   6    0   1.
EX  0    70   6    0   1.
EX  0    74   6    0   1.
EX  0    78   6    0   1.
EX  0    82   6    0   1.
EX  0    86   6    0   1.
EX  0    90   6    0   1.
EX  0    94   6    0   1.
EX  0    98   6    0   1.
EX  0    102  6    0   1.
EX  0    106  6    0   1.
LD  5    0    0    0   3.7e7
GN  0    0    0    0   13.        6.000E-03
RP  0   91   73    1   0.         0.        1.       5.
EN
```

Appendix G

System Parameters

The following table consist of the properties and parameters of the BLR third generation system.

Transmitter and receiver subsystem	
Transmitter	
Measured Peak transmitted power, P_t	1kW
Efficiency of the system, ϵ_{TX}	-1.755dB
Pulse width, τ	$1\mu s$
T/R switch	passive
Receiver	
Dynamic range	62-122dB
Digitiser	12bit
Filter type	Butterworth
Filter bandwidth, B (3dB)	1MHz
Filter bandwidth, B_6 (6dB)	1.2MHz
$B_6\tau$	1.2
rx1 effective temperature, T_{RX_1}	1400K
rx2 effective temperature, T_{RX_2}	1450K
rx3 effective temperature, T_{RX_3}	1470K
Calibration (i.e. $T_{r'} = (A_t^2 - N_{offset})/G$)	
rx1 noise offset, N_{offset_1}	8.00
rx2 noise offset, N_{offset_2}	9.24
rx3 noise offset, N_{offset_3}	7.59
rx1 apparent gain, G_1	0.0062
rx2 apparent gain, G_2	0.0064
rx3 apparent gain, G_3	0.0052

Antenna subsystem (third generation)

Receiving Array

Max Gain	15.22 dBi
Beam-width (3dB)	30 - 32°
Side lobe: Gain	-0.54 dBi
Side lobe: Angle	60°

Transmitting Array

Max Gain	19.74 dBi
Beam-width (3dB)	16 - 18°
Side lobe: Gain	0.93 dBi
Side lobe: Angle	53°
Vestigial lobe: Gain	7.13 dBi
Vestigial lobe: Angle	26°

Coupling (measured)

Array pair AB	-44dB
Array pair AC	-50dB
Array pair BC	-46dB

Appendix H

Comparison Data

The following tables are the times and dates for the radiosondes launched from Buckland Park, Grob aircraft flights near Buckland Park and radiosondes launched from Adelaide Airport.

BUCKLAND PARK RADIOSONDES: Measurements of winds from these flights were calculated either using GPS or Omega networks. Dates and times correspond to the start of the sonde flight.

	Date	Time (UTC)
GPS	31st July 1997	0306, 0637, 0951, 1354, 1636, 1927, 2237
	1st August 1997	0055, 0400, 0552, 0805
Omega	12 September 1997	0918, 1329, 1731, 2140
	13 September 1997	0127, 0537, 0926, 1324, 1418, 1748, 2159
	14 September 1997	0133, 0535
	26 September 1997	0550, 0836, 1131, 1435, 1733, 2035

Table H.1: Dates of launch times for radiosonde launched from the Buckland Park field site. Two types of radiosondes were used for determining wind velocities, GPS and Omega sonde.

GROB 109B AIRCRAFT FLIGHTS: Each of the time periods given below consisted of several observation runs. Depending on conditions and what phenomena was being observed, the individual run could be a long or short vertical sounding or fixed altitude observation.

Date	Time Period (UTC)
18th July 2000	0159 to 0406
31st July 2000	0146 to 0410
12th October 2000	0152 to 0432
20th October 2000	0254 to 0601

Table H.2: Observation periods of flights of the Grob G109B aircraft.

ADELAIDE AIRPORT RADIOSONDES: Wind measurements are determined by a wind-finding radar which tracks the balloons launched at the times given below.

Month	Date (Launch times) UTC			
June 2000	12(11,23),	13(11,23),	14(11,–),	15(11,23)
	16(–,23),	17(11,23),	18(11,23),	19(11,23)
	20(11,23),	21(11,23),	22(11,–),	
July 2000	06(11,23),	07(11,23),	08(11,23),	09(11,23)
	10(11,23),	11(11,23),	12(–,23),	13(–,23)
	14(11,23),	15(11,23),	16(11,–),	17(11,23)
	15(11,23),	16(11,–),	17(11,23),	18(11,23)
	19(11,–),	20(–,23),	21(11,23),	22(11,23)
	23(11,23),	24(11,–),	31(11,23),	
August 2000	01(11,23),	02(11,23),	03(11,23),	04(11,23)
	05(–,23),	07(11,23),	08(11,23),	09(11,23)
	10(11,–),	17(11,23),	18(11,23),	19(11,23)
	20(–,23),	21(11,23),	22(11,23),	23(11,23)
	24(11,23),	25(11,23),	26(11,–),	28(11,23)
	29(11,23),	30(11,23),	31(11,23)	

(cont)

(cont)

Month	Date (Launch times) UTC			
September 2000	01(11,23),	02(11,23),	04(11,23),	05(11,23)
	06(11,23),	07(11,–),	08(11,–),	09(11,23)
	10(11,–),	11(11,23),	12(11,23),	13(11,–)
	18(11,23),	19(11,–),	20(11,23),	21(11,23)
	22(11,–),	23(11,23),	24(–,23),	25(11,23)
	26(11,23),	27(11,23),	28(11,23),	29(11,23)
	30(11,23)			
October 2000	01(11,23),	02(11,23),	03(11,23),	04(–,23)
	05(–,23),	06(11,–),	07(11,23),	08(11,23)
	09(11,23),	10(11,23),	11(11,23),	12(–,23)
	13(11,23),	14(11,–),	15(11,23),	16(11,23)
	17(11,23),	18(–,23),	19(11,23),	20(11,23)
	21(–,23),	22(11,–)		

Table H.3: Dates of launch times for radiosondes launched from Adelaide Airport. Times of launches were either 1100 UTC or 2300 UTC. Only times where data was available are shown. If only one flight was available, for a given day, a '–' is inserted in the other time.

Appendix I

RASS speaker specifications

Specifications for VAF E-115 speaker for RASS operation.

Construction
Marine Ply construction
2-pack lacquer finish
Fibreglass cone woofers with synthetic rubber roll surrounds

Dimension

Height	1209 mm
Width	1002 mm
Depth	492 mm
Weight Approx	120 kg

Frequency Response

80 Hz - 180 Hz	± 1.5 dB
70 Hz - 210 Hz	± 3.0 dB

Impedance

Nominal	6 W
Z min	5.7 W
Z max	19.6W @ 85 Hz

Sensitivity
109 dBA @ 1 m @ 1 Watt RMS @ 6 W (2.45 VRMS)
110.25 dBA @ 1m @ Equivalent of 1 Watt RMS @ 8 W (2.83 VRMS)

Power Handling @ Maximum SPL within passband
Continuous (1) (100% Duty Cycle indefinitely)
800 Watts RMS @ 6W (69.3 VRMS)
138 dBA

Continuous (2) (30 minutes continuous or 50% Duty cycle indefinitely)
1000 Watts RMS @ 6W (77.46 VRMS)
139 dBA

Peak (1 minute continous or 5% duty cycle indefinitely)
2000 Watts RMS @ 6W (109.5 VRMS)
142 dBA

Appendix J

A VHF boundary layer radar: First results

This is a reprint of a paper published in *Radio Science* **33**, 845-860 (1998).

Radio Science, Volume 33, Number 4, Pages 845–860, July–August 1998

A VHF boundary layer radar: First results

R. A. Vincent, S. Dullaway, A. MacKinnon, I. M. Reid, and F. Zink
Department of Physics, University of Adelaide, Adelaide, South Australia, Australia

P. T. May
Bureau of Meteorology Research Centre, Melbourne, Victoria, Australia

B. H. Johnson
Atmospheric Radar Systems, Adelaide, South Australia, Australia

Abstract. The development of a novel VHF radar designed to measure winds and temperatures in the planetary boundary layer is described. The radar operates at 54.1 MHz and is compact and easily transportable. The antenna system consists of 12 Yagis grouped into three subarrays arranged in the form of an equilateral triangle. Transmission takes place on the whole array, and reception takes place on the three subarrays, with winds measured by the spaced antenna technique over a height range between 300 and 3000 m. Results from field trials conducted in southern Australia in a variety of meteorological conditions are presented. Comparisons with high-resolution radiosondes launched from the radar site show excellent agreement, with rms differences between radiosonde and radar wind components being about 1.5 m s^{-1}. Observations carried out in rain show that echoes from precipitation are clearly distinguishable from clear-air echoes. Unlike UHF radars, this means that vertical air velocities can be measured during precipitation, and the evolution of drop-size distributions can be studied down to low altitudes. It is shown that temperatures derived from a radio acoustic sounding system are measured up to heights near 2 km, depending on background wind conditions.

1. Introduction

Stratosphere-troposphere (ST) radars or wind profilers are powerful tools for atmospheric research and operational meteorology [e.g., *Gage*, 1990]. While the ST radar field is relatively mature, development has proceeded in step with advances in technology. In the last few years, the advent of cheap, powerful computers, together with inexpensive computer memory for storing raw data and reliable solid-state transmitters, have opened up new possibilities for ground-based radar studies of the atmosphere. Developments in conceptual techniques include the use of interferometry to improve estimates of pointing directions and correct such important parameters as vertical air velocity. The ultimate aim is to derive as many atmospheric parameters as possible in real time to aid research and forecasting.

The last decade has seen the development and large-scale deployment of boundary layer (BL) profilers. These low-power systems have been designed for the express purpose of observing many of the important meteorological phenomena that occur in the lowest part of the troposphere. Typically, frequencies near 1 GHz are used for UHF boundary layer radars. Examples are the widely used radar system developed at NOAA's Aeronomy Laboratory which uses a frequency of 915 MHz [e.g., *Ecklund et al.*, 1988, 1990; *Carter et al.*, 1995] and the L-band (1.357 GHz) system developed by the Kyoto University group [e.g., *Hashiguchi et al.*, 1995]. Systems such as these are being used to investigate boundary layer wind and temperature fields and, since they are sensitive to hydrometeors, the precipitation field.

Paper number 98RS00828.
0048-6604/98/98RS-00828$11.00

Radars operating in the lower VHF band (~50 MHz) have primarily been used to measure winds to as high an altitude as possible, which requires the use of physically large antennas and high transmitter powers. However, effects such as long recovery times in transmit-receive systems and reflections or ringing in antennas and transmission cables mean that these larger systems generally cannot make measurements in the lowest 1–2 km of the atmosphere. However, pioneering work by the French group in Toulon show that it is possible to use small antennas and make useful BL measurements at VHF [e.g., *Crochet et al.*, 1994; *Fillot et al.*, 1997].

Operating at UHF offers many advantages. These include (1) the use of antennas that are physically small but relatively large compared with the radar wavelength, so that narrow beams can be generated; (2) low external noise; and (3) the availability of wide bandwidths, which means good height resolution. On the other hand, when precipitation or heavy cloud is present, echoes from hydrometeors dominate echoes from the clear air, which makes measurements of vertical velocity difficult. This is a particular limitation when radio acoustic sounding systems (RASS) are used to measure atmospheric temperatures at UHF with vertical pointing beams, since the sound velocity should be corrected for the vertical wind [e.g., *Angevine et al.*, 1994a]. Another limitation with RASS at UHF is that the acoustic frequencies (~0.8–1.6 KHz) suffer rapid attenuation, which limits the upper height to which temperatures can be obtained [*May et al.*, 1988].

The advantages in operating at VHF include the following:

1. Precipitation echoes are comparable in strength to, or weaker than, the clear-air echoes, and the precipitation and clear-air echoes are usually well separated in the Doppler spectrum. Hence a single VHF radar can simultaneously study the dynamics and cloud microphysics of precipitating clouds [e.g., *Rajopadhyaya et al.*, 1993].
2. Measurement of the vertical gradient of the vertical velocity gives the divergence of the wind field, especially in storm conditions when the vertical motions and gradients are large.
3. VHF BL radars are unlikely to suffer the problems with contamination by bird and bat echoes that UHF BL radars often encounter [*Wilczak et al.*, 1995; *May*, 1995].
4. A VHF/RASS boundary layer system should also have a better height coverage than a similar UHF system because the lower-frequency sound waves used suffer much less attenuation.

Thus a 50-MHz BL system has many advantages for the study of shallow weather systems, such as summertime cold fronts across southern Australia [*Wilson and Stern*, 1985]. Other applications include sea-breeze fronts which trigger convection. Finally, there is much that we do not understand about scattering processes from the atmosphere. Measurements should be made at a range of frequencies in the VHF and UHF bands to investigate these processes as well as exploit the research and operational potential of all systems.

The Atmospheric Physics group at the University of Adelaide has been developing radars at MF/HF and VHF for studies of both the upper and lower atmospheres. A major design goal has been to develop systems that have as many features in common as possible. Here we describe a VHF (54.1 MHz) radar that has been developed since 1994 for boundary layer studies. The aim is to study winds and temperatures in the lowest 2–3 km of the atmosphere with good height and time resolution and to extend the scope of boundary layer studies to include precipitation and vertical air motions in the presence of precipitation. The overall system design is briefly described in section 2, and some of the first wind and RASS measurements are presented and discussed in section 3.

2. System Design

A number of factors were taken into account in the development of the Adelaide VHF boundary layer (BL) radar. The prime requirements were that the system should be flexible in operation, relatively easy to transport, and power efficient so that it could be used at remote sites. A lower height limit of about 300 m was specified, and it was required to measure winds regularly to heights of 2–3 km in order to overlap with observations made with a ST VHF radar located at the Buckland Park field site [*Vincent et al.*, 1987].

To achieve these aims, the system shares a number of features common to other radar systems recently developed by our group in Adelaide. In order to obtain high mean power it was decided to use a compact, modular, solid-state transmitter that is capable of a high duty cycle (10%). The modular nature of the transmitter means that transmit-receive antennas can be configured in different ways to allow different wind measuring techniques (e.g., Doppler, spaced antenna, and interferometric) to be investigated and used as appropriate. A receiver and data acquisition system (RDAS) was developed with wide dynamic range and sufficient amounts of memory (RAM) for the temporary storage of raw data. The data are then downloaded to the host computer for on-line analysis/permanent storage while the next sequence of data is being acquired. For operational flexibility, as many operating parameters (e.g., receiver gain, height range, height increment, etc.) as possible are placed under computer control. This enables a wide range of experiments to be configured in software and operated sequentially. System control and data analyses are undertaken with a PC computer that is easily networked. It is therefore both simple and inexpensive to add more computing power as required. Data are analyzed with a proprietary data analysis and display package and stored on disk for further off-line processing. Raw data can also be stored for later analysis in other ways.

2.1. Antenna Configuration

The low-height performance of 50-MHz ST systems is limited by the use of large antenna arrays and problems associated with ringing after the transmitter pulse, which hampers receiver recovery. Thus a VHF BL radar requires small antennas, which implies wide beam widths, so that ground clutter and interference to and from other operators may be a problem. Fast transmit-receive switches must be used and antenna ringing minimized to ensure reception at low heights. It was decided to utilize a spaced antenna (SA) configuration so that only vertically pointing beams are used. This arrangement is more compact than Doppler systems, and it eliminates the height-smearing problem that occurs when obliquely pointing wide beams are used for Doppler sounding [*Fillot et al.*, 1997] as well as potential problems associated with anisotropic backscatter which complicate wide-beam Doppler measurements [*Röttger*, 1984]. Another potential advantage of the SA configuration is that the data can be used for interferometric studies as well as conventional spaced antenna wind measurements. Interferometric techniques can then be used to study the scattering irregularities and have the potential to correct for possible contamination of the vertical velocity measurements caused by tilted layers [*Vincent and Röttger*, 1980].

Figure 1 shows the antenna configuration adopted for initial measurements with the VHF BL system. The arrangement is a compromise between making the subarrays as small as possible to minimize ringing and large enough to ensure an adequate power-aperture product. Three subarrays, each consisting of groups of four three-element Yagis, are arranged in an equilateral triangle. The whole array is used for transmission and each group is used for reception. An equilateral triangle arrangement reduces the chances of systematic biases in SA wind measurements, as can occur if other configurations, such as a right-angle triangle, are used. The optimum spacing of antennas in SA mode is when the mean cross correlation at zero lag is about 0.5 [*Briggs*, 1984]. Preliminary trials showed that the basic spacing should be at least 1.5λ (8.32 m), and this was chosen as the initial spacing. A reevaluation of the spacing took place after the radar had operated in a variety of meteorological conditions, as discussed in section 3.1.

The configuration adopted ensures that grating lobes on transmission are not significant. Figure 2 shows plots of the one-way polar diagrams for the receiving and transmitting arrays. The transmitting array has a half-power half width of 10°, corresponding to an effective area of about 250 m^2, while the respective values for the receiving antennas are 18° and about 80 m^2. However, as *May* [1990] has shown, the overall effective area of the system depends on the scattering mechanism. For the situation of isotropic volume-scatter the effective area is given by

$$A_{\text{eff}} = \frac{2A_T A_R}{(A_T + A_R)} \tag{1}$$

where A_T and A_R are the respective areas for the transmitting and receiving antennas. In this case, $A_{\text{eff}} \approx 120\ \mathrm{m}^2$. One problem with such relatively wide beams is the possible effects of ground clutter, but by suitably spacing and orientating the Yagi antennas it is possible to partly null out clutter and interference that arrive at low elevations.

2.2. Operating Parameters

Table 1 summarizes the range of possible operating parameters. In the evaluation of the system a 1-μs pulse length was used to achieve the desired 150-m range resolution, and a 2-MHz receiver bandwidth was selected to ensure that fast receiver recovery occurs and the desired lower height limit of about 300 m is attained. A particular feature of the system is the high degree of computer control of the system configuration, such as height coverage, range resolution, and so on. If necessary, a number of different ex-

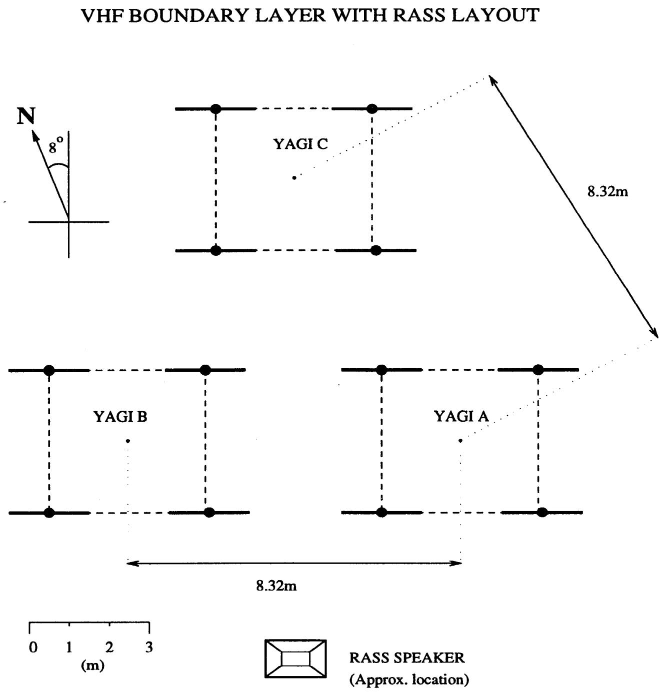

Figure 1. Plan view of VHF boundary layer radar antennas.

periments can be programmed to take place in any desired sequence. This is particularly useful while, as at present, the optimum operating parameters for SA wind and RASS measurements were being determined.

Initial tests suggest that in the spaced antenna mode the operating parameters shown in Table 2 give satisfactory performance. These values give a lower detectable wind speed of ~1 m s^{-1} and an upper limit of about 80 m s^{-1}. With these settings the mean power is about 20 W, giving a power-aperture product of at least 2500 W m^2. The complex amplitudes received at the three antennas are analyzed in the standard method using the full correlation analysis (FCA) discussed by *Briggs* [1984]. The quality of the data was assessed using the standard criteria described by *Briggs* [1984], although only data with signal-to-noise ratios (SNR) greater than 0 dB (after coherent integration) were accepted, as modeling studies show that the accuracy of SA wind determinations decreases rapidly for smaller signal-to-noise ratios [*Holdsworth*, 1995].

3. Initial Results

Initial tests of the BL system were carried out at the University of Adelaide's Buckland Park field station (35°S, 138°E), where it is located immediately adjacent to a VHF ST profiler [*Vincent et al.*, 1987]. The site is very flat and upwind of any significant topography. However, the site is rather crowded with buildings, antenna masts, etc., and there is the potential for significant ground clutter, which can make the detection of the clear-air echoes difficult. Fortunately, clutter has not proved to be a major problem, except at the lowest range gates of 300–450 m, and is easily distinguished from atmospheric echoes by its characteristic slow fading. A number of algorithms are being tested to reduce the effects of ground clutter and intermittent clutter due to aircraft, including the use of wavelet transforms [*Jordan et al.*, 1997].

In order to assess the performance of the radar, a series of intercomparisons were made during the period July 31 to September 26, 1997, with simultaneous measurements made with high-resolution ra-

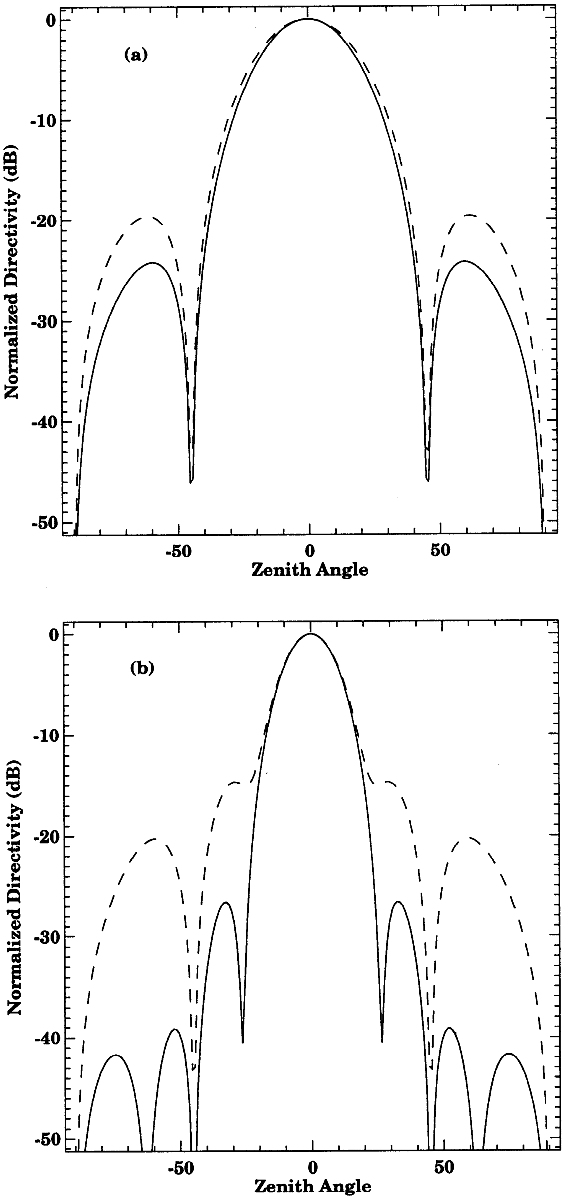

Figure 2. Antenna polar diagrams. The solid lines indicate the *E* plane, and the dashed lines indicate the *H* plane. (a) Receiving antenna. (b) Transmitting antenna.

Table 1. Operating Parameters of the VHF Boundary Layer Radar

Parameter	Value
Transmitter power	3×350 W peak envelope power
Transmit/receive switch	passive, $\sim$1-μs recovery time
Antenna bandwidth	$\sim$4 MHz
Receiver bandwidth*	2 MHz to 250 kHz
Pulse length*	0.7–10 μs
Maximum duty cycle	10%
Sample height*	100-m minimum, 25-m increments
Pulse repetition frequency*	up to 50 kHz
Coherent integration*	up to 4096 points
Digitizers	12-bit
Signal averagers	24-bit
Memory	1 Mbyte per receiver

*Software selectable.

diosondes (Vaisala RS80-15) launched from Buckland Park. Three campaigns were carried out in a variety of meteorological conditions, including significant precipitation. Campaign I occurred between July 31 and August 1, campaign II took place between September 12 and 15, and the final campaign occurred on September 26, 1997. Results from all three campaigns were used to evaluate the performance of the radar, such as accuracy of wind measurements. To illustrate the capabilities of the system, we focus on some of the results from the first two campaigns, which were conducted under very different weather conditions.

Table 2. Typical Spaced Antenna Parameters Used in Campaigns

Parameter	Value
Parameter	Value
Pulse repetition frequency*	20,480 Hz
Number of coherent integrations*	1,024
Number of data points per sample*	1,024
Height coverage*	300–3200 m
Record length*	52.4 s
Range resolution*	150 m
Maximum lag*	4 s
Sample rate	0.05 s

*Software selectable.

3.1. Radar and Radiosonde Wind Comparisons

A primary goal of the campaigns was to assess the accuracy of the radar wind measurements by comparing them with radiosondes equipped with medium- to high-resolution wind-finding systems. For campaign I a Global Positioning System (GPS) tracking system was used, while for the campaigns starting on September 12 and 26, the balloons were tracked using VLF Omega navigation signals. For each flight the radar winds at each 150-m range gate were averaged over a period of 20 min, centered on the time at which the balloon had reached an altitude of 1 km. At least three radar observations were required at a given level to produce a mean value. No consensus averaging [*Strauch et al.*, 1984] was used in producing the mean wind velocities. In all, there were 29 flights and 144 samples.

Figure 3 shows scatterplots of the zonal (u) and meridional wind (v) components. It is apparent that the observations are highly correlated ($r = 0.95$), with the points distributed reasonably evenly around the line of unit slope. Only in the case of the v component are there any significant outliers, with six points lying about 5 m s^{-1} away from the line. These points came from two consecutive soundings in which there appeared to be significant curvature in the wind field. Table 3 summarizes the results of the comparisons. There are two lines for each wind component, with the second line corresponding to the case where the two soundings mentioned previously were discounted. Whether these soundings are included or not, the comparisons are very good, with rms differences between the radar and radiosonde winds being about 1.5 m s^{-1}.

These results compare very favorably with the results from similar studies. Many earlier comparisons were between profiler and radiosonde release sites separated by many tens of kilometers, and so some of the differences could be ascribed to spatial variability. For example, *Vincent et al.* [1987] compared 50-MHz ST profiler winds measured at Buckland Park with radiosondes released from Adelaide Airport, situated some 36 km to the south. They found rms speed differences in the 2–6 km height range of 3–4 m s^{-1}. The most extensive intercomparison using collocated soundings is that of *Weber and Wuertz* [1990], who compared 915-MHz profiler and radiosonde observations conducted at Stapleton Airport in Denver, Colorado, over a 2-year period. After editing their data to remove outliers, they found rms component differences of about 2.5 m s^{-1}.

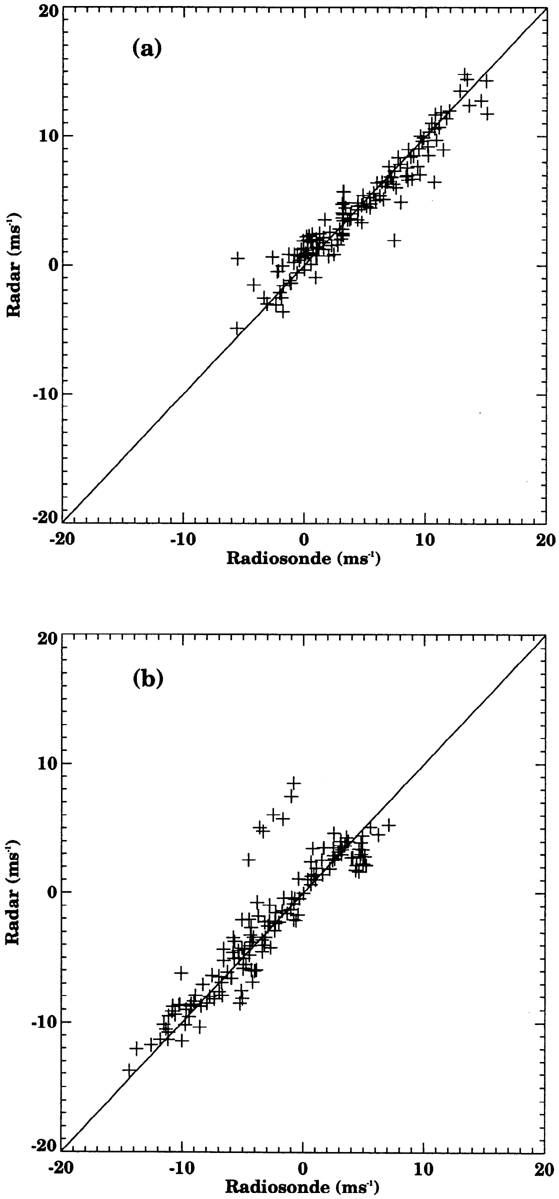

Figure 3. Scatterplot of wind velocities measured by radar and radiosondes. (a) zonal component and (b) meridional component. Lines of unit slope are shown.

There are fewer comparisons of boundary layer measurements. *Hashiguhi et al.* [1995] report rms

Table 3. Statistics of Radiosonde/Profiler Comparisons for Zonal (u) and Meridional (v) Wind Components

	Correlation	Mean Difference, ms^{-1}	Intercept, ms^{-1}	Slope	RMS, ms^{-1}
u	0.96	-0.05	0.72	0.86	1.4
	(0.96)	(-0.10)	(0.74)	(0.83)	(1.4)
v	0.94	-0.47	0.12	0.93	2.2
	(0.98)	(-0.13)	(0.26)	(0.94)	(1.3)

Profiler observations are averaged over 20 min from the time of launch of the radiosondes, and comparisons were made at each radar range bin whenever there were three or more radar observations in that bin. There were a total of 29 profiles for each instrument. The intercept and slope refer to the weighted least squares fit straight line to the scatterplots shown in Figure 3, while the rms values indicate root-mean-square difference between radiosonde and radar data. The values in parentheses refer to comparisons with two flights removed (see text).

component differences of better than 3 m s^{-1} when they compared L-band boundary layer profiler winds with winds derived from radiosondes released from the radar site. An extensive comparison using Tropical Ocean-Global Atmosphere/Coupled Ocean-Atmosphere Response Experiment (TOGA-COARE) data taken with 915-MHz profilers and radiosondes reveals rms differences of less than 1 m s^{-1} [*Riddle et al.*, 1996]. *Angevine and MacPherson* [1995] compared 915-MHz profiler wind measurements with simultaneous aircraft observations and found rms differences of less than 1 m s^{-1}. The differences are site dependent. For example, *May* [1995] found differences of ~2–3 m s^{-1} in a highly convective boundary layer during the day in central Australia. Comparisons were even worse at night because of scattering from bats.

The excellent agreement between the wind velocities measured here by the two techniques probably reflects the low spatial variability inherent in this comparison. As noted, Buckland Park is situated on the flat Adelaide Plains upwind of any significant topography, so spatial variability was minimized as the balloons drifted away from the site. It should be noted, however, that this comparison ignores the errors inherent in the radiosonde soundings. One factor that is often ignored in these comparisons is the smoothing required to reduce the effects of the pendulum motion of the sonde package. This smoothing acts as a low-pass filter that reduces the amplitude of short-vertical-wavelength wind variations. The length of the filter in the GPS-sonde measurements was 60 s and was 240 s in the Omega-sonde wind determinations. Given the ~4 m s^{-1} ascent rate of the balloons, the effective height resolution of the radiosondes is several hundred meters. This reduces the small-scale wind variations relative to those observed by the radar. Some of the Omega-sonde data were reprocessed with a shorter filter length of 150 s to see how significant this effect was. The rms deviation from the wind speeds processed with the normal 240-s filter was about 0.7–1 m s^{-1}. As expected, the deviations were largest where the wind curvature was greatest.

There are a number of factors that influence the accuracy of radar wind measurements using the spaced antenna technique. As noted above, the optimum antenna spacing is where the spatial correlation is about 0.5. Ground-pattern statistics obtained from the full correlation analysis (FCA) were used to test how well this was satisfied with the present arrangement, as well as to provide other useful information on the scattering irregularities. In the FCA, the ground diffraction pattern is modeled as a series of concentric ellipses of constant correlation, ρ. The size and orientation of the characteristic ellipse for which $\rho = 0.5$ are convenient measures of the average pattern scale and orientation. Pattern-scale statistics obtained from spaced antenna measurements in the three campaigns are summarized in Table 4. The most probable value of 8.5 m is identical to the antenna spacing of 8.3 m (1.5λ), which shows that the spacing was close to optimal. Table 4 also shows another useful pattern parameter, the axial ratio, which

Table 4. Characteristics of Ground Diffraction Pattern

	Most Probable	Mean
Pattern scale, m	8.5	11.2
Axial ratio	1.125	1.48

is a measure of the elongation of the characteristic ellipse. The most probable and mean values are both less than 1.5, which in practice means that the average pattern is not significantly different from circular [*Wright and Pitteway*, 1978].

Profiles of the pattern scale with height, such as those given in Figure 4 for the first two campaigns, suggest that there is a small increase in pattern scale with increasing height. As the pattern scale and the angular spectrum or width of the backscattered radiation are a Fourier transform pair [e.g., *Briggs*, 1992], this indicates that there is a narrowing of the angular spectrum with height and hence a change in the aspect sensitivity of the scattering irregularities. In order to make a quantitative estimate of the width of the angular spectrum it is necessary to make some assumptions about the angular dependence of the antenna polar diagrams and of the angular spectra. The almost circular nature of the correlation functions suggests that energy is backscattered almost uniformly from around the zenith and is just a function of the zenith angle φ. Assuming that the antenna polar diagrams and angular spectrum have a Gaussian dependence and that the irregularities are confined to narrow layers, then the relationship between the spatial correlation function and angular spectrum has the simple form given by

$$\rho(r) = \exp(-\pi s_o^2 r^2), \tag{2}$$

where $s_o = \sin\varphi_o$ and r is the antenna separation in radar wavelengths [*Briggs*, 1992]. If

$$\sigma(s) \propto \exp(-s^2/s_I^2), \tag{3}$$

$$G_T(s) \propto \exp(-s^2/s_T^2), \tag{4}$$

$$G_R(s) \propto \exp(-s^2/s_R^2), \tag{5}$$

describe the angular spectrum s_I of the irregularities and G_T and G_R are the transmitter and receiver polar diagrams as a function of $s = \sin\varphi$, respectively, then

$$\frac{1}{s_o^2} = \frac{1}{s_I^2} + \frac{1}{s_T^2} + \frac{1}{s_R^2}. \tag{6}$$

In the present case, $\varphi_T = 12°$ and $\varphi_R = 21.8°$, so, from the measured values of pattern scale, $\rho_{0.5}$, it is straightforward to estimate φ_I, the angular width of the atmospheric echoes.

The scale at the top of Figure 4 gives the conversion of the pattern scale to angular width. An infinite value corresponds to isotropic scatter. The rather narrow angular widths observed in the lowest range gates are probably caused by incomplete removal of slow fading clutter. However, the decrease in φ_I with height is most likely real. There are at least two reasons for the effect. First, the backscattering irregularities may be more aspect sensitive in the more stable free atmosphere above the well-mixed boundary layer. Second, it is possibly a selection effect, as irregularities which scatter energy preferentially from overhead are more likely to be observed by the vertically pointing radar at longer ranges, where the SNR are smallest.

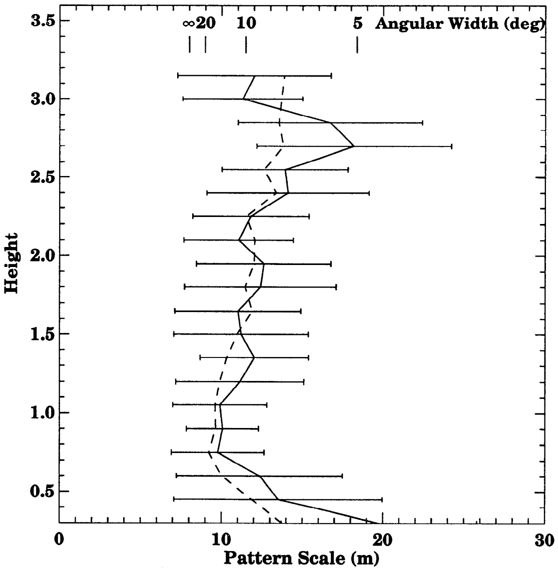

Figure 4. Vertical profiles of mean pattern scale for campaign I (solid line) and campaign II (dashed line). The scale at the top gives the angular width of the backscattered echoes.

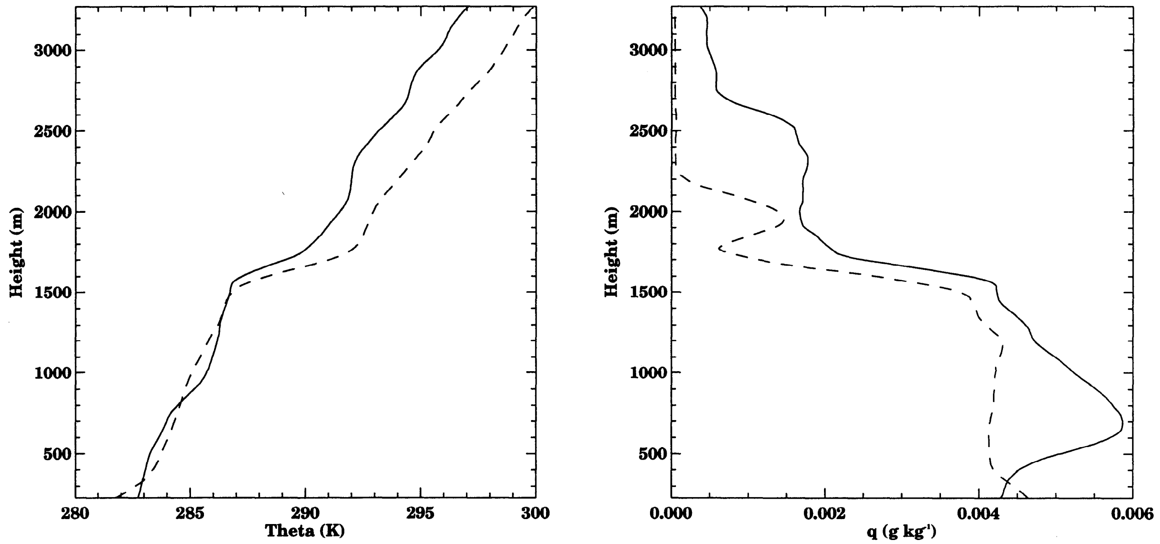

Figure 5. Vertical profiles of (left) potential temperature and (right) specific humidity derived from radiosonde soundings at 1206 LT (solid line) and 0206 LT (dashed line).

3.2. Campaign I

During this period a strong high-pressure region (~1035 hPa) was centered over the site. The BL observations were interleaved with observations with another radar also undergoing tests at Buckland Park, so the effective sample period was 2 min. Eleven radiosondes were launched at intervals of approximately 3 hours.

Day and night profiles of potential temperature and specific humidity q are shown in Figure 5. There is a marked subsidence inversion clearly evident in all profiles. The daytime boundary layer is reasonably well mixed but contains a localized stable layer at a height of about 800 m and a corresponding maximum in specific humidity. The nighttime profile shows a residual mixed layer overlying a typical ground-based radiation inversion. Figure 6 shows the time-height cross section of the signal-to-noise ratios (SNR). Values were smoothed over 30 min to reduce some of the short-term variability. There is a clear relationship between the strong subsidence inversion and the layer of enhanced reflectivity, analogous to the results of *Angevine et al.* [1994b] with a 915-MHz profiler. This example is particularly clear compared with typical 915-MHz estimates of boundary layer depth, but it is not evident if it is the result of the difference in radar frequency or of the intense subsidence inversion. The nighttime profiles show the growth of a nocturnal inversion at altitudes below 400 m and a fossil mixed layer (residual layer) that is very evident in q at heights below 1200 m. During the night, there is no heating from below to produce turbulent fluctuations of temperature and moisture (and hence scattering irregularities) in the fossil mixed layer, a condition exacerbated by the light winds.

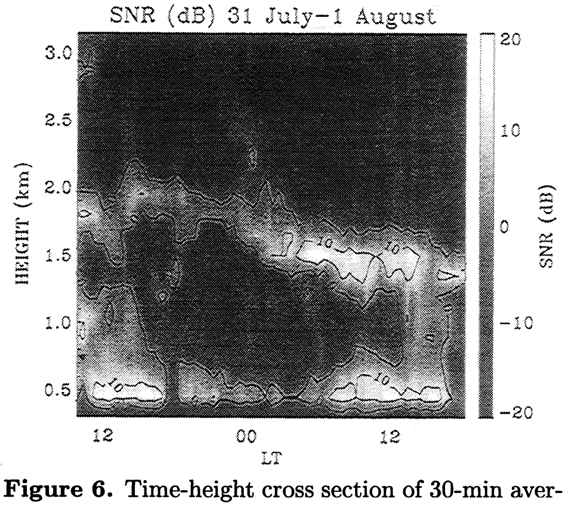

Figure 6. Time-height cross section of 30-min average signal-to-noise ratios observed in campaign I.

Meteorological parameters recorded during the radiosonde ascents can be used to gain some insight into radar performance. The received power P_R is related to the range R and radar reflectivity η by

$$P_R \propto \frac{\eta}{R^2} \tag{7}$$

The reflectivity is related to the turbulent refractive index C_n^2, which, in turn, can be expressed in terms of the outer scale of turbulence and the gradient of radio refractive index, M, where

$$\begin{aligned} M &= -77.610^{-6}\frac{p}{T}\left(\frac{\partial ln\theta}{\partial z}\right) \\ &\left[1+\frac{15500q}{T}\left(1-\frac{1}{2}\frac{\partial lnq/(\partial z)}{\partial ln\theta/(\partial z)}\right)\right] \end{aligned} \tag{8}$$

and z is height [*VanZandt et al.*, 1978]. Vertical profiles of M^2 were constructed from profiles of temperature T, pressure p (measured in hectopascals), potential temperature q, and specific humidity. The observations were made with 2-s time resolution, equivalent to approximately 8–10 m height resolution.

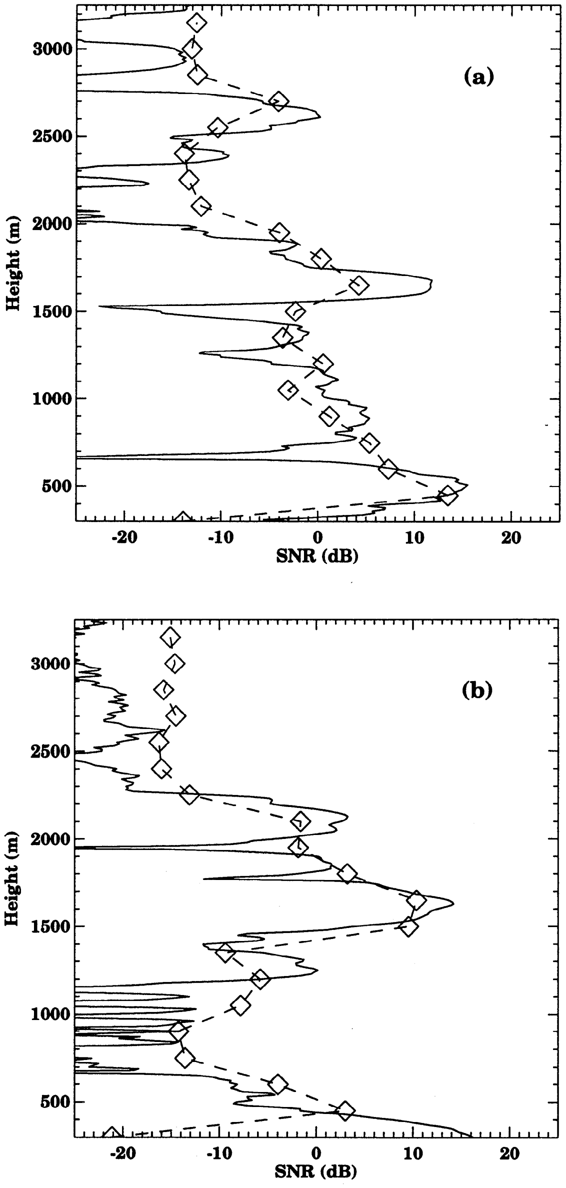

Figure 7. Vertical profiles of refractivity from radiosondes (solid line) and radar (dashed line) measurements for (a) 1200 LT July 31, 1997, and (b) 0206 LT August 1, 1997.

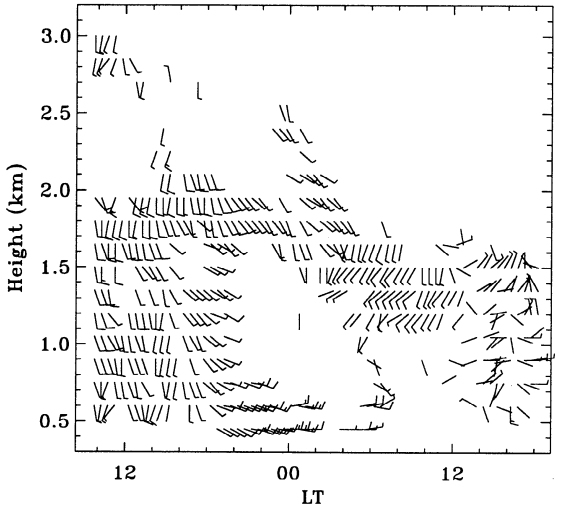

Figure 8. Half-hour average horizontal winds measured between July 31 and August 1, 1997. A half barb represents 2.5 m s^{-1}, and a full barb represents 5 m s^{-1}.

Figure 7 compares SNR values in decibels observed by the radar and estimated from the radiosonde soundings during both day and night conditions. The range-corrected reflectivity profiles constructed from the sonde values have been smoothed to give a height resolution comparable to the radar and have been increased by an arbitrary factor of 175 dB to bring them into approximate coincidence with the radar

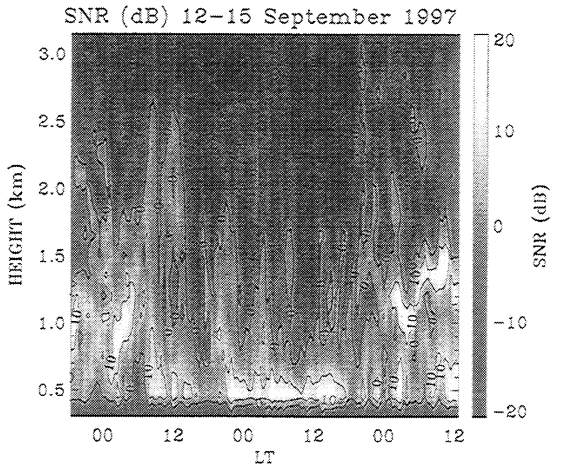

Figure 9. Same as for Figure 6, but for campaign II.

values. It is evident that the profiles agree rather well in shape and indicate that the time delays in the radar system were calibrated reasonably correctly. Both the sonde and radar profiles are characterized by strong peaks at heights near 1500 m and very weak reflectivities at night at heights between 500 and 1200 m.

The corresponding horizontal wind field is shown in Figure 8. The winds were very light, rarely exceeding 5 m s^{-1}. No winds were recorded in the lowest range gate at 300 m due to slower recovery in one of the receivers. However, winds were frequently measured at the second lowest range gate at 450 m, and observations extended to heights near or above 2 km. Noticeable gaps in the wind measurements occurred during periods centered on 0000 and 1000–1200 LT on August 1. In the latter interval, no winds were measured at heights near 0.5 km, despite the fact that the SNR was near 10 dB. The cause was the presence of stronger than average slow fading ground clutter superimposed on the atmospheric echoes. This emphasizes the need for improved clutter suppression. The gap centered on midnight was caused by SNR values that fell as low as -20 dB in the height range between 600 and 1500 m.

3.3. Campaign II

The second case study centered on the passage of a cutoff low across the radar site. A time-height cross section of SNR is shown in Figure 9, and Figure 10 shows the wind field, where its vortex nature is clearly evident. The SNR plot shows little evidence of the layering so evident in Figure 6, and this is also evident in profiles of potential temperature and humidity (Figure 11), which show a much smoother variation with height than is evident in the profiles in Figure 5. The high SNR means that there were often sufficient useful echoes to produce winds at most times at heights between 450 m and 3000 m.

During this campaign, quite heavy rain fell on occasion. The rain gave the opportunity to test the capability of the profiler to distinguish rain echoes from the signals scattered from the clear air despite the expected large amount of spectral broadening due to the wide beam width. That rain echoes can be detected is illustrated in Figure 12, which shows stacked plots of Doppler spectra normalized to the strongest signal in each spectrum. The spectra, which were constructed by averaging nine spectra obtained in a 16-min interval, show strong precipitation echoes with downward velocities in the range 5–10 m s^{-1} in the height range between 500 and 2000 m. At this time the precipitation system was quite shallow. Satellite measurements of cloud top temperatures over Adelaide at this time were only about -10°C, with deeper cloud about 300 km to the east.

The important point is that the clear-air echo can be used to measure the vertical air velocity as a function of height. The ability to distinguish the clear-air and precipitation echoes is also an impor-

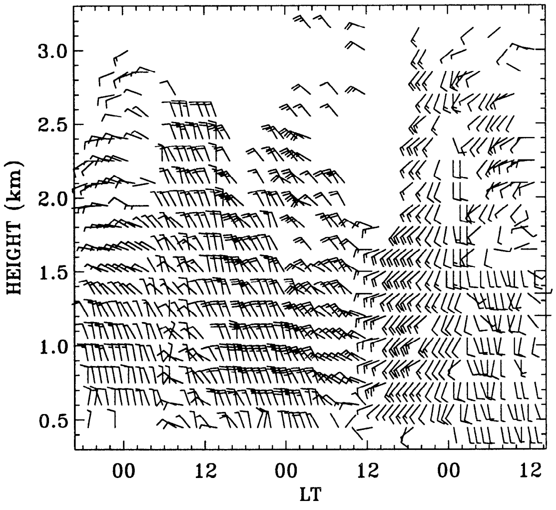

Figure 10. Same as for Figure 8, but for campaign II.

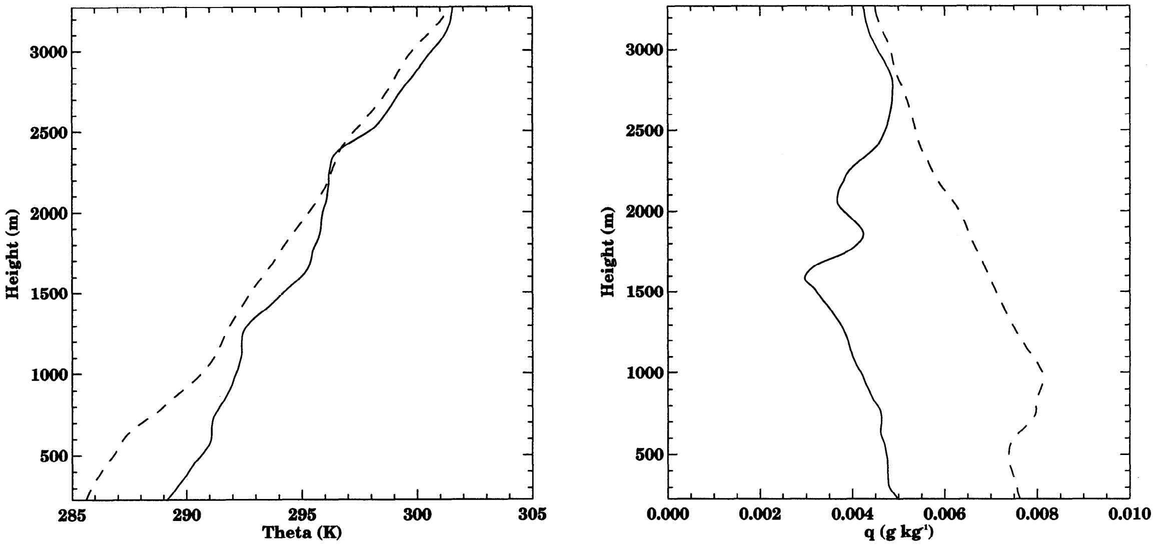

Figure 11. Velocity profiles of (left) potential temperature and (right) specific humidity derived from soundings on September 13 at 1057 LT (solid line) and 2348 LT (dashed line).

tant factor in the deconvolution procedures required to deduce drop-size distributions [*Rajopadhyaya et al.*, 1993]. All these factors illustrate the capability of the VHF profiler for observing mesoscale detail within weather systems, including vertical wind measurements in rain.

3.4. RASS Measurements

In common with other profiler-based RASS systems, the Adelaide BL RASS uses a FM CW acoustic excitation to ensure that a range of temperatures can be measured [*May et al.*, 1990]. Pseudorandom, sawtooth, and triangular sweep types are software selectable, together with appropriate bandwidths and dwell times to ensure a good match at the Bragg frequency [*May et al.*, 1990; *Angevine et al.*, 1994a]. The use of fast digitizers, and limited amounts of coherent integration give an effective sample rate of 320 Hz and ensure a Nyquist frequency significantly higher than the acoustic echo. The power spectra computed from the 1024 point samples at each height encompass both the acoustic-echo peak near 120 Hz and the clear-air echo near 0 Hz.

A number of different modes of operation of the RASS have been evaluated. The acoustic source, which is free running to ensure a flat spectrum over the range of operation [*Angevine et al.*, 1994a], is fed to a 1-kW audio amplifier which drives a vertically pointing stadium horn. Table 5 summarizes the mode of operation currently in use. Data are recorded for 6.4 s and then transferred to the computer; allowing for data transfer and power spectral analysis, the effective sample time is about 10 s. Usually, about 20–30 spectra are incoherently summed to improve the signal-to-noise ratios, which means that the time resolution of the temperature retrievals is 4–5 min. The spectral parameters for the acoustic echo are computed by the moment method, and the vertical velocity derived from the clear-air echo is used to correct the sound speed before it is converted to virtual temperature [e.g., *Angevine et al.*, 1994a].

Comparisons with RASS measurements and virtual temperatures computed from the temperature and humidity profiles derived from collocated radiosonde soundings are shown in Figure 13. RASS measurements were made over a period of 15–20 min near the time of the release of the sondes, and the values shown are the result of averaging four to five data sets so that the bars give an idea of the degree of variability in the retrieved temperatures. It is apparent that the agreement is excellent. The plots also illustrate that temperatures can be measured from heights as low as 500 m to as high as at least 2500 m. However, they also illustrate some of the difficulties that can be encountered with the present experimental setup. *Bauer and Peters* [1993] and *May*

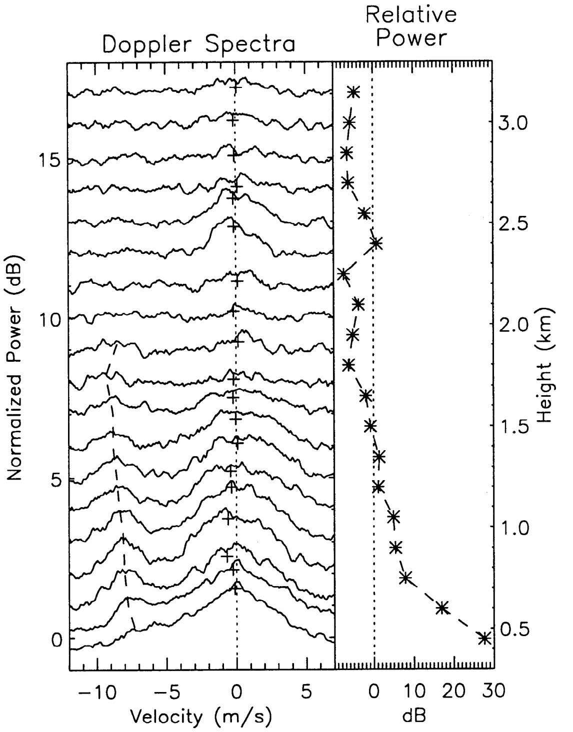

Figure 12. Stacked Doppler spectra obtained between 0400 and 0416 LT on September 14, 1997. At each height the first moment of the clear-air spectral peak, indicated by a plus sign, gives the vertical velocity. The dashed line shows the position of the peak of the precipitation echo. The vertical profile of relative echo power of the clear air peak is shown in the right panel.

et al. [1996] have shown that the RASS signal is focused onto a diffraction-limited spot approximately the size of the transmitting antenna. The small antennas used here mean that the acoustic spot is also small and is easily advected out of the radar beam by the background horizontal winds. It was necessary to carefully place the speaker upwind of the transmitting array to ensure the good height coverage evident in Figure 13a. Future developments include multiple acoustic sources.

4. Conclusions

Here we have discussed the development of a VHF (50 MHz) boundary layer radar and illustrated its capabilities with some of the first results obtained with the system. The system is compact and modular in nature so that it can be operated to use a range of wind-measuring techniques. A notable feature is that very useful wind and temperature measurements were obtained with quite small antennas for transmission and reception. The antennas are a compromise between wanting to make them as small as possible to minimize ringing and thus achieve the desired lower height limit and making them large enough to obtain sufficient gain to attain the desired upper height limit and to reduce clutter and interference.

Initial measurements made with the new boundary layer VHF radar show that its performance meets the design specifications, with wind and temperature measurements being made with good accuracy on a regular basis to over 2 km in altitude. The ability to distinguish rain echoes from the clear-air echo has also been demonstrated. This is an important attribute, which will allow the study of precipitation drop-size distributions to be extended downward into the boundary layer. Overall, the performance compares well with UHF profilers operating near 1 GHz at a similar stage of their development [*Ecklund et al.*, 1990; *Hashiguchi et al.*, 1995].

The next stage is to improve the height coverage. Wind and temperature measurements are made reg-

Table 5. Typical Radio Acoustic Sounding System Operating Parameters

Parameter	Value
Pulse repetition frequency*	20,480 Hz
Number of coherent integrations*	64
Number of data points per sample*	2,048
Height coverage*	100–3100 m
Record length	6.4 s
Range resolution*	150 m
Nyquist frequency	160 Hz
Acoustic frequency range*	118–126 Hz
Acoustic power	∼150 W
Acoustic excitation*	FM CW sawtooth sweep
Acoustic steps*	200
Frequency step*	0.04 Hz
Dwell time (per frequency step)*	100 ms

*Software selectable.

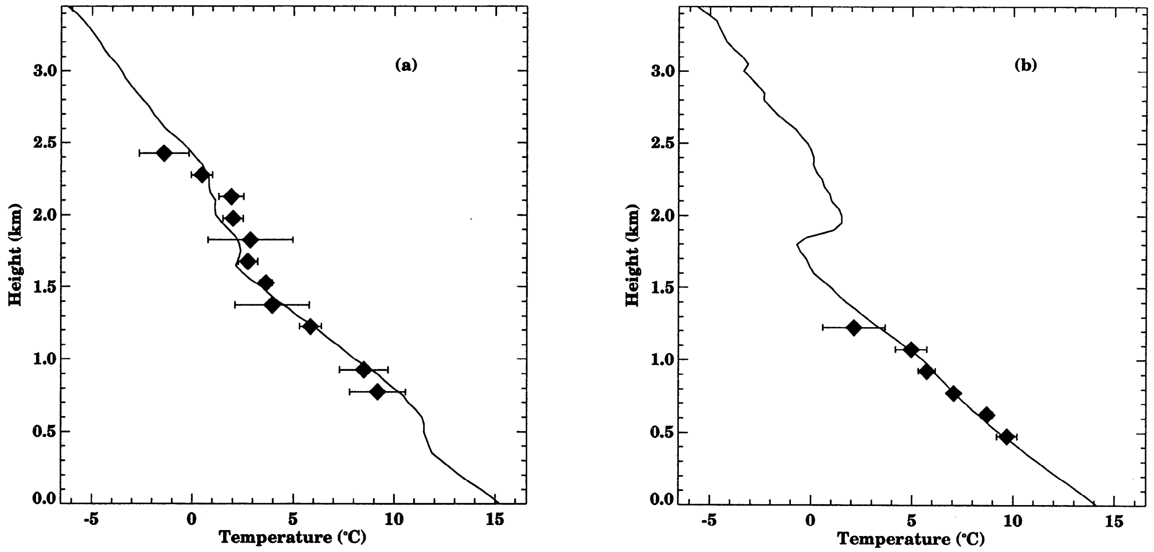

Figure 13. (a) Profile of virtual temperature derived from a radiosonde sounding at 1530 LT on October 18, 1997. Radio acoustic sounding system measurements made from 1500 to 1515 LT are indicated by diamonds. (b) Same as for (a), but for 1750 LT on October 19, 1997 with RASS measurements made from 1732 to 1805 LT.

ularly to heights as low as 450 m and sometimes as low as 300 m. Recent testing shows that it is possible to get to lower heights by using pulse lengths of 0.75 μs and exploiting the capacity of the system to make observations with a 100-m range resolution. Similarly, the upper height limit is improved by increasing the mean power, either by using pulse coding or using longer pulses to give a 300-m resolution. Using 300-m pulses, it has been possible to achieve observations as high as 5000 m. It should also be possible to use somewhat larger antennas for both transmission and reception, which will improve the power-aperture product and hence over-all system sensitivity. Tests of the system with these improvements are now in progress, as are tests using interferometric techniques to better define the dominant directions of scatter and correct the vertical velocities.

Acknowledgments. The development of the radar was made possible by the support of grant A69331543 from the Australian Research Council. The help and provision of radiosonde equipment by J. Stickland, Australian Bureau of Meteorology, and M. J. Reeder, Monash University, are gratefully acknowledged.

References

Angevine, W. M., and J. I. MacPherson, Comparison of wind profiler and aircraft wind measurements at Chebogue Point, Nova Scotia, *J. Atmos. Oceanic Technol., 12*, 421-426, 1995.

Angevine, W. M., W. L. Ecklund, D. A. Carter, K. S. Gage, and K. P. Moran, Improved radio acoustic sounding techniques, *J. Atmos. Oceanic Technol., 11*, 42-49, 1994a.

Angevine, W. M., A. B. White, and S. K. Avery, Boundary layer depth and entrainment zone characterization with a boundary layer profiler, *Boundary Layer Meteorol., 68*, 375-385, 1994b.

Bauer, M., and G. Peters, On the altitude coverage of temperature profiling by RASS, in *26th International Conference on Radar Meteorology*, pp. 487-489, Am. Meteorol. Soc., Boston, Mass., 1993.

Briggs, B. H., The analysis of spaced sensor records by correlation techniques, in *Handbook for MAP*, vol. 13, edited by R. A. Vincent, pp. 166-186, SCOSTEP, Secr. Univ. of Ill., Urbana, 1984.

Briggs, B. H., Radar measurements of aspect sensitivity of atmospheric scatterers using spaced-antenna correlation techniques, *J. Atmos. Sol. Terr. Phys., 54*, 153-165, 1992.

Carter, D. A., K. S. Gage, W. L. Ecklund, W. M. Angevine, P. E. Johnston, A. C. Riddle, J. Wilson, and C. R. Williams, Developments in UHF lower tropospheric wind profiling at NOAA's Aeronomy Laboratory, *Radio Sci., 30*, 977-1001, 1995.

Crochet, M., C. Bourdier, and E. Spano, VHF ST radar for low altitude investigations, in *Proceedings of the 6th Workshop on Technical and Scientific Aspects of MST Radar*, edited by B. Edwards, pp. 128-131, SCOSTEP, Secr. Univ. of Ill., Urbana, 1994.

Ecklund, W. L., D. A. Carter, and B. B. Balsley, A UHF wind profiler for the boundary layer: Brief description and initial results, *J. Atmos. Oceanic Technol., 5*, 432-441, 1988.

Ecklund, W. L., D. A. Carter, B. B. Balsley, P. E. Currier, J. L. Green, B. L. Weber, and K. S. Gage, Field tests of a lower tropospheric wind profiler, *Radio Sci., 25*, 899-906, 1990.

Fillol, J.-M., P. Broche, and M. Crochet, Retrieval of stratified atmospheric reflectivity and wind velocity using inverse methods: Application to a VHF ST mini-radar, *J. Atmos. Sol. Terr. Phys., 59*, 1159-1177, 1997.

Gage, K. S., Radar observations of the free atmosphere: Structure and dynamics, *Radar in Meteorology*, edited by D. Atlas, pp. 534-565, Am. Meteorol. Soc., Boston, Mass., 1990.

Hashiguchi, H., S. Fukao, T. Tsuda, M. D. Yamanaka, D. L. Tobing, T. Sribimati, S. W. Harijono, and H. Wiryosumarto, Observations of the planetary boundary layer over equatorial Indonesia with an L-band clear-air Doppler radar: Initial results, *Radio Sci., 30*, 1043-1054, 1995.

Holdsworth, D. A., Signal analysis with applications to atmospheric radars, Ph.D. thesis, 371 pp., Univ. of Adelaide, Adelaide, South Aust., Australia, 1995.

Jordan, J. R., R. J. Lataitis, and D. A. Carter, Removing ground and intermittent clutter contamination from wind profiler signals using wavelet transforms, *J. Atmos. Oceanic Technol., 14*, 1280-1297, 1997.

May, P. T., Spaced antenna versus Doppler radars: A comparison of techniques revisited, *Radio Sci., 25*, 1111-1119, 1990.

May, P. T., The Australian nocturnal jet and diurnal variations of boundary-layer winds over Mt. Isa in north-eastern Australia, *Q. J. R. Meteorol. Soc., 121*, 987-1003, 1995.

May, P. T., R. G. Strauch, and K. P. Moran, The altitude coverage of temperature measurements using RASS with wind profiler radars, *Geophys. Res. Lett., 15*, 1381-1384, 1988.

May, P. T., R. G. Strauch, K. P. Moran, and W. L. Ecklund, Temperature sounding by RASS with wind profiler radars: A preliminary study, *IEEE Trans. Geosci. Remote Sens., 28*, 19-28, 1990.

May, P. T., T. Adachi, T. Tsuda, and R. J. Lataitis, The spatial structure of RASS echoes, *J. Atmos. Oceanic Technol., 13*, 1275-1284, 1996.

Rajopadhyaya, D., P. T. May, and R. A. Vincent, A general approach to the retrieval of rain dropsize distributions from VHF wind profiler Doppler spectra: Modelling results, *J. Atmos. Oceanic Technol., 10*, 710-717, 1993.

Riddle, A. C., W. M. Angevine, W. L. Ecklund, E. R. Miller, D. B. Parsons, D. A. Carter, and K. S. Gage, In situ and remotely sensed horizontal winds and temperature intercomparisons obtained using integrated sounding systems during TOGA COARE, *Beitr. Phys. Atmos., 69*, 49-61, 1996.

Röttger, J., The MST radar technique, in *Handbook for MAP*, vol. 13, edited by R. A. Vincent, pp. 187-232, SCOSTEP, Secr., Univ. of Ill., Urbana, 1984.

Strauch, R. G., D. A. Merritt, K. P. Moran, K. B. Earnshaw, and D. Van de Kamp, The Colorado wind profiling network, *J. Atmos. Oceanic Technol., 1*, 37-49, 1984.

VanZandt, T. E., J. L. Green, K. S. Gage, and W. L. Clark, Vertical profiles of refractivity turbulence structure constant: Comparison of observations by the Sunset radar with a new theoretical model, *Radio Sci., 13*, 819-829, 1978.

Vincent, R. A., and J. Röttger, Spaced antenna VHF radar observations of tropospheric velocities and irregularities, *Radio Sci., 15*, 319-335, 1980.

Vincent, R. A., P. T. May, W. K. Hocking, W. G. Elford, B. H. Candy, and B. H. Briggs, First results with the Adelaide VHF radar: Spaced antenna studies of tropospheric winds, *J. Atmos. Sol. Terr. Phys., 49*, 353-366, 1987.

Weber, B. L., and D. A. Wuertz, Comparison of rawinsonde and wind profiler radar measurements, *J. Atmos. Oceanic Technol., 7*, 157-174, 1990.

Wilczak, J. M., et al., Contamination of wind profiler data by migrating birds: Characteristics of corrupted data and potential solutions, *J. Atmos. Oceanic Technol., 12*, 449-467, 1995.

Wilson, K. J., and H. Stern, The Australian summertime cool change, 1, Synoptic and sub-synoptic aspects, *Mon. Weather Rev., 113*, 177-201, 1985.

Wright, J. W., and M. L. V. Pitteway, Computer simulations of ionospheric radar drift measurements and their analysis by correlation methods, *Radio Sci., 13*, 189-210, 1978.

S. Dullaway, A. MacKinnon, I. M. Reid, R. A. Vincent, and F. Zink, Department of Physics, University of Adelaide, Adelaide, SA 5005, Australia. (e-mail: rvincent@physics.adelaide.edu.au)

B. H. Johnson, Atmospheric Radar Systems, 1/12 Sterling St., Thebarton, SA 5031, Australia. (e-mail: bjohnson@atrad.com.au)

P. T. May, Bureau of Meteorology Research Centre, PO Box 1289K, Melbourne, VIC 3001, Australia. (e-mail: p.may@bom.gov.au)

(Received December 17, 1997; revised March 5, 1998; accepted March 10, 1998.)

References

Adachi, T. (1996), Detailed Temperature Structure of Meteorological Disturbances Observed with RASS (Radio Acoustic Sounding System), PhD thesis, Kyoto University.

Adachi, T., Tsuda, T., Masuda, Y., Takami, T., Kato, S. & Fukao, S. (1993), 'Effects of the acoustic and radar pulse length ratio on the accuracy of radio acoustic sounding system (RASS) temperature measurements with monochromatic acoustic pulses', *Radio Science* **28**(4), 571–583.

Alvarez, H., Aparici, J., May, J. & Olmos, F. (1997), 'A 45-MHz continuum survey of the southern hemisphere', *Astron. Astrophys. Suppl. Ser.* **124**, 315–328.

Angevine, W. M. (1991), Temperature Profiling Using a 915 MHz Wind Profiler with RASS, *in* 'Proceedings of the 5th International Workshop on Technical and Scientific Aspects of MST Radar, Aberystwyth, UK, Aug. 6-9, 1991', pp. 155–156.

Angevine, W. M. & Ecklund, W. L. (1994), 'Errors in Radio Acoustic Sounding of Temperature', *Journal of Atmospheric and Oceanic Technology* **11**, 837–842.

Angevine, W. M. & MacPherson, J. I. (1995), 'Comparison of wind profiler and aircraft wind measurements at Chebogue Point, Nova Scotia', *Journal of Atmospheric and Oceanic Technology* **12**(2), 421–426.

Angevine, W. M., White, A. B. & Avery, S. K. (1994), 'Boundary-layer depth and entrainment zone characterization with a boundary-layer profiler', *Boundary Layer Meteorology* **68**, 375–385.

Arikawa, Y., Furumoto, J., Tsuda, T. & Adachi, T. (1998), Fine Structure of the Troposphere Observed with the MU Radar/RASS, *in* 'Fourth International Symposium on Tropospheric Profiling: Needs and Technologies, Snowmass, Colorado', pp. 16–18.

ARRL (1994), *The ARRL Antenna Book*, The American Radio Relay League.

Arshinov, Y. F., Bobrovnikov, S. M., Zuev, V. E. & Mitev, V. M. (1983), 'Atmospheric temperature measurements using pure rotational Raman lidar', *Applied Optics* **22**, 2984–2990.

Atlas, D., Srivastava, R. C. & Seckhon, R. S. (1973), 'Doppler Radar Characteristics of Precipitation at Vertical Incidence', *Reviews of geophysics and space physics* **11**(1), 1–36.

Baker, P. W. (1980), 'Estimation of the parameters of a turbulent drifting medium by a least squares analysis of spaced sensor measurements', *Radio Science* **16**(2), 213–217.

Balsley, B. B., Jensen, M. L. & Frehlich, R. G. (1998), 'The use of state-of-the-art kites for profiling the lower atmosphere', *Boundary Layer Meteorology* **87**, 1–25.

Baltink, H. K. (1998), Assesment of Accuracy of Boundary-Layer Windprofiler/RASS Data by Comparison with Tower Measurements, *in* 'Fourth International Symposium on Tropospheric Profiling: Needs and Technologies, Snowmass, Colorado', pp. 31–33.

Baltink, H. K. & Reid, I. M. (2000), CaPRIX: an intercomparison of a VHF and UHF lower tropospheric windprofiler, *in* 'Fifth International Symposium on Tropospheric Profiling: Needs and Technology, Adelaide Australia', pp. 261–263.

Barletti, R., Ceppatelli, G., Paterno, L., Righini, A. & Speroni, N. (1976), 'Mean vertical profile of atmospheric turbulence relevant for astronomical seeing', *J. Opt. Soc. Am.* **66**, 1380–1383.

Bowick, C. (1982), *RF Circuit Design*, H. W. Sams.

Bracewell, R. N. (1978), *The Fourier Transform and its applications*, McGraw-Hill.

Briggs, B. H. (1968), 'On the analysis of moving patterns in geophysics, - I. Correlation analysis', *Journal of Atmospheric and Terrestrial Physics* **30**, 1777–1788.

Briggs, B. H. (1980), 'Radar observations of atmospheric winds and turbulence: A comparison of techniques', *Journal of Atmospheric and Terrestrial Physics* **42**, 823–833.

Briggs, B. H. (1984), The analysis of spaced sensor records by correlation techniques, *in* 'Handbook for the Middle Atmosphere Program', Vol. 13, SCOSTEP Secretariat, University of Illinois, pp. 166–186.

Briggs, B. H. (1992), 'Radar measurements of aspect sensitivity of atmospheric scatterers using spaced-antenna correlation techniques', *Journal of Atmospheric and Terrestrial Physics* **54**(2), 153–165.

Briggs, B. H., Phillips, G. J. & Shinn, D. H. (1950), 'The analysis of observations on spaced receivers of the fading of radio signals', *Proc. Phys. Soc.* **63B**, 106–121.

Briggs, B. H. & Vincent, R. A. (1992), 'Spaced-antenna analysis in the frequency domain', *Radio Science* **27**(2), 117–129.

Brown, G. M. & Chapman, J. W. (1972), 'An investigation of the ground diffraction pattern of radio waves reflected by the ionosphere', *Journal of Atmospheric and Terrestrial Physics* **34**, 1445–1454.

Brown, J. H. & Good, R. E. (1984*a*), Thermosonde and UHF Radar Measurements of C_n^2 at Westford, Massachusetts - July 1981. AFGL-TR-84-0109.

Brown, J. H. & Good, R. E. (1984*b*), Thermosonde C_n^2 measurements in Hawaii - August 1982. AFGL-TR-84-0110.

Bufton, J. L., Minott, P. O., Fitzmaurice, M. W. & Titterton, P. J. (1972), 'Measurements of turbulence profiles in the troposphere', *J. Opt. Soc. Am.* **62**, 1068–1070.

Burke, G. J. & Poggio, A. J. (1977), *Numerical Electromagnetic Code (NEC) - Method of Moments*, Naval Technical Information Service (U.S. Department of Commerce).

Candusso, J. P., Crochet, M. & Pettré, P. (1998), Wind observation in the Troposphere: Comparison between radiosounding and small VHF profiler measurements in Adélie Land, Antarctica, *in* 'Fourth International Symposium on Tropospheric Profiling: Needs and Technologies, Snowmass, Colorado', pp. 46–48.

Carter, D. A., Ecklund, W. L., Gage, K. S., Spowart, M., Cole, H. L., Chamberlain, E. F., Dabbert, W. F. & Wilson, J. (1992), 'First Test of a Shipboard Wind Profiler', *Bulletin of the American Meteorological Society* **73**, 1587–1593.

Carter, D. A., Gage, K. S., Ecklund, W. L., Angevine, W. M., Johnston, P. E., Riddle, A. C., Wilson, J. & Williams, C. R. (1995), 'Developments in UHF lower tropospheric wind profiling at noaa's aeronomy laboratory', *Radio Science* **30**(4), 977–1001.

CEOS (2000), 'Committee on Earth Observation Satellites CDROM 2000', Centre National d'Etudes Spatiales.

Cervera, M. A. & Reid, I. M. (1995), 'Comparison of simultaneous wind measurements using colocated VHF meteor radar and MF spaced antenna radar systems', *Radio Science* **30**(4), 1245–1261.

Chadwick, R. B. & Moran, K. P. (1980), 'Long-term measurements of C_n^2 in the boundary layer.', *Radio Science* **15**(2), 355–361.

Chandra, H. & Briggs, B. H. (1978), 'The effect of filtering on ionospheric drift parameters determined by full correlation analysis', *Journal of Atmospheric and Terrestrial Physics* **40**, 541–548.

Chau, J. L. & Balsley, B. B. (1998*a*), 'Interpretation of angle-of-arrival measurements in the lower atmosphere using spaced antenna radar systems', *Radio Science* **33**(3), 517–533.

Chau, J. L. & Balsley, B. B. (1998*b*), 'A statistical comparison of VHF techniques to study clear-air vertical velocities in the lower atmosphere using the jicamarca radar', *Radio Science* **33**(6), 1565–1583.

Chau, J. L., Doviak, R. J., Muschinski, A. & Holloway, C. L. (2000), 'Tropospheric measurements of turbulence and characteristics of Bragg scatterers using the Jicamarca VHF radar', *Radio Science* **35**(1), 179–193.

Clifford, S. F., Wang, T. & Priestley, J. T. (1978), 'Spot size of the radar return from a radar-acoustic sounding system (RASS) due to atmospheric refractive turbulence', *Radio Science* **13**(6), 985–989.

Cohn, S. A. & Angevine, W. M. (2000), 'Boundary Layer Height and Entrainment Zone Thickness Measured by Lidars and Wind-Profiling Radars', *Journal of Applied Meteorology* **39**, 1233–1247.

Cohn, S. A., Brown, W. & Parsons, D. (2000), MAPR: An advanced UHF spaced antenna wind profiler, *in* 'Fifth International Symposium on Tropospheric Profiling: Need and Technology, Adelaide, Australia', pp. 61–63.

Cohn, S. A., Holloway, C. L., Oncley, S. P., Doviak, R. J. & Lataitis, R. J. (1997), 'Validation of a UHF spaced antenna wind profiler for high-resolution boundary layer observations', *Radio Science* **32**(3), 1279–1296.

Crochet, M. & Bourdier, C. (1989), 'Low Altitudes Investigations at VHF', *Handbook for the Middle Atmosphere Program* **28**, 564–566.

Crochet, M., Bourdier, C. & Spano, E. (1994), VHF ST radar for low altitude inverstigations, *in* 'Proceedings of the 6th International Workshop on Technical and Scientific Aspects of MST Radar, Chung-Li, Taiwan, Aug. 17-20, 1993', pp. 128–131.

Dalaudier, F., Sidi, C., Crochet, M. & Vernin, J. (1994), 'Direct Evidence of "Sheets" in the Atmospheric Temperature Field', *Journal of Atmospheric Sciences* **51**(2), 237–248.

Doviak, R. J., Lataitis, R. J. & Holloway, C. L. (1996), 'Cross correlations and cross spectra for spaced antenna wind profilers, 1. Theoretical analysis', *Radio Science* **31**(1), 157–180.

Doviak, R. J. & Zrnić, D. S. (1993), *Doppler Radar and Weather Observations*, 2nd edn, Academic Press.

Dullaway, S. (1999), A VHF Boundary-Layer Radar, Master's thesis, University of Adelaide.

Ecklund, W. L., Carter, D. A. & Balsley, B. B. (1988), 'A UHF Wind Profiler for the Boundary Layer: Brief Description and Initial Results', *Journal of Atmospheric and Oceanic Technology* **5**(3), 432–441.

Ecklund, W. L., Carter, D. A., Balsley, B. B., Currier, P. E., Green, J. L., Weber, B. L. & Gage, K. S. (1990), 'Field test of a lower tropospheric wind profiler', *Radio Science* **25**(5), 899–906.

Ecklund, W. L., Williams, C. R., Johnston, P. E. & Gage, K. S. (1999), 'A 3-GHz Profiler for Precipitating Cloud Studies', *Journal of Atmospheric and Oceanic Technology* **16**(3), 309–322.

Ehret, G., Hoinka, K. P., Stein, J., Fix, A., Kiemle, C. & Poberaj, G. (1999), 'Low stratospheric water vapor measured by an airborne DIAL', *Journal of Geophysical Research* **104**(31), 31,351–31,359.

Farley, D. T. (1983), Coherent integration, *in* 'Handbook for the Middle Atmosphere Program', Vol. 9, SCOSTEP Secretariat, University of Illinois, pp. 507–508.

Fedor, L. S. & Plywaski, W. (1972), 'The interpretation of ionospheric radio drift measurements-IV. The effects of signal coupling among spaced sensor channels', *Journal of Atmospheric and Terrestrial Physics* **34**, 1285–1303.

Feltz, W. F., Smith, W. L., Knuteson, R. O., Revercomb, H. E., Woolf, H. M. & Howell, H. B. (1998), 'Meteorological applications of temperature and water vapor retrievals from the ground-based atmospheric emitted radiance interferometer', *Journal of Applied Meteorology* **37**, 857–875.

Fillol, J. M., Broche, P. & Crochet, M. (1997), 'Retrieval of stratified atmospheric reflectivity and wind velocity using inverse methods: application to a VHF ST mini-radar', *Journal of Atmospheric and Terrestrial Physics* **59**(10), 1159–1175.

Foote, G. B. & duToit, P. S. (1969), 'Terminal velocity of raindrops aloft', *Journal of Applied Meteorology* **8**, 249–253.

Franke, S. J. (1990), 'Pulse compression and frequency domain interferometry with a frequency-hopped MST radar', *Radio Science* **25**(4), 565–574.

Frisch, A. S., Weber, B. L., Strauch, R. G., Merritt, D. A. & Moran, K. P. (1986), 'The Altitude Coverage of the Colorado Wind Profilers at 50, 405 and 915 MHz', *Journal of Atmospheric and Oceanic Technology* **3**, 680–692.

Gage, K. S. & Balsley, B. B. (1980), 'On the scattering and reflection mechanisms contributing to clear air radar echoes from the troposphere, stratosphere and mesosphere', *Radio Science* **15**, 243–257.

Gage, K. S., Balsley, B. B. & Green, J. L. (1981), 'Fresnel scattering model for the specular echoes observed by VHF radar', *Radio Science* **16**, 1447–1453.

Gage, K. S., Ecklund, W. L. & Balsley, B. B. (1985), 'A modified Fresnel scattering model for the parameterization of Fresnel returns', *Radio Science* **20**(6), 1493–1502.

Gage, K. S. & Green, J. L. (1978), 'Evidence for specular reflection from monostatic VHF radar observations of the stratosphere', *Radio Science* **13**(6), 991–1001.

Garratt, J. R. (1994), *The atmospheric boundary layer*, Cambridge University Press.

Gill, A. E. (1982), *Atmosphere-Ocean Dynamics*, Academic Press, San Diego.

Golley, M. G. & Rossiter, D. E. (1970), 'Some tests of methods of analysis of ionospheric drift records using an array of 89 aerials', *Journal of Atmospheric and Terrestrial Physics* **32**, 1215–1233.

Good, R. E., Watkins, B. J., Quesada, A. F., Brown, J. H. & Loriot, G. B. (1982), 'Radar and optical measurements of C_n^2', *Applied Optics* **21**(18), 3373–3376.

Görsdorf, U. & Lehmann, V. (2000), 'Enhanced Accuracy of RASS-Measured Temperatures Due to an Improved Range Correction', *Journal of Atmospheric and Oceanic Technology* **17**, 406–416.

Gossard, E. E. (1977), 'Refractive index variance and its height distribution in different air masses', *Radio Science* **12**(1), 89–105.

Gossard, E. E., Chadwick, R. B., Neff, W. D. & Moran, K. P. (1982), 'The use of ground-based doppler radars to measure gradients, fluxes and structure parameters in elevated layers', *Journal of Applied Meteorology* **21**, 211–226.

Gossard, E. E., Gaynor, J. E., Zamora, R. J. & Neff, W. D. (1985), 'Finestructure of Elevated Stable Layers Observed by Sounder and In Situ Tower Sensors', *Journal of Atmospheric Sciences* **42**(20), 2156–2169.

Grund, C. J., Banta, R. M., George, J. L., Howell, J. N., Post, M. J., Richter, R. A. & Weickmann, A. M. (2000), 'High-resolution Doppler lidar for boundary layer and cloud research', *Journal of Atmospheric and Oceanic Technology* . in press.

Hacker, J. M. (1997), From the atmospheric boundary layer into the stratosphere. The story of the airborne atmosphere research group of Flinders University, *in* 'Proceedings of the 20th OSTIV Congress, St. Auban, France'.

Hashiguchi, H., Fukao, S., Tsuda, T., Yamanaka, M. D., Tobing, D. L., Sribimawati, T., Harijono, S. W. B. & Wiryosumarto, H. (1995), 'Observations of the planetary boundary layer over equatorial Indonesia with an l-band clear-air Doppler radar: Initial results', *Radio Science* **30**(4), 1043–1054.

Hildebrand, P. H. & Sekhon, R. S. (1974), 'Objective Determination of the Noise Level in Doppler Spectra', *Journal of Applied Meteorology* **13**(10), 808–811.

Hobbs, B. G. (1998), Measurements of tropospheric scatter with a new multi-beam, multi-receiver VHF Doppler radar, PhD thesis, University of Adelaide, Adelaide, South Australia.

Hobbs, B. G., Reid, I. M. & Greet, P. A. (1996), 'Mesospheric rotational temperatures determined from the OH(6-2) emission above Adelaide, Australia', *Journal of Atmospheric and Terrestrial Physics* **58**(12), 1337–1344.

Hobbs, B. G., Reid, I. M. & Holdsworth, D. A. (2000), 'Evidence of tilted layers in angle of arrival and Doppler beam steering power measurements', *Radio Science* **35**(4), 983–997.

Hocking, W. K. (1983), 'On the extraction of atmospheric turbulence parameters from radar backscatter Doppler spectra - I. Theory', *Journal of Atmospheric and Terrestrial Physics* **45**(1), 89–102.

Hocking, W. K. & Mu, P. K. L. (1997), 'Upper and middle tropospheric kinetic energy dissipation rates from measurements of C_n^2 - review of theories, in-situ inverstigations, and experimental studies using the Buckland Park atmospheric radar in Australia', *Journal of Atmospheric and Terrestrial Physics* **59**(14), 1779–1803.

Hocking, W. K., Ruster, R. & Czechowsky, P. (1986), 'Absolute reflectivities and aspect sensitivities of VHF radio wave scatterers measured with the SOUSY radar', *Journal of Atmospheric and Terrestrial Physics* **48**(2), 131–141.

Hocking, W. K., Schmidt, G. & Czechowsky, P. (1983), Absolute calibration of the SOUSY VHF stationary radar. Max-Plank-Institut fur Aeronomie, Report PAE-W-00-83-14, Katlenburg-Lindau, F.R.G.

Holdsworth, D. A. (1995), Signal analysis with applications to atmospheric radars, PhD thesis, University of Adelaide, Adelaide, South Australia.

Holdsworth, D. A. (1999*a*), 'Influence of instrumental effects upon the full correlation analysis', *Radio Science* **34**(3), 643–655.

Holdsworth, D. A. (1999*b*), 'Spatial correlation analysis revisited: Theory, and application to "radar backscatter model" data', *Radio Science* **34**(3), 629–641.

Holdsworth, D. A. & Reid, I. M. (1995*a*), 'A simple model of atmospheric radar backscatter: Description and application to the full correlation analysis of spaced antenna data', *Radio Science* **30**(4), 1263–1280.

Holdsworth, D. A. & Reid, I. M. (1995*b*), 'Spaced antenna analysis of atmospheric radar backscatter model data', *Radio Science* **30**(5), 1417–1433.

Holland, G. J., Webster, P. J., Curry, J., Tyrrell, G., Gauntlett, D., Brett, G., Becker, J., Hoag, R. & Vaglienti, B. (2000), 'The aerosonde robotic aircraft: A new paradigm for environmental observations', *Bulletin of the American Meteorological Society* . submitted.

Holloway, C. L., Doviak, R. J., Cohn, S. A., Lataitis, R. J. & Van Baelen, J. S. (1997), 'Cross correlations and cross spectra for spaced antenna wind profilers, 2, Algorithms to estimate wind and turbulence', *Radio Science* **32**(3), 967–982.

Holton, J. . R. (1992), *An Introduction to Dynamic Meteorology*, third edn, Academic Press, New York.

Houghton, J. T. (1986), *The Physics of Atmospheres*, second edn, Cambridge University Press.

Houze, R. A. (1993), *Cloud Dynamics*, Academic Press.

Jordan, J. R., Leach, J. L., Costa, D. M., Templeman, B. D. & Neff, W. D. (2000), First tests of a buoy-mounted 915 MHz radar wind profiler, *in* 'Fifth International Symposium on Tropospheric Profiling: Needs and Technology, Adelaide, Australia', pp. 85–87.

Kelleher, R. F. (1966), 'Some statistical properties of the ground diffraction patterns of vertically reflected radio waves', *Journal of Atmospheric and Terrestrial Physics* **28**(2), 213–223.

Kessler, E., Eilts, M. & Thomas, K. (1986), 'A Look at Profiler Performance', *Handbook for the Middle Atmosphere Program* **20**, 72–84.

Klaus, V., Goupil, P., Seloyan, I., Chérel, G., Durbe, R. & Frappier, A. (2000), Extended Capabilities of the VHF Radar at CNRM New Developments and Experimental Results with RASS, *in* 'Fifth International Symposium on Tropospheric Profiling: Need and Technology, Adelaide, Australia', pp. 235–237.

Kraus, J. D. (1988), *Antennas*, second edn, McGraw-Hill.

Kropfli, R. A., Katz, I., Conrad, T. G. & Dobson, E. B. (1968), Simultaneous radar reflectivity measurements and refractive index spectra in the clear atmosphere, *in* 'Prepr. Radar Meteorol. Conf., 13th', pp. 270–271.

Kudeki, E. (1993), Radar interferometry in the frequency and spatial domain, *in* 'Proceedings of the 6th International Workshop on Technical and Scientific Aspects of MST Radar, Chung-Li, Taiwan, Aug. 17-20, 1993', pp. 234–237.

Kudeki, E. & Stitt, G. R. (1987), 'Frequency domain interferometry: A high resolution radar technique for studies of atmospheric turbulence', *Geophysical Research Letters* **14**(3), 198–201.

Kudeki, E. & Woodman, R. F. (1990), 'A post-statistics steering technique for MST radar applications', *Radio Science* **25**(4), 591–594.

Larsen, M. F. & Röttger, J. (1989), 'A Spaced Antenna Technique for Radar Wind Profiling', *Journal of Atmospheric and Oceanic Technology* **6**(6), 920–938.

Lataitis, R. J. & Clifford, S. F. (1996), 'Effect of atmospheric turbulence on the spot size of a radio-acoustic sounding system: A calculation revisited', *Radio Science* **31**(6), 1531–1540.

Lhermitte, R. (1987), 'A 94-GHz Doppler Radar for Cloud Observations', *Journal of Atmospheric and Oceanic Technology* **4**(1), 36–48.

Low, D. J. (1996), Studies of the lower atmosphere with a VHF wind profiler, PhD thesis, University of Adelaide, Adelaide, South Australia.

Lucas, C., Vincent, R. A., MacKinnon, A. D. & May, P. T. (2000), Rainfall and Drop Size Distribution Retrievals from a VHF Boundary Layer Radar, *in* 'Fifth International Symposium on Tropospheric Profiling: Need and Technology, Adelaide, Australia', pp. 397–399.

Luce, H., Dalaudier, F., Crochet, M. & Sidi, C. (1996), 'Direct comparison between in situ and VHF oblique radar measurements of refractive index spectra: A new successful attempt', *Radio Science* **31**(6), 1487–1500.

Marshall, J. M., Peterson, A. M. & Barnes. Jr., A. A. (1972), 'Combined radar-acoustic sounding system', *Applied Optics* **11**(1), 108–112.

Martner, B. E., Wuertz, D. B., Stankov, B. B., Strauch, R. G., Westwater, E. R., Gage, K. S., Ecklund, W. L., Martin, C. L. & Dabberdt, W. F. (1993), 'An Evaluation of Wind Profiler, RASS, and Microwave Radiometer Performance', *Bulletin of the American Meteorological Society* **74**(4), 599–613.

Masuda, Y. (1988), 'Influence of wind and temperature on the height limit of a radio acoustic sounding system', *Radio Science* **23**(4), 647–754.

Masuda, Y., Awaka, J., Nakamura, K., Adachi, T. & Tsuda, T. (1992), 'Analysis of the radio acoustic sounding system using a chirped acoustic wave', *Radio Science* **27**(5), 681–691.

Matuura, N., Masuda, H., Inuki, S., Kato, S., Fukao, S., Sato, T. & Tsuda, T. (1986*a*), 'Radio acoustic measurement of temperature profile in the troposphere and stratosphere', *Nature* **323**, 426–428.

Matuura, N., Masuda, Y., Inuki, H., Kato, S., Fukao, S., Sato, T. & Tsuda, T. (1986*b*), 'Radio acoustic measurement of temperature profile in the troposphere and stratosphere', *Nature* **323**, 426–428.

May, P. T. (1986), VHF radar studies of the troposphere, PhD thesis, University of Adelaide, Adelaide, South Australia.

May, P. T. (1988), 'Statistical errors in the determination of wind velocities by the spaced antenna technique', *Journal of Atmospheric and Terrestrial Physics* **50**(1), 21–32.

May, P. T. (1990), 'Spaced antenna versus Doppler radars: A comparison of techniques revisited', *Radio Science* **25**(6), 1111–1119.

May, P. T. (1993), 'Comparison of wind-profiler and radiosonde measurements in the tropics', *Journal of Atmospheric and Oceanic Technology* **10**(1), 122–127.

May, P. T., Adachi, T., Tsuda, T. & Lataitis, R. J. (1996), 'The Spatial Structure of RASS Echoes', *Journal of Atmospheric and Oceanic Technology* **13**, 1275–1284.

May, P. T., Moran, K. P. & Strauch, R. G. (1989), 'The Accuracy of RASS Temperature Measurements', *Journal of Applied Meteorology* **28**(12), 1329–1335.

May, P. T., Strauch, R. G. & Moran, K. P. (1988), 'The altitude coverage of temperature measurements using RASS with wind profiler radars', *Geophysical Research Letters* **15**, 1381–1384.

May, P. T., Strauch, R. G., Moran, K. P. & Ecklund, W. L. (1990), 'Temperature Sounding by RASS with Wind Profiler Radars: A Preliminary Study', *IEEE Transactions on Geoscience and Remote Sensing* **28**(1), 19–28.

Meek, C. E. (1990), 'Triangle size effect in spaced antenna wind measurements', *Radio Science* **25**(4), 641–648.

Mitra, S. N. (1949), 'A radio method of measuring winds in the ionosphere', *Proceedings of the Institute of electrical engineers* **96**, 441–446.

Moran, K. P. & Strauch, R. G. (1994), 'The Accuracy of RASS Temperature Measurements Corrected for Vertical Air Motion', *Journal of Atmospheric and Oceanic Technology* **11**, 995–1001.

Muschinsk, A. R. & Wode, C. (1998), 'First in situ evidence for coexisting submeter temperature and humidity sheets in the lower free troposphere', *Journal of Atmospheric and Terrestrial Physics* **55**(18), 2893–2906.

Muschinski, A. R., Frehlich, R., Jensen, M., Hugo, R., Hoff, A., Eaton, F. & Balsley, B. (2000), 'Fine-scale measurements of turbulence in the lower troposphere: An intercomparison between a kite and balloon-borne, and a helicopter-borne measurement system', *Boundary Layer Meteorology* . in press.

Nastrom, G. D., Gage, K. S. & Ecklund, W. L. (1986), 'Variability of Turbulence, 4-20 km, in Colorado and Alaska from MST Radar Observations', *Journal of Geophysical Research* **91**(D6), 6722–6734.

Nathanson, F. E. & Smith, P. L. (1972), A modified coefficient for the weather radar equation, *in* 'Prepr., Radar Meteorol. Conf., 15th', pp. 228–230.

North, E. M. & Peterson, A. M. (1973), 'RASS, a remote sensing system for measuring low-level temperature profiles', *Bulletin of the American Meteorological Society* **54**(9), 912–919.

Ochs, G. R. & Lawrence, R. S. (1972), Temperature and C_n^2 profiles measured over land and ocean to 3km above the surface. NOAA TR ERL 251-WPL 22 U. S. Dept. of Commerce.

Ottersten, H. (1969), 'Atmospheric structure and radar backscattering in clear air', *Radio Science* **4**(12), 1179–1193.

Palmer, R. D., Larsen, M. F., Woodman, R. F., Fukao, S., Yamamoto, M., Tsuda, T. & Kato, S. (1991), 'VHF radar interferometry measurements of vertical velocity and the effect of tilted refractivity surfaces on standard Doppler measurements', *Radio Science* **26**(2), 417–427.

Palmer, R. D., Woodman, R. F., Fukao, S., Tsuda, T. & Kato, S. (1990), ‘Three-antenna poststatistics steering using the MU radar’, *Radio Science* **25**(6), 1105–110.

Palmer, R. D., Yu, T. Y. & Chilson, P. B. (1999), ‘Range imaging using frequency diversity’, *Radio Science* **34**(6), 1485–1496.

Peters, G. (2000), Simultaneous Cloud Observations with K-Band Radar and LIDAR, *in* ‘Fifth International Symposium on Tropospheric Profiling: Needs and Technologies, Adelaide Australia’, pp. 193–195.

Peters, G. & Kirtzel, H. J. (1994), ‘Measurements of Momentum Flux in the Boundary Layer by RASS’, *Journal of Atmospheric and Oceanic Technology* **11**, 63–75.

Peters, G., Timmermann, H. & Hizpeter, H. (1983), ‘Temperature sounding in the planetary boundary layer by RASS - system analysis and results’, *Int. J. Remote Sensing* **4**(1), 49–63.

Rajopadhyaya, D. K., Avery, S. A., May, P. T. & Cifelli, R. C. (1999), ‘Comparison of precipitation estimation using single and dual frequency wind profilers’, *Journal of Atmospheric and Oceanic Technology* **16**, 165–173.

Rajopadhyaya, D. K., May, P. T. & Vincent, R. A. (1993), ‘A General Approach to the Retrieval of Raindrop Size Distributions from Wind Profiler Doppler Spectra: Modeling Results’, *Journal of Atmospheric and Oceanic Technology* **10**(5), 710–717.

Rapoport, V. O., Fedoseev, Y. G., Belova, N. I., Sazonov, Y. A. & Zinichev, V. A. (1996), ‘Operating decameter RASS near Nishny Novgorod and perspectives for far radio-acoustic sounding using the Sura HF-radar’, *Journal of Atmospheric and Oceanic Technology* **58**(8/9), 1033–1037.

Reid, I. M. (1988), ‘MF Doppler and spaced antenna radar measurements of upper and middle atmosphereic refractivity structures’, *Journal of Atmospheric and Terrestrial Physics* **50**(2), 117–134.

Reid, I. M. (1995), Radar Hardware, *in* ‘MST Second International School of Atmospheric radar, Hilton Head Island, South Carolina, USA’.

Reid, I. M., Johnson, B. H., Holdsworth, D. A., MacKinnon, A. D., Stickland, J., Sharp, A., Vincent, R. A. & Zink, F. (1998), A new VHF radar for use in Operational Meteorology, *in* ‘Fourth International Symposium on Tropospheric Profiling: Needs and Technologies, Snowmass, Colorado’, pp. 264–267.

Rishbeth, H. & Garriot, O. K. (1969), *Introduction to ionospheric physics, International geophysics series, Vol. 14*, Academic Press, New York.

Röttger, J. (1981), ‘Investigations of lower and middle atmosphere dynamics with spaced antenna drifts radars’, *Journal of Atmospheric and Terrestrial Physics* **43**(4), 277–292.

Röttger, J. (1989), 'The Instrumental Principles of MST Radars and Incoherent Scatter Radars and the Configuration of Radar System Hardware', *Handbook for the Middle Atmosphere Program* **30**, 54–113.

Röttger, J. & Ierkic, H. M. (1985), 'Postset beam steering and interferometer applications of VHF radars to study winds, waves, and turbulence in the lower and middle atmosphere', *Radio Science* **20**(6), 1461–1480.

Röttger, J. & Vincent, R. A. (1978), 'VHF radar studies of tropospheric velocities and irregularities using spaced antenna techniques', *Geophysical Research Letters* **5**(11), 917–920.

Rüster, R. (1994), 'Analysis and interpretation of VHF-radar data', *Ann. Geophysicae* **12**, 725–732.

Sharp, A. & Reid, I. M. (2000), Comparison of winds derived from atmospheric profiler and from balloon tracked by wind finding radar, *in* 'Fifth international symposium on Tropospheric Profiling: Needs and Technologies, Adelaide, Australia', pp. 121–123.

Sheppard, E. L., Larsen, M. F., Palmer, R. D., Fukao, S., Yamamoto, Y., Tsuda, T. & Kato, S. (1993), 'A statistical comparison of spaced antenna and spatial interferometry wind estimation', *Radio Science* **28**(4), 585–593.

Solheim, F. S., Godwin, J. R., Westwater, E. R., Han, Y., Keihm, S. J., Marsh, K. & Ware, R. (1998), 'Radiometric profiling of temperature, water vapor, and cloud liquid water using various inversion methods', *Radio Science* **33**, 393–404.

Stitt, G. R. & Bowhill, S. A. (1986), Improving range resolution with a frequency hopping technique, *in* 'Handbook for the Middle Atmosphere Program', Vol. 20, SCOSTEP Secretariat, University of Illinois, pp. 448–457.

Strauch, R. G., Merritt, D. A., Moran, K. P., Earnshaw, K. B. & Van de Kamp, D. (1984), 'The Colorado Wind-Profiling Network', *Journal of Atmospheric and Oceanic Technology* **1**(1), 37–49.

Takahashi, K., Masuda, Y., Matuura, N., Kato, S., Fukao, S., Tsuda, T. & Sato, T. (1988), 'Analysis of acoustic wavefronts in the atmosphere to profile the temperature and wind with a radio acoustic sounding system', *J. Acoust. Soc. Am* **84**(3), 1061–1066.

Tatarskii, V. I. (1961), *Wave propagation in a turbulent medium*, McGraw-Hill. Translated by R. A. Silverman.

Tatarskii, V. I. (1971), *The effects of the turbulent atmosphere on wave propagation*, U.S. Department of Commerce, Springfield, Virginia, pp. 74–76. Translated from the Russian, Israel Prog. for Sci. Translations.

Terman, F. E. & Pettit, J. M. (1952), *Electronic measurements*, second edn, McGraw-Hill.

Tsuda, T. (1989), ‘Data acquisition and processing’, *Handbook for the Middle Atmosphere Program* **30**, 151–189.

Tsuda, T., May, P. T., Sato, T., Kato, S. & Fukao, S. (1988), ‘Simultaneous observations of reflection echoes and refractive index gradient in the troposphere and lower stratosphere’, *Radio Science* **23**(4), 655–665.

Tsuda, T., Sato, T., Hirose, K., Fukao, S. & Kato, S. (1986), ‘MU radar observations of the aspect sensitivity of backscattered VHF echo power in the troposphere and lower stratosphere’, *Radio Science* **21**, 971–980.

Van Baelen, J. S., Tsuda, T., Richmond, A. D., Avery, S. K., Kato, S., Fukao, S. & Yamamoto, M. (1990), ‘Comparison of VHF Doppler beam swinging and spaced antenna observations with the MU radar: First results’, *Radio Science* **25**(4), 629–640.

VanZandt, T. E., Green, J. L., Gage, K. S. & Clark, W. L. (1978), ‘Vertical profiles of refractivity turbulence structure constant: Comparison of observations by the Sunset Radar with a new theoretical model’, *Radio Science* **13**(5), 819–829.

Vernin, J., Barletti, R., Ceppatelli, G., Paterno, L., Righini, A. & Speroni, N. (1979), ‘??’, *Applied Optics* **18**, 243–247.

Vincent, R. A. (1984), ‘MF/HF Radar Measurements of the Dynamics of the Mesopause Region - A Review’, *Journal of Atmospheric and Terrestrial Physics* **46**, 961–974.

Vincent, R. A., Dullaway, S., MacKinnon, A., Reid, I. M., Zink, F., May, P. T. & Johnson, B. H. (1998), ‘A VHF boundary layer radar: First results’, *Radio Science* **33**(4), 845–860.

Vincent, R. A. & Lesicar, D. (1991), ‘Dynamics of the equatorial mesosphere: First results with a new generation partial reflection radar’, *Geophysical Research Letters* **5**, 825–828.

Vincent, R. A., May, P. T., Hocking, W. K., Elford, W. G., Candy, B. H. & Briggs, B. H. (1987), ‘First results with the Adelaide VHF radar: Spaced antenna studies of tropospheric winds’, *Journal of Atmospheric and Terrestrial Physics* **49**(4), 353–366.

Vincent, R. A. & Röttger, J. (1980), ‘Spaced antenna VHF radar observations of tropospheric velocities and irregularities’, *Radio Science* **15**(2), 319–335.

Weber, B. L. & Wuertz, D. B. (1990), ‘Comparison of rawinsonde and wind profiler radar measurements’, *Journal of Atmospheric and Oceanic Technology* **7**(1), 157–174.

Weber, B. L., Wuertz, D. B., Strauch, R. G., Merritt, D. A., Moran, K. P., Law, D. C., Van de Kamp, D., Chadwick, R. B., Ackley, M. H., Barth, M. F., Abshire, N. L., Miller, P. A. & Schlatter, T. W. (1990), ‘Preliminary Evaluation of the

First NOAA Demonstration Network Wind Profiler', *Journal of Atmospheric and Oceanic Technology* **7**(6), 909–918.

White, A. B., Senff, C. J. & Banta, R. M. (1999), 'A Comparison of Mixing Depths Observed by Ground-Based Wind Profilers and an Airborne Lidar', *Journal of Atmospheric and Oceanic Technology* **16**, 584–590.

Wilczak, J. M., Strauch, R. G., Ralph, F. M., Weber, B. L., Merritt, D. A., Jordan, J. R., Wolfe, D. E., Lewis, L. K., Wuertz, D. B. & Gaynor, J. E. (1995), 'Contamination of Wind Profiler Data by Migrating Birds: Characteristics of Corrupted Data and Potential Solutions', *Journal of Atmospheric and Oceanic Technology* **12**(3), 449–467.

Woithe, J. (2000), Optical studies of the mesopheric region, PhD thesis, University of Adelaide, Adelaide, South Australia.

Woodman, R. F. & Guillén, A. (1974), 'Radar observations of winds and turbulence in the stratosphere and mesosphere', *Journal of Atmospheric Sciences* **31**, 493–505.

Wulfmeyer, V. & Bösenberg, J. (1998), 'Ground-based differential absorption lidar for water-vapor profiling: Assessment of accuracy, resolution, and meteorological applications', *Applied Optics* **37**, 3825–3844.

Wulfmeyer, V., Newsom, R. K., Senff, C. J. & Hardesty, R. M. (2000), Investigation of the structure of the tropical marine boundary layer using shipborne Doppler LIDAR, *in* 'Fifth international symposium on Tropospheric Profiling: Needs and Technology, Adelaide, Australia', pp. 127–129.